Proceedings of the 15th CEReS International Symposium on Remote Sensing

"Achievement and New Challenge of Environmental Remote Sensing"

December 15-16, 2009
Chiba University, Japan

Published by
Center for Environmental Remote Sensing (CEReS),
Chiba University, Japan
1-33 Yayoi-cho, Inage-ku, Chiba-shi, 263-8522 Japan

Cover Designed by T. Ishiyama

Proceedings of the 15th CEReS International Symposium on Remote Sensing

"Achievement and New Challenge of Environmental Remote Sensing"

December 15(Tue)-16(Wed), 2009

Organized by

Center for Environmental Remote Sensing (CEReS), Chiba University, Japan

(Editors)

N. Tsunematsu, A. Kondoh, and R. Tateishi

Contents

(Oral Session)

Current Status and Future Perspective of CEReS Satellites Data Archive and Distribution

Higuchi, A.[1*], M.K. Yamamoto[1], M. Hayasaki[1], H. Takenaka[1], T. Kitayama[1]
S. Aoki[1], M. Chiba[1], H. Kuze[1], A. Kondoh[1], J.T. Sri Sumantyo[1], F. Nishio[1]
[1]*Center for Environmental Remote Sensing (CEReS), Chiba University, 1-33 Yayoi, Inage, Chiba 263-8522, Japan*
**E-mail: higu@faculty.chiba-u.jp*

Abstract

Primary function of Center for Environmental Remote Sensing (CEReS) is to provide satellite dataset such as GMS, MTSAT-1R, and NOAA/AVHRR for research community. We started data archive system (DAS) re-construction since 2005. New DAS based on PC servers and RAID storages with Free Open Source Software (FOSS). Such configuration changes allow us to easy-expansion of DAS and random data access via internet, thus downloaded files by users have been increased since 2005. In addition, activities of Virtual Laboratory (VL) for diagnosing the climate system accelerate the volume of archived satellite data since 2007. Our primary task in VL is collection and utilizations of geostationary meteorological satellites, thus we re-process raw full-disk data into grided format (after geometric correction) and open through the internet. Such data processing is not only contributed to VL also related communities. We will play an important role as one of data active archive center (DAAC) in Asia for satellite and related dataset.

Keywords: CEReS, data archive system (DAS), geostationary meteorological satellites, virtual laboratory (VL)

1. Introduction

The earth observation from the space (satellite observations) is effective method to diagnose the earth environment. For more utilization of satellite data, the establishment of data active archive center (DAAC) was urgent issue. To account for the needs, Center for Environment Remote Sensing (CEReS) was established in 1995. From initial stage, CEReS was tasked to process and produce the basic satellite dataset as a function of DAAC.

2. History of CEReS DAAC

2.1. First stage (1995-2004)

After the CEReS establishment, we installed two receiving systems for GMS5 and NOAA/AVHRR. In addition, a tape archiver (300TB max. capacity) was installed. It was not suitable for random access, but it should be noted that it was best solution to account for technology in 1990's (**Fig. 1**).

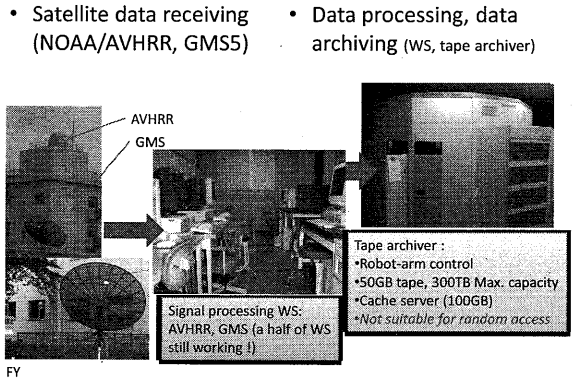

Fig. 1 Schematic illustration of DAAC in the first stage (1995-2004)

2.2. Second stage (2005-2006)

To satisfy the needs from users, we started to re-construct our data archive system (DAS). Since 2005, two PC servers with several RAID storages (total 12TB in capacity) were installed and operated (**Fig. 2**). New DAS was based on Free Open Source Software (FOSS) account for the scalability of easy-expansion (e.g., install additional RAID storage), easy-modification of configurations (version up). Most of advantage of adaptation of PC server based DAS is easy access to dataset via internet (by anonymous ftp protocol). In fact, download users were rapidly increased by the re-construction of DAS, thus our DAAC was truly renewal as D"A"AC.

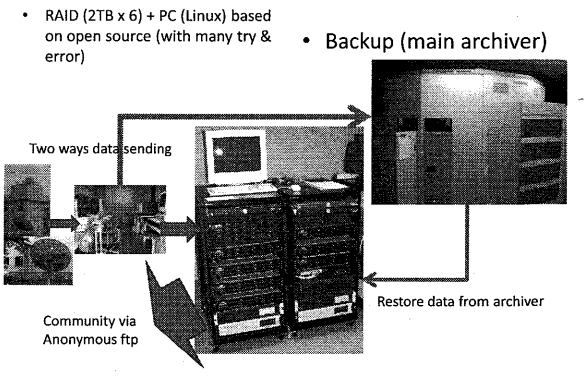

Fig. 2 Same as Fig. 1 but for the second stage (2005-2006)

3. Current DAAC activity highlights

3.1. Third stage of DAAC (start of VL: 2007-)

Since 2007, Virtual Laboratory (VL) for diagnose the Earth climate system with formation of Center for Climate

Table 1 Specifications of grided resampling format released by VL-CEReS for geostationary meteorological satellites.

GEO	Res.	Width	Grided	Release Status
MTSAT-1R	VIS: 0.01° IR: 0.04°	80° –200°	V.2.0 Released	Semi-Real time releasing
FY2-C, -D	0.04°	44.6° –164.6° (-C) 26° - 146° (-D)	V.2.0 Released	Semi-Real time releasing
METEOSAT (India)	0.04°	-2.5° –117.5°	V.1.95 (develop ver.)	Registration
METEOSAT	0.04°	-60° –60°	V. 1.95 (develop ver.)	Registration
GOES-W, -E	0.04°	225° –345° 165° –285°	V.2.0 Released	Semi-Real time releasing

Gridded resampling format (*level 1b*) Specification

- 60S – 60N, hourly (GOES 3 hourly, due to scan schedule)
- Data: image body (split each band), with calibration table
- 2 byte original data → big endian byte order
- Compressed by bzip2 (xxxxirx.tar.bz2, xxxxvis.tar.bz2)
- anonymous ftp servers (METEO restricted due to data policy)

System Research (CCSR) of Univ. Tokyo, Hydrospheric Atmospheric Research Center (HyARC) of Nagoya Univ., Center for Atmospheric and Oceanic Studies (CAOS) of Tohoku Univ. and CEReS. Our primary task in VL is to collect and utilized geostationary meteorological satellites (GEO, such as MTSAT-1R, FY2 series, Meteosat, MSG series and GOES-E, -W series; Yamamoto et al, 2009). To achieve them, we installed the receiving system for FY2 and define the output product to release dataset. Table 1 summarizes the specification of GEO product by VL-CEReS. We called gridded format of which already geometric correction procedure is conducted based on in-orbit navigation derived from header information of raw data. To account for re-radiometric calibration processes mentioned later, dataset consists of image body (filled by raw CCD count) and calibration table to convert from CCD to physical variables such as Tbb. Version 2 is the product of which improved the accuracy of geometric correction. Currently we collected a ten year (1998-2008) GEO and released via anonymous ftp servers as follows:

MTSAT-1R: *ftp://mtsat-1r.cr.chiba-u.ac.jp/*

FY series: *ftp://fy.cr.chiba-u.ac.jp/*

GOES series: *ftp://goes.cr.chiba-u.ac.jp/*

Meteosat and MSG[1]: *ftp://meteosat.cr.chiba-u.ac.jp/*

[1] Due to data policy of EUMETSAT, data access restricted authorized by IP clients and users.

Activities of VL-CEReS accelerate the number of downloaded files through the CEReS DAAC (**Fig. 3**) and capacity of DAS (**Fig. 4**). Until 10 December 2009) we have been performed 3.2 million data downloaded, furthermore number of downloaded files from outside of Chiba Univ. rapidly increased in 2009. To account for the scale of remote sensing-related communities, we truly contribute as one of DAAC in Japan. In the aspect of DAS, we re-constructed DAS approximately once per a year. Due to expensive management cost, we stopped the operation of a tape archiver in 2006.

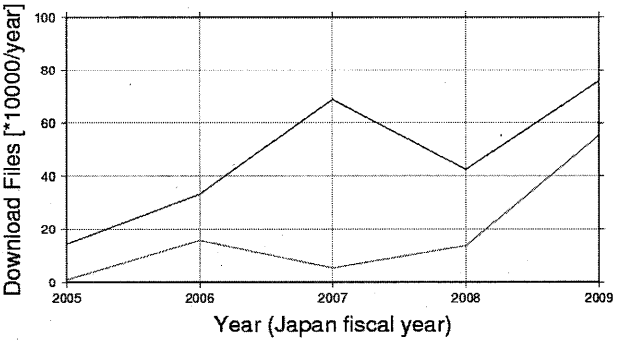

Fig. 3 Annual downloaded files from DAAC. Black line shows download from Chiba Univ., red line represents from outside of Chiba Univ. Unit is 10,000 files per year.

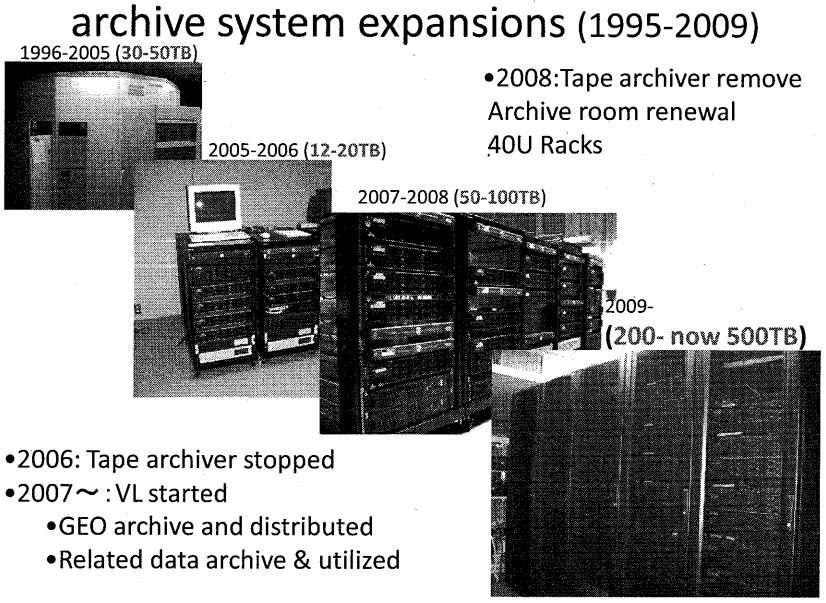

Fig. 4 Expansion of CRES-DAS since 1995.

A kind of risk owned by the operation stop of tape archiver; however the reduced costs can invest to new DAS. In 2008, replacement of tape archiver allows us to efficient space usage for DAS. In the end of 2008, we moved DAS into a new server room of which located tape archiver with enhancement of air-conditioner's power. With every-years re-construction of DAS, total capacity of DAS have been changed as 12-20 TB in 2005-2006, 50-100TB in 2007-2008 and 200-500TB in 2009. Now we face the door of "peta-byte (PB)" volume and it seems to open the door during 2010. Because we exactly need more data capacity to accelerate our activity.

3.2. Collaborations with several organizations

3.2.1. With Chiba Univ. Library (CUWiC)

Since 2006, we tried to collaboration with Chiba Univ. Library by the support of National Institute of Informatics (NII) e-Science project. In 2007, we made the prototype of searching engine of which can search article, report (CURATOR, developed by Library) and NOAA/AVHRR images. We called this system Chiba University Wisdom Collection (CUWiC http://cuwic.ll.chiba-u.jp/). Now CUWiC has a function of insert "tag" into each image by internet users, for example "a day of typhoon 16 attacked Japan". This challenge is one of tests how to utilize satellite image into other communities.

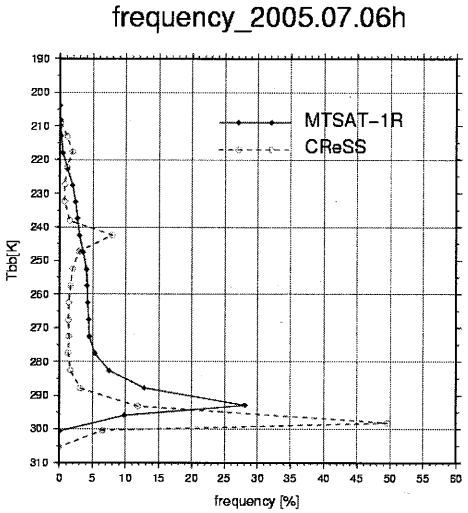

Fig. 6 Frequencies of Tbb in 2005 July 06UTC derived from CReSS-SDSU and MTSAT-1R (after Tsunashima, 2009).

3.2.2. Collaborations with atmospheric model developers (validation of CReSS; VL)

From the start of VL, we are done the performance check of Cloud Resolving Model (CRM) by satellite data one of our task for the collaborations. The Cloud Resolving Storm Simulator (CReSS) developing by Dr. Tsuboki, HyARC of Nagoya Univ. is research oriented CRM based on non-hydrostatic assumptions. We evaluated CReSS output through the Satellite Data Simulation Unit (SDSU) developed by Dr. Masunaga, HyARC of Nagoya Univ. with real-world satellite output such as MTSAT-1R, AMSR-E (Kato, 2008; Tsunashima,

2009; Hayasaki et al. 2009). Through a series of validation studies of CReSS, CReSS unfortunately tended to overshooting clouds (higher in cloud height, faster in cloud development stage: **Fig. 6**). This is relatively universal feature in CRM and recently CReSS improves microphysics then overshooting features reduced by the improvements (Hayasaki et al., 2009). Such interactions truly improve the CRM performance.

3.2.3. Collaborations with company (WNI) and operational agencies (MSC/JMA, GSICS)

Collaborations expand into the WNI and operational agencies (**Fig. 7**). In the case of WNI, since 2005, CEReS and WNI developed the system to provide radiation product based on MTSAT-1R (Takenaka et al., 2009, **Fig. 8**). Now we send the radiation product based on neural network to WNI, product is used to provide information of UV for cable TV in WNI. Such collaboration is one of linkage to the company.

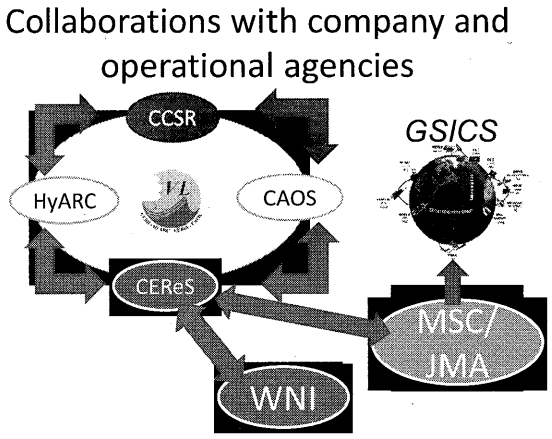

Fig. 7 Schematic illustration of collaborations with WNI and MSC/JMA, GSICS.

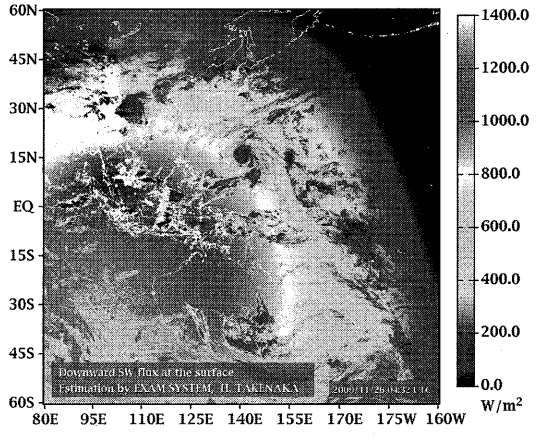

Fig. 8 Neural network retrieved downward solar radiation at the surface derived from MTSAT-1R.

To diagnose climate system by satellite data, calibrations of space-borne sensors is important issue. In VL-CEReS also pay attention about the calibration process. Global Space-based Inter-Calibration System (GSICS) is a framework of operational agencies under WMO. We also corroborate with Meteorological Satellite Center (MSC) in JMA to develop calibration methodologies for GEO, then updated (calibrated) GEO would be utilized for higher products such as radiation components.

4. Concluding remarks

We introduced our DAS and DAAC histories, current activities and collaborative researches examples briefly. As a future perspective, we will keep our function of DAAC as one of hub DAAC in Asia related satellite data. CEReS is now to having a responsibility to keep the function of DAAC as a nationwide corporation institute. Before to represent the responsibility, we truly need a big dataset to achieve our research, thus biggest users are ourselves. In addition, we will keep our DAAC position as a kind of "neutral" and "open" for all spectra. Essentially, university is based on the spirit of "open policy", we will follow it. Moreover, we will pay an attention for collaborative researches on the several ways. As introduced in this report, possibilities to utilize the satellites data are not small, so we will demonstrate "the power of satellite data". Finally, our DAS is always developing phase (with try and errors), so we also sometimes feel the difficulties to maintain our DAS. However we believe that we can enjoy the development of higher-stage DAS as a fun.

Acknowledgements

Our DAS and DAAC activities have been supported by the Ministry of Education, Science, Sports and Culture, Japan (MEXT) and Chiba University. In addition, we thank Dr. Kajiwara, (Dr. Kou, Dr. Shinagawa, Mr. Ikeda) who is (were) the staff of CEReS and contributed DAS.

References

1) Hayasaki et al (2009): AGU fall meeting

2) Kato, Y. (2008): Master Thesis, Graduated School of Science, Chiba University, Japan.

3) Takenaka et al (2009): JGR (revised).

4) Tsunashima, S. (2009): Graduation Thesis, School of Science, Chiba University, Japan.

5) Yamamoto et al (2009): AOGS meeting

Observation of Weather and Climate with the Meteosat and Metop Satellites

Johannes Schmetz, Dieter Klaes and Marianne König

EUMETSAT, 64295 Darmstadt, Germany

Abstract

The paper provides an overview of the meteorological satellite systems operated by EUMETSAT: The first generation of European geostationary Meteosat satellites started with the launch of Meteosat-1 in 1977 under the responsibility of ESA (European Space Agency). A series of seven satellites provided a continuous service acquiring half-hourly images in three spectral bands. Meteosat-7 is now still used for observing the Indian Ocean area. The advent of the first Meteosat Second Generation (MSG) satellite in 2002, renamed to Meteosat-8 with the start of operations, marked a major step forward in terms of observing capability. MSG satellites take images in twelve spectral channels every 15 minutes. The operational products derived from MSG data provide essential information for numerical weather prediction (NWP) and Nowcasting. The MSG system is now a dual satellite system with Meteosat-9 as prime satellite and Meteosat-8 providing rapid imaging services. Two more MSG satellites will be launched before the next generation (Meteosat Third Generation: MTG). The first polar orbiting meteorological satellite of EUMETSAT, named Metop-A, was launched in October 2006. Metop provides advanced observations of temperature and humidity profiles, wind, ozone and trace gases. The instrumentation is based on a continuity of known instruments and novel techniques. Notable are the hyperspectral thermal infrared observations with IASI (Infrared Atmospheric Sounding Interferometer) which also plays a key role for the observation of climate parameters and as reference instrument for satellite intercalibration . Two more Metop satellites are scheduled for launch.

1. INTRODUCTION

Operational meteorology utilizes two types of satellites to provide the required information: *Low Earth Orbiting (LEO)* satellites fly at relatively low altitudes of around 800 kilometres above the Earth, mostly in polar (sun-synchronous) orbits, and can provide information with higher spatial resolution. The whole surface of the Earth is then observed twice a day. More than one polar satellite, with different equatorial crossing times, is required for more frequent observations.

Geostationary satellites (GEO) are in the equatorial plane at an altitude of about 36,000 kilometres above Earth and have the same revolution time as the Earth itself and therefore always view the same area. They can perform frequent imaging and are ideal to observe rapidly changing phenomena like clouds and water vapour. The disadvantage of the geostationary orbit is the far distance from the surface/atmosphere system which puts stringent requirements on the signal-to-noise performance of the instruments.

EUMETSAT contributes to the global space-based observing system coordinated under CGMS (Coordination Group for Meteorological Satellites) and WMO (World Meteorological Organisation) with both types of meteorological satellites namely the Meteosat series in geostationary orbit and the Metop satellites in a sun-synchronous polar orbit with an Equator

crossing time at 0930LST (Local Solar Time)(descending clock).

2. FIRST GENERATION OF METEOSAT

The main instrument is a multispectral radiometer, which provided and still provides image data in three spectral bands:

- 0·5-0·9 μm visible band, 5 7 - 7·1 μm infrared water vapour (WV) absorption band, 10·5-12·5 μm thermal infrared window (IR) band.

Currently Meteosat-7 provides an operational service at 57° E over the Indian Ocean.

3. METEOSAT SECOND GENERATION (MSG)

Like the first Meteosat series the MSG satellites are spin-stabilized, however, capable of greatly enhanced Earth observations. The satellite's 12-channel imager, known as the spinning enhanced visible and infrared imager (SEVIRI), observes the full disk of the Earth with an unprecedented repeat cycle of 15 minutes in 12 spectral channels and improved spatial resolution (see Table 1). Meteosat-8 was launched in 2002 and Meteosat-9 followed in December 2005.

The MSG programme consists of a series of four identical satellites, expected to provide observations and services over at least 15 years. Each satellite has an operating lifetime of seven years. As with the first Meteosat system, the new generation, starting with Meteosat-8, is a dual-satellite service, with one additional satellite in orbit, primarily as back-up and useful for rapid scanning, i.e. for limited latitudinal scan with a shorter repeat cycle.

3.1. Earth imaging with the second generation of Meteosat

The primary mission of the second-generation Meteosat satellites is the continuous observation of the Earth's full disk with a multi-spectral imager. The repeat cycle of 15 minutes for full-disk imaging provides multi-spectral observations of rapidly changing phenomena such as deep convection. It also provides for better retrieval of wind fields, which are obtained from the tracking of clouds and water vapour features and gives unprecedented capabilities to detect preconvective instability and the change of cloud microphysics with time.

Channel No.	Spectral Band (μm)	Characteristics of Spectral Band (μm) for Meteosat-8		
		λ_{cen}	λ_{min}	λ_{max}
1	VIS0.6	0.635	0.56	0.71
2	VIS0.8	0.81	0.74	0.88
3	NIR1.6	1.64	1.50	1.78
4	IR3.9	3.90	3.48	4.36
5	IR6.2	6.25	5.35	7.15
6	IR7.3	7.35	6.85	7.85
7	IR8.7	8.70	8.30	9.1
8	IR9.7	9.66	9.38	9.94
9	IR10.8	10.80	9.80	11.80
10	IR12.0	12.00	11.00	13.00
11	IR13.4	13.40	12.40	14.40
12	HRV	Broadband (0.4 – 1.1 μm)		

Table 1: Spectral characteristics of the spinning enhanced visible and infrared imager (SEVIRI) on Meteosat-8 in terms of central, minimum and maximum wavelength of the channels .

The imaging is performed by utilizing the combination of satellite rotation and scan mirror stepping. The images are taken from south to north and east to west. The eight thermal IR and three solar channels have a sampling distance of three kilometers at nadir and scan the full disk of the Earth. The high-resolution visible channel provides images with one kilometer sampling at nadir. Data rate limitations confine the high-resolution visible images to half the Earth in an east-west direction; however, the exact coverage of the Earth is programmable. The SEVIRI data have a 10-bit digitization and the radiometric performance of Meteosat-8 (see Schmetz et al., 2002) is excellent and exceeds the specification by far.

As an additional scientific payload, MSG satellites carry a geostationary Earth radiation budget (GERB) instrument (Harries et al., 2005) that

observes the broadband thermal infrared and solar radiances exiting the Earth's atmosphere. GERB makes accurate measurements of the shortwave and longwave components of the radiation budget at the top of the atmosphere. GERB data are of interest for climatological studies and also for comparison with and validation of weather forecast models (Allan et al., 2005).

3.2. Products from Meteosat Second Generation

The application of the second generation of Meteosat satellites ranges from nowcasting and short-term forecasting to numerical weather prediction and climatological studies. Continuity for meteorological products from the first generation satellites is provided through products centrally derived at EUMETSAT. Those include inter alia atmospheric motion vectors (AMVs), cloud analysis (Lutz, 2000), and atmospheric humidity. In addition there are novel products such as atmospheric instability (König and de Coning, 2009) and total ozone derived over the entire MSG field of view.

The instability monitoring as an important novel application is described here in some more detail: Convective systems often develop in thermodynamically unstable airmasses. As the convective systems have the potential to develop into severe storms, it is of high interest to identify the storm potential while the system is still in a pre-convective state. A number of instability indices have been defined to describe such situations. Traditionally, these indices are taken from temperature and humidity soundings by radiosondes. As radiosondes have only of very limited temporal and spatial availability there is a demand for satellite-derived indices. The GII product consists of a set of indices which describe the layer stability of the atmosphere. It comprises four classic instability indices: i) the Lifted Index, ii) the K Index, iii) the KO Index, iv) the Maximum Buoyancy Index. The total precipitable water is added as a fifth index describing the airmass.

The retrieval of these parameters from satellite data is only possible under cloud-free conditions. Figure 1 depicts the Global Instability Index (GII) derived over Europe for 30 July 2006. It is an example of the Lifted Index, retrieved over 3x3 pixel areas, where negative values are indicative of potential instability. The region over central eastern Europe was on this particular day characterised by an unstable airmass, shown in yellow and red colours. White areas are clouds or the region outside the processing area.

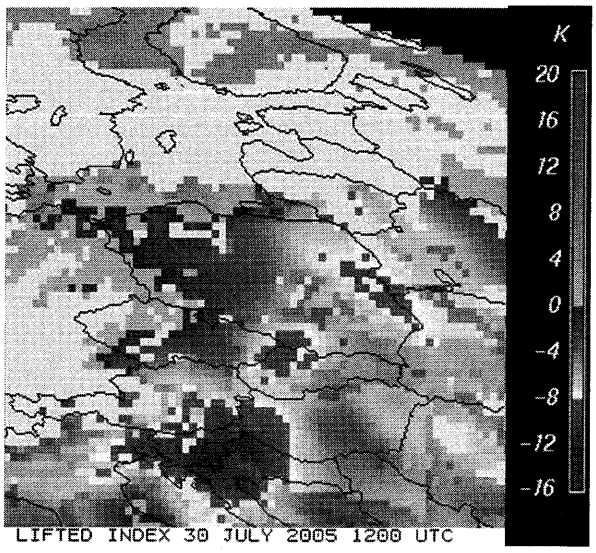

Figure 1: Lifted index computed from Meteosat-8 radiances for 30 July 2006 at 1200 UTC over central, Eastern Europe. Yellow and red indicates areas with instable airmass.

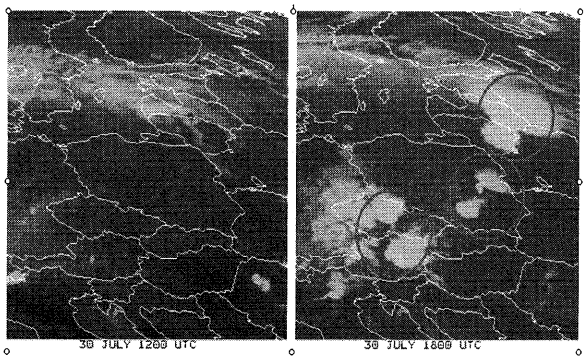

Figure 2: Meteosat-8 channel 9 images corresponding to the area in Figure 1. Left panel at 1200 UTC and right panel at 1800 UTC when strong convective system had formed.

Figure 2 is the IR window image at 1200 UTC (left panel) and at 1800 UTC (right panel), respectively. The midday image is basically cloud-free in the regions that are indicated as unstable in Figure 1. In the late afternoon at 1800 UTC we observe a strong storm activity. This example nicely depicts a case where instability indices, as they are derived in the GII product, are useful to anticipate the onset of strong convection.

Winds in terms of atmospheric motion vectors (AMVs) are the most important product from geostationary satellites for Numerical Weather Prediction (NWP) models. They are generated operationally by all of the operators of geostationary meteorological satellites. The

method of deriving a wind vector is in principle quite simple (e.g. Schmetz et al., 1993): cloud or water vapour features are tracked from one image to the next, thereby measuring a displacement vector. Assuming that the displacement vector represents a wind and assigning the vector to the correct height, one obtains a wind vector. The basic technique can be applied to clouds in both infrared and visible satellite imagery, as well as to other tracers, such as the patterns of atmospheric water vapour. Quite difficult is the height assignment of the displacement vectors, which often necessitates multispectral techniques (Nieman et al., 1993). And last but not least quality control is essential in order to produce good AMV products (Holmlund, 1998).

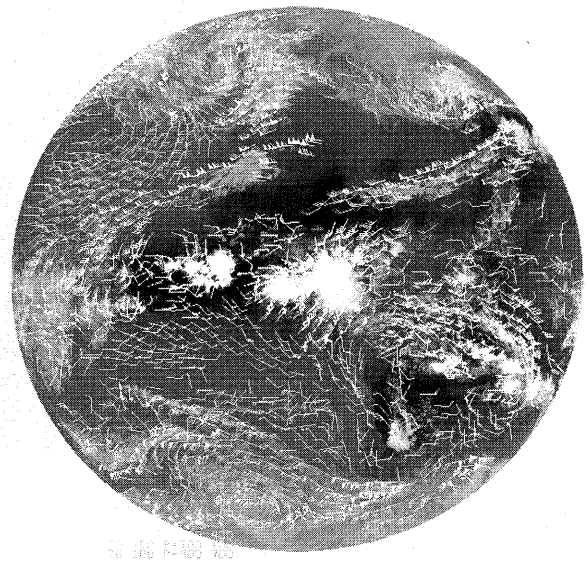

Figure 3: Example of an Atmospheric Motion Vector (AMV) product from Meteosat-8 for 23 February 2003. Different colours correspond to different altitudes.

4. THE EUMETSAT POLAR SYSTEM (EPS)/METOP

4.1. Overview

The first satellite of the EUMETSAT Polar System (EPS), called Metop series, was launched in October 2006. Metop-A provides advanced observations of temperature and humidity profiles, wind, ozone and other trace gases. The instrumentation of Metop is a judicious balance between continuity of known instruments and novel observations, notably the hyperspectral thermal infrared observations with an interferometer and radio occultation measurements. Metop satellites are also the European contribution to the space-based global observing system and to the joint European/US operational polar satellite system. Metop covers the mid-morning (9:30) orbit, whereas the US continues to cover the afternoon orbit. The three Metop satellites are expected to provide services for at least fourteen years. A detailed description is provided by Klaes et al. (2007).

With eight instruments taking observations of the earth-atmosphere system, Metop provides both continuity to previous operational measurements and also progress through data from novel instruments. AVHRR (Advanced Very High Resolution Radiometer), and the Advanced TIROS (Television and Infrared Operational Satellite) Operational Vertical Sounder (ATOVS) package, composed of HIRS-4 (High Resolution Infrared Radiation Sounder), AMSU-A (Advanced Microwave Sounding Unit - A) and MHS (Microwave Humidity Sounder). MHS is a EUMETSAT development and replaced the AMSU-B instrument in the ATOVS suite, while NOAA provides the AMSU-A, HIRS/4 and AVHRR instruments. MHS is already in space since the launch of NOAA-18 in May 2005.

The IASI (Infrared Atmospheric Sounding Interferometer) instrument is novel technology, developed by CNES, and introduces hyperspectral resolution sounding capabilities in the infrared (Hébert et al., 2004).

Some payload components have been developed from the heritage of proven research missions of the European Space Agency (ESA). One of these components is GOME-2 (Global Ozone Monitoring Experiment, Callies et al., 2000) building on the heritage of GOME-1, another one is the ASCAT (Advanced Scatterometer, Gelsthorpe et al., 2000), which draws on the ERS active microwave instrument (AMI) heritage.

The impact of radio-occultation measurements like GRAS (GNSS Receiver for Atmospheric Sounding, von Engeln et al., 2009), has been successfully demonstrated through impact studies in Numerical Weather Prediction (Healy, 2008).

4.2. ATOVS

Continuity is an important aspect to operational services. For nearly two decades the information on temperature and humidity soundings and surface information (including

clouds) for numerical weather prediction and other applications, has been provided by the ATOVS suite supported by the AVHRR imager for both morning and afternoon missions, on the NOAA satellites. The instrument suite is common to the two components of the Initial Joint Polar System (IJPS), i.e. Metop-A and the future Metop-B (AM satellites) and NOAA-18 and the NOAA-19 (PM satellites). It consists of four instruments, three of which are provided by NOAA.

i) the High Resolution Infrared Radiation Sounder (HIRS/4) measures temperature and humidity of the global atmosphere in cloud-free or partly cloudy conditions and is or will be on Metop-A and -B. HIRS/4 is a filter-wheel radiometer, which measures radiances in 19 infrared channels, and one additional channel in the visible. An important improvement to HIRS/4 is the 10 km IFOV (Instantaneous Field of View) in contrast to the 20 km IFOV of the previous HIRS version.

ii) The Advanced Microwave Sounding Unit-A (AMSU-A) measures the temperature of the global atmosphere in nearly all weather conditions. AMSU-A provides microwave atmospheric measurements in 15 channels between 23.8 GHz and 89 GHz mainly for temperature sounding.

iii) The Microwave Humidity Sounder (MHS) provides atmospheric measurements in five microwave channels for humidity measurements. MHS has been developed under EUMETSAT responsibility and replaces the previous generation AMSU-B microwave humidity sounder. MHS has been flying on NOAA-18 – and NOAA-19 which are the first components of the IJPS (Initial Joint Polar System) in space - since May 2005 and February 2009 respectively.

iv) The Advanced Very High Resolution Radiometer (AVHRR/3) is a six channel imager and provides globally visible, near infrared and infrared imagery of clouds, the ocean and land surface. The AVHRR data on Metop are provided globally at the full resolution, i.e.1.1 km at nadir.

4.3. IASI

The Infrared Atmospheric Sounding Interferometer (IASI) introduces a new technology to operational satellite observation. The purpose of IASI to measure temperature, water vapour and trace gases at a global scale. The measurement principle is based on Michelson interferometry providing 8461 spectral channels, aligned in three bands between 3.62 μm (2760 cm^{-1}) and 15.5 μm (645 cm^{-1}). The unapodised resolution is between 0.3 and 0.4 cm^{-1}, with a spectral sampling of 0.25 cm^{-1}. IASI samples the earth-atmosphere system with instantaneous fields of views (IFOV) of 12 km at nadir and a sampling distance around 25 km. Included in the IASI instrument is an Integrated Imaging System (IIS). It is used to provide the Earth location of the IASI pixels at 1 km accuracy through co-registration with the AVHRR pixels during the Level 1 processing. The mapped AVHRR information is used to classify inhomogeneous IASI scenes (Phillips and Schlüssel, 2005) and to determine the cloud coverage within a IASI pixel. The IIS is a broadband radiometer sensitive between 10 and 12 μm.

IASI data is used in synergy with the microwave sounding instruments to which the scan is synchronized. Products include, besides Level 1 radiance spectra, vertical profiles of temperature, humidity and ozone at global scale. The accuracy is of the order of 1 K per 1 km layer for temperature and about 15% for humidity (Schlüssel and Goldberg, 2002) which can be achieved throughout most of the troposphere and lower stratosphere, however it is currently difficult to obtain closer to the surface. Important is that IASI radiances do provide the higher vertical resolution required by global NWP. In addition, greenhouse gases such as ozone, nitrous oxide, carbon dioxide, and methane are retrieved and contribute to environmental change monitoring (e.g. Turquety et al., 2004). Furthermore surface temperature, surface emissivity, and cloud characteristics are retrieved from IASI data. Figure 4 shows the high-resolution spectra in terms of equivalent brightness temperature from the IASI hyperspectral sounder for tropical (red), mid latitude (green) and a cold arctic (blue) atmospheres, respectively. Measurements at such high spectral resolution (8461 channels) provide the basis for resolving the vertical structure of temperature and humidity in an unprecedented way and also offer unique opportunities for climate monitoring. The impact of IASI on Numerical Weather Prediction (NWP) is very positive. In fact recent work at ECMWF has shown the outstanding importance of the microwave and hyperspectral infrared soundings (i.e. from IASI) on the numerical forecasts.

Furthermore IASI, together with the AIRS instrument of NASA, is a reference instrument for the operational satellite inter-calibration pursued in the WMO-led Global Space-based Satellite Intercalibration System (GSICS); for details see: http://gsics.wmo.int/

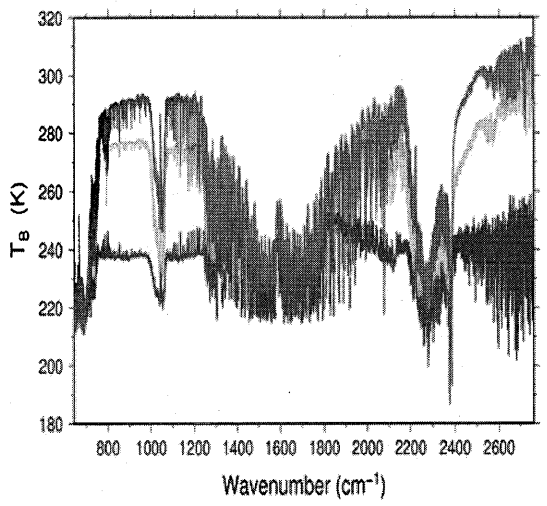

Figure 4: Spectra in terms of equivalent brightness temperature from the IASI hyperspectral sounder for tropical (red), mid latitude (green) and a cold arctic blue) atmospheres, respectively.

4.4. ASCAT and GOME–2

Two instruments on Metop have a heritage to missions on the ESA Earth Remote Sensing (ERS) Satellites, namely the Advanced Scatterometer (ASCAT) and the Global Ozone Monitoring Experiment (GOME-2).

i) The Advanced Scatterometer (ASCAT) provides near-surface wind speed and direction over the global oceans. ASCAT is a real aperture, vertically polarized C-band radar. ASCAT doubles the coverage of the surface (compared to the earlier instrument on ERS) with two swaths of measurements, one on each side of the sub-satellite track.
Six ASCAT antennas illuminate the surface sequentially with pulses at a carrier frequency of 5.225 GHz. The backscatter signal is measured to determine the Bragg scattering from the sea surface. Wind speed and direction are estimated using a model, which relates them to the normalised radar backscattering cross section ($\sigma 0$). The data are collected from three azimuth angles (45, 90 and 135 °) across both of the 550-km wide swaths on both sides of the nadir track. ASCAT provides ocean surface winds at 50 km resolution over a 25 x 25 km^2 grid along and across both swaths. In addition a high-resolution wind product is generated at 25-km horizontal resolution on a 12.5 x 12.5 km^2 grid.

ii) Global Ozone Monitoring Experiment (GOME-2) provides the possibility to monitor the Ozone total column and profiles and components related to Ozone chemistry in the Earth's atmosphere. The instrument on Metop profits from experience gained over many years of observation and data analysis with the GOME-1 instrument on ERS-2. GOME-2 has an increased spatial sampling of 80 x 40 km^2 , an increased Earth coverage due to increased swath width (1920 km), improved polarisation measurements (12 bands), enhanced on-board calibration through added white light source and increased spectral sampling.

GOME-2 measures the backscattered UV-VIS radiation in four band between 240 and 790 nm, at a spectral resolution between 0.25 and 0.5 nm. The accuracy of Ozone total column and profiles is better than 5 % and 15 % above 30 hPa respectively and better than 50 % below 30 hPa respectively. The objective is 3 % for columns and 10 % for profiles at all levels. Additional intended products are vertical columns of BrO, OClO, NO_2 and SO_2, which can be retrieved with accuracies better than 20 %.

4.5 GNSS Receiver for Atmospheric Sounding (GRAS)

GRAS measures the temperature of the upper troposphere and in the stratosphere with high vertical resolution in all weather conditions and potentially measures humidity in the troposphere (Klaes et al., 2007, von Engeln et al., 2009). GRAS makes use of the GPS (Global Positioning System) satellite constellation. An occultation occurs for GRAS whenever a GPS satellite rises or sets over the horizon as observed by Metop and the ray path from its transmitter traverses the Earth's atmospheric limb. The bending angle attributable to this ray contains information on the refractivity and thereby on temperature and humidity. With more than 30 GPS satellites, the GRAS instrument observes over 600 occultations per day, distributed quite

uniformly over the globe.

5. CONCLUDING REMARKS

Seven Meteosat's of the first generation provided and still provide operational services since 1977, imaging the full disk of the Earth every 30 minutes in three spectral bands. With Meteosat-8 a new series of geostationary satellites has started. Meteosat-9 is now the prime MSG satellite. MSG satellites now offer a wealth of new observational capabilities: The multispectral imaging and the high temporal repeat cycle benefit weather forecasting and will improve severe weather warning. Significant benefits come through the assimilation of products in numerical weather models and through improved Nowcasting applications (e.g. Menzel et al., 1998). Four Meteosat satellites of the second generation are foreseen to cover operational services until 2016 and beyond. Then the first Meteosat third generation satellite is expected to be launched.

The EUMETSAT Polar System (EPS) with the Metop satellites, developed jointly with the European Space Agency (ESA) and CNES, and had its first launch in October 2006. It establishes the European contribution to the global polar meteorological space observing capabilities. The Metop satellites form together with the NOAA (and in the future the NPOESS (National Polar Orbiting Environmental Satellite System)) satellites a joint polar system, with Metop serving the morning orbit around 0930h and the US satellites the 1330h Equator crossing time. Metop provides on the one hand continuity to current systems, through continuation of the proven ATOVS instrument suite and the AVHRR imager, on the other hand it includes novel capabilities, like IASI which provides high spectral resolution sounding and radiances very beneficial to NWP. Furthermore IASI has a high potential for climate monitoring because of its high spectral resolution, good calibration and good instrument characterisation; it is also a reference instrument for GSICS (Global Space-Based Intercalibration System). Instruments with heritage from ESA Earth observation missions (ASCAT and GOME-2) are utilised operationally and provide sea surface winds and soil moisture and ozone, aerosol and trace gas products, respectively. With GRAS the radio occultation principle is introduced for the first time into an operational satellite system and demonstrates the capability to provide high quality soundings in near real time from radiooccultation (von Engeln et al., 2009).The Metop satellites will provide more than 15 years of operations. They assure long-term and consistent observations that provide a sustained basis for improved utilization in NWP. Furthermore it is a key element for a sustained global climate-monitoring from satellite.

For details on instruments and general information the reader is referred to: www.eumetsat.int

6. REFERENCES

1) Allan R. P., A. Slingo, S.F. Milton and I. Culverwell 2005: Exploitation of Geostationary Earth Radiation Budget data using simulations from a numerical weather prediction model: Methodology and data validation. J. Geo. Res., 110, D14111, doi: 10.1029/2004JD005698

2) Harries J.E. et al. 2005: The Geostationary Earth Radiation Budget Project. Bull. Am. Meteorol. Soc., 86, 945-960

3) Healy S.B., 2008: Forecast impact experiment with a constellation of GPS radio occultation receivers. Atmospheric Science Letters, 9: 111-118, 2008.

4) Hébert, P., D. Blumstein, C. Buil, T. Carlier, G. Chalon, P. Astruc, A. Clauss, D. Siméoni, B. Tournier, 2004: IASI Instrument: Technical description and Measured Performances. Proceedings of the 5th International Conference on Space Optics (ICSO 2004), 30March –2 April 2004, Toulouse, 49 - 56.

5) Holmlund, K., 1998: The utilization of statistical properties of satellite-derived atmospheric motion vectors to derive quality indicators. Wea. and Forecasting. 13, 1093 -1104.

6) Klaes, K. D., M. Cohen, Y. Buhler, P. Schlüssel, R.Munro, J-P Luntama, A.von Engeln, E. Ó Clérigh, H. Bonekamp, J. Ackermann, J. Schmetz, 2007: An Introduction to the EUMETSAT Polar System (EPS/Metop). Bull. Amer. Met. Soc. Vol.88, No.7.

7) König, M., E. de Coning, 2009: The MSG Global Instability Indices Product and Its Use as a Nowcasting Tool. Amer. Met. Soc. Vol. 24, DOI:10.1175/2008WAF2222141.1

8) Lutz, H-J., 2000. Cloud Processing for Meteosat Second Generation. EUMETSAT Technical Memorandum No. 4

9) Menzel, J. M., F. C. Holt, T. J. Schmit, R. M. Aune, A. J. Schreiner, and D. G. Gray, 1998: Application of GOES-8/9 soundings to weather

forecasting and nowcasting. Bull. Amer. Meteor. Soc., 79, 2059-2077.
10) Nieman, S., J. Schmetz and W.P. Menzel, 1993: A comparison of several techniques to assign heights to cloud tracers. J. Appl. Meteorology, 1559 - 1568.
11) Phillips, P. and P. Schlüssel, 2005: Classification of IASI inhomogeneous scenes using co-located AVHRR data. Proceedings SPIE the International Society for Optical Engineering. Remote Sensing of Clouds and the atmosphere X Vol. 5979, pp 29-41.
12) Schlüssel, P. and M. Goldberg, 2002: Retrieval of Atmospheric Temperature and Water Vapour from IASI Measurements in partly cloudy situations. Adv. Space Res., Vol. 29, No. 11, 1703 – 2706.
13) Schmetz, J., K. Holmlund, J. Hoffman, B. Strauss, B. Mason, V. Gaertner, A. Koch and L. van de Berg, 1993: Operational cloud motion winds from METEOSAT infrared images, J. Appl. Meteorology, 32, 1206 - 1225.
14) Schmetz, J., P. Pili, S.A. Tjemkes, D. Just J. Kerkmann, S. Rota and A. Ratier, 2002: An Introduction to Meteosat Second Generation (MSG), Bull. Amer. Meteor. Soc., 83, 977-992
15) Turquety, S. Hadji-Lazaro, J. Clerbaux, C. Hauglustaine, D. A. Clough, S. A. Cassé, V. Schlüssel, P. Megie, G. 2004: Operational trace gas retrieval algorithm for the Infrared Atmospheric Sounding Interferometer. Journal of Geophysical Research Vol. 109 No. 21 pp. D21301
16) vonEngeln, A.., S. Healy, C. Marquardt, Y. Andres and F. Sancho, 2009: Geophysical Research Let., Vol. 36, DOI:10.1029/2009GL039968

Achievement of CEReS Research Projects

Project 1

Subject:
Monitoring and analysis of global surface environmental changes by satellite data

Members:
Ryutaro Tateishi, Akihiko Kondoh, Atsushi Higuchi, Chiharu Hongo, and Fumihiko Nishio

Objective of the project:
The final objective of this project is to understand the present situation and changes of global surface environment. The project consists of the following three parts. The first part is to produce global/local datasets of land cover, percent tree cover, snow/ice distribution from satellite data to know the present surface environment. The second part is to extract global surface changes by detecting vegetation changes from global 20-30 year satellite data and by analyzing it with climate data. The third part is to analyze detail environmental changes considering natural and human factors in Landsat scene scale of the test sites of East Asia.

Summary of Achievement
A new calibration method for global time series AVHRR data were developed, and user-friendly global MODIS data were published. Global land cover and percent tree cover data were completed and published with reference data. New findings were obtained by the analysis of global/continental vegetation changes as well as by the analysis of rice crop and meteorological conditions.

Details of Achievement

Achievement 1: Preprocessing of global satellite data

1-1 Re-calibration of NOAA/AVHRR over Land [1)]
NOAA/NASA Pathfinder AVHRR Land (PAL) is one of popular products for global vegetation monitoring. We reconsidered the radiometric re-calibration method of PAL as a function of the days after lunch for each spacecraft (NOAA-7, -9, -11, -14). After the re-calibration, it was confirmed that PAL data overestimated NDVI value in the period of NOAA-11.

1-2 Production of global MODIS data of 2003
User-friendly new global MODIS data observed in 2003 were produced. The source data are MOD43B4 NBAR, which are 16-day composite, 7-band, 1-km, 10-degree tile data. Cloud pixels in this source MODIS data observed in 2003 were removed by temporal interpolation. The cloud free MODIS data were reprojected into a latitude/longitude coordinate system, and mosaicked to produce data of five continents (Eurasia, North America, South America, Africa, and Oceania) and three island regions. The final MODIS products are available from http://www.cr.chiba-u.jp/databaseGGI.htm (GG-5).

Achievement 2: Production of global land cover data

2-1 Global land cover [2), 3)]
A new 1-km global land cover data were produced using the above MODIS 2003 data. This land cover product was produced as a part of Global Mapping project. The product is called Global Land Cover by National Mapping Organizations (GLCNMO). It has 20 land cover classes defined using the Land Cover Classification System (LCCS). The overall accuracy with the weight of the mapped area coverage is 72.1%. The land cover product is available from http://www.cr.chiba-u.jp/databaseGGI.htm (GG-6).
Furthermore, training data used in this project are available from the same site (GG-7),
and existing regional/national land cover maps used as references in this project are available from (GG-8).

2-2 Global percent tree cover [4)]
A new 1-km global percent tree cover data were produced using the above MODIS 2003 data. This product was produced as a part of Global Mapping project. The global percent tree cover product is available from http://www.cr.chiba-u.jp/databaseGGI.htm (GG-9).

Achievement 3: Findings in global/continental vegetation changes

3-1 Global vegetation changes by PAL datasets [5), 6)]
Decadal accumulation of Satellite Products such as PAL enables the extraction of inter-annual variation of vegetation status over the globe. Changes are explained by both climatic-driven and human-driven factors.

3-2 Vegetationl changes in Siberian-ecotone [7)]
Long-term satellite observations of Siberian-ecotone between tundra and boreal forest detect increasing trend of annual maximum NDVI, which may be the new signal of ecosystem change caused by global warming.

3-3 Global possible land cover changes by 1981-2000 AVHRR data [8)]
Possible land cover changed areas were mapped globally using 1981-2000 AVHRR data from the view point of

vegetation increase/decrease in time series AVHRR NDVI.

3-4 Regional differences in a surface temperature/vegetation index (TVX) matrix derived from AVHRR data [9)]

The combined analysis of a surface temperature and vegetation index both derived from NOAA/AVHRR were conducted over monsoon Asia. Over the Tibetan Plateau, two unique envelope TVX slopes can be found. The reason for two slopes is mainly due to the energy consumption in the melting layer.

Achievemnt 4: Cloud and precipitation system climatology revealed by TRMM and related space-borne sensors [10), 11)]

We mainly analyzed a ten years TRMM sensors (PR, TMI, VIRS) to focus on the spatial and seasonal features of clouds/precipitation. In the global scale, a half of captured images are covered by clouds. However, regional characteristics of cloud/precipitation are larger than amplitude of seasonal cycles in cloud/precipitation.

Achievement 5: Analysis of the relationships between meteorological elements and rice crop situation index [12), 13)]

An analysis of rice crop situation index and meteorological data of 50 years in the past shows that the rice crop situation index in the North Japan was affected by the cumulative temperature, and that the index of the southward from Tohoku tended to be affected by the sunshine duration. In the EL Nino and the La Nina year, except for Hokkaido, the index was affected by the sunshine duration than the cumulative temperature.

Publications

1) Kurita, H., A. Higuchi, Y. Kurosaki and K. Tanaka, Some considerations for the post-launch calibration of the visible and near-infrared channels in the Pathfinder AVHRR Land (PAL), Int. J. of Remote Sensing, 2009 (to be submitted).
2) Alimujiang Kasimu and Ryutaro Tateishi, GLCNMO global urban mapping, validation and comparison with existed global urban maps, Journal of the Remote Sensing Society of Japan, 28(5) 427-440, 2008
3) Ryutaro Tateishi, Javzandulam Tsend-Ayush, Mohamed Aboel Ghar, Hussam Al-Bilbisi, and Takaki Okatani, Sampling methods for validation of large area land cover mapping, Journal of the Remote Sensing Society of Japan, 27(3), 195-204, 2007
4) Rakhmatuloh, Daisuke Nitto, Hussam Al Bilbisi, Kota Arihara, and Ryutaro Tateishi, Estimating percent tree cover using regression tree method with very-high-resolution QuickBird images as training data, Journal of the Remote Sensing Society of Japan, 27(1),.1-12, 2007
5) Akihiko Kondoh, Vegetation and land cover change detection by global remote sensing and its causal analyses, Journal of Japan Society of Hydrology & Water Resources, 17(5), 459-467, 2004 (in Japanese with English Abstract)
6) Akihiko Kondoh, Ryutaro Tateishi, Eleonora Runtunuwu, Jong-Geol Park, Realting vegetation activity to climatic variation and atmospheric CO_2 content, Journal of Japan Society of Hydrology & Water Resources, 15(2), 128-138, 2002 (in Japanese with English Abstract)
7) Hideaki Sakai, Rikie Suzuki, Akihiko Kondoh, Recent signal of vegetation changes in Siberia using satellite data, Journal of Japan Society of Hydrology & Water Resources, 21(1), 50-56, 2008 (in Japanese with English Abstract)
8) Toshiyuki Kobayashi and Ryutaro Tateishi, Global possible land cover change mapping 1981-2000 time-series AVHRR/NDVI data, J. of the Remote Sensing Society of Japan,.27(3), 216-227, 2007 (in Japanese)
9) Higuchi, A., T. Hiyama, Y. Fukuta, R. Suzuki, Y. Fukushima, The behavior of a surface temperature/vegetation index (TVX) matrix derived from 10-day composite AVHRR images over monsoon Asia. Hydrological Processes, 21 (9), 1148-1156, 2007.
10) Yamamoto, K.M., F.A. Furuzawa, A. Higuchi and K. Nakamura, Comparison of diurnal variations in precipitation systems observed by TRMM PR, TMI and VIRS, J. of Climate, 21 (16), 4011-4028, 2008.
11) Yamamoto, K.M., A. Higuchi and S. Kikuchi, Climatological changes in rain and non-rain days over the East Asian region using long term rain gauge observation data. From Headwaters to the Ocean: Hydrological Changes and Watershed Management,Taniguchi et al. (Eds), Taylor & Francis, 31-35, 2009.
12) Chiharu Hongo, K. Niwa, J. Yokobori, R. Yamada and M. Kuwahara, Development of an efficient sugar beet cultivation support system using the agricultural spatial information –Prediction of root yield using meteorological data and satellite data-, Journal of Sugar Beet Research (in press)
13) Katsuhisa Niwa, Nobutaka Seino, Jun Yokobori, Koji Kikuchi and Chiharu Hongo, Effect of soil type on the time-course of changes in sugar beet(Beta vulgaris L.) productivity in Tokachi District, Hokkaido, Lapan, Soil Science and Plant Nutrition, 54, 928-937, 2008

Monitoring and analysis of global surface environmental changes by satellite data

Ryutaro Tateishi[1], Akihiko Kondoh[1], Atsushi Higuchi[1], Chiharu Hongo[1], and Fumihiko Nishio [1],

[1]*Center for Environmental Remote Sensing(CEReS), Chiba University*

1-33 Yayoi-cho, Inage-ku, Chiba 263-8522 Japan, tateishi@faculty.chiba-u.jp

Abstract

The Project 1 of the CEReS research project aims to understand the present situation and changes of global surface environment. This project is an integrated project of several sub-projects. This paper describes a framework of the Project 1 and its achievements which include Re-calibration of NOAA/AVHRR over Land, Production of global MODIS data of 2003, Global land cover, Global percent tree cover and Behavior of a surface temperature/vegetation index (TVX) matrix derived from 10-day composite AVHRR images over monsoon Asia.

Keywords **:** land cover, percent tree cover, AVHRR, MODIS

1. Introduction (Framework of Project 1)

For the final goal of understanding global change, the Project 1 consists of the following three parts. The first part is to produce global/local datasets of land cover, percent tree cover, snow/ice distribution from satellite data to know the present surface environment. The second part is to extract global surface changes by detecting vegetation changes from global 20-30 year satellite data and by analyzing it with climate data. The third part is to analyze detail environmental changes considering natural and human factors in local scale of the test sites of East Asia.

Fig. 1 shows overall concept of the Project 1. In order to obtain global surface information, preprocessing of global satellite data is prerequisite. In this project two preprocessing has been completed. One is post-launch calibration of Pathfinder AVHRR Land (PAL) data. The other one is cloud removal of MODIS 16-day composite data.

In the step of "Mapping current environment", land cover and percent tree cover has been completed.

In the step of "Change/trend analysis," global/continental vegetation changes have been found[1)-5)].

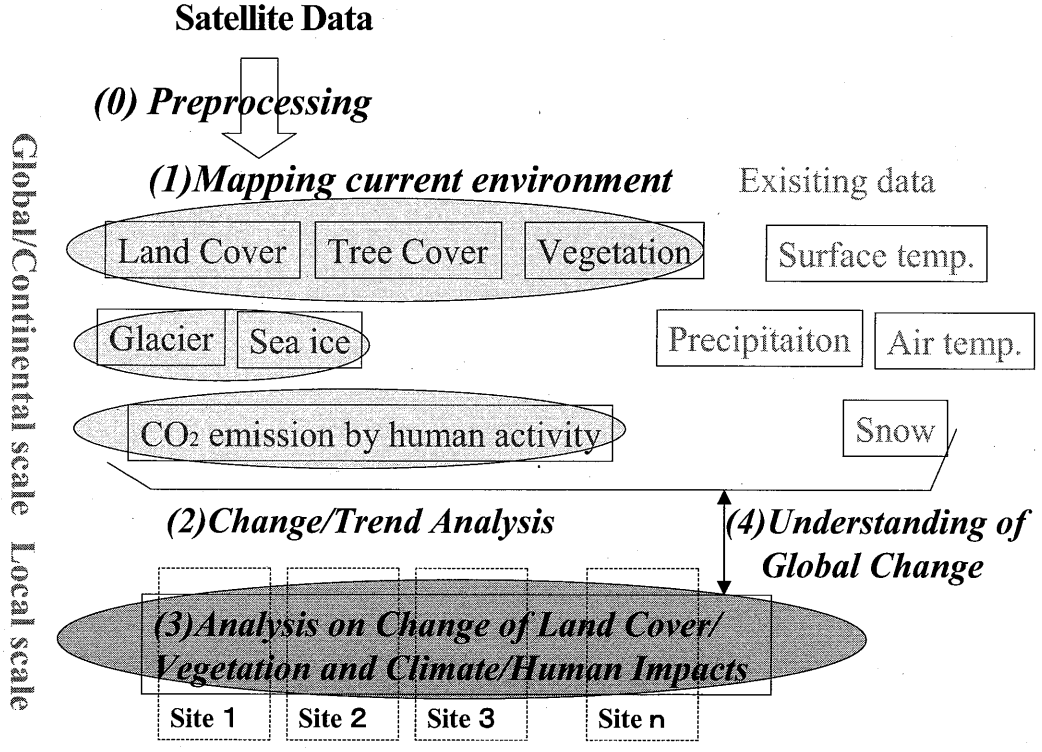

Fig. 1 Framework of Project 1

The environmental analysis of local scale focused on "analysis on change of land cover/vegetation and climate/human impacts" is closely related with the Project 4 of CEReS research projects, these are reported in the Achievement of Project 4.

2. Re-calibration of NOAA/AVHRR over Land[6)]

Long-term datasets derived by satellite observations are important for terrestrial studies. The longest records are daily daytime observations by the Advanced Very High Resolution Radiometers (AVHRRs) carried on NOAA spacecrafts. However, NOAA/AVHRR data are affected by spacecraft orbital delay (SOD). To address these effects, the Pathfinder AVHRR over Land (PAL) data have been derived from NOAA/AVHRR data using a time-dependent calibration method. This study examined the effect of time-dependent calibration on PAL and proposes a recalibration approach using optical channels. To evaluate the calibration effect, daily PAL (Daily-PAL) data were used, with bright clouds sampled as a white reference. The time series from clouds samples showed increasing trends in the visible channels of NOAA-14 and in the near-infrared channels of NOAA-9, -11, and -14. To recalibrate these data, the proposed time-dependent recalibration formula was used. To assess the effect of the recalibration process on the estimated normalized difference vegetation index (NDVI), annual mean global maps were created for the periods of NOAA-11 and NOAA-14. For NOAA-11, the global mean differences of the original and recalibrated NDVI in 1989 and 1992 were -0.003762 and -0.016555, respectively. On the other hand, no significant effect of recalibration was confirmed in the NDVI for NOAA-14. For the NOAA-14 period, improving the quality of related parameters is important for improving the dataset.

3. Production of global MODIS data of 2003

Global MODIS data observed in 2003 were preprocessed for wide use of global environmental stidies. The source MODIS data are of the MODIS/TERRA Nadir BRDF-Adjusted Reflectance 16-DAY L3 Global 1 KM SIN Grid Product (MOD43B4 NBAR). These are 16-day composite, 7-band, 1-km, 10-degree tile data. The source MODIS data were reprojected into a latitude/longitude coordinate system, and mosaicked to produce data of five continents (Eurasia, North America, South America, Africa, and Oceania) and three island regions, as presented in Fig. 2. Mosaicking and reprojection were done using MODIS Reprojection Tool (MRT) software. Geometric accuracy after mosaicking is 141–277 m in RMSE for the east–west direction or north–south direction in each continent when compared with Landsat images from GLCF from the University of Maryland as a correct location.

Cloud-contaminated pixels were replaced through linear interpolation of two cloud-free pixels before and after the cloud pixel in cases where the cloud-contaminated period is equal or less than six 16-day periods. The cloud-contaminated pixel was replaced by the average of 2002 and 2004 MODIS data at the same location and the same time of the year if it is more than six 16-day periods. The processed MODIS data is available from from the CEReS website (http://www.cr.chiba-u.jp/databaseGGI.htm [GG-5]).

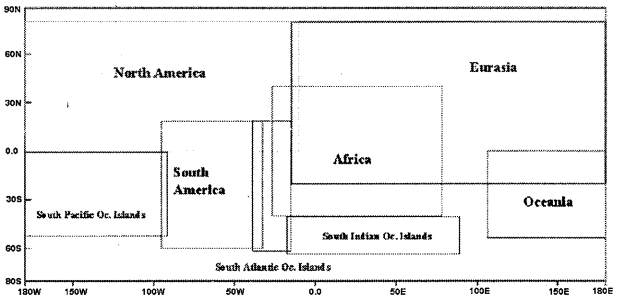

Fig.2 Regions of continental MODIS data

4. Global land cover

A 1-km global land cover dataset—Global Land Cover by National Mapping Organizations (GLCNMO)—was produced, as shown in Fig.3, both as the Project 1 of CEReS research project and as a part of Global Mapping project organized by the International Steering Committee for Global Mapping (ISCGM). It has 20 land cover classes defined using the Land Cover Classification System (LCCS). Of them, 14 classes were derived using supervised classification. The remaining six were classified independently: Urban, Tree Open, Mangrove, Wetland, Snow/Ice, and Water. Primary source data of this land cover mapping were eight periods of 16-day composite 7-band 1-km MODIS data of 2003. Training data for supervised classification were collected using Landsat images, MODIS NDVI seasonal change patterns, and comments from National Mapping Organizations with reference to Google Earth, Virtual Earth, and existing regional maps. The overall accuracy with the weight of the mapped area coverage is 81.2%, assessed using global 600 points collected through stratified random sampling. The data are available from the Global Mapping project website (http://www.iscgm.org/) or from the CEReS website (http://www.cr.chiba-u.jp/database

GGI.htm [GG-6]). The MODIS data used, land cover training data, and a list of existing regional maps are also available from the CEReS website. This mapping attempt demonstrates that training/validation data accumulation from different mapping projects must be promoted to support future global land cover mapping.

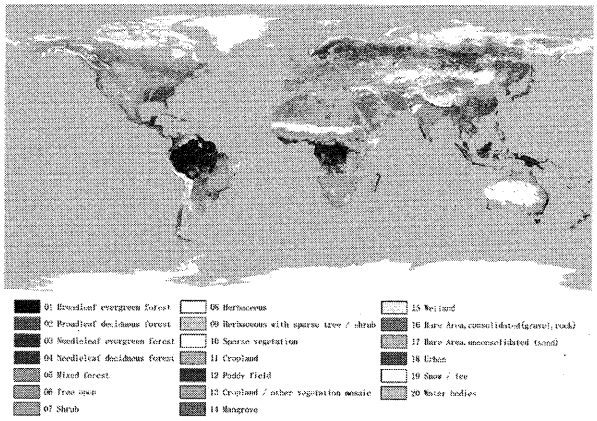

Fig.3 Global land cover - GLCNMO

5. Global percent tree cover

A 1-km global percent tree cover dataset was produced by the same project framework as the global land cover –GLCNMO, as shown in Fig. 4. It was produced from MODIS data of 2003 by the authors using decision tree method. Training data of the percent tree cover were collected globally from 221 sites with various land cover types. In fact, 68 sites are from pan-sharpened QuickBird images; 153 sites are from Google Earth images. Decision rules were obtained using MODIS predictor variables and training data using Cubist tool, a commercial regression tree program. Estimates of the percent tree cover from MODIS data were done using an NLCD mapping tool developed for a national land cover project of the United States Geological Survey (USGS). The produced data are available from the Global Mapping project website (http://www.iscgm.org/) or from the CEReS website (http://www.cr.chiba-u.jp/databaseGGI. htm [GG-9]).

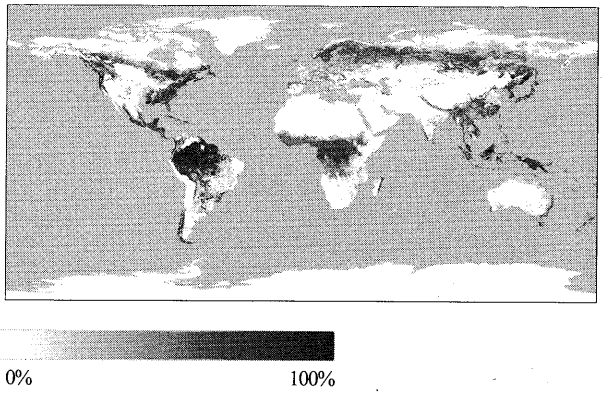

Fig.4 Global percent tree cover

5. The behavior of a surface temperature/vegetation index (TVX) matrix derived from 10-day composite AVHRR images over monsoon Asia[5)]

This study focuses on a Temperature/Vegetation Index (TVX) matrix that combines surface temperature (Ts) and a normalized difference vegetation index (NDVI). The results of our study show the behavior of the TVX matrix on continental scales. The study domain includes eastern Eurasia and monsoon Asia-regions with great variability in land-surface conditions. The data used included a 10-day composite Advanced Very High Resolution Radiometer (AVHRR) dataset compiled by the US Geological Survey (USGS). The relaxation in the determination algorithm for TVX slope (an upper envelope line in a TVX matrix box) was conducted to obtain both the negative and positive slope. The TVX slope can be derived from previous studies as the monsoon advanced and retreated over the tropics. However, over the Tibetan Plateau, a time series of the TVX slope showed an opposite sign compared to those in previous studies (represented by a positive TVX slope). Scatter plotting of the TVX matrix pixel sets was conducted for the evaluation of a variety of TVX matrix pixels. The TVX slope error sometimes occurred over arid regions because of a few green pixels corresponding to oases or irrigated areas. On the Tibetan Plateau,
'two' TVX slopes, both negative and positive, were found in the scatter plot. The reason for the two TVX slopes is the energy consumption in the soil, particularly, the phase change from frozen to liquid water (Fig.5). However, further study will be required to understand the mechanisms on the Plateau.

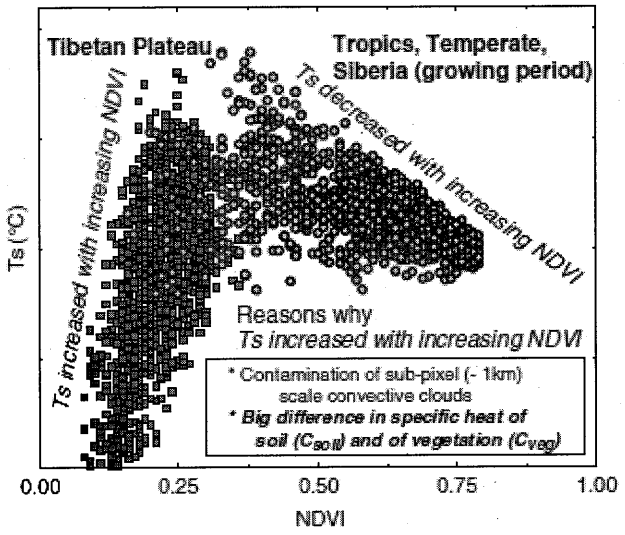

Fig. 5 Schematic diagram of 'two' TVX slopes in TVX matrixes (after Higuchi et al., 2007[5]).

References

1) Akihiko Kondoh, Vegetation and land cover change detection by global remote sensing and its causal analyses, Journal of Japan Society of Hydrology & Water Resources, 17(5), 459-467, 2004(in Japanese with English Abstract)

2) Akihiko Kondoh, Ryutaro Tateishi, Eleonora Runtunuwu, Jong-Geol Park, Realting vegetation activity to climatic variation and atmospheric CO_2 content, Journal of Japan Society of Hydrology & Water Resources, 15(2), 128-138, 2002 (in Japanese with English Abstract)

3) Hideaki Sakai, Rikie Suzuki, Akihiko Kondoh, Recent signal of vegetation changes in Siberia using satellite data, Journal of Japan Society of Hydrology & Water Resources, 21(1), 50-56, 2008(in Japanese with English Abstract)

4) Toshiyuki Kobayashi and Ryutaro Tateishi, Global possible land cover change map using 1981-2000 time-series AVHRR/NDVI data, J. of the Remote Sensing Society of Japan,.27(3), 216-227, 2007 (in Japanese)

5) Higuchi, A., T. Hiyama, Y. Fukuta, R. Suzuki, Y. Fukushima, The behavior of a surface temperature/ vegetation index (TVX) matrix derived from 10-day composite AVHRR images over monsoon Asia. Hydrological Processes, 21 (9), 1148-1156, 2007.

6) H. Kurita, A. Higuchi, Y. Kurosaki and K. Tanaka, Some considerations for post-launch calibration of visible and near-infrared channels of Pathfinder AVHRR Land (PAL), International Journal of Remote Sensing, 2009 (accepted)

Quantifying double- and triple- cropping areas in South Asia, using time-series MODIS images in 2005

Xiangming Xiao[1], Chandrashekhar Biradar[1], Audrey Wang[1]

[1] Department of Botany and Microbiology, and Center for Spatial Analysis, University of Oklahoma, 101 David L. Boren Blvd, Norman, OK 73019, USA, xiangming.xiao@ou.edu; chandra.biradar@ou.edu, audrey.wang@ou.edu

Abstract

South Asia, also known as Southern Asia (Pakistan, India, Bangladesh, Bhutan, Nepal, and Sri Lanka) has approximately one fifth of the world's population, and it is the most densely populated geographical region in the world. Agriculture intensification (e.g., double- and triple- crops in a year per unit cropland area, irrigation) in South Asia plays an important role in food security, water resources, carbon cycle and climate as well as animal health and human health. There is a need for mapping and monitoring spatial patterns and temporal dynamics of cropping intensity in South Asia. We have recently developed a mapping algorithm that is based on the temporal profile analysis (TPA) of vegetation indices (Normalized Differenced Vegetation Index (NDVI), Enhanced Vegetation Index (EVI), and Land Surface Water Index (LSWI)) for individual pixels and land cover types. The resultant cropping intensity maps were evaluated with agricultural census data from India. The TPA algorithm is applied to identify and map cropping intensity (double- and triple- crops in a year per unit cropland area) in South Asia, using the MODIS 8-day Land Surface Reflectance (MOD09A1) data in 2005 as input. The MODIS-based phenology algorithm estimates that South Asia a total area of 81.2 million ha of multiple- (including both double- and triple-) cropping area. The resultant MODIS-derived map of multiple-cropping croplands at 500-m spatial resolution in 2005 was compared with the state and district levels using the agricultural census data. The results of this study demonstrate the potential of the phenology algorithm in delineating multiple cropped areas.

Keywords: vegetation indices, multiple cropping,

1. Introduction

Traditional approaches for estimating cropland area and cropping intensity in a country are agricultural census statistics and land survey (Frolking et al. 2006; Qiu et al. 2003). These activities are often a time-consuming and resources-intensive process carried out by governmental agencies. Moreover, these statistics are not readily available to the public in the same calendar year.

Space-borne remote sensing technology provides an alternative and independent approach for mapping cropland area and cropping intensity in a country (Galford et al. 2008; Wardlow and Egbert 2008; Xiao et al. 2003). Over the last few decades satellite remote sensing has been widely used to map croplands at local, national and global scales (Dash et al. 2007; Frolking et al. 1999; Lobell and Asner 2004; Loveland et al. 2000; Thenkabail et al. 2005).

As part of the NASA Earth Observing System (EOS) program, the Moderate Resolution Imaging Spectroradiometer (MODIS) onboard the Terra satellite has acquired daily images of the globe since February 2000. Recently several studies have used MODIS data to map land cover at river basins in India, for example, the Ganges and Indus river basin (Thenkabail et al. 2005) and the Krishna river basin (Biggs et al. 2006). The MODIS data are also used to generate global land cover product at 1-km spatial resolution, including croplands (Friedl et al. 2002)..All of these regional and global land cover data products include the area and distribution of croplands, but they provide no information on cropping intensity (single-, double and triple cropping per unit of arable land).

The objective of our study is to assess the potential of MODIS images for identifying multiple (double- and triple-) cropping fields. India was selected as the case study area for MODIS-based large-scale mapping of cropping intensity because it has a large area of multiple cropping fields and ground-based survey data are available for the evaluation of MODIS-based maps. We have recently reported the resultant map of multiple cropping in India in 2005 (Biradar et al.

2009). In this paper we apply the same mapping algorithm to map multiple cropping in other South Asia countries (Pakistan, Bangladesh, Bhutan, Nepal, and Sri Lanka). Our specific objective is to generate an updated continental-scale database of cropping intensity in South Asia; and the resultant data product at moderate spatial resolution (500-m) could be used for various analyses that address food security, water use and management, biogeochemical cycles and climate in South Asia.

2. Data and Methods

2.1. Description of MODIS data

Moderate Resolution Imaging Spectroradiometer (MODIS) is an optical sensor onboard the Terra and Aqua satellites. MODIS scans the entire Earth's surface every 1 to 2 days, acquiring data in 36 spectral bands. Out of the 36 spectral bands, 7 bands are designed for the study of vegetation and land surfaces: blue (459–479 nm), green (545–565 nm), red (620–670 nm), near infrared (NIR1: 841–875 nm, NIR2: 1230–1250 nm), and shortwave infrared (SWIR1: 1628–1652 nm, SWIR2: 2105-2155 nm). Daily global imagery is provided at spatial resolutions of 250-m (red and NIR1) and 500-m (blue, green, NIR2, SWIR1, SWIR2). The MODIS Land Science Team provides a suite of standard MODIS data products to users, including the 8-day composite MODIS Surface Reflectance Product (MOD09A1). There are forty-six 8-day composites in a year, starting with Julian date of January 1 each year. The MOD09A1 data are organized in tile fashion and freely available to the public from the US Geological Survey EROS Data Center (http://edc.usgs.gov).

We downloaded the MDO09A1 datasets in 2005 from the USGS EDC website. For each MODIS 8-day composite the following four indices are calculated: (1) Normalized Differential Vegetation Index (NDVI; (Tucker 1979)), (2) Enhanced Vegetation Index (EVI; (Huete et al. 2002)), (3) Land Surface Water Index (LSWI; (Xiao et al. 2005b)) and (4) Normalized Difference Snow Index (NDSI(Hall et al. 2002)), using surface reflectance values from the blue, green, red, NIR1and SWIR1 bands (see equations below).

$$NDVI = \frac{\rho_{nir} - \rho_{red}}{\rho_{nir} + \rho_{red}}$$

$$EVI = 2.5 \times \frac{\rho_{nir} - \rho_{red}}{\rho_{nir} + 6 \times \rho_{red} - 7.5 \times \rho_{blue} + 1}$$

$$LSWI = \frac{\rho_{nir} - \rho_{swir}}{\rho_{nir} + \rho_{swir}}$$

$$NDSI = \frac{\rho_{green} - \rho_{nir}}{\rho_{green} + \rho_{nir}}$$

All these four indices are used in a number of large-scale agricultural studies (Xiao et al. 2006; Xiao et al. 2005a). Cloudy observations within a year (forty-six 8-day composites) were identified and gap-filled, following the procedure described in earlier studies (Xiao et al. 2006; Xiao et al. 2005a)

2.2. Description of agricultural statistical and census data

Agricultural census data were not readily available for the all South Asian countries. However, we have data for India, which covers more than 65% of the total land area in south Asia. Agricultural census data contain state-, district-, and *taluka*- level statistics on crop sown area, irrigated and arable land area, multiple cropping area (area sown more than once), total cropland area, and total sown area. These data usually collected from the village-level land records called *Patwaris* (village revenue agency). The data collected at this smallest administrative unit is aggregated (up-scaled) to the entire country through village, community development blocks, *taluka*, district and state.

2.3. MODIS-based phenology algorithm – temporal profile analysis approach

Seasonal dynamics of three vegetation indices were analyzed for identifying and mapping multiple croplands (double- and triple- croplands). Figure 1 shows seasonal dynamics of three vegetation indices in 2004-2005 for a double cropping site in India. For the first crop (crop-1), vegetation indices started to increase in June, which suggests that crops were planted when the rainy season (*Kharif*) arrived, reached a peak value in August, and then declined gradually until harvest took place in November. The second crop (crop-2), also called Rabi crop, starts to plant in February and is harvested in later April in the following year. The bimodal dynamics in Figure 1 represents the crop cycle in February – April (*Rabi*), and the crop cycle in June – early December (*Kharif*).

For identifying multiple cropping cycles in an image pixel, our temporal profile analysis of vegetation indices involve identification of lowest and highest EVI value for the first cycle (crop-1) and then for the second cycle form the second highest and lowest EVI values; and then repeat the procedure of trough search for the third vegetation growth cycle trough dates of LSWI time series (see Biradar and Xiao et al., 2009 for more details).

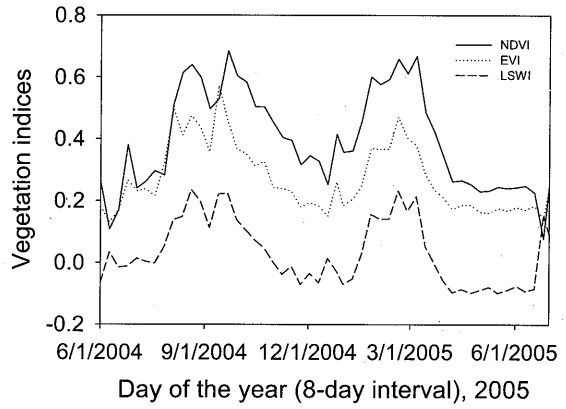

Figure 1. The seasonal dynamics of the vegetation indices form June 2004- June 2005; an example for the double cropland site in India

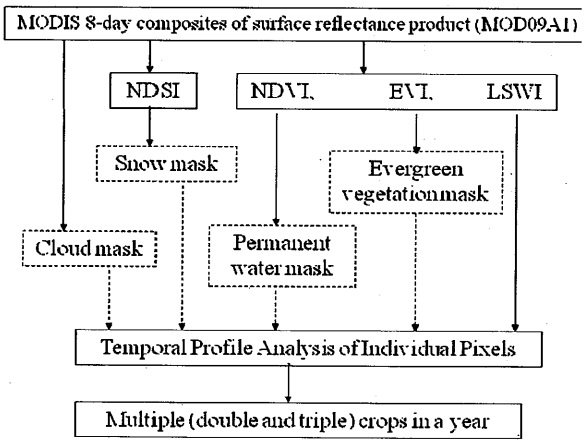

Figure 2. The schematic diagram for regional implementation of the phenology-based algorithm for identifying and mapping multiple cropping croplands, using the 8-day MODIS land surface reflectance product (MOD09A1), (from Biradar and Xiao, 2009, IJRS)

This computational algorithm is applied to all the individual pixels for delineating number of cropping cycles in a year. We assume that those pixels with two and triple vegetation growth cycles in a year as double- and triple- cropping croplands, respectively.

For regional implementation of the multiple-crop mapping algorithm, we first generated masks of snow cover, clouds, permanent water body and evergreen vegetation types (Figure 2), using the procedures that were described in details in a previous publication (Xiao et al., 2006). Those pixels that were identified as permanent water body and evergreen vegetation were excluded from analysis of multiple cropping.

3. Results

The MODIS-based phenology algorithm estimates 81.3 million ha of multiple cropping area in South Asia for the year 2005. Figure 3 shows the spatial distribution of multiple cropping areas (double- and triple- cropping fields) in 2005 in South Asia at 500-m spatial resolution. The multiple cropped fields occur extensively in India, Pakistan and Bangladesh and some extent in Sri Lanka, Myanmar, and Nepal. Double cropping area in India, Pakistan and Bangladesh occur largely in the floodplain and valleys of major rivers, for example, the Ganges and Indus river basins. India has the highest double cropped area (54.3 million ha) followed by Pakistan (12.5 million ha), Myanmar (6.4 million ha) and Bangladesh (4.1 million ha) (Table 1).

Table 1. A summary table of multiple (double- and triple-) cropping in South Asia countries, based on MODIS data and agricultural census data in 2005.

Country name	Total geographical area ($\times 10^3$ ha)	Multiple cropped area ($\times 10^3$ ha)	Total cultivated area ($\times 10^3$ ha)
Bangladesh	14,757.00	4,135.35	8,429.00
Bhutan	3,839.40	234.72	149.00
India	328,727.00	54,275.69	169,534.00
Maldives	29.8	0.84	12.00
Myanmar	67,657.80	6,414.87	10,611.00
Nepal	14,718.10	2,073.31	2,475.00
Pakistan	80,394.00	12,533.18	22,270.00
Sri Lanka	6,561.00	1,611.20	1,916.00
South Asia	516,684.10	81,279.15	215,396.00

The MODIS-based cropping intensity was evaluated with estimation from the national agricultural census data in India

(Biradar and Xiao 2009). The assessment results show an acceptable accuracy and performance of the Modis based algorithms for mapping cropping intensity. The multiple cropping statistics were not available for comparison of the MODIS estimates for the all south Asian nations. However, we have statistics for India, which contribute65% of the total multiple cropland area in South Asia. Table 2 shows the state-level comparison of the MODIS derived estimates with national agricultural census data. The comparison of the multiple-cropping area at the state level between the MODIS estimate in 2005 and the agricultural estimates in 2004/2005 shows a strong correlation (coefficient of determination r2=0.90; N=27). The accuracy assessment of the MODIS estimates shows the 81% agreement in double cropping. The detailed descriptions of accuracy assessment provided in the previous publication (Biradar and Xiao 2009).

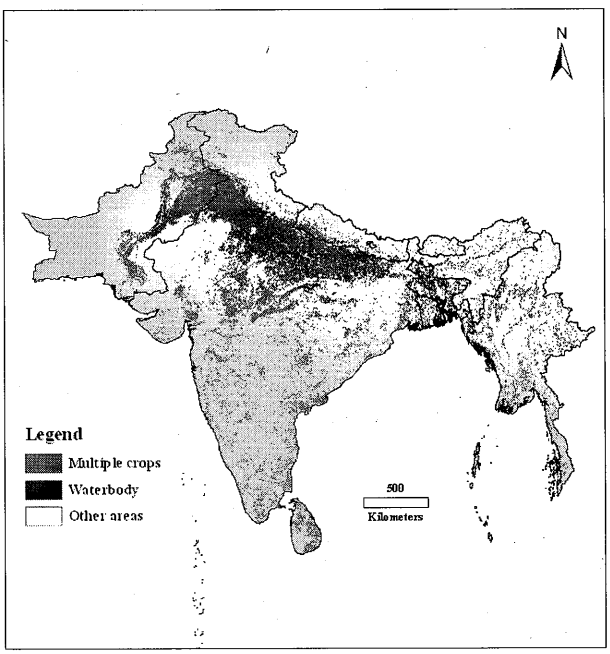

Figure 3. The spatial distribution of multiple cropping areas (double- and triple- crops in a year)) in the South Asia in 2005. It is derived from MODIS data in 2005 at 500-m spatial resolution.

4. Discussion and Summary

Agriculture is one major land use and land cover of the Earth. Because of the diverse range of natural environments and human needs, agriculture cover estimates makes an important contribution to the scientific community, the public, and decision-makers. The regular assessment of the agricultural intensification and geospatial information on crop intensity (number of crops per year), calendar (planting date, harvesting date), and irrigation is critically needed to better understand the impacts of agriculture on biogeochemical cycles (e.g., carbon, nitrogen, and trace gases), water, and climate dynamics.

Several earlier studies used complex methods to estimate vegetation phenology and forest cover assessment (Friedl et al. 2002; Galford et al. 2008; Sakamoto et al. 2006). In this study, we used a temporal profile analysis of MODIS-derive vegetation indices (NDVI, EVI and LSWI) to identify cropping intensity (double- and triple- cropping per year) at individual pixels over large spatial domains.

Table 2. State-level comparison of the multiple cropping area between the estimates from the national agricultural census in 2004-05 and the estimates in 2005 from the MODIS-based mapping in India.

States and Union Territories	Multiple cropping area in 2004/2005 by Agricultural Census ($\times 10^3$ ha)	Multiple cropping area in 2005 by MODIS-based mapping ($\times 10^3$ ha)
Andhra Pradesh	2,191	2,257
Arunachal Pradesh	91	111
Assam	1,209	1,120
Bihar	1,827	4,595
Chhattisgarh	946	277
Goa	36	9
Gujarat	1,570	1,455
Haryana	2,898	3,523
Himachal Pradesh	415	394
Jammu & Kashmir	349	514
Jharkhand	0	53
Karnataka	2,308	632
Kerala	841	229
Madhya Pradesh	5,228	8,145
Maharashtra	1,041	2,339
Manipur	0	48
Meghalaya	46	69
Mizoram	0	58
Nagaland	71	43
Orissa	2,979	458
Punjab	3,583	4,399
Rajasthan	4,514	5,249

Sikkim	0	5
Tamil Nadu	792	1,804
Tripura	0	39
Uttar Pradesh	16,683	17,631
Uttaranchal	468	334
West Bengal	4,149	1,977
Union Territories	43	75
Total (India)	54,276	57,841

This approach takes advantage of MODIS-derived time series data (at 8-day interval) of vegetation indices that vary seasonally and are correlated with biophysical and biochemical properties of vegetation and the land surface. The spatial pattern of multiple cropped areas derived from the MODIS images at 500-m pixel resolution (Figure 3 and table 2) generally agrees with that of national agricultural census data (Table1 2; also refer (Biradar and Xiao 2009).

In summary we report a simple approach that aims to map and monitor multiple cropping areas, using multi-temporal MODIS image data at 500-m spatial resolution (Figure 3). In this paper we generate geospatial datasets of cropping intensity for South Asia in 2005 at 500-m spatial resolution. The resultant geospatial dataset of multiple cropping area, could be used to address many important questions relevant to science and policy of global changes, including hydrology (Doll and Siebert 2002), climate, and health (Gilbert et al. 2007; Gilbert et al. 2008).

Acknowledgements

This study was supported by the NASA Interdisciplinary Science program (NAG5-10135), the NASA Land Cover and Land Use Change program (NAG5-11160, NNG05GH80G), the US National Institutes of Health Fogarty International Center (R01-TW007869), and the Wildlife Conservation Society, New York, USA.

References

1) Biggs, T.W., Thenkabail, P.S., Gumma, M.K., Scott, C.A., Parthasaradhi, G.R., & Turral, H.N. (2006). Irrigated area mapping in heterogeneous landscapes with MODIS time series, ground truth and census data, Krishna Basin, India. International Journal of Remote Sensing, 27, 4245-4266

2) Biradar, C., & Xiao, X. (2009). Quantifying the area and spatial distribution of double- and triple-cropping cropland in Inda with multi-temporal MODIS imagery in 2005. International Journal of Remote Sensing, In Press

3) Biradar, C.M., Thenkabail, P.S., Noojipady, P., Li, Y.J., Dheeravath, V., Turral, H., Velpuri, M., Gumma, M.K., Gangalakunta, O.R.P., Cai, X.L., Xiao, X.M., Schull, M.A., Alankara, R.D., Gunasinghe, S., & Mohideen, S. (2009). A global map of rainfed cropland areas (GMRCA) at the end of last millennium using remote sensing. International Journal of Applied Earth Observation and Geoinformation, 11, 114-129

4) Dash, J., Mathur, A., Foody, G.M., Curran, P.J., Chipman, J.W., & Lillesand, T.M. (2007). Land cover classification using multi-temporal MERIS vegetation indices. International Journal of Remote Sensing, 28, 1137-1159

5) Doll, P., & Siebert, S. (2002). Global modeling of irrigation water requirements. Water Resources Research, 38, -

6) Friedl, M.A., McIver, D.K., Hodges, J.C.F., Zhang, X.Y., Muchoney, D., Strahler, A.H., Woodcock, C.E., Gopal, S., Schneider, A., Cooper, A., Baccini, A., Gao, F., & Schaaf, C. (2002). Global land cover mapping from MODIS: algorithms and early results. Remote Sensing of Environment, 83, 287-302

7) Frolking, S., Xiao, X.M., Zhuang, Y.H., Salas, W., & Li, C.S. (1999). Agricultural land-use in China: a comparison of area estimates from ground-based census and satellite-borne remote sensing. Global Ecology and Biogeography, 8, 407-416

8) Frolking, S., Yeluripati, J.B., & Douglas, E. (2006). New district-level maps of rice cropping in India: A foundation for scientific input into policy assessment. Field Crop Research, 98, 164-177

9) Galford, G.L., Mustard, J.F., Melillo, J., Gendrin, A., Cerri, C.C., & Cerri, C.E.P. (2008). Wavelet analysis of MODIS time series to detect expansion and intensification of row-crop agriculture in Brazil. Remote Sensing of Environment, 112, 576-587

10) Gilbert, M., Xiao, X.M., Chaitaweesub, P., Kalpravidh, W., Premashthira, S., Boles, S., & Slingenbergh, J. (2007). Avian influenza, domestic ducks and rice agriculture in Thailand. Agriculture Ecosystems & Environment, 119, 409-415

11) Gilbert, M., Xiao, X.M., Pfeiffer, D.U., Epprecht, M., Boles, S., Czarnecki, C., Chaitaweesub, P., Kalpravidh, W., Minh, P.Q., Otte, M.J., Martin, V., & Slingenbergh, J. (2008). Mapping H5N1 highly pathogenic avian

influenza risk in Southeast Asia. Proceedings of the National Academy of Sciences of the United States of America, 105, 4769-4774

12) Hall, D.K., Riggs, G.A., Salomonson, V.V., DiGirolamo, N.E., & Bayr, K.J. (2002). MODIS snow-cover products. Remote Sensing of Environment, 83, 181-194

13) Huete, A., Didan, K., Miura, T., Rodriguez, E.P., Gao, X., & Ferreira, L.G (2002). Overview of the radiometric and biophysical performance of the MODIS vegetation indices. Remote Sensing of Environment, 83, 195-213

14) Lobell, D.B., & Asner, G.P. (2004). Cropland distributions from temporal unmixing of MODIS data. Remote Sensing of Environment, 93, 412-422

15) Loveland, T.R., Reed, B.C., Brown, J.F., Ohlen, D.O., Zhu, Z., Yang, L., & Merchant, J.W. (2000). Development of a global land cover characteristics database and IGBP DISCover from 1 km AVHRR data. International Journal of Remote Sensing, 21, 1303-1330

16) Qiu, J., Tang, H., Frolking, S., Boles, S., Li, C., Xiao, X., Liu, J., Zhuang, Y., & Qin, X. (2003). Mapping single-, double-, and triple-crop agriculture in China at 0.5ox0.5o by combining county-scale census data with a remote sensing-derived land cover map. Geocarto International, 18, 3-13

17) Sakamoto, T., Van Nguyen, N., Ohno, H., Ishitsuka, N., & Yokozawa, M. (2006). Spatio-temporal distribution of rice phenology and cropping systems in the Mekong Delta with special reference to the seasonal water flow of the Mekong and Bassac rivers. Remote Sensing of Environment, 100, 1-16

18) Thenkabail, P.S., Schull, M., & Turral, H. (2005). Ganges and Indus river basin land use/land cover (LULC) and irrigated area mapping using continuous streams of MODIS data. Remote Sensing of Environment, 95, 317-341

19) Tucker, C.J. (1979). Red and Photographic Infrared Linear Combinations for Monitoring Vegetation. Remote Sensing of Environment, 8, 127-150

20) Wardlow, B.D., & Egbert, S.L. (2008). Large-area crop mapping using time-series MODIS 250 m NDVI data: An assessment for the US Central Great Plains. Remote Sensing of Environment, 112, 1096-1116

21) Xiao, X.M., Boles, S., Frolking, S., Li, C.S., Babu, J.Y., Salas, W., & Moore, B. (2006). Mapping paddy rice agriculture in South and Southeast Asia using multi-temporal MODIS images. Remote Sensing of Environment, 100, 95-113

22) Xiao, X.M., Boles, S., Liu, J.Y., Zhuang, D.F., Frolking, S., Li, C.S., Salas, W., & Moore, B. (2005a). Mapping paddy rice agriculture in southern China using multi-temporal MODIS images. Remote Sensing of Environment, 95, 480-492

23) Xiao, X.M., Liu, J.Y., Zhuang, D.F., Frolking, S., Boles, S., Xu, B., Liu, M.L., Salas, W., Moore, B., & Li, C.S. (2003). Uncertainties in estimates of cropland area in China: a comparison between an AVHRR-derived dataset and a Landsat TM-derived dataset. Global and Planetary Change, 37, 297-306

24) Xiao, X.M., Zhang, Q.Y., Hollinger, D., Aber, J., & Moore, B. (2005b). Modeling gross primary production of an evergreen needleleaf forest using MODIS and climate data. Ecological Applications, 15, 954-969

An attempt to characterize the changes in grasslands as agricultural resources in Mongolia

Akira Hirano
Japan International Research Center for Agricultural Sciences (JIRCAS)
Development Research Division
1-1 Ohwashi, Tsukuba, Ibaraki, Japan 305-0044,
akhirano@jircas.affrc.go.jp

Abstract

Grasslands are an important land use and land cover in Mongolia. It is particularly unique that more than 99 per cent of Mongolia's agricultural area is grasslands. Changes in this vast agricultural area have implications not only for the country's economic future prospect but also for impact on regional environment. The use of satellite based 8-km vegetation index time-series dataset over 20 years (1981-2000) signaled potentially contrasting spatial patterns before and after 1990 when the country moved from planned economy to market economy. The concentration of declining vegetation activity in the north-central region particularly after 1990 appeared to coincide with the distribution of croplands and the areas of increasing livestock density.

Keywords **:** grasslands, agriculture, Mongolia, vegetation trends

1. Introduction

Mongolia is the second largest landlocked country in the world, only after Kazakhstan, situated in between Russia and China. The country has a total area of over 1.56 million square km and is located on a high Mongolian plateau ranging from 900 to 1500 m in elevation. Rocky desert and grassy semi-arid temperate steppe cover most of the land. Forests, which are limited to the mountainous areas, cover about 7 per cent of its entire territory.

Grasslands are an important land use and land cover in Mongolia. It is particularly unique that more than 99 per cent of its agricultural area is grasslands: permanent meadows and pastures. Changes in this vast agricultural area, totaling 1.15 million square km in aerial extent, have implications not only for the country's economic future prospect but also for impact on regional environment.

Herding, which has been practiced for thousands of years still is the country's main economic activity. Cultivation plays a minor role in Mongolian agriculture because less than one per cent of the land is farmable. Crops are grown in the northern part of the country, some with the help of irrigation. Principal crops include wheat, potatoes, barley, and oats. The production of hay and fodder for livestock feed is also important.

Climate is the limiting element of Mongolian agriculture. The period of grazing, the growth and quality of cultivated and natural plants, the timing and methods of performing many animal and crop production tasks depend directly on climatic and weather conditions. It has a dry continental climate, with long cold winters and short warm summers. Most precipitation comes during the summer's short rainy season. Rainfall seldom exceeds 380 mm in the northern mountains and 125 mm in the southern areas (Fig. 1).

Suttie (2005) reported that Mongolian grasslands, although hard grazed, are still in good order. However, there are other reports suggesting ongoing desertification by climate change due to anthropogenic or natural causes. This study aims to attempt to characterize the changes in these extensive agricultural recourses both due to climatic and anthropogenic origins, primarily using satellite-derived spatial pattern of vegetation trends at the continental scale.

2. Data and Methods

2.1 GIMMS NDVI dataset

The Global Inventory Modeling and Mapping Studies (GIMMS) normalized difference vegetation index (NDVI) dataset, with an 8-km resolution was used to evaluate the time-series vegetation trends. The Global Land Cover Facility (GLCF) of the United States provided the dataset. These data were originally constructed from NOAA AVHRR measurements and was corrected for calibration, view geometry, volcanic aerosols, and other effects not related to actual vegetation change (Tucker *et al.*, 2005).

Previous efforts suggested NDVI proved best or at least comparable among other proposed types of vegetation indices such as soil-adjusted vegetation index (SAVI),

modified- and transformed soil-adjusted vegetation index (MSAVI and TSAVI) for estimating the actual vegetation condition when no location-specific soil characteristics and vegetation densities are available (Yamamoto *et al.*, 1997; Purevdorj *et al.*, 1998).

2.2 Vegetation Trend Analysis

Vegetation trend for each pixel location was calculated using a series of maximum NDVI value for each year based on the simple time series regression model (Fig. 2). The process of selecting annual maximum NDVI for each pixel disregards the seasonal timing of the NDVI values (Rowland *et al.*, 1996). The calculation resulted in a collection of slopes at each location. Only pixels with statistically significant increase or decrease ($P < 0.05$) were used for the assessment of spatiotemporal pattern (Hirano *et al.*, 2006) and the same approach was taken in this study. In order to see if vegetation trends present similar or different spatial pattern before and after the major socioeconomic turning point in Mongolia, decadal trends were separately calculated and compared.

2.3 Comparison of trend distribution with other spatial data

Statistically significant per-pixel vegetation trends were cross-referenced with the European Space Agency (ESA) GlobCover Land Cover dataset: 300-m resolution land cover data (ESA/ESA GlobCover Project, 2008), 90-m resolution Shuttle Radar Topography Mission (SRTM) elevation dataset (Farr *et al.*, 2007), and global climate layer (WorldClim) (Hijmans *et al.*, 2005). Ten-year-averaged number of livestock density distribution by Province before and after 1990 was also compared with the vegetation trends.

3. Results and Discussions

About 12 per cent of the entire Mongolian territory showed statistically significant vegetation trends between 1981 and 2000. Ten-year trends (1981-1990; 1991-2000) were color-coded and overlaid on land cover data (Fig. 3). Visual comparison indicated spatially different distribution pattern of improving and degrading trends – particularly to be noted being concentration of negative trends in the north-central region after 1990. When broken down by corresponding land cover types, it was found that much degrading trends after 1990 were observed in croplands land cover (Fig. 4). It is assumed that significant amount of both active and abandoned croplands after the introduction of market economy showed negative trends in vegetation dynamics. Ratio of trends distribution by elevation stayed more or less the same before and after 1990. Majority of degrading trends were observed in areas with annual precipitation between 200-300mm after 1990, which suggested drier condition deteriorating vegetation vigor. However, further climatic trend analysis should be carried out in order to draw concrete conclusion in this context.

Mongolian statistics showed sharp increase in number of livestock after 1990. Lots of state-operated farmland labor force was reported to turn to herding. Economic incentive encouraged larger number of livestock per household. Density map of livestock by Province showed generally straightforward agreement with changes in vegetation trends – where concentration of increasing livestock density corresponding to concentration of negative vegetation dynamics (Fig. 5). This infers the potential impact of overgrazing leading to grasslands degradation.

4. Concluding Remarks

Spatiotemporal vegetation information derived from satellite remote sensing data has often proved useful in characterizing environmental changes over land areas at various spatial-scale. In this particular study, changes in extensive grasslands in the entire Mongolian territory were evaluated in the context of socio-economical changes. This characterization is still at its primitive stage but provides clues to topical areas of interest that require further attention to be studied.

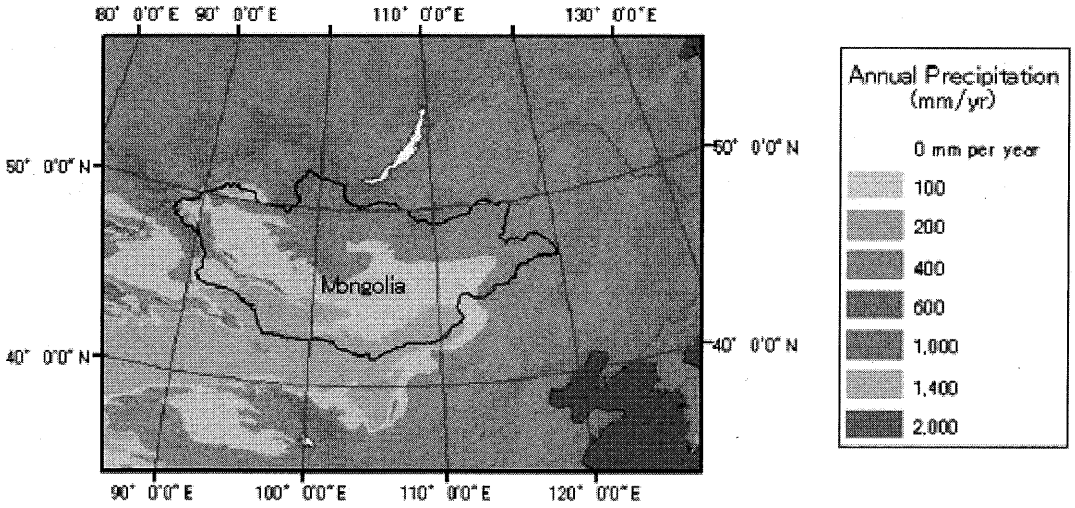

Fig. 1 Location of Mongolia and distribution of its annual precipitation.

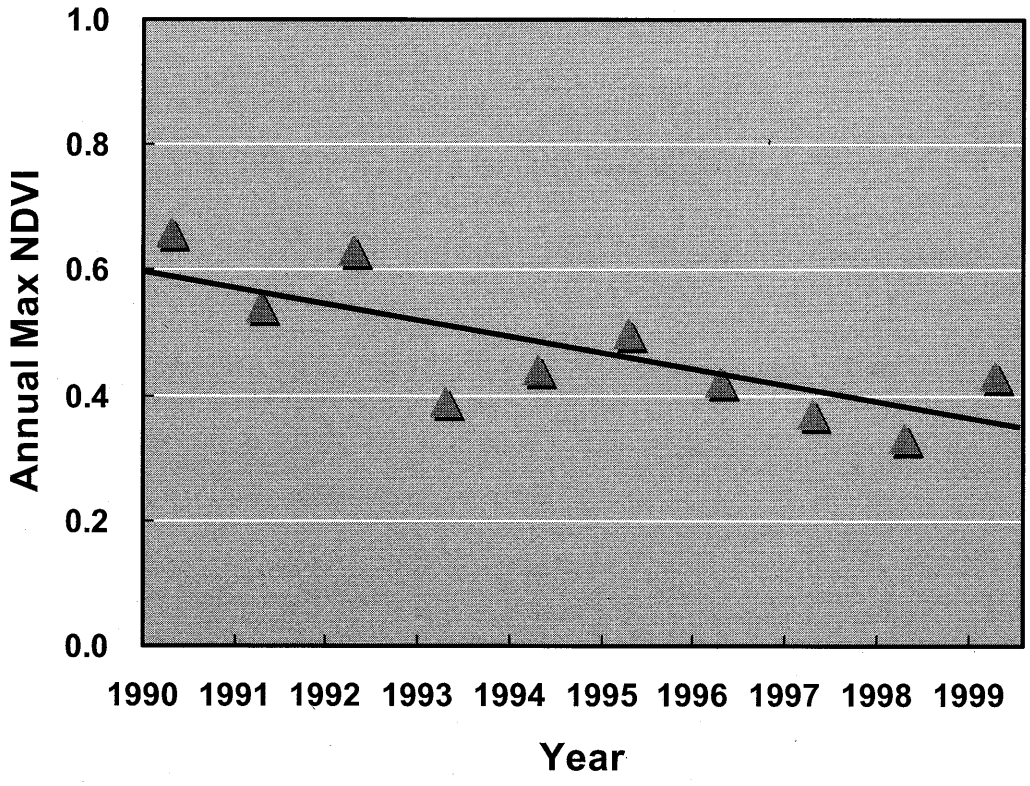

Fig. 2 Conceptual diagram of vegetation trend using annual maximum NDVI values.

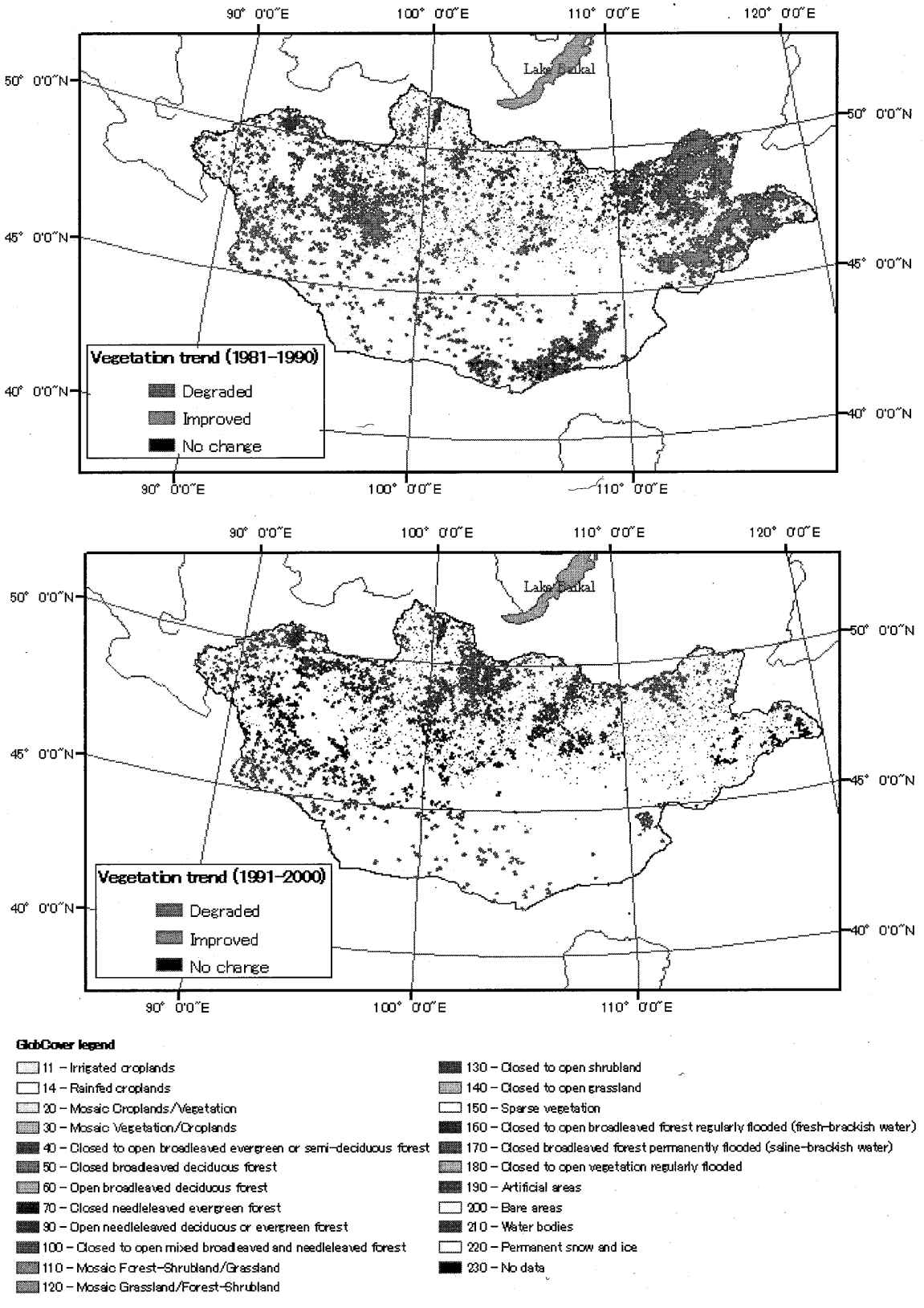

Fig. 3 Distribution of statistically significant vegetation trends (1981-1990; 1991-2000) overlaid on GlobCover land cover dataset.

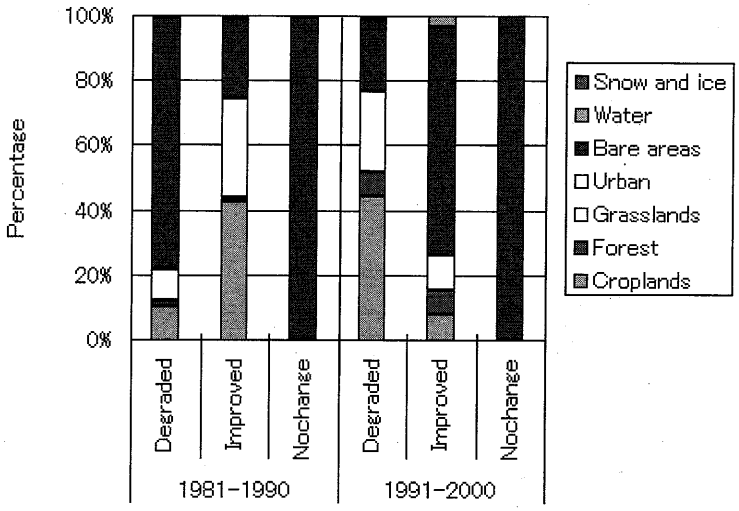

Fig. 4 Changes in vegetation trends by percentage land cover (1981-1990 vs. 1991-2000).

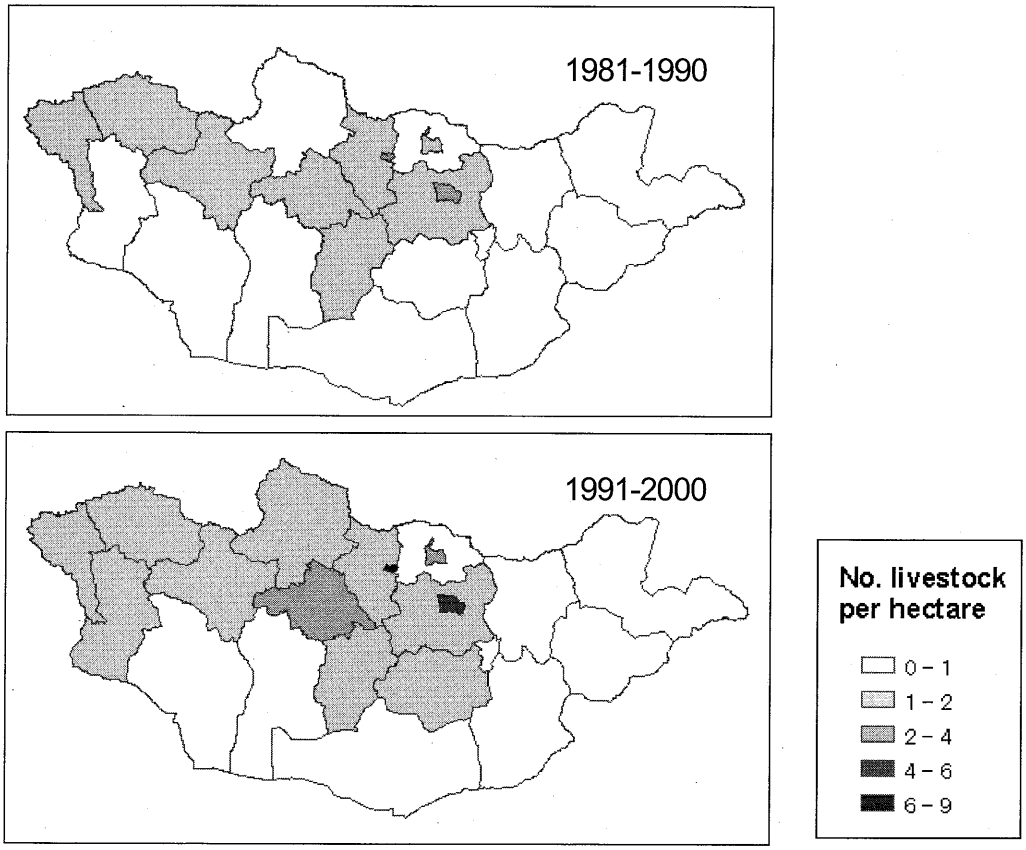

Fig. 5 Density map of livestock (sheep equivalent) by Province.

Acknowledgements

This work is a part of JIRCAS/Mongolian State University of Agriculture (MSUA) collaborative research "Development of a sustainable agro-pastoral system in the dry areas of Northeast Asia" (2006-2010).

References

1) ESA/ESA GlobCover Project, 2008. GlobCover Land Cover v2 2008 database. European Space Agency, European Space Agency GlobCover Project, led by MEDIAS-France, http://ionia1.esrin.esa.int/index.asp.

2) FAO, FAOSTATS <http://faostat.fao.org/>, accessed on December 12, 2009.

3) Farr, T.G., P.A. Rosen, E. Caro, R. Crippen, R. Duren, S. Hensley, M. Kobrick, M. Paller, E. Rodriguez, L. Roth, D. Seal, S. Shaffer, J. Shimada, J. Umland, M. Werner, M. Oskin, D. Burbank, D. Alsdorf, 2007. The Shuttle Radar Topography Mission, *Reviews of Geophysics*, 45, RG2004, doi:10.1029/2005RG000183.

4) Hijmans, R.J., S.E. Cameron, J.L. Parra, P.G. Jones, and A. Jarvis, 2005. Very high resolution interpolated climate surfaces for global land areas. *International Journal of Climatology*, vol. 25, pp. 1965-1978.

5) Hirano, A., K. Toriyama, and H. Komiyama, 2006. Spatiotemporal characterization of Mongolian grassland based on vegetation trend analysis, *Proceedings, the 27th Asian Conference on Remote Sensing (ACRS)*, CD-ROM.

6) Purevdorj, T., R. Tateishi, T. Ishiyama, and Y. Honda, 1998. Relationships between vegetation cover and vegetation indices, *International Journal of Remote Sensing*, vol.19, no.18, pp. 3519-3535.

7) Rowland, J., A. Nadeau, J. Brock, R. Klaver, D. Moore, and J.E. Lewis, 1996. *Vegetation index for characterizing drought patterns*. In: Raster Imagery in Geographic Information Systems, edited by Morain, S. and S.L. Baros, Onward Press, Santa Fe, NM, pp. 247-254.

8) Suttie, J.M., 2005. Grazing management in Mongolia. In: *Grasslands of the World*, edited by Suttie, J. M., S. G. Reynolds, and C. Batelo, Plant Production and Protection Series No.34, FAO-UN, Rome, pp. 265-304.

9) Tucker, C.J., J.E. Pinzon, M.E. Brown, D.A. Slayback, E.W. Pak, R. Mahoney, E.F. Vermote, and N. El Saleous, 2005. An extended AVHRR 8-km NDVI dataset compatible with MODIS and SPOT vegetation NDVI data, *International Journal of Remote Sensing*, vol.26, no.20, pp. 4485-4498.

10) Yamamoto, H., Y. Honda, K. Kajiwara, C. Okano, S. Huang, and M Matsuoka, 1997. The analysis of field data measured in grassland for biomass monitoring using satellite data, *Journal of the Japan Society of Photogrammetry and Remote Sensing*, vol.36, no.4, pp. 38-49. (In Japanese with English summary).

Centrographic Analysis of Urban Growth in Xinjiang

Anwaer Maimaitiming[①②③] Xiaolei Zhang[②] Huhua Cao[④]

①School of Geographic Sience and Tourism, Xinjiang Normal University, Urumqi, 830054;
②Xinjiang Institute of Ecology and Geography, Chinese Academy of Science, Urumqi, 830011;
③Graduate Institute of Chinese Academy of Science, Beijing, 10049;
④Department of Geography, University of Ottawa, Canada, Ottawa, K1N6N5

Abstract: Xinjiang has experienced considerable urban growth in the past fifty years, especially since the implementation of socio-economic reforms in 1978. When Xinjiang was founded as a Uygur Autonomous Region in 1955, there were only three cities with an urban population of 870 thousand, while in 2008 it had 21 cities with a total urban population with 8.45 million. Such an urban growth is attributed to the boost in the number of cities and the urban population. Urban expansion enhanced geographic inequality between the two major regions in Xinjiang. Compared to the Norhtern part, Southern Xinjiang only has 33.3% of the total cities and 35% of the urban population. Using centrographic analyses, this study aims at explaining the movement of urban center in Xinjiang during the past three decades. The conclusions are the following: 1.The center of city gravity moved to southwest, while the center of town gravity moved to southwest first then returned back to northeast; 2. The main factors which effected the movement of urban center in Xinjiang are government new rural economy system (1980), the new urban definition(1984) and superior geographical location as well as better socio-economic conditions are main factors .

Key words: Xinjiang; urban growth; saptial pattern; Centrographic Analysis

1 Introduction

Xinjiang has experienced considerable urban growth in the past sixty years, especially since the implementation of socio-economic reforms in 1978. When Xinjiang was founded as a Uygur Autonomous Region in 1955, there were only three cities with an urban population of 870 thousand, while in 2008 it had 21 cities with a total urban population with 8.45 million. Such an urban growth is attributed to the boost in the number of cities and the urban population. Urban expansion enhanced geographic inequality between the two major regions in Xinjiang. Compared to the Norhtern part, Southern Xinjiang only has 33.3% of the total cities and 35% of the urban population.

The urbanization in developing countries has attracted attentions of many scholars since the end of World War II (Cohen, 2004; Pugh 1995; Henderson 2002; Jo, 2002). They studied urban growth in developing countries from different point of view. The urban study in China

Foundation item: National Natural Science Foundation of China(40761008)
Anwaer Maimaitiming (1973-), male, Associate professor, PhD candidate
Research field: urbanization and regional development
E-mail: anwaer@xjnu.edu.cn, Tel: 0991-5332875(Mobile), 4333985(O), Fax: 0991-4332535
Corresponding Author: *Zhang Xiaolei (zhangxl@ms.xjb.ac.cn)*

has only begun since the last decade of 20th century, but has already well documented in the literature (Chan, 1992; Fan, 1999; George, 1999, 2002; Han et al., 1994; Hsu, 1994; Tian et al., 2002; Wang, 1999; Xu et al., 2002; Yang, 1998; Yao et al., 1999; Goldstein, 1990; Gu, 1999; Li et al., 1998; Chan et al., 2003; Victor et al., 1997; Ingram, 1998). The selected cases of Chinese urbanization mostly are concentrated in the east coast metropolitan centres such as Beijing (Gu, 2003), Jiangsu (Ma, 1994; Wang, 1999), Shanghai (Han, 2000), Fujian (Zhu, 2000), Guangzhou (Piper, 1999), Zhejiang (Xu, 2002) and Pearl River Delta (George, 1999). There were very a few case studies on the western provinces (Yue et al., 2004), especially of Xinjiang. Among some studies on Xinjiang, scholars analyzed the spatial feature of towns, the economic difference of urban system, spatial imbalance of urbanization and the status quo and significance of urbanization in Xinjiang(Gong, ei al. 2008;Chen, 2008; Shi, 2008). Very few researches focus on the centrographic analysis of urbanization in Xinjiang.

The regions emphasized in former studies have highly distinguishing social and economic environment from Xinjiang. Socially, Xinjiang is a minority concentrated multi-national area, 60% of population is minorities; economically, it is an under developed region. More than 60% of its total employment is engaged in agriculture. Per capita GDP is 4 times lower than the Shanghai City (Xinjiang Statistical Yearbook 2009). Therefore the systematic research of urban development in Xinjiang not only can be helpful for the local planning and regional development, but also has the inspiration meaning to urban development in other minority regions.

2 Methodology and Data

Urbanization level in this study is measured by using the proportion of urban populations. This study adopts the official definitions of urban population which refer to the permanent residents of urban area such as districts, streets and resident comities in cities and towns. There are 21 cities and 229 towns in Xinjiang in 2008. The spatial pattern is analyzed on the basic of 87 county level administrative regions and three large geographic units, namely Northern Xinjiang, Eastern Xinjiang and Southern Xinjiang.

Data used in this study come from Xinjiang Census 1982, 1990 and 2000, Xinjiang Statistical Yearbook 2001, 2004 and 2009.

The analytical part of this research we used centrographic analysis. Centrographic analysis is an advanced spatial analysis method, which has experienced a rapid renewal over the last few years, in large part due to its integration with GIS. This technique provides the equivalent of statistical measures of central and dispersion tendencies adapted for two-dimensional geographical space (Caprio, 1970). Jones (1980) presents centrographic measures as describing the three most important characteristics of a spatial phenomenon: its location, dispersion and form.

3 Urbanization Process in Xinjiang

3.1 Brief History of Urbanization in Xinjiang

When Xinjiang was founded as a Uygur Autonomous Region in 1955, there were only three cities: Urumqi and Gulja city in the north and Kashkar city in the south with an urban population of 870 thousand (Geographic Society of Xinjiang, 1993). Urbanization rate was only 12.21%. From 1953, Central government began to pay more sustained attention to

Xinjiang and then urbanization began to change its pace and spatial structure. Urban development in Xinjiang had gone through the following distinct stages.

Initial period of urbanization (1949-1959): The main features of Xinjiang's urbanization in this period are as follows:

Firstly, urbanization pace was faster than the national average. In 1949, there was only one city, Urumqi, in Xinjiang. From 1949 to 1959, the urbanization rate of Xinjiang increased by 11.23 %, 7.77% higher than the national average. The urban population reached 1.56 million, with the urbanization rate of 23.44%. Secondly, the main explanation for the rapid increase in urban population during the period is industrialization and the expansion of non-agricultural economic activities accelerated by the First Five-Year Plan, mainly the development of mining and processing industry. At that time, the key point of urban construction in Xinjiang was Urumqi city as well as Karamay. As a result there were designated three new cities. The number of cities reached to four. Third, inter-provincial in-migration was the main source of urban population. There were two forms of in-migration, organized and spontaneous. At that time the organized in-migration had been increasing rapidly. During the mid 1950s annual net in-migration of 250,000 was dominated by production and construction corps in-migrants. 1949-1953 Xinjiang get net in-migration from other provinces such as Beijing, Jingsu, Zhejiang, Hubei, Hunan, and Shandong 330 thousand people.

De-urbanization stage (1960 -1965): This was the economic recovery and adjustment period. Urbanization in Xinjiang had the following characteristics: firstly, government increased the urban criteria. Like other provinces in China, Xinjiang has to decrease urban population by deporting or "sending down" to the countryside. As a result, 61 thousand urban populations were reduced and faced de-urbanization phenomenon. Secondly, urbanization rate was dropped and the disparity with the national average was enlarged. In 1965, the percentage of urban population in Xinjiang dropped from 23.44% to 18.93%, while the national average rate reduced from 10.5% to 9.2%.

Stagnation and Slow development stage (1966-1977): In this stage, urbanization was stagnated or slow developed due to the Cultural Revolution and associated misguided ideology. The campaign of "up to mountain and down to the villages" force urban educated youth to move out of the cities to resettle in rural villages or remote areas. Only three new cities were designated in the 11 years. The number of cities and towns reached to 7 and 53 respectively with the urban population of 2.76 million. 610 thousand urban populations increased in this period but its proportion stayed at 22.86%, 0.58% lower the end of the first stage.

High Speed Urbanization stage (1978 to 1990): The economic reforms since 1978 have brought deep changes to China's urban-rural relations. Market economy and rural system reform have created a great impetus for the remarkable growth of small towns, which functioned as the rural economic center. Especially since the relaxed urban and town criteria in 1984 re-energized small cities and towns have flourished all over the China. At that time, however, the pattern of structural change of cities in Xinjiang has been the result of political consideration. Each prefecture designated at least one city as a political center. Then the number of cities rose significantly from 7 in 1978 to 16 in 1990, an increase of 9 new cities in 12 years, more than two times than the four new cities established over the previous two

decades. The number of towns also increased from 53 in 1978 to 131 in 1990. At the same time urban population increased from 3.21 million to 6.86 million with the proportion of 44.86%.

Stable Development period (1990 to 2000): From 1990 to 2000, economic factors played more roles in growth of cities. The Development of cities was effectively guided by economic needs. In this period, the number of cities rose from 16 to 19, increased 3 new cities. At the same time, the number of towns increased from 131 to 197. Despite of the growth of the cities and towns, urban population and its proportion dropped to 6.2 million and 33.75% respectively mainly due to the new urbanization criteria in 2000 census.

Accelerate urban growth period (2000 to 2008): In 2000, Chinese central government announced a major, new initiative -"Great Western Development Strategy" to develop China's poor, backward western regions. This strategy brings Xinjiang a historic opportunity for urban development. Along with the implementation of this new favorable regional development strategy, population and industrialization grew rapidly in these areas, especially in Xinjiang. Xinjiang entered accelerate urban growth stage again. Three new cities and 32 new towns were designated in these eight years with the nearly 4% of annual growth rate. Urbanization rate reached 39.64% with 8.45 million of the urban population. In this period, Southern Xinjiang has gone through more urbanization than the North and East. Two of the three new cities and 22 of the 32 new towns are located in Southern Xinjiang, while one city and seven towns are in North and only three towns are in East.

3.2 Centrographic Analysis of urbanization in Xinjiang during last three decades

The centrographic analysis shows a significant reorganization of the spatial distribution of cities and towns in Xinjiang over the three decades (Figure 1). Figure 1consists of 5 thematic maps, 3 of them corresponding respectively to cities and towns in three different time period (1982, 1990, and 2008). Each of the maps contains one hierarchical ellipse representing the migratory phenomenon of urbanization. Another two maps consist of three ellipses of the special distribution of cities and towns, each of ellipses representing each year.

The center of gravity (CG) of an ellipse in centrographic analysis is the relative center of the region being studied, according to the weight of each of its geographical unit. When studying the spatial distribution of a phenomenon, if the phenomenon is distributed unevenly, it can be interesting take into consideration the weight of each geographical unit and therefore to assign this weight to each point. The calculation of the coordinates of the center of gravity will take into account the disparities in the weights of geographical units in the region. The center of gravity is a useful reference point for the comparison of several geographical units at points in the same geographical region or for the comparison of the position of one geographical unit over time (Cao, 2003). We calculated weighted centers of gravity for the spatial distribution of urban population for the three time periods 1982, 1990 and 2008, and presented them in Figure 1. The evolution of the forms of the ellipses and the changes in their major and minor axes in Centrographic analysis indicate the dispersion of the research phenomenon under study in relation to the two spatial dimensions. In order to report better the spatial distribution of the research objects, the ellipse can be oriented according to the track with most variation (Cao, 2003). In this study we also examined the evolution of the forms of the ellipses and changes in their major and minor axes to better understand the process of urban concentration in Xinjiang.

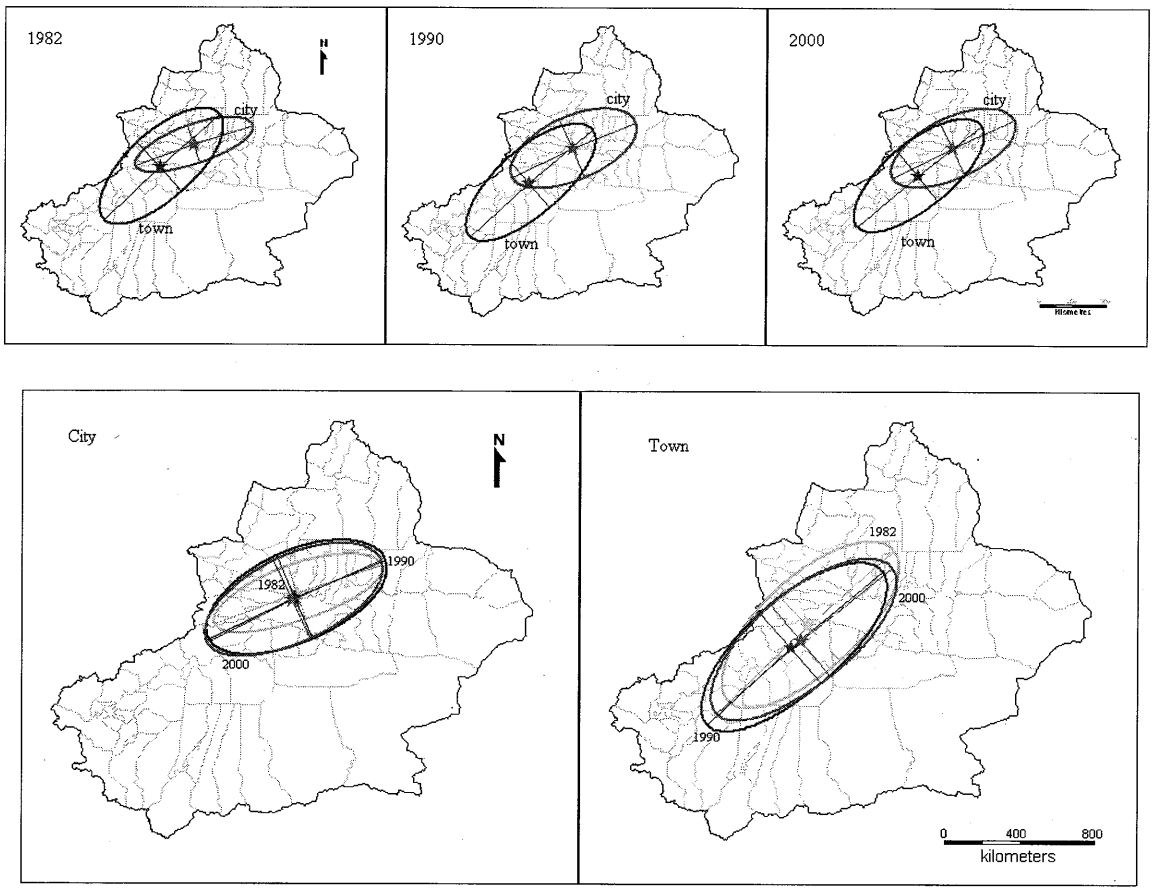

Figure 1 Centrographic analysis of the distribution of cities and towns in Xinjiang, 1982-2000

3.2.1 City vs. town

1n 1982, the center of gravity for cities was located in Sawan County (N43.49°, E85.15°), while the center of towns was located in eastern corner of Bay County (N42.37°, E82.86°), wich is 225 km southwest of city center. In 1990, the center of city gravity moved 19 km to southwest and placed in Hejing County (N43.33°, E85.07°). At the same period, the town center also has the same moving trend with a bigger scale than cities. It was located in Toksu County (N41.58°, E82.08°), moved 110km to southwest. The distance between city center and town center enlarged to 315 km. In 2008, however, the center of city gravity was also located in Hejing County but still continued its direction towards southwest (N43.27°, S84.94°) and made a movement of 14 km to southwest, while the center of town gravity changed its direction and moved 50km back to northeast. This time it was located in Bay County (N41.85°, E82.55°) again. The distance between the two centers decreased to 250 km.

Statistics confirm that, in 1982 the area of ellipse for cities was only 116300 km^2, while it was 256600 for towns. In 1990, both of these ellipses expanded to north and south directions, covers the area of 206400 km^2 and 269000 km^2 respectively. However, the ellipse for cities expended 77.5%, much bigger than 4.8% of that for towns. Contrarily, in 2008, both of the ellipses have a trend of reduction. Now the covered scopes of them are reduced to 195200 $km^2$and 260400 km^2, the ellipse for cities shrink 5.4%, 2.2% larger than that of 3.2% for towns.

What is more, the major and minor axis of ellipses for cities has experienced more

changes then that for towns. For example, the major axis of ellipse for cities, which is the horizontal length of the ellipses, measured 682.8 km in 1982, while it measured 876.5 km for towns. In 1990, they extended to 747.1 km and 925.5 km respectively. Yet, the axis for cities changed 9.5%, while the axis for towns altered 5.6%. In 2008, they measured 744.1 and 901.6, shortened 0.4% and 2.6%. The minor axis of ellipse, which is the vertical length of the interior ellipse, was 216.9 km for cities and 372.9 for towns in 1982. In 1990, it was 351.9 for cities and 370.9 for towns. In the eight years the minor axis of ellipse increased 62%, while that of towns decreased 0.7%. In 2008, both of them have same trend of reduction. It reduced 5.1% for cities and 0.6% for towns. This shows that decentralization in the first stage and concentration in the second period was more obvious for cites than towns.

3.2.2 Temporal change

In 1982, the center of gravity for cities was located in Sawan County (N43.49°, E85.15°), while the center of towns was distributed in eastern corner of Bay County (N42.37°, E82.86°). In 1990, both of them moved to southwest, and the area, major and minor axis of both ellipses expanded with the exception of minor axis for towns. In 2008, the center of city gravity still continued its direction towards southwest, while the center of town gravity returned back to northeast. Nevertheless, covered area, major and minor axis of both ellipses decreased. This indicates that the distribution of cities and towns was tending to be balanced from 1978 to 1990, while it is concentrated in the northern area in 2008. This kind of tendency displays more obviously in the city than towns (Table 1).

Table 1 Centrographic Analysis Parameters

	1982	1990	2008	Difference 1982-1990	Difference 1990-2008	Difference 1982-2008
City						
Area of ellipse(km^2)	116300	206400	195200	+77.5%	-5.4%	+67.8%
Major Axis(km)	682.8	747.1	744.1	+9.5%	-0.4%	+9.1%
Minor Axis(km)	216.9	351.9	334.1	+62.2%	-5.1%	+54%
Ellipse orientation (degrees)						
Town						
Area of ellipse(km^2)	256600	269000	260400	+4.8%	-3.2%	+1.5%
Major Axis(km)	876.5	925.5	901.6	+5.6%	-2.6%	+2.9%
Minor Axis(km)	372.9	370.2	368.0	-0.7%	-0.6%	-1.3%
Ellipse orientation (degrees)						
City + Town						
Area of ellipse(km^2)	180200	246000	228400	+36.5%	-7.2%	+26.8
Major Axis(km)	761.8	844.9	821.6	+10.9	-2.8%	+7.9%
Minor Axis(km)	301.3	370.9	354.1	+23.1	-4.5	+17.5
Ellipse orientation (degrees)						

This kind of movement of city and town centers has some relations of government urban policy as well as economic development in Xinjiang. From 1982 to 1990 the main propelling force of urbanization in Xinjiang was the administrative strength. In 1982, there were only eight cities and 64 towns in Xinjiang. From the 1982 to 1990, the number of cities and towns rose to sixteen and 131 respectively with the rapid annual growth rate of 9.05% and 9.37%. This is because Chinese government launched new rural economy system in 1980 and

changed the urban definition in 1984. According to new urban definition in China, those areas where local governments of county level or higher are designated as urban areas irrespective of the size of their permanent resident population *(Asian Development Bank, 2002)*. Therefore, 8 counties are turned into cities as capital cities of prefectures, 67 new towns were designated. As a result, the city and town distributions tend to the homogenization. This is partial explanation for why the CG shifted to south as well as spatial disparity urbanization was lower in this period. After 1990, urbanization speed slowed down and began to concentration on the economic belt of northern slope of Tianshan Mountain. At that time economic development played the major role in the urbanization. After1990, six new cities are established serving as economic center and four of them are located on the economic belt of northern slope of Tianshan Mountain because of the superior geographical location and better economic development of these areas.

4 Conclusion and discussion

1.Tthe center of city gravity moved to southwest, while the center of town gravity moved to southwest first then returned back to northeast.

2. The main factors which effected the movement of urban center in Xinjiang are government new rural economy system (1980), the new urban definition(1984) and superior geographical location as well as better socio-economic conditions are main factors.

Reference

Bureau of Xinjiang Statistical Yearbook (2001-2008), *Xinjiang Statistical Yearbook 2001-2008,* China Statistics Press.

Caprio R. J. (1970) Centrography and Geostatistics *The Professional Geographer* 22(1) pp.15-19

Census Committee of Xinjiang Uygur Autonomous Region (1982) Xinjiang Third Census.

Census Committee of Xinjiang Uygur Autonomous Region (1991) Xinjiang Fourth Census 1990, China Statistical Press.

Census Committee of Xinjiang Uygur Autonomous Region (2001) Xinjiang Fifth Census 2000, China Statistical Press

China National Census Committee (2001) China Fifth Census 2000, China Statistical Press.

China State Statistical Bureau (1991), *Zhongguo Chengshi Tongji Nianjian 1991 (China Urban Statistical Yearbook 1991),* Beijing: China Statistical Press.

China State Statistical Bureau (2003), *Zhongguo Chengshi Tongji Nianjian 2003 (China Urban Statistical Yearbook 1991),* Beijing: China Statistical Press.

Chan K. W. (1992) Economic Growth Strategy and Urbanization Policies in China, 1949-1982 *International Journal of Urban and Regional Research* 16(2) pp.275–305

Chen C.F. and Ma H.L.(2008).An Analysis of the Balanced Development of Urbanization and Regional Economy in Xinjiang Since our Reform and Opening to the Outside, Joumal of Henan University of Technology，(Social Science),4(2):pp:13-15

Cohen B. (2004) Urban Growth in Developing Countries: A Review of Current Trends and a Caution Regarding Existing Forecasts *World Development* Vol. 32, No. 1, pp.23-51

Fan C. C. (1999) The Vertical and Horizontal Expansions of China's City System *Urban Geography* 20(6) pp.493–515

Geographic Society of Xinjiang, (1993) "*Geographic Handbook of Xinjiang*," Xinjiang Peoples Press, p. 213

George C. S. LIN (1999) Transportation and Metropolitan Development in China's Pearl River Delta: The Experience of Panyu *Habit at International* 23(2) pp.249-270

George C. S. LIN (2002) The Growth and Structural Change of Chinese Cities: A Contextual and Geographic Analysis *Cities* 19(5) pp.299–316

Goldstein S. (1990) Urbanization in China, 1982-1987: Effect of Migration and Reclassification *Population and Development Review* Vol. 16, No. 4, pp.673-701

Gong J.J., Ye M. Zhou C.X. et al. Reaserch of Urbanization Development Region Difference in Xinjiang[J]. Journal of Taiyuan Normal University, 2008,7(4)pp.114-117

Gu C. L. (1999) *China Urban Geography* the Commercial Press Library 129-145

Han S. (2000) Shanghai between state and market in urban transformation *Urban Studies* 37 (11) pp.2091–2112

Han S. S. and Wong S. T. (1994)The Influence of Chinese Reform and Pre-reform Policies on Urban Growth in the 1980s *Urban Geography* 15(6) pp.537–564

Henderson V. (2002) Urbanization in developing countries *The World Bank Research Observer* 17(1) pp.89-112

Hsu M. L. (1994) The Expansion of the Chinese Urban System, 1953-1990 *Urban Geography* 15(6) pp.514–536

Ingram G. K. (1998) Patterns of Metropolitan Development: What Have We Learned? *Urban Studies* 35(7) pp.1019- 1035

Jo J. C. and Adler S. (2002) North Korean Planning: Urban changes and Regional Balance *Cities* 19(3) pp.205-215

Jones B. G. (1980) Application of Centrographic Techniques to the Study of Urban Phenomena: Atlanta, Georgia 1940-1975 *Economic Geography* 56(3) pp.201-222

Li Z. and Zhao S. X. B. (1998), "Re-examining China's "Urban" Concept and the Level of Urbanization," *The China Quarterly*, 154 pp.330 - 381.

Ma L. J. C. and Ming F. (1994), "Urbanisation from below: the growth of towns in Jiangsu, China," *Urban Studies*, 31 (10) pp.1625-1645

Piper G. (1999) China's Urban Transformation: Patterns and Processes of Morphological Change in Beijing, Shanghai and Guangzhou, *Urban Studies*, 36(9) pp.495 – 1521

Pugh, C. (1995) Urbanization in developing countries: an overview of economic and policy issues in the 1990s *Cites* 12(6) pp. 381-398

Shi Z.(2008),Study on Coordination of Urbanization and Economic Devlopment in Xinjiang, Journal of Hotan Pedagogical College, 28(2), pp:32-33

Tian G. J., Liu J. Y. and Zhang Z. X. (2002) Urban Functional Structure Characteristics and Transformation in China *Cities* 19(4) pp. 243–248

Victor F.S.S. and Yang, C. (1997) Foreign-investment-induced exo-urbanization in the Pearl River Delta, China *Urban Studies*. 34 (4) pp.647–677

Wang D. (1999) Socioeconomic characteristics of urbanization in Southern Jiangsu, China *International Journal of Social Economics* 26(1/2/3) pp.290-297

Xu W.and Tan K. C. (2002) Impact of reform and economic restructuring on rural system in China: a case study of Yuhang, Zhejiang. *Journal of Rural Studies* 18 pp.65-81

Yang R.M. (1998) Grey Relevance Analysis for China Urbanization and Non-agriculturalization *Areal Research and Development* (in Chinese) 17(1) pp.17-19

Yao S. M., Zhang L.S., Cheng, S. , et al. (1999) Consideration on Urban Growth in Economy Development Areas of Changjiang Basin *Resources and Environment in the Yangtze Basin* 8(1) pp.9-16

Yue W. Z., Xu J. H. and Xie, Y. W. (2004) A Study on Urban System Structure and its Fractal Model in Gansu Province of China *Areal Research and Development* (in Chinese) 23(1) pp.6-20

Zhu, Y. (2000) In Situ Urbanization in Rural China: Case Studies from Fujian Province *Development and Change* 31(2) pp.413-434

Achievement of CEReS Research Projects

Project 2

Subject:
Study on land surface – land cover, vegetation change of Eurasia continent

Members:
Yoshiaki Honda, Koji Kajiwara

Objective of the project:
The main purpose of this project is t o grasp the land surface change originating from vegetation structure change on lar ge area especially on Eurasia continent. This ac tivity will connect to clarify the carbon dioxide interchange between land and atmosphere.

On the above point of view , we have been de veloping a m onitoring m ethod using satellite optical sensors focus ed on the detection of 3D structure in formation of vegetation-c overed surface especially on forest area. 3D structure change of forest area means its biomass change.

Summary of Achievement
Main tar get of our res earch is biomass esti mation of fores t area using m ulti-angle spectru m observation f rom satellite. In or der to actualize it, the estimati on m odel related to bi- directional reflectance has been developed. Additionally, in-situ data collection method also developed.

For next generation Earth observation satellite se ries of JAXA/ GCOM-C1, our activity have set to develop several satellite products such as biomass, roughness index, shadow index, fAPAR, and so on.

Details of Achievement

Achievement 1: Multi-angle spectrum observation method development
1-1 Forest canopy BRF measurement using unmanned helicopter
Developed forest canopy BRF observation method using GPS and computer controlled unmanned helicopter with on-board spectroradiometer . Within 30 minutes, totally 26 spectrum data from different observation angle on principal and cross-principal plane can be observed. This system can observe same sensor-target geometry on different sun angle or time.
1-2 Rapid BRF measurement for large area using unmanned helicopter
Using on-board spectroradiometer equipped fixed 3 different angles, large area BRF measurement can be obtained. Combining 1-1 method and simulator described 3-1, BRF representing satellite IFOV can be estimated.

Achievement 2: Canopy structure measurement method development
2-1 Canopy surface measurement from the air
Using unmanned helicopter, on-board laser scanner departed from the canopy only 30 to 50m can detect precise structure of the canopy surface structure. The resolution of DSM generated from observed data is sprier to airborne laider.
2-2 Tree structure parameter measurement from the ground
Using the laser scanner equipped on robot-arm or other platform, tree structure parameter such as DBH, tree height, crown diameter has been developed.

Achievement 3: Bi-directional Reflectance Factor (BRF) simulator development
3-1 BRF simulator uses observed DSM and BRF
In order to calculate the realistic surface situation, generated DSM from helicopter observation data is used. For BEF mode based on linier mixing model also used observed spectrum. Developed simulator can reconstruct the BRF of existed forest.

Achievemnt 4: Vegetation physical parameter estimation
4-1 fAPAR estimation from satellite data
Using MODIS visual bands data, fAPAR estimation method has been developed. The estimation model has been developed from in-situ data of forest incoming, reflected, transmitted light.

Publications

1) Jules R. Dim, Koji Kajiwara, Yoshiaki Honda, Radiometric signature and spatial variability of the vegetation coverage of a boreal forest, International Journal of Remote Sensing Vol. 29, No. 23, 10 December 2008, pp6851-6871,2008
2) Jules R. Dim, Koji Kajiwara, Yoshiaki Honda, Airborne Laser Scanning Derived Vegetation Structuresand Impact on Solar Radiation Scattering, Remote Sensing of Environment, 2008,
3) Junichi Susaki, Keitarou Hara, Koji Kajiwara and Yoshiaki Honda, "Robust Estimation of BRDF Model Parameters", Remote Sensing of Environment, vol.89, pp.63-71, 2004
4) Koji Kajiwara, YoshiakiHonda, Akiko Ono,Yusaku Ono, Development of bidirectional refl ectance function for above-ground vegetation biomass estimation using SGLI sensor,Remote Sensing 2008, CDS322, 7106-26,2008
5) Koji Kajiwara, Yusaku Ono, Yoshiaki Honda, Conifer Forest Biomass Estimation Using Multi Angle Spectrum Observation,2008 Conference of International Symposium on Remote Sensing, 2008
6) Y.HONDA, M.Moriyama, A.Ono, K.KAJIWARA, A study on possibility of land vegetation observation with SGLI/GCOM-C, Remote Sensing 2007, Palazzo degli Affari Conference Centre, FIRENZE Florence, Italy, 2007.9.17～2007.9.21
7) Jules R. Dim, Koji Kajiwara, Yoshiaki Honda, Vegetation Canopy Structural and Physical Variability Based on Radiometric and Laser Analysis, Remote Sensing 2007,Palazzo degli Affari Conference Centre, FIRENZE Florence, Italy, 2007.9.17～2007.9.21
8) Jules R. Dim (JST-SORST), Koji Kajiwara, Yoshiaki Honda(CEReS Chiba Univ, SORST JST), Reflectance Mechanism and Biophysical Characteristics of a Boreal Forest through Analyses of Airborne Spectral Radiance Observations, 2006AGU (American Geophysical Union) Fall Meeting 2006.
9) Kazuy uki Honma, Koji KAJIWARA, Yoshiaki HOND A, Dev elopment of 3D S tructure Measurement Sy stem using Laser Scan ning data and Radio-Controlled Helicopter , The 26th Asian Conference on Remote Sensing(ACRS2005), 2005
10) Y oshiaki HOND A(CEReS, JST .SORST), Hirokazu Y AMAMOTO, Mas ahiro HORI, Hiroshi Murakam i, Nobuyuki Kikuchi(J AXA), Global environm ent monitoring using the next generation satellite sens or, SGLI/GCOM-C, In ternational Geoscience And Rem ote Sensing Symposium(IGARSS)2005, COEX, Seoul, Korea, 2005.7.28, p.4208-4210.
11) Y oshifumi T akafuji, Koji Kajiwara, Y oshiaki Honda (Center for En vironmental Rem ote Sensing, Chiba University ,Japan/SORST,JST), VEGET ATION CLASSIFICA TIONS BY STRUCTURES ESTIMATED FROM DIFFERENCE OF BRF , 25th Asian Conference Rem ote Sensing , The Sheraton Chiang Mai Hotel, 2004
12) Masaki Dem izu, Koji kajiwara, Y oshiaki Honda (Center for Environm ental Rem ote Sen sing, Chiba University , Japan/SORST ,JST), Developm ent of V egetation S tructure Measure ment System using Stereo pair Images and Laser Scanning data, ISRS 2004.
13) Koji kaji wara, Y oshiaki Hon da(Center for Environmental Rem ote Se nsing, Develop m ent of Measurement Method for Phy sical Param eter Re lated Photo-s ynthetic Active Radiation in Deciduous Confer Forest, ISRS 2004.

Project 3

Subject:
Evaluation of radiation budget on the basis of satellite data and ground observation network, and study of long-term changes in atmospheric parameters

Members:
Tamio Takamura and Hiroaki Kuze

Objective of the project:

The satellite evaluation of radiation budget in the Earth's surface system provides basic quantities required for the study of the global climate change including model studies. The accurate understanding of radiation budget is indispensable for studying dynamic behavior of vegetation, hydrology, and ocean environment. The purpose of this project is to investigate the long-term changes in the radiation budget of the East Asia region and related atmospheric parameters in a comprehensive manner, employing both the satellite data and ground-network data.

Summary of Achievement

New algorithms have been developed and tested for extracting various atmospheric parameters from satellite data. Simultaneous observations with ground instruments, including a network observation called SKYNET, are used for validation as well as improvement of the algorithms. Regional and seasonal variations of aerosol, cloud, and radiation amounts have been studied.

Details of Achievement

Achievement 1: Variations of atmospheric parameters and long-term radiation budget using remote sensing data

1-1 Algorithm development for radiation budget studies[1),2)]

Land surface albedo is a key parameter in radiation budge and climate modeling studies. An empirical anisotropy correction model for estimating land surface albedo has been developed for snow free land surfaces under clear sky conditions. The proposed model can be used for direct estimation of surface albedo from a single BRF observation.[1)] The cloud optical thickness(COT) derived from the GMS-5/SVISSR is examined to estimate short-wave radiation budget. By comparing with MODIS COT, the GMS-5-retrieved COT has been corrected.[2)]

1-2 Measurement of time-integral of photosynthesis for NPP estimation in Mongolia[3)]

We applied the monthly mean PAR for vegetation photosynthesis to estimate the NPP from Landsat ETM+ data for a semi-arid area of Mongolia. The estimated NPP results were compared with ground measurement data.

1-3 Long-term characterization of seasonal variation of tropospheric aerosols in Chiba[4)]

Seasonal variations of tropospheric aerosol properties in Chiba, Japan, are investigated by means of sun-photometer measurement (1999–2005), ground sampling (1998–2004), and wind data. The influence of anthropogenic particles from local sources as well as that of Asian dust particles have been detected and discussed. The seasonal variation is remarkable also in the chemical analysis data.

1-4 Estimation of shortwave radiation budget using ADEOS II/GLI data[5)]

The downward and upward solar radiation at the surface and at the top of the atmosphere are estimated using GLI aerosol and cloud products. The ground-observed data using *i*-sky radiometer are used for evaluating the satellite-derived aerosol and cloud products.

Achievement 2: Collection of ground-validation data and improvement in satellite data analysis

2-1 Dual-site lidar observations and satellite data analysis for regional cloud characterization[6)]

Lidar data observed by two continuously operated portable automated lidar (PAL) systems and images from the visible and thermal infrared channels of AVHRR sensor onboard NOAA16 satellite are employed for the characterization of cloud heights and cloud types.

2-2 Influence of inhomogeneous cloud fields on satellite observations[7)]

GMS-5/SVISSR-retrieved cloud optical depth (COD) appeared mostly lower than that of Terra-MODIS. The major factors causing such COD differences are the satellite viewing and solar conditions, the cloud thermodynamic phase differentiation and particle effective radius, and the cloud inhomogeneity. Here the emphasis is put on the examination of the cloud inhomogeneity effect.

2-3 A high-efficiency aerosol scatterometer for the calibration of multi-wavelength lidar data[8)]

A scatterometer was developed to measure the aerosol scattering coefficient at the ground level, on the basis of an integrating sphere, cw lasers, and a controlled flow of the ambient air, including aerosol particles.

2-4 Aerosol mass extinction efficiency studied by continuous lidar measurements[9)]

Continuous data of the atmosphere monitored using a portable automated lidar are correlated with the concentration of ground-measured suspended particulate matter (SPM). When the boundary layer is well mixed, high correlation makes it possible to calculate the mass extinction efficiency of the aerosols in the atmosphere.

2-5 The influence of ambient humidity on the aerosol mass concentration measurements[10)]

The influence of humidity is considered on the concentration of the suspended particulate matter measured with a β-ray counter. For the monthly data taken in September 2005, the difference in relative humidity between inside the instrument (48%) and outside the laboratory (78%) resulted in approximately 53% larger aerosol mass concentration after the correction, also affecting the mass extinction efficiency.

Achievement 3: Analysis of atmospheric environment based on ground-network observations

3-1 Intercomparison between lidar and airborne measurements near Tokyo during ACE-Asia[11)]

In April 2001 during the ACE-Asia campaign, intercomparison studies were carried out near Tokyo using ground-based lidar networks as well as aircraft observations. Modest concentrations of Asian dust in the free troposphere was found to extend up to an altitude of 8 km.

3-2 Study of atmospheric brown cloud and its radiative effect[12), 13)]

Simultaneously measured sky-radiation and surface -solar-flux data are used to retrieve aerosol optical properties. Data sets from several SKYNET sites suggest that Asian dusts become blacked during the movement because of mixing with soot particles produced over the industrial/urban area of China.[12)] In a campaign conducted on Cheju Island, the values of aerosol radiative forcing suggest that the aerosols might consist of more or less yellow sand in comparison with the results simulated using typical aerosol models.[13)]

3-3 Aircraft and ground-based observations of boundary layer CO_2 concentration[14)]

Concentrations of atmospheric CO_2 and aerosol were measured in a field campaign conducted in winter 2006 around Mt. Tsukuba, Japan using ground-based CO_2 analyzers, a lidar, and sky radiometers as well as CO_2 analyzers onboard an aircraft. A sudden increase of downward winds, due to the approach of an anticyclonic synoptic flow, resulted in a rapid decrease in both the CO_2 and aerosol concentrations in the boundary layer.

Publications

1) Y. Cui, Y. Mitomi, and T. Takamura, An empirical anisotropy correction model for estimating land surface albedo for radiation budget studies, Remote Sensing of Environment 113, 24-39, 2009.
2) H. Takenaka, T.Y. Nakajima, I. Okada, J.R. Dim and T. Takamura, Cloud optical thickness estimation from GMS-5/SVISSR, J. Remote Sensing Soc. Japan, 29(2), 392-397, 2009.
3) Y. Xiong, K. Muramatsu, M. Hirata, K. Oishi, I. Kaihotsu, T. Takamura, S. Furumi and N. Fujiwara, Approximation method for time-integral of photosynthesis for NPP estimation using remote sensing data: case study in Mongolia, J. Remote Sensing Soc. Japan, 25(2), 179-190, 2005.
4) S. Fukagawa, H. Kuze, G. Bagtasa, S. Naito, M. Yabuki, T. Takamura, N. Takeuchi, Characterization of seasonal and long-term variation of tropospheric aerosols in Chiba, Japan, Atm.Environ. 40(12), 2160, 2006.
5) T. Takamura, H. Takenaka, Y. Cui, T.Y. Nakajima, A. Higurashi, S. Fukuda, N. Kikuchi, T. Nanakajima, I. Sano and R.T. Pinker, Aerosol and cloud validation system based on SKYNET observations: estimation of shortwave radiation budget using ADEOS II/GLI data, J. Remote Sensing Soc. Japan, 29(1), 40-53, 2009.
6) G. Bagtasa, C. Liu, N. Takeuchi, H. Kuze, S. Naito, A. Sone, and H. Kan, Dual-site lidar observations and satellite data analysis for regional cloud characterization, Optical Review, 14(1), 39-47, 2007.
7) J.R. Dim, T. Takamura, I. Okada, T.Y. Nakajima, and H. Takenaka, Influence of inhomogeneous cloud fields on satellite observations, J. Geophys. Res., 112(D13202), doi:10.1029/2006JD007891, 2007.
8) S. Fukagawa, H. Kuze, N. Lagrosas, N. Takeuchi, High-efficiency aerosol scatterometer that uses an integrating sphere fro the calibration of multiwavelength lidar data, Appl.Optics, 44(17), 3520-3526, 2005.
9) N. Lagrosas, H. Kuze, N. Takeuchi, S. Fukagawa, G. Bagtasa, Y. Yoshii, S. Naito, M. Yabuki, Correlation study between suspended particulate matter and portable automated lidar data, Aerosol Science 36, 439-454, 2005.
10) G. Bagtasa, N. Takeuchi, S. Fukagawa, H. Kuze, S. Naito, Correction in aerosol mass concentration measurements with humidity difference between ambient and instrumental conditions, Atmospheric Environment 41, 1616-1626, 2007.
11) T. Murayama, S.J. Masonis, J. Redemann, T.L. Anderson, B. Schmid, J.M. Livingston, P.B. Russell, B. Huebert, S.G. Howell, C.S. McNaughton, A. Clarke, M. Abo, A. Shimizu, N. Sugimoto, M. Yabuki, H. Kuze, S. Fukagawa, K.L. Maxwell, R.J. Weber, D.A. Orsini, B. Blomquist, A. Bandy, D. Thornton, An intercomparison of lidar-derived aerosol optical properties with airborne measurements near Tokyo during ACE-Asia, J.Geophysi.Res., 108(D23), 6551-8671, 2003.
12) D.-H. Kim, B.-J. Sohn, T. Nakajima and T. Takamura, Aerosol radiative forcing over east Asia determined from ground-based solar radiation measurements, J.Geophys. Res., 110, D10S22, doi:10.1029/2004JD004678, 2005.
13) T. Takamura, N. Sugimoto, A. Shimizu, A. Uchiyama, A. Yamazaki, K. Aoki, T. Nakajima, B. J. Sohn, and H. Takenaka, Aerosol radiative characteristics at Gosan, Korea, during the Atmospheric Brown Cloud East Asian Regional Experiment 2005, J. Geophys.Res., 112, D22S36, doi:10.1029/2007JD008506, 2007.
14) R. Saito, T. Tanaka, H. Hara, H. Oguma, T. Takamura, H. Kuze, and T. Yokota, Aircraft and ground-based observations of boundary layer CO_2 concentration in anticyclonic synoptic condition, Geophys.Res.Lett., 36, L07807, doi:10.1029/2008GL037037, 2009.

Achievement of Project 3: Evaluation of radiation budget on the basis of satellite data and ground observation network, and study of long-term changes in atmospheric parameters

Hiroaki Kuze[1], Tamio Takamura[1], and Naoko Saitoh[1]
[1]*CEReS, Chiba University*
1-33 Yayoi-cho, Inage-ku, Chiba 263-8522, Japan
hkuze@faculty.chiba-u.jp, takamura@faculty.chiba-u.jp

Abstract

The long-term changes in the radiation budget of the East Asia region and related atmospheric parameters have been investigated in a comprehensive manner, employing both the satellite data and ground-network data. Through the recent activities of this project, new algorithms have been developed and tested for extracting various atmospheric parameters from satellite data. Simultaneous observations with ground instruments, including a network observation called SKYNET, are used for validation as well as improvement of the algorithms. Regional and seasonal variations of aerosol, cloud, and radiation amounts have been studied.

Keywords **:** atmospheric remote sensing, radiation budget, aerosol, cloud, atmospheric correction, satellite observation, calibration, ground observation, GOSAT, greenhouse gases

1. Introduction

The satellite evaluation of radiation budget in the Earth's surface system provides basic quantities required for the study of the global climate change including model studies. The accurate understanding of radiation budget is indispensable for studying dynamic behavior of vegetation, hydrology, and ocean environment. The purpose of this project is to investigate the long-term changes in the radiation budget of the East Asia region and related atmospheric parameters in a comprehensive manner, employing both the satellite data and ground-network data. Details of recent achievements will be described in the following sections.

2. Variations of atmospheric parameters and long-term radiation budget using remote sensing data

2.1 Algorithm development for radiation budget studies

Land surface albedo is a key parameter in radiation budge and climate modeling studies. An empirical anisotropy correction model for estimating land surface albedo has been developed for snow free land surfaces under clear sky conditions.[1)] The proposed model can be used for direct

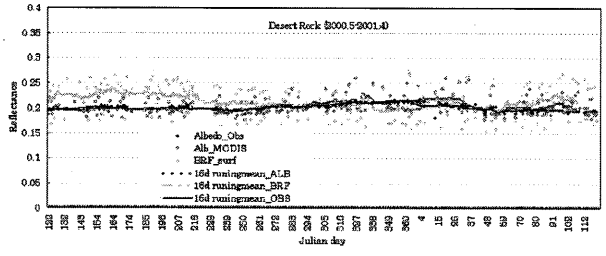

Fig. 1 Comparison of MODIS and surface albedo[1)]

esti

mation of surface albedo from a single BRF observation (Fig. 1). The cloud optical thickness (COT) derived from the GMS-5/SVISSR is examined to estimate short-wave radiation budget. By comparing with MODIS COT, the GMS-5-retrieved COT has been corrected.[2)]

2.2 Measurement of time-integral of photosynthesis for NPP estimation in Mongolia

We applied the monthly mean PAR for vegetation photosynthesis to estimate the NPP from Landsat ETM+ data for a semi-arid area of Mongolia.[3)] The estimated NPP results were compared with ground measurement data.

2.3 Long-term characterization of seasonal variation of tropospheric aerosols in Chiba

Seasonal variations of tropospheric aerosol properties in Chiba, Japan, are investigated by means of sunphotometer measurement (1999–2005) (Fig. 2), ground sampling (1998–2004), and wind data.[4)] The influence of anthropogenic particles from local sources as well as that of Asian dust particles have been detected and discussed. The seasonal variation is remarkable also in the chemical analysis data.

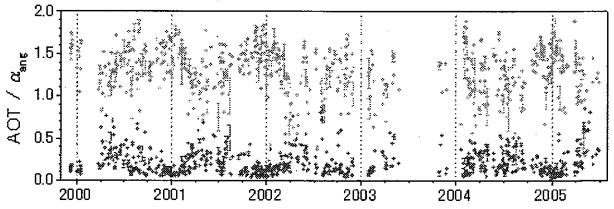

Fig. 2 Long-term variations of aerosol optical thickness (AOT) at 500nm (green) and Angstrom exponent (orange) Average values around noon are plotted.[4)]

2.4 Estimation of shortwave radiation budget using ADEOS II/GLI data

The downward and upward solar radiation at the surface and at the top of the atmosphere are estimated using GLI aerosol and cloud products.[5)] The ground-observed data using i-sky radiometer are used for evaluating the satellite-derived aerosol and cloud products.

3. Collection of ground-validation data and improvement in satellite data analysis

3.1 Dual-site lidar observations and satellite data analysis for regional cloud characterization

Lidar data observed by two continuously operated portable automated lidar (PAL) systems and images from the visible and thermal infrared channels of AVHRR sensor onboard NOAA16 satellite are employed for the characterization of cloud heights and cloud types.[6)]

3.2 Influence of inhomogeneous cloud fields on satellite observations

GMS-5/SVISSR-retrieved cloud optical depth (COD) appeared mostly lower than that of Terra-MODIS.[7)] The major factors causing such COD differences are the satellite viewing and solar conditions, the cloud thermodynamic phase differentiation and particle effective radius, and the cloud inhomogeneity. Here the emphasis is put on the examination of the cloud inhomogeneity effect.

3.3 A high-efficiency aerosol scatterometer for the calibration of multi-wavelength lidar data

A scatterometer (Fig. 3) was developed to measure the aerosol scattering coefficient at the ground level, on the basis of an integrating sphere, cw lasers, and a controlled flow of the ambient air, including aerosol particles.[8)]

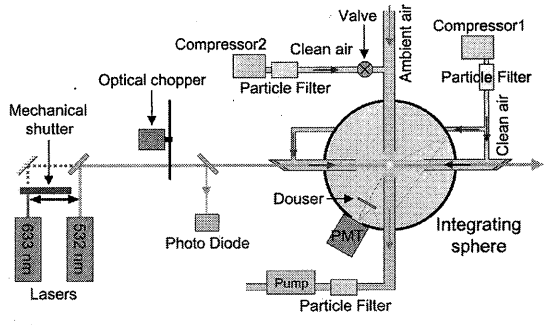

Fig. 3 Aerosol scatterometer based on an integrating sphere.

3.4 Aerosol mass extinction efficiency studied by continuous lidar measurements

Continuous data of the atmosphere monitored using a portable automated lidar are correlated with the concentration of ground-measured suspended particulate matter (SPM).[9)] When the boundary layer is well mixed, high correlation makes it possible to calculate the mass extinction efficiency of the aerosols in the atmosphere.

3.5 The influence of ambient humidity on the aerosol mass concentration measurements

The influence of humidity is considered on the concentration of the suspended particulate matter measured with a β-ray counter.[10)] For the monthly data taken in September 2005, the difference in relative humidity between inside the instrument (48%) and outside the laboratory (78%) resulted in approximately 53% larger aerosol mass concentration after the correction, also affecting the mass extinction efficiency.

4. Analysis of atmospheric environment based on ground-network observations

4.1 Intercomparison between lidar and airborne measurements near Tokyo during ACE-Asia

In April 2001 during the ACE-Asia campaign, intercomparison studies were carried out near Tokyo using ground-based lidar networks as well as aircraft observations. Modest concentrations of Asian dust in the free troposphere was found to extend up to an altitude of 8 km.[11)]

4.2 Study of atmospheric brown cloud and its radiative effect

Simultaneously measured sky-radiation and surface-solar-flux data are used to retrieve aerosol optical properties. Data sets from several SKYNET sites suggest that Asian dusts become blackened during the movement because of mixing with soot particles produced over the industrial/urban area of China.[12)] In a campaign conducted on Cheju Island, Korea, the values of aerosol radiative forcing suggest that the aerosols might consist of more or less yellow sand in comparison with the results simulated using typical aerosol models (Fig. 4).[13)]

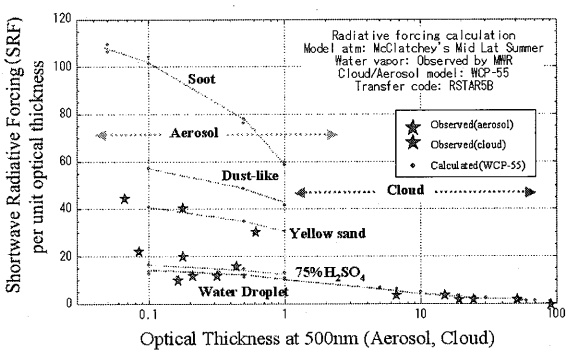

Fig. 4 Shortwave radiative forcing vs. optical thickness.

4.3 Aircraft and ground-based observations of boundary layer CO_2 concentration

Concentrations of atmospheric CO_2 and aerosol were measured in a field campaign conducted in winter 2006 around Mt. Tsukuba, Japan using ground-based CO_2 analyzers, a lidar, and sky radiometers as well as CO_2 analyzers onboard an aircraft.[14] A sudden increase of downward winds, due to the approach of an anticyclonic synoptic flow, resulted in a rapid decrease in both the CO_2 and aerosol concentrations in the boundary layer.

5. Development of algorithm for retrieving CO_2 vertical profiles from GOSAT satellite

5.1 Greenhouse gases observing satellite/thermal and near infrared sensor for carbon observation

The Greenhouse Gases Observing Satellite (GOSAT) is a sun-synchronous orbital satellite developed by NIES, Ministry of Environment, and JAXA for global observations of greenhouse gases.[15] The satellite was successfully launched from the Tanegashima Space Center in Japan on 23 January 2009. The GOSAT completed its system checkout, and started its regular operational observations, including both nadir and off-nadir measurements, of approximately 56,000 ground points every three days. It carries two sensors: the Thermal and Near Infrared Sensor for Carbon Observation (TANSO)-FTS and the TANSO-Cloud and Aerosol Imager (CAI). The former is a Fourier transform spectrometer that measures near infrared and thermal infrared radiances for detecting atmospheric gases. The latter is an imager to detect clouds and aerosols in the instantaneous field of view (IFOV) of the TANSO-FTS. The TANSO-FTS consists of four spectral bands: Band 1 (0.75-0.78 μm), Band 2 (1.56-1.72 μm), Band 3 (1.92-2.08 μm), and Band 4 (5.5-14.3 μm)[16]. The maximum optical path difference of the TANSO-FTS is ±2.5 cm; thus, the full width at half maximum of the instrumental line shape (spectral resolution) is approximately 0.2 cm^{-1}. We use the Band 4 spectra, which include CO_2 absorption band from 700 to 800 cm^{-1} (hereafter referred to as the "CO_2 15-μm band").

5.2 Retrieval methods

A non-linear maximum *a posteriori* (MAP) method[17] is adopted to retrieve CO_2 vertical profiles from the CO_2 15-μm band. In the CO_2 retrieval, we introduce linear mapping between vertical layer grids for radiative transfer calculation (hereafter referred to as "full grids") and grids for CO_2 retrieval ("retrieval grids"). We divide the atmosphere from 1100 to 0.1 hPa into 110 layers, and define the layers as the full grids. We define the retrieval grids on the basis of the CO_2 averaging kernel functions. We select channels for the CO_2 retrieval using CO_2 information content in the CO_2 15-μm band. Through CO_2 retrieval simulations, we confirmed that selecting 100 channels on the basis of CO_2 information content for all layers, 10 channels for the region above 55 hPa, and 50 channels for the region below 800 hPa was sufficient to achieve CO_2 retrieval with 1% accuracy from the troposphere through the stratosphere. In the CO_2 retrieval, uncertainties in the estimates of profiles of temperature, water vapor, and ozone are considered as a part of measurement spectral noise. For the GOSAT operational data processing, outputs from the NIES transport model[18] are used as *a priori* CO_2 profiles. The *a priori* error covariance matrix is determined from errors in the NIES transport model[19].

5.3 Preliminary CO_2 retrieval results

We now analyze the interferograms obtained by the TANSO-FTS to determine several correction parameters for a nonlinearity correction and a phase correction. Although several adjustments based on its in-orbit calibrations have to be applied to the interferograms, we retrieved CO_2 profiles from the not-well calibrated Band 4 spectra by using the

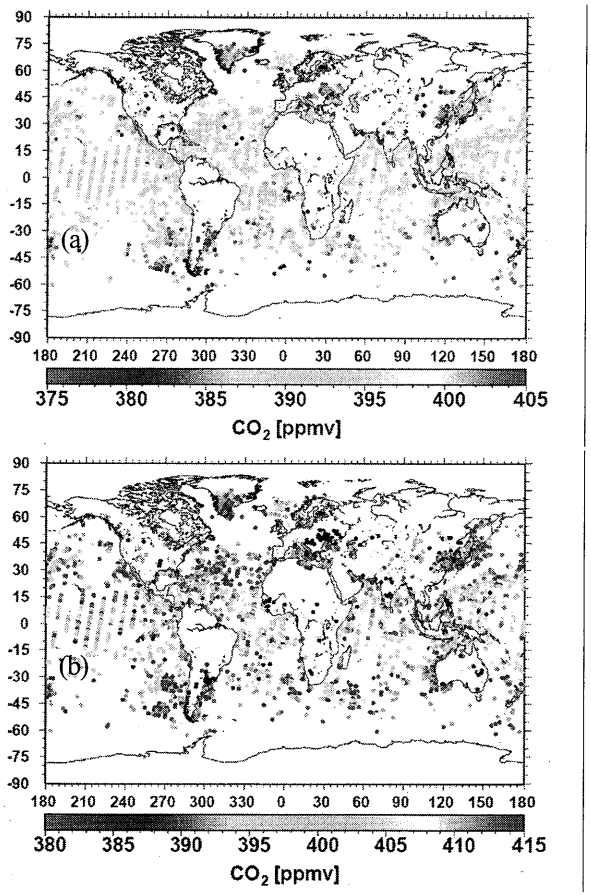

Fig. 5 CO_2 concentrations retrieved from the TANSO-FTS Band 4 spectra obtained from April 6 to 8, 2009 on (a) 770 hPa pressure level; (b) 500 hPa pressure level.

developed algorithm. Figure 5 shows CO_2 concentrations retrieved from the clear-sky Band 4 spectra obtained in the daytime from April 6 to 8, 2009. In the daytime, judgment of clear-sky or cloudy conditions is based on the cloud flags provided by the TANSO-CAI. As shown in Figure 5(a), a reasonable latitudinal gradient in CO_2 concentrations can be seen at 770 hPa; CO_2 concentrations over the land in the Northern Hemisphere are higher than those over the ocean and in the Southern Hemisphere. In the middle troposphere, however, evident positive biases exist at low latitudes.

References

1) Y. Cui, Y. Mitomi, and T. Takamura, An empirical anisotropy correction model for estimating land surface albedo for radiation budget studies, Remote Sensing of Environment 113, 24-39, 2009.

2) H. Takenaka, T.Y. Nakajima, I. Okada, J.R. Dim and T. Takamura, Cloud optical thickness estimation from GMS-5/SVISSR, J. Remote Sensing Soc. Japan, 29(2), 392-397, 2009.

3) Y. Xiong, K. Muramatsu, M. Hirata, K. Oishi, I. Kaihotsu, T. Takamura, S. Furumi and N. Fujiwara, Approximation method for time-integral of photosynthesis for NPP estimation using remote sensing data: case study in Mongolia, J. Remote Sensing Soc. Japan, 25(2), 179-190, 2005.

4) S. Fukagawa, H. Kuze, G Bagtasa, S. Naito, M. Yabuki, T. Takamura, N. Takeuchi, Characterization of seasonal and long-term variation of tropospheric aerosols in Chiba, Japan, Atm.Environ. 40(12), 2160, 2006.

5) T. Takamura, H. Takenaka, Y. Cui, T.Y. Nakajima, A. Higurashi, S. Fukuda, N. Kikuchi, T. Nanakajima, I. Sano and R.T. Pinker, Aerosol and cloud validation system based on SKYNET observations: estimation of shortwave radiation budget using ADEOS II/GLI data, J. Remote Sensing Soc. Japan, 29(1), 40-53, 2009.

6) G Bagtasa, C. Liu, N. Takeuchi, H. Kuze, S. Naito, A. Sone, and H. Kan, Dual-site lidar observations and satellite data analysis for regional cloud characterization, Optical Review, 14(1), 39-47, 2007.

7) J.R. Dim, T. Takamura, I. Okada, T.Y. Nakajima, and H. Takenaka, Influence of inhomogeneous cloud fields on satellite observations, J. Geophys. Res., 112 (D13202), doi:10.1029/2006JD007891, 2007.

8) S. Fukagawa, H. Kuze, N. Lagrosas, N. Takeuchi, High-efficiency aerosol scatterometer that uses an integrating sphere fro the calibration of multiwavelength lidar data, Appl.Optics, 44(17), 3520-3526, 2005.

9) N. Lagrosas, H. Kuze, N. Takeuchi, S. Fukagawa, G Bagtasa, Y. Yoshii, S. Naito, M. Yabuki, Correlation study between suspended particulate matter and portable automated lidar data, Aerosol Science 36, 439-454, 2005.

10) G Bagtasa, N. Takeuchi, S. Fukagawa, H. Kuze, S. Naito, Correction in aerosol mass concentration measurements with humidity difference between ambient and instrumental conditions, Atmospheric Environment 41, 1616-1626, 2007.

11) T. Murayama, S.J. Masonis, J. Redemann, T.L. Anderson, B. Schmid, J.M. Livingston, P.B. Russell, B. Huebert, S.G Howell, C.S. McNaughton, A. Clarke, M. Abo, A. Shimizu, N. Sugimoto, M. Yabuki, H. Kuze, S. Fukagawa, K.L. Maxwell, R.J. Weber, D.A. Orsini, B. Blomquist, A. Bandy, D. Thornton, An intercomparison of lidar-derived aerosol optical properties with airborne measurements near Tokyo during ACE-Asia, J.Geophysi.Res., 108(D23), 6551-8671, 2003.

12) D.-H. Kim, B.-J. Sohn, T. Nakajima and T. Takamura, Aerosol radiative forcing over east Asia determined from ground-based solar radiation measurements, J.Geophys. Res., 110, D10S22, doi:10.1029/2004JD004678, 2005.

13) T. Takamura, N. Sugimoto, A. Shimizu, A. Uchiyama, A. Yamazaki, K. Aoki, T. Nakajima, B. J. Sohn, and H. Takenaka, Aerosol radiative characteristics at Gosan, Korea, during the Atmospheric Brown Cloud East Asian Regional Experiment 2005, J. Geophys. Res., 112, D22S36, doi:10.1029/2007JD008506, 2007.

14) R. Saito, T. Tanaka, H. Hara, H. Oguma, T. Takamura, H. Kuze, and T. Yokota, Aircraft and ground-based observations of boundary layer CO_2 concentration in anticyclonic synoptic condition, Geophys.Res.Lett., 36, L07807, doi:10.1029/2008GL037037, 2009.

15) T. Hamazaki, Y. Kaneko, A. Kuze, and K. Kondo, Fourier transform spectrometer for Greenhouse Gases Observing Satellite (GOSAT), Proc. of Soc. Photo Opt. Instrum. Eng., 73-80, 2005.

16) A. Kuze, T. Urabe, H. Suto, Y. Kaneko and T. Hamazaki, The instrumentation and the BBM test results of Thermal And Near infrared Sensor for carbon Observation (TANSO) on GOSAT, Proc. of Soc. Photo Opt. Instrum. Eng., 10.1117/12.677113, 2006.

17) C.D. Rodgers, Inverse method for atmospheric sounding, World Scientific Publishing, 2000.

18) S. Maksyutov, P. K. Patra, R. Onishi, T. Saeki, and T. Nakazawa, NIES/FRCGC global atmospheric tracer transport model: description, validation, and surface sources and sinks inversion, J. Earth. Sim., 9, 3-18, 2008.

19) N. Eguchi, R. Saito, T. Saeki, Y. Nakatsuka, D. Belikov and S. Maksyutov, A priori covariance estimation for CO_2 and CH_4 retrievals, J. Geophys. Res., in revision, 2009.

Introduction of FrameFree Studio for Visualization and Analyzing on Environmental Remote Sensing

Nobuo Akiyoshi
Monolith Co., LTD
2F-6-4, Azabu-Jyuban, 2-chome, Minato-ku, Tokyo, Japan
E-mail:nobu@monolith-prime.co.jp

1. Abstract

The FrameFree Studio, software product of Monolith Co., has been planed and developed for Medical purpose imaging, Scientific visualization, Analyzing and Modeling in this decade.

The most distinguish point of the FrameFree Studio is that having pixel by pixel full automatic matching algorithm(1), mesh image representation and data volume reduction, very flexible interpolation functionality with parameter operation, drastic reduction effect of data volume of movie and very unique movie image representation system (Patented in Japan(2), USA(3), China, Korea, etc).

2. Introduction

Almost existent movie system is based on afterimage theory by viewing many images in short period for human eyes (frame by frame system), but FrameFree imaging system is totally different, the basic process is as follows.

Encoding system is that calculate matching information full automatically between 2 key frames pixel by pixel, making matching information map (about 2 KB mathematical function, very small amount of data volume), then output unique FrameFree file format composed by key frames and intermediate mathematical function map .

Decoding system is that input FrameFree format, output movie by real time rendering process by computer using 2 key frames and intermediate mathematical function map, this method of viewing process enable to operate movie very flexible by user oriented parameter specification.

For example, changing real time rendering speed parameter enable to get movie representation speed without limitation, normal movie could be changed into super slow motion movie, changing real time rendering direction enable to change representation direction of movie very easily as well.

Also analyzing the intermediate mathematical function map, enable to detect the moving vector information between 2 key frames, it means very useful analyzing system for observation data could be able to get and to develop very powerful simulation system introducing by physical logic or theoretical algorithm through collaboration with researcher, scientist and computer expert .

3. Application Examples

Fig.1 Analysis of NDVI image

Visualization and Analysis

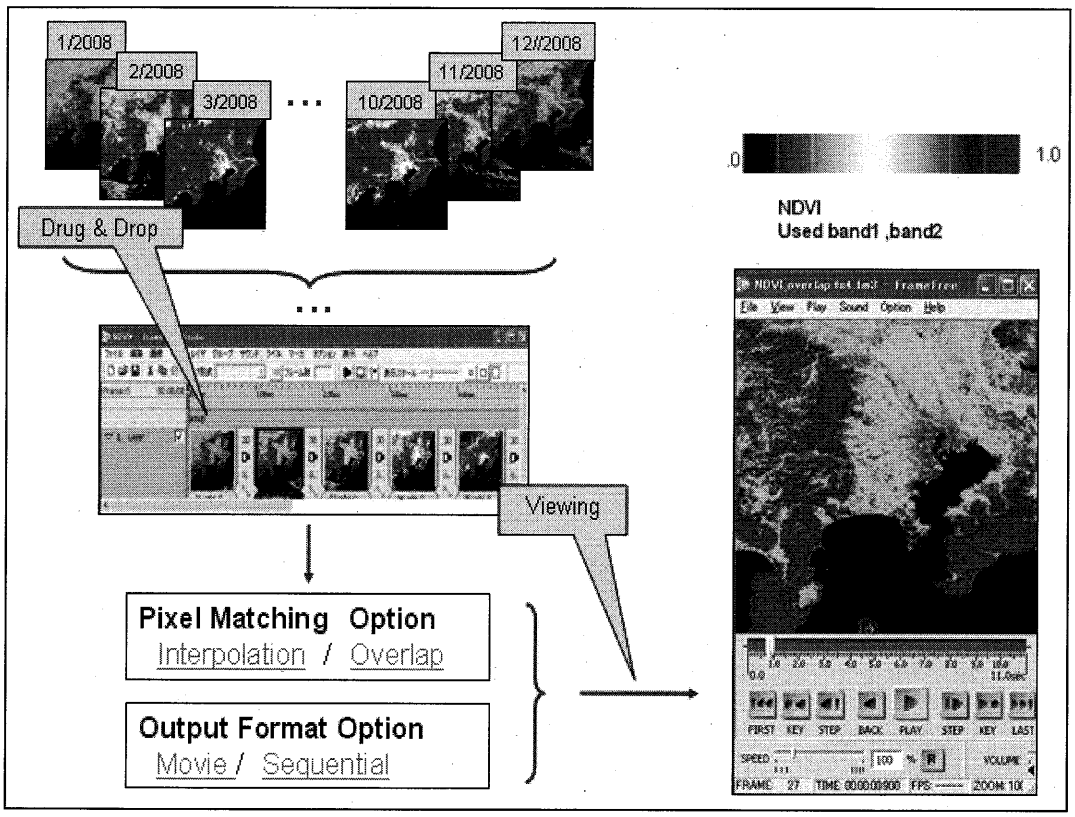

Fig.2 Weather Forecast

Discrete Cloud Image Smoothing

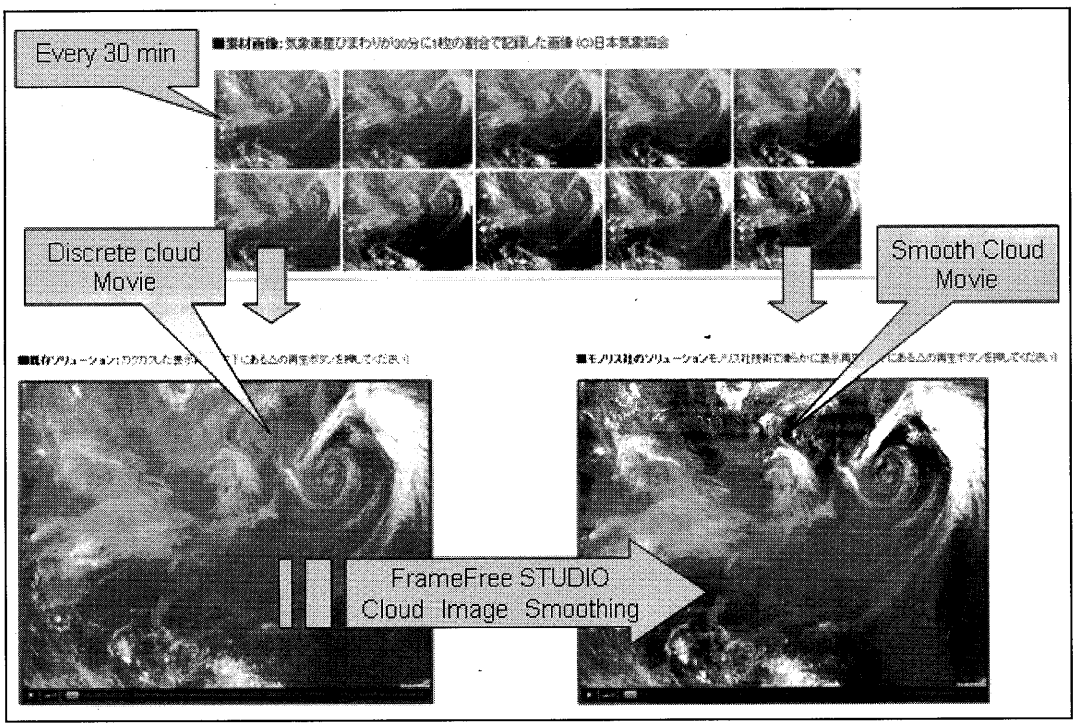

Fig.3 Arctic Ice Summer Minimum
Observation and Prospect （1990-2049）

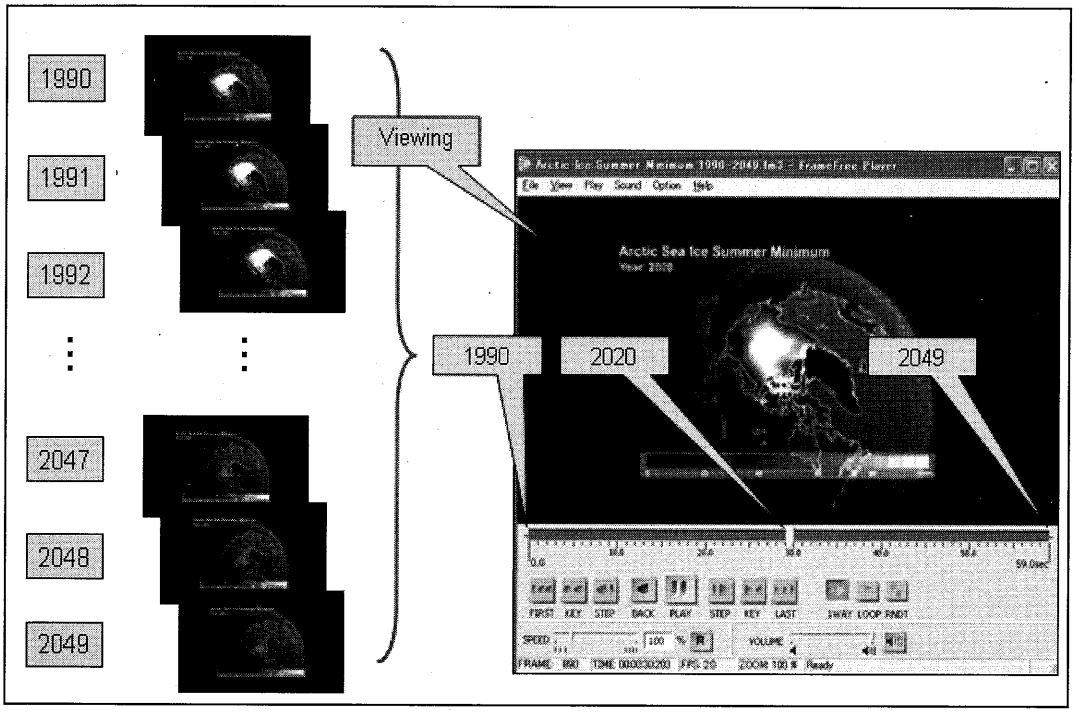

Fig.4 Grey Typhoon Images (Oct, 6, 2009-Oct, 8, 2009/1H)

Brightness Temperature

Analyzing by Adaptive Mesh Structure

Calculating moving vector, direction and strength, speed and acceleration

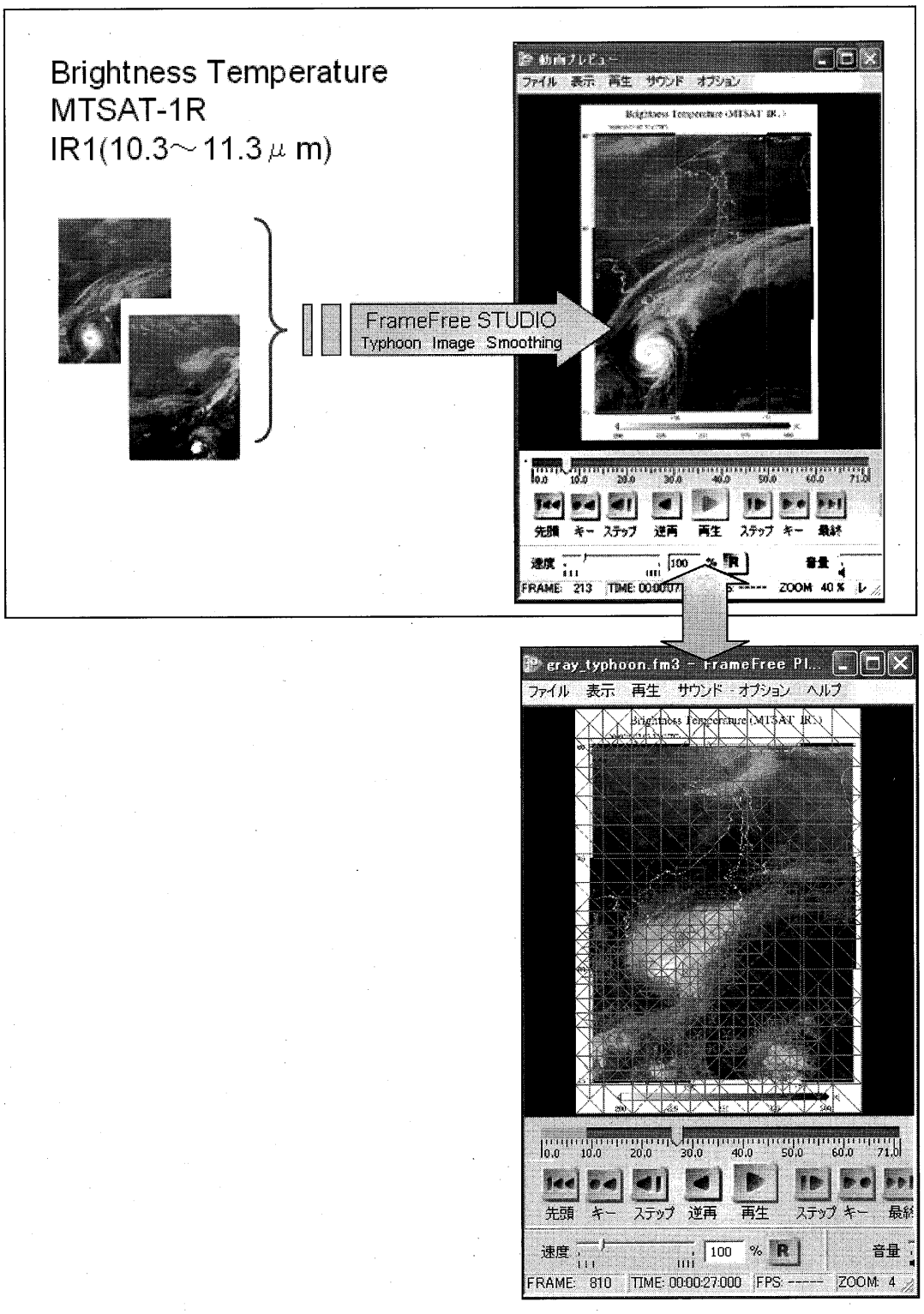

4. Conclusions and Future work

As the first step, to awake the crisis of the Global Environment Change how serious to the ordinary people, the visualization information service using FrameFree Studio is very easy to realize with very reasonable cost.

But the next step is required more accurate and having analyzing system for scientific approach with calibration and validation, so I believe that we need to collaborate with expert of Environmental Remote Sensing researcher and Laboratory in world wide scale to develop and to establish new visualization, analyzing system and useful user needs oriented application.

5. Acknowledgements

This time, I appreciate to get opportunity to join to the 15th CEReS International symposium entitled "Achievement and New Challenge of Environmental Remote Sensing", and to be able to introduce our company's software FrameFree Studio.

I would like to extend to my gratitude to Dr. Hiroaki Kuse and the member of the Kuse Laboratory, Dr. Atsushi Higuchi, Dr. Ryutaro Tateishi and Dr. Fumihiko Nishio of the Director of the CEReS.

Also I would like to extend my gratitude to the Ministry of Education, Science, Sports and Culture, Japan (MEXT), and National University Corporation Chiba University.

6. References and Patents

(1) Yosihisa Shinagawa and Tosiyasu L. Kunii, "Unconstrained Automatic Image Matching Using Multiresolutional Critical-Point Filters", IEEE Transactions on Pattern Analysis and Machine Intelligence, Volume 20,Numer 9,September 1998

(2) Patent Registered Japan : No. 2927350

(3) Patent Registered USA : No. 6018592

Achievement of CEReS Research Projects

Project 4

Subject:
Application of remote sensing methods to regional issues --- enlightenment activities by means of the synergy effect of various spatial data

Members:
Akihiko Kondoh, Hiroaki Kuze, Chiharu Hongo

Objective of the project:
Presently several earth observation satellites are operating simultaneously and new satellite programs are planned. In this circumstance, the use of satellite data is expected to be important for understanding the regional environment and for exploiting a new field of application. In this project, by integrating and freely providing the spatial information such as satellite data and geographical information, we expect to generate synergetic effect with the combination of CEReS research method and result, then to create a new field and to feedback the scientific results to a local.

Summary of Achievement
Satellite remote sensing was applied to various problems existing in Asian region. The problems to be solved include water problems, food problems, air pollution, and many. New remote sensing techniques were developed for advanced agriculture, air pollution monitoring, and so on. Satellite imageries and their secondary data were open to public through world wide web to promote the utilization of satellite remote sensing.

Details of Achievement

Achievement 1: Water problems in China

1-1 Hydrological cycle in North China Plain, China [1)]
Fields research was started in 1998 concerning hydrological cycle (including flux studies) and its implications to water problems in North China Plain (NCP). Decadal collaboration with Chinese colleagues achieved proper recognition of current situation and future perspective of water resources in semi-arid NCP.

1-2 China's Great flood in 1998[2)]
China suffered great flood in Changjiang, Songhua and Nenjiang in 1998. Especially, flood hazard in Changjiang got worldwide news coverage. Because 1998 was the warmest year after global warming got a position of primary global concern, the floods were tend to be considered as the effect of global warming. Detailed monitoring of flood by satellite and field research with Chinese colleges revealed the floods are influenced not only by climatic change but also by human factors.

Achievement 2: Environmental monitoring in Asia

2-1 Herbaceous plant monitoring in semi-arid environment[3)]
Herbaceous plant that supports environment and life in semi-arid region was vulnerable to climatic change. The response of herbaceous plant to weather conditions was examined in Mongolia and Inner-Mongolian Plateau. The outcomes gave an implication on the response of grassland ecosystem to the global warming.

2-2 Groundwater degradation in arid region[4)]
Groundwater as a primary water resource in arid region was investigated in United Arab Emirates, Turpan basin in western China, and the Dead Sea Basin, Jordan. Synthetic research including remote sensing revealed the occurrence of groundwater, changes in groundwater cycle, geochemical characteristics, accompanied water problems, and so on. The outcomes offered valuable knowledge for integrated water managing in arid regions.

2-3 Hydrological changes in Xinjiang, China[5)]
The response of regional water resources to the climatic changes was investigated in Xinjiang, China. Water resources were changing under the influences of both human factors and climatic factors. The outcome presented the holistic perspective of future water resources in Xingjiang.

2-4 Heat island studies in Tokyo Metropolitan Area[6)]
Heat islands in Tokyo Metropolitan Area were researched by using remote sensing and GIS. The results showed the decadal changes in heat islands and its effect to local weather conditions.

Achievement 3: Air pollution monitoring

3-1 Measurement of NO_2 and aerosol in the urban atmospheric using differential optical absorption spectroscopy (DOAS) with an aviation obstruction light source [7), 8), 9), 10)]
We proposed a novel DOAS method that is based on a white flashlight source and a compact CCD spectrometer. By using an optical path length of 5.5 km, for instance, NO_2 and SPM concentrations can be measured with an accuracy of 1 ppb and 1 $\mu g/m^3$, respectively. The DOAS method acquires a data point every five minutes, much more frequent than the data (every one hour) provided from the Ministry of the Environment

Atmospheric Environmental Regional Observation System (AEROS).

3-2 Measurement of atmospheric pollutants using differential optical absorption spectroscopy (DOAS) with a PC projector light source [11)]

The DOAS measurement with an aviation obstruction light is limited to the daytime. Moreover, the measurement cannot be carried out where no obstruction flashlight is situated. Alternatively, we proposed the use of a commercially available PC projector as a white-light source. This is relatively inexpensive, yet the possibility of unattended, continuous operation is quite suitable for the DOAS measurement. This light source is portable, and it can be used during both daytime and night time. A conventional PC projector was successfully used as a DOAS light source in Seoul, Chiba and Nagano, making it possible to observe the data for 24 hours.

Achievement 4: Utilization of Spatial Information Data project

4-1 Development of an efficient sugar beet cultivation support system [12,13)]

To assess the feasibility of developing an efficient sugar beet cultivation support system to effectively reduce the costs of beet cultivation, beet collection and sugar production using an agricultural spatial information data, and also to predict the root yield of sugar beet three months before the harvesting season, an analysis of satellite data and meteorological data was carried out in this study.

Achievement 5: Environmental Information Base Projects

5-1 Land Information Browsing System

Homepages that publish digital thematic maps was constructed on WWW and open to public through internet. The datasets include secondary products of satellite data and thematic maps on land characteristics.

5-2 Satellite Image Browsing System

Homepages that exhibit past satellite images were constructed on WWW and open to public through internet. Past imageries after 1972 could produce new information through synergy with clients.

Publications

1) Yanjun Shen, Yongqiang Zhang, Akihiko Kondoh, Changyuan Tang, Jianyao Chen, Jieying Xiao, Yasuo Sakura, Changming Liu and Hongyong Sun(2004): Seasonal variation of energy partitioning in irrigated lands, Hydrological Processes, 18, 2223-2234.
2) Li, J. Kondoh, A. and Nakayama,D.:(1999):Analyses on Floods of 1998 in China. Journal of Japan Society of Hydrology and Water Resources, 12(4), 307-318.
3) Kondoh, A. , Kaihotsu, I., Hirata, M., and Azzaya, D.(2005): Interannual Variation of Phenology and Biomass in Mongolian Herbaceous Vegetation. Journal of Arid Land Studies, 14(4), 209-218. (in Japanese with English Abstract)
4) Ahmad Al-Hanbali and Akihiko Kondoh(2008):Groundwater vulnerability assessment and evaluation of human activity impact (HAI) within the Dead Sea groundwater basin, Jordan.Hydrogeology Journal,DOI 10.1007/s10040-008-0280-7.
5) Dilinur Aji, Akihiko Kondoh, Changyuan Tang(2008):Analysis of hydrological changes of lakes and rivers in XinJiang using GIS techniques and remote sensing data. IAHS Publ., 319, 175-183.
6) Shiraki,Y., Higuchi A., and Kondoh, A.(2009): The effect of an urban environment on the precipitation in areas around Tokyo. Environmental Sciences, 22(3), 187-195. (in Japanese with English Abstract)
7) Si, F., J. Liu, P. Xie, Y. Zhang, W. Liu, H. Kuze, C. Liu, L. Nofel and N. Takeuchi, Determination of aerosol extinction coefficient and mass extinction efficiency by DOAS with a flashlight source, Chinese Phys., 14(11), 2360-2364, 2005.
8) Si,F., H. Kuze, Y. Yoshii, M. Nemoto, N. Takeuchi, T. Kimura, T. Umekawa and T. Yoshida, Measurement of regional distribution of atmospheric NO_2 and aerosol particles with flashlight long-path optical monitoring, Atmospheric Environment, 39(27), 4959-4968, 2005.
9) Si, F., J. Liu, P. Xie, Y. Zhang, W. Liu, H. Kuze, L. Nofel and N. Takeuchi, Correlation study between suspended particulate matter and DOAS data, Advances in Atmospheric Sciences, 23(3), 461-467, 2005.
10) Yoshii, Y., H. Kuze and N. Takeuchi, Long-path measurement of atmospheric NO_2 with an obstruction flashlight and a charge coupled device spectrometer, Applied Optics, 42(21), 4362-4368, 2003.
11) Harada, I., D. Kataoka, M. Miyazaki, H. Kuze, T.Ichinose, Measurement of atmospheric pollutants by means of differential optical absorption spectroscopy (DOAS) with a PC projector light source, International Journal of Climatology, 2009 (to be submitted).
12) Chiharu Hongo, K. Niwa, J. Yokobori , R. Yamada and M. Kuwahara, Development of an efficient sugar beet cultivation support system using the agricultural spatial information –Prediction of root yield using meteorological data and satellite data-, Journal of Sugar Beet Research (in press)
13) Katsuhisa Niwa, Nobutaka Seino, Jun Yokobori, Koji Kikuchi and Chiharu Hongo, Effect of soil type on the time-course of changes in sugar beet(Beta vulgaris L.) productivity in Tokachi District, Hokkaido, Lapan, Soil Science and Plant Nutrition, 54, 928-937, 2008

Application of remote sensing methods to regional issues

- Promotion of regional environmental studies in Asia -

Akihiko Kondoh[1], Hiroaki Kuze[1], Chiharu Hongo[1]

[1]*Center for Environmental Remote Sensing (CEReS), Chiba University*

1-33 Yayoi-cho, Inage-ku, Chiba 263-8522 Japan, kondoh@faculty.chiba-u.jp

Abstract

In the context of the Project 4, a partial results on area studies and advanced databases were presented in this paper. As a connection to Project 1, results of global surface changes detection were explained first to find the local surface changes. Several important outcomes were selected and gave brief explanation. To find and organize the achievements of area studies, spatial database should be developed. Final part of the paper reported the example of databases on spatial information.

Keywords: area studies, Asia, advanced databases, collaboration for solution

1. Introduction

A lot of earth observation satellites have been operating during last decades, and new satellite programs are planned. In this circumstance, satellite data is expected to be useful for understanding the regional environment and for the solution of regional environmental issues. In project 4, we expect to generate synergetic effect with remote sensing and many other fields which deals with environmental issues by integrating spatial information and field experiences.

The majors of principle members are geography, atmospheric sciences, and agriculture sciences. So we set up the four main themes.

- Area studies in Asia
- Atmospheric environment
- Application to agriculture
- Advanced databases

Satellite remote sensing has been applied to various problems existing in Asian region. The problems to be solved in the project include water problems, food problems, air pollution, and many. New remote sensing techniques were developed for advanced agriculture, air pollution monitoring, and so on. Satellite imageries and their secondary data were open to public through world wide web to promote the utilization of satellite remote sensing.

The spectrum of our research target is too large. In this paper, we will introduce the outcomes from area studies, and advanced databases. Please refer to the papers included in the proceedings for remaining themes.

2. Selected Achievement

2.1 Detection of environmental changes by global remote sensing

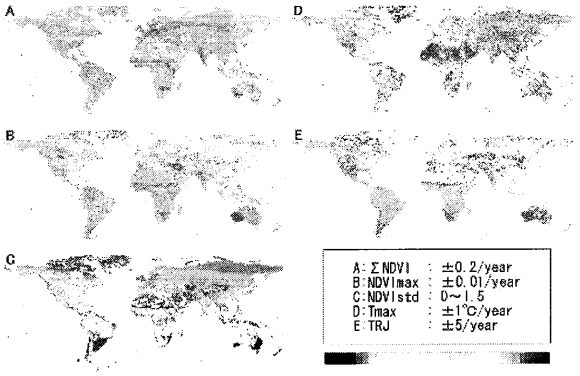

Fig.1 The results of global trend analyses between 1982 and 2000 by NOAA/AVHRR (Kondoh, 2004 .

Global issues are appeared by the problem on the relationship between human and nature in a region. This is the reason why area studies should be promoted. However, there are vast amount of problems to be solved on the globe. Each problem may be small but deep, and essential problem in the local people. To find the problems, global change detection scheme is applied to global dataset derived from NOAA/AVHRR.

Fig.1 shows the result of trend analyses between 1982 and 2000 using indices derived from *NDVI* and *Brightness Temperature* Kondoh, 2004). By combining these diagrams, important surface changes can be detected. One of important outcome is the detection of vegetation changes in the ecotone of tundra and boreal forest in Eastern Siberia shown in Fig. 2 (Sakai *et al.*, 2008).

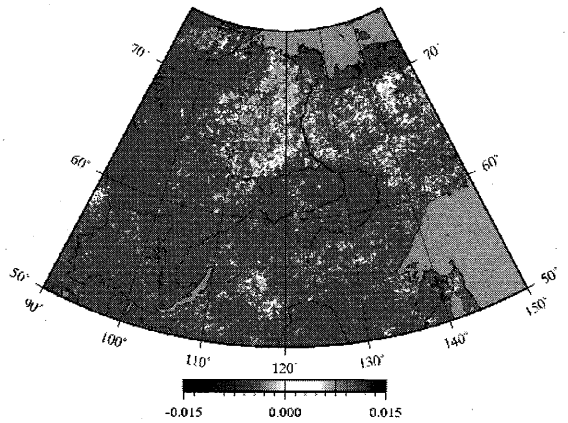

Fig.2 Increasing trend in annual maximum NDVI in red color, which suggests vegetation change possibly by global

The contents of this section is a part of *Project 1*. A great deal of the achievements of area studies can be located and interpreted on the framework of global change mapping.

2-2 Selected area studies in Asia

(1) Water problems in North China Plain, China

We started the discussion of the project in 1997 with Chinese colleagues, and fields research was started in 1998. This project is concerning hydrological cycle and its implications to water problems in North China Plain (NCP). The field work include groundwater survey, flux measurement, hill slope study, and of course remote sensing.

NOAA/AVHRR and GMS data received in CEReS are used to monitor surface wetness. Combined method with NDVI and Brightness temperature by NOAA/AVHRR, and thermal inertia monitoring by GMS showed good performance to detect surface wetness (Kondoh and Oyamada, 2000).

Decadal collaboration with Chinese colleagues achieved proper recognition of current situation and future perspective of water resources in semi-arid NCP.

(2) China's Great flood in 1998

China suffered great flood in Changjiang, Songhua and Nenjiang in 1998. Because 1998 was the warmest year after global warming got a position of primary global concern, the floods were tend to be considered as the effect of global warming, and got worldwide news coverage.

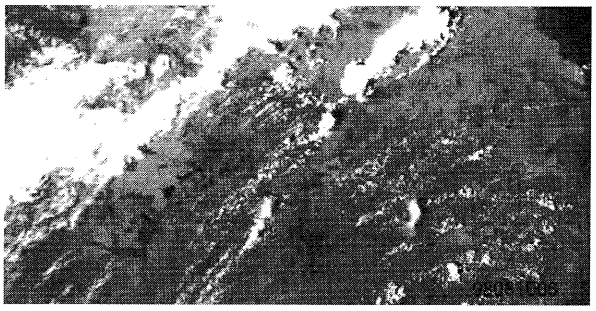
Fig.3 The NOAA/AVHRR image in August 10, 1998 received in CEReS. At this date, bank was collapsed in one place, and retarding basins was filled by water.

Detailed monitoring of flood by satellite and field research with Chinese colleagues revealed the flood was a normal big one, and the effect of climatic changes was hard to be recognized (Li *et al.*, 1999).

NOAA/AVHRR images received in CEReS could send imageries of changing inundation area in the middle reach of Changjiang River through WWW. Fig.3 shows the image in August 10 when water level in Changjiang was the highest.

(3) Glassland monitoring in semi-arid environments

Herbaceous plant that supports environment and life in semi-arid region was vulnerable to climatic change. The response of herbaceous plant to weather conditions was examined in Mongolia and Inner-Mongolian Plateau. The outcomes gave an implication on the response of grassland ecosystem to the global warming.

In the grassland ecosystem, vegetation activity is strongly depended on water availability. If global warming may cause desiccation, herbaceous plant got the serious damage (e.g. Kondoh *et al.*, 2005).

(4) Groundwater degradation in arid region

Groundwater as a primary water resource in arid region was investigated in United Arab Emirates, Turpan basin in western China, and the Dead Sea Basin, Jordan, and many sites in Asia. Synthetic research including remote sensing revealed the occurrence of groundwater, changes in groundwater cycle, geochemical characteristics, accompanied water problems, and so on. The outcomes offered valuable knowledge for integrated water management in arid regions.

(5) Hydrological changes in Xinjiang, China

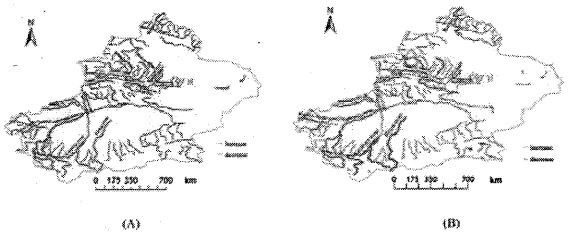

Fig.4 Changes in annual discharge. Red and blue denote increase and decrease, respectively. (A) 1956-1986, (B) 1987-2000. Recent increase in Northern Xinjiang is apparent.

The response of regional water resources to the climatic changes was investigated in Xinjiang, China. Water resources were changing under the influences of both human and climatic factors. The outcome presented the holistic perspective of future water resources in Xinjiang.

Fig.4 shows the detected hydrological change in the rivers in Xinjiang. Increase in discharge may implicate the effect of global warming (Aji *et al.*, 2008).

(5) Heat island studies in Tokyo Metropolitan Area

Heat islands in Tokyo Metropolitan Area were researched by using remote sensing and GIS. The results showed the decadal changes in heat islands and its effect to local weather conditions (e.g. Harada and Kondoh, 2005; Shiraki *et al.*, 2008).

2-3 Environmental Information Base Projects

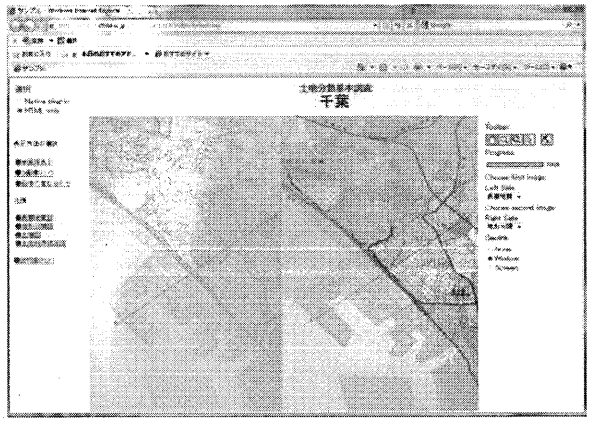

Fig.5 An example of land information systems. Characteristics of land can be interpreted by inspecting the browse maps. This system can be used substitute of Hazard Maps.

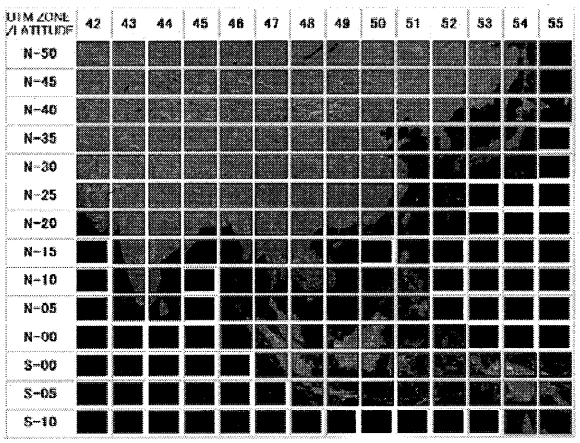

Fig.6 Potal site of satellite image browsing system.

(1) Land Information Browsing System

Homepages that publish digital thematic maps was constructed on WWW and open to public through Internet. The datasets include secondary products of satellite data and thematic maps on land characteristics. Fig.5 shows an example of such a homepage.

(2) Satellite Image Browsing System

Homepages that show past satellite images were constructed on WWW and open to public through Internet. Accumulation of past imageries after 1972 could produce new information through synergy with clients who are the specialist of many fields and sectors.

By inspecting images through this page, we can find many environmental changes that may be serious issue to be solved in the region. Fig.6 shows the portal site of such a image browsing system. When you click the tile (48, N-28), the

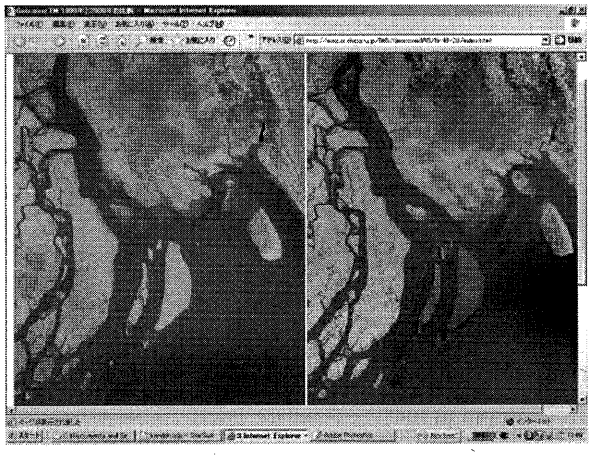

Fig.7 Landsat images in 1990 and 2000. Original images are NASA Geocover TM Mosaics.

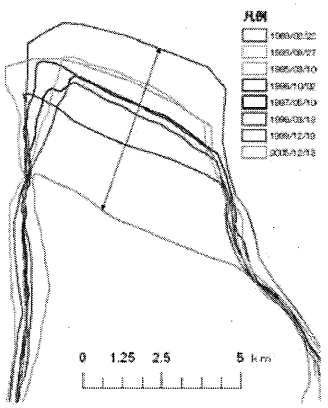

Fig. 8 Time changes in northern coast of Hatiya Island, Bangladesh (Original diagram by Ohtani, 2009).

pop-up appears (Fig.7) and find the changes in coastal lines in Bangladesh between 1990 and 2000.

The recognition of the fact may urged us to study the time changes of the coast in the mouth of Ganges. Fig. 8 shows the changes in the coast line at the north part of Hatiya Island. The coast lines are delineated by JERS1 SAR data because SAR is all-weather type sensor. Image analyses reveals the coast had been recessed about 5 kilometers during past 15 years. The recession rate show the correlation to precipitation amount that means the erosion is a working of nature.

3. Final remarks

Global issues are appeared as a problem in a region. We have to keep close observation of the any places in the world, especially in Asia. Satellite remote sensing is a powerful tool to detect surface changes due to its temporal and spatial nature.

However, outcomes of area studies often consider as case studies. We do emphasize the importance of area studies because the world consists of many regions. There is no universal means to solve all the regional issues. We should accumulate the outcomes and experiences from the region.

To organize the many achievements from the region, databases should be constructed to share the outcome from the regions. Solution should be based on the collaboration among different fields and different sectors.

Remote sensing is a effective tools in the collaboration work because accumulation of Earth Observation Data during past 30 years is vast. Change detected include the effects of climatic and human factors. The problem is the one concerning the relationship between nature and human in a region. We have to share the solution between science and local sectors based on the real understanding of the problem. It is the goal of *the Project 4*.

We have to find the signals of environmental changes, and locate it to global spatial framework toward satellite environmental change science. Solution should based on collaboration.

References

Kondoh,A and Oyamada, Y. (2000): Monitoring surface moisture and vegetation status by NOAA and GMS over North China Plain. *Advances in Space Research*, 26(7), 1055-1058.

Li, J. Kondoh, A. and Nakayama,D.: (1999) :Analyses on Floods of 1998 in China. *Journal of Japan Society of Hydrology & Water Resources*, 12(4), 307-318

Dilinur Aji, Akihiko Kondoh, Changyuan Tang (2008):Analysis of hydrological changes of lakes and rivers in XinJiang using GIS techniques and remote sensing data. *IAHS Publ.*, 319, 175-183.

Kondoh, A. , Kaihotsu, I., Hirata, M., and Azzaya, D.(2005): Interannual Variation of Phenology and Biomass in Mongolian Herbaceous Vegetation. *Journal of Arid Land Studies*, 14(4), 209-218. (in Japanese with English Abstract)

Harada, I. and Kondoh, A.(2005): Using Landsat TM/Band6 and temperature data of AMeDAS to study the changes observed in the expanding heat island of Tokyo Metropolis. *Journal of Geography*, 114(5), 705-723.(in Japanese with English Abstract)

Shiraki,Y., Higuchi A., and Kondoh, A.(2009): The effect of an urban environment on the precipitation in areas around Tokyo. *Environmental Sciences,* 22(3), 187-195. (in Japanese with English Abstract)

Study on The Bortala River Watershed Hydrological Process Effects on The Climate Warming

DILINUER AJI[1,2], HAILONG JING [1,2] , AKHIKO KONDOH [3], AIKEBAER[4]

[1]School of Geographic Science and Tourism, Xinjiang Normal University, China

[2]Xinjiang Laboratory of Lake Environment and Resources in Arid Zone, China

[3]Center for Environmental Remote Sensing, Chiba University, Japan

[4]Bohe Basin Management Department of Bozhou, China

Email: dilnura@xjnu.edu.cn

Abstract

Bortala River, originated from the Alatao Mountain in Xinjiang China, is supplied mainly by the melting snow. The annual melting snow is about 45% of the total annual run-off. The annual monthly maximum run-off usually occurs in June, run-off in April to June consists 60% of the total in snow-melt seasons. Temperature of the river basin has started to heat up since late 80s in last century, and the annual mean temperature raised from 5.5 that is in 60s to 7.9 in 2000s, annual precipitation has been in the tendency of rising too, especially got its peak in springs. Along with the climatic warming, there has been an enormous change in the hydrological process of the river, it mainly includes that the monthly maximum run-off in June has shifted to May, the total monthly run-off has increased about 15%, and the percentage of monthly melting snow in April to June in total run-off has raised from 60% to 70%. In the change tendency of long standing, raising of the temperature mainly occurs in winter, increasing of the precipitation in winter is also distinct, the hydrological process is mainly obvious decreasing of the run-off in summer and obvious increasing of the run-off in spring. Analysis by the image data of the same time shows that the hydrological process caused by climatic warming has already effected the land use/cover changes around the lake Ebnur that situated in the lower reaches of the river.

Key words: Bortala River, Hydrological process, melting snow, run-off, climate warming

1. Introduction

Seasonal snow cover is the major water source at many high mountain areas. There are over 1 billion populations globally who depend on these snow water as their water resource supply. It is used in family, agriculture and industry, including power generation in some cases. Over 80% water resources in Xinjiang are formed at the mid and high mountain areas

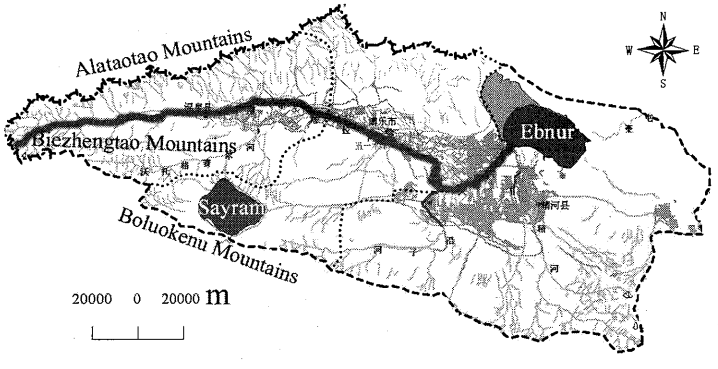

Fig.1 Location map of the study area

around basins. Glaciers, snow cover and melt water at high mountain areas are the major recharge sources of rivers. With temperature rise caused by global change at cold areas of high mountains, the change of precipitation is sensitive here.

In this research, recent changes of hydrological processes in Bortala River were specially discussed. Multi-temporal satellite dates and meteorological observations of Bortala River basin were used for evaluating the climatic changes of Bortala River basin. Finally, the relationship between the change of hydrological processes in Bortala River and the climatic change in the area were discussed by using the Mann-Kendall way.

2. Object area

Bortala River is located at Hongbielindaban, the junction of Alatao Mountain and Biezhentao Mountain. The area of drainage basin is 11367km^2, and the total length of the river is 252km. It passes through Wenquan County from west to east, and flows into Ebnur Lake via Bole(Fig1). The source of the ditch passes up to Kazakhstan. We take the river basin above Wenquan County as the upstream of Bortala River basin, that is, the drainage basin above Wenquan Meteorological Station. With the length of about 100km, Wenquan Meteorological Station at the upstream of Bortala River is located at 44°59′N and 81°04′E within Wenquan County. With the altitude of 1133m, Wenquan Hydrologic Station enjoys the annual average precipitation 199.7mm from 1971 to 1980. Among them, 39% in spring, 36.3% in summer, 17.9% in autumn, 6.8% in winter. Bortala River is fed with snowmelt, rainfall and underground water.

3.Used data and Methodology

In this study, multi-spectral image data, multi-temporal meteorological and hydrological observations of Bortala River basin for about past 50 years, are used as an input data for evaluating the change of hydrological processes in Bortala River and the climatic change of Bortala River basin. For analyzing the climatic change for study area We extracted the precipitation and temperature data of the study area during the period 1959~2008 from the meteorological and hydrological station which located in Bortala River basin.

A subset of each of the Landsat MSS digital images(1972, 1977), Landsat TM digital image(1990), and Landsat ETM+ digital image(2003), were used for evaluating water area change detection of Ebnur lake region. Only the TM and ETM+ images were used for another three lake regions. The digital images were geometrically calibrated to each other to facilitate their comparison for Ebnur lake region. The 1990 Landsat TM image, which was supplied by Earth Satellite Corporation, had already been rectified and georeferenced to UTM map projection (Zone 44), and WGS1984 ellipsoid. Then, this image was therefore employed as a reference scene to which the 1972 Landsat MSS scene, the 1977 Landsat MSS scene, and the 2003 Landsat ETM+ scene of Ebnur lake region were registered. Using image to image registration, the other 3 images (MSS of 1972, MSS of 1977, and ETM+ of 2003) were matched to the TM image with the total root mean square error (RMSE) of less than half-pixels. The nearest neighbor resampling method was used to avoid altering the original pixel values of the image data. Finally, the relationship between the change of hydrological processes in Bortala river and the

climatic change in the area were discussed.

4. Results and Discussions

4.1 Climate change

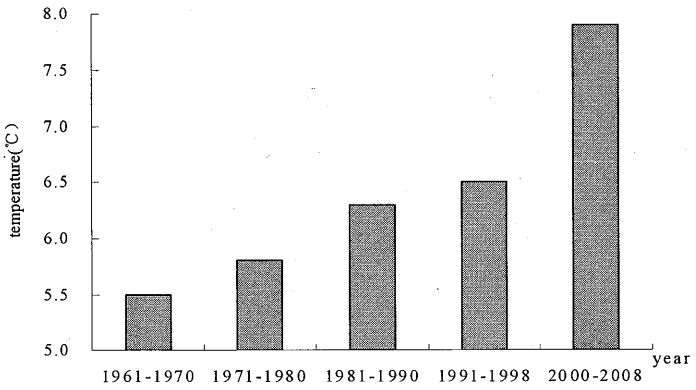

Fig.2 Average temperature distribution over 10years at Bortala Methodological Station in 1961~2008.

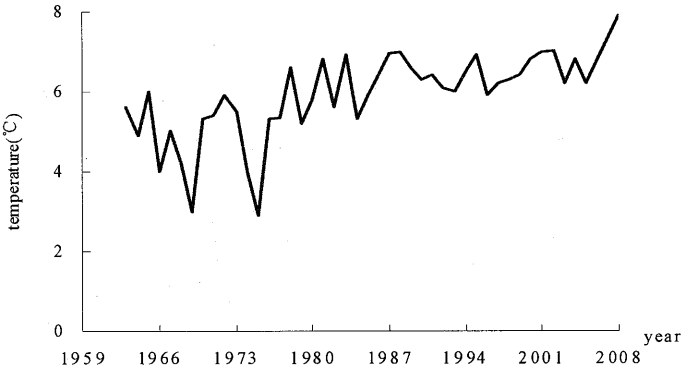

Fig.3 Yearly temperature at Bortala Methodological Stationof Bortala River basin from 1959~2008.

4.1.1 Temperature rise due to climatic warming is obvious. The average temperature rises to 7.9□in the 2000s from 5.1 in the 1960s(Fig2,Fig3), Among them, temperature rise in winter reaches its peak(Fig4).

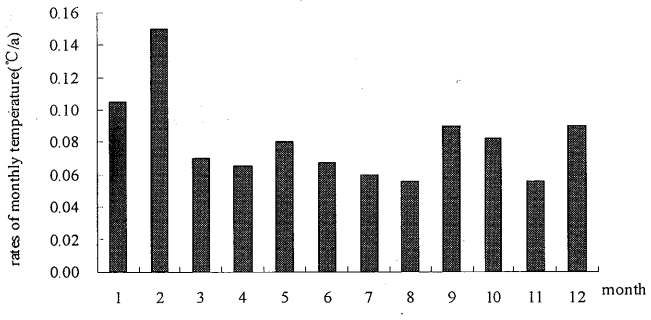

Fig.4 Increasing rates of monthly temperature change in Bortala River Basin during 1959~2008.

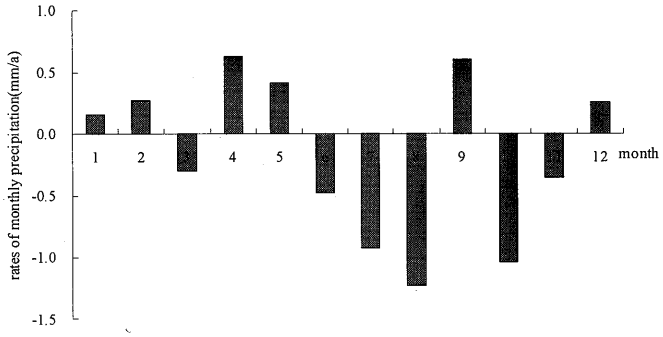

Fig.5 Increasing rates of monthly precipitation in Bortala River basin during 1959~2008.

4.1.2 Annual precipitation is on the rise. The increase of rainfall mainly occurs in winter and early spring; while precipitation is on the decline from June to August and from October to November. The greatest reduction occurs from June to August in most cases(Fig.5).

4.2 land use/cover change around Lake Ebnur

There are four scenes of MSS (1972,1977), TM (1990) and ETM+ (2003) images that include the Lake Ebnur region, and they were used for the post-classification change detection as shown in Fig6.Cultivated, and water, were the major land use/cover classes of interest in this study. Based on Fig6, cultivated area has a continuing increase, which increased from 54.2km² in 1972 to 127.3km² in 1977, to 267.2km²in 1990, and then to 734.4km² in 2003 for the studied area of Lake Ebnur region. The water class has also showed a significant change in this area. In 1972, there were 528.2km²of water area (or 12%), which declined to 524.8 km² (or 11.9%) by1977. On the contrary, the water area has increased in 1990 from 547.6 km² (or 12. 4%) to 1029.2 km² (or 23.4%) in 2003, which means, the water area changes of Lake Ebnur were governed by cultivated changes from 1972 to 1990. After 1990, water area has doubled without regard to even the growth of cultivated area.

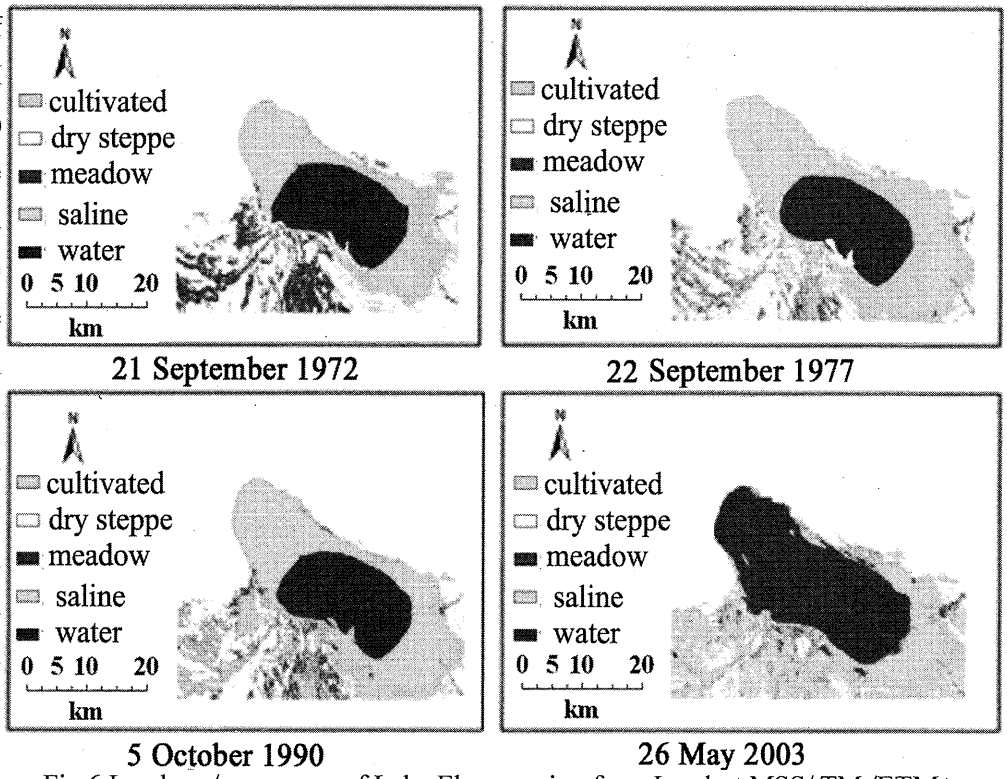

Fig.6 Land use/cover map of Lake Ebnur region from Landsat MSS/ TM /ETM+

4.3 Hydrological processes

With climatic warming, the change of hydrologic processes of rivers within the year is conspicuous. It is mainly reflected in the following: the maximum runoff is advanced from June to May, and the runoff within the year moves forward.

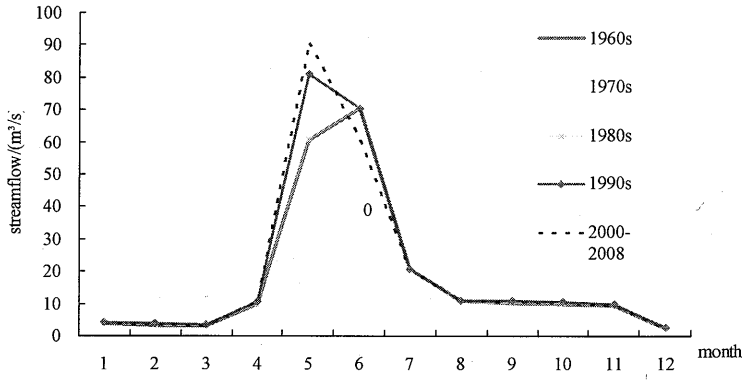

Reference

Dyurgerov M. Mountain and subpolar glaciers show an increase in sensitivity to climate warming and intensification of the water cycle [J]. Journal of Hydrology, 2003,282:164-1761.

Adaptation for global warming

Hiroyoshi Ishibasi
Center for Environmental Remote Sensing, Chiba University,
1-33 Yayoi-cho Inage-ku chiba-shi (Japan),
IshibashiH@faculty.chiba-u.jp

Abstract

Through this writing, the author intends to introduce the significance of the establishment of the endorsed chair for global warming at Center for Environmental Remote Sensing, Chiba University. Then, it focuses on general approach to environmental issues related to weather based on much experience that we have been engaging in production and diffusion of various weather services. Finally, it addresses the possibility that Transportation Weather contribute to reduce environmental load.

Keywords: global warming, weather service, transportation, modal shift, northern sea route

1. The establishment of the endorsed chair and its significance

Joint project between Weathernews Inc. and Center for Environmental Remote Sensing at Chiba University started several years ago. In an effort to enhance research and collaboration between industry and academia, we established the endorsed chair inside the center last fall. We hope this place for the industrial-academic research to be an interface that academic researches are taken advantage of for practical use which contributes to the society.

It has been a while since IPCC report pointed out the possibility that greenhouse gas emission caused by human activities can accelerate global warming. Along the way, effect to global warming has been monitored, and the phenomenon to be ascertained popped up and then studied.

At the same time, announcement of the effects by global warming, and giving research on possible countermeasure and adaptation are also important. Coincidentally, COP15 was held in Copenhagen in December 2009 to discuss scheme of post-Kyoto, which gives me a feeling that proposal of countermeasures / handling / adaptation for global warming and concrete actions to realize them are important and urgent to achieve the greenhouse gas reduction target. We hope more and more people to be concerned about environmental issues including global warming, to recognize it is near-at-hand matters, to deepen understanding on them, to research and verify countermeasures / handling / adaptation for such issues, to propose concrete countermeasures, and take actions to realize the proposal.

Setting up the main theme of the endorsed chair as "Research on handling and adaptation for global warming taking advantage of remote sensing and meteorological / hydrographical information," we give researches related to connection between transportation and weather in particular. More concretely, our ongoing researches are 1) development of the Northern Sea Route through the Arctic Ocean, 2) observation on snow ice on road surface by micro wave in Transportation Weather field, and 3) investigation of effects caused by global warming with remote sensing and numerical model.

Transportation operated outside (Sea, Sky, Road, etc...) is strongly affected by weather on a daily basis, therefore many Transportation Weather services have been provided to reduce such influence for achieving business goals.

Weather service has its history that it has been developing together with transportation (shipping industry and aviation industry). The CO2 emission from transportation activities which has strong connection with weather accounts for 20% of the entire CO2 emission of Japan [1]. This figure shows that it would be great contribution to achieve the greenhouse gas reduction target if the challenge to reduce CO2 emission in the field, therefore we believe proposal of a new service in Transportation Weather field which aspires for contribution to the environment results in global warming prevention.

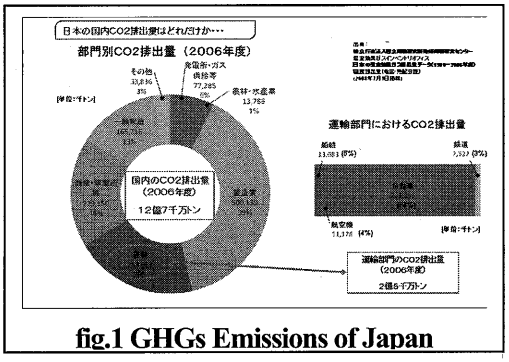

fig.1 GHGs Emissions of Japan

Take the T (Taboo) in the letter G from CHAN"G"E, and

you get CHANCE, meaning that you need to approach the issue without having any "taboo" in mind when you tackle a whole new challenge or value-creation. I strongly believe CHANGE become CHANCE only when there is no "Taboo" in your mind.

Unfavorably, in terms of the discussions regarding the amount of CO2 emission in logistics field, each company insists on legitimacy of one's way of logistics. It follows that there is "taboo" that they don't go into adopting other ways of logistics. The important challenge with collaboration between industry and academia surely needs an idea which is not limited to such vicious trend and taboo. I want to achieve carrying through "Transportation Weather" by industrial academic collaboration.

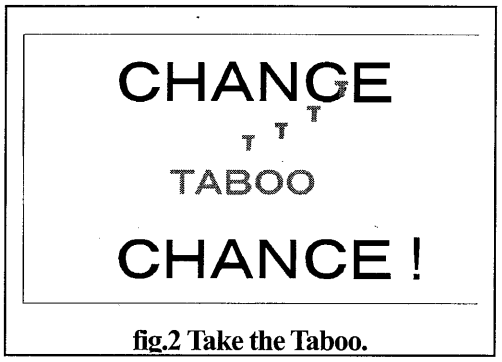

fig.2 Take the Taboo.

2. An approach to the environment issue from the meteorological point of view

Recent increasing recognition and literacy of weather information service have boosted up public nature of weather information, and now its stage has reached to such high level that Weather is advocated to be the fifth public utilities asset following Water, Energy, Transportation and Communication (WETComW). Due to this high level enhancement on public utilities asset, public recognition of weather information is moving from a stage that it is granted to a stage that it is thought to be self-fulfilling management, "weather around you can be predicted by yourself." Meanwhile, weather itself may not be controlled by human being. It is extremely difficult, could be said impossible, to control weather from both technological and economical perspective, like making rain happen or diffusing storms. On the other hand, most environmental issues such as global warming are thought to be stemmed from accumulation of long-term human activities. Therefore, I believe It may be no exaggeration to say "we can control, or at least change, the environment." However, this issue could not be solved by one's understanding or effort. Every single challenge surely needs cooperation by lots of people. One's power is so small that seems it can change nothing. However, its effect can be enormous by cooperating with many people. Given the above, challenges to environmental issues are surely the themes which require public asset management with the mind of helping others succeed.

By the way, I believe that countermeasure and adaptation to global warming should not be discussed in the context of "Saving" but in the context of "Best yield." Economic activities should not be hindered by the notion of "Saving" which brings shrink way of thinking. What is important to this approach is to pursue "Best yield" by eliminating waste, and unevenness, and doing something impossible. To achieve stable economic growth, the countermeasure and adaptation should be balanced, which enables more effective economic growth, while trying to reduce environmental load in the context of "Best yield."

Most industry and economic activities are more or less affected by weather condition in some way such as delay or halt of its works, which degrade best yield. Therefore, many weather services have been provided to reduce such influence for achieving their business goals. By taking advantage of weather service, you can reduce negative effect caused by weather condition, and therefore be able to achieve your business goals more effectively, which definitely leads to "Best yield."

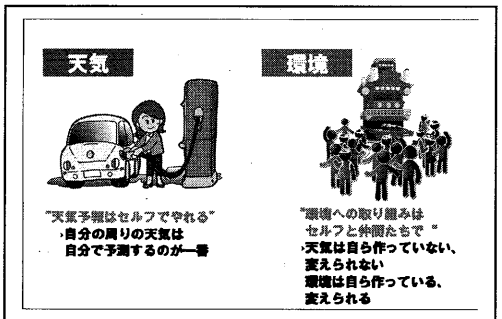

fig.3 Weather and environment.

3. Transportation weather and environmental load

3.1. CO2 Emission load in the Transportation Industry

Total CO2 emission of Japan amounts to 1,270,000,000 ton (in 2006), and 20% of them are emitted from Transportation industry, which is 250,000,000 ton, following Manufacturing industry which accounts for 39% of the total CO2 emission. Looking into the details of Transportation industry, automobiles annually emit 220,000,000 ton (88%), then ships 13,000,000 ton (5%), airplanes 11,000,000 ton (4%), and trains 8,000,000 ton (3%) [1].

Given the statistics above, implementing CO2 emission reduction to Transportation industry, particularly to automobiles, can make great contributions to reduce total CO2 emission of Japan. Therefore, proposal of environment-oriented new service centered at Transportation industry will contribute to counter global warming.

3.2. Modal Shift approach to the domestic commercial logistics among the Truck, coastal ferry ship, train and air transportation (The holistic optimization by Monitoring System)

Expanding our vision form Transportation to logistics, Modal Shift is catching attention as a means to reduce CO2 emission. Modal Shift is alternation of transportation mode, historically from transportation by truck to train or ship which enable mass transportation therefore have less environmental load. After it is presented as a means to energy saving after oil crisis of the 1970's, several effects have been expected on Transportation issues (ease congestions / reduce traffic accidents) and on the environment (reduce gas emission including CO2).

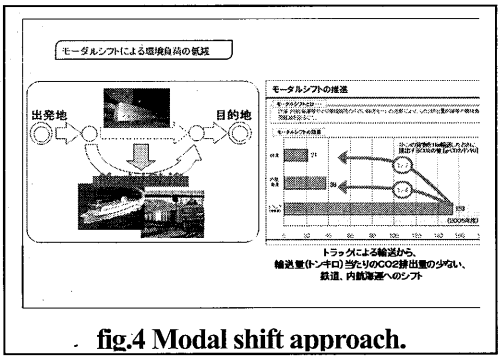

fig.4 Modal shift approach.

Some statistics on energy effectiveness and environmental load of each transportation mode show that trains and ships are superior transportation mode than trucks in terms of environmental load because they need less energy and emit less CO2, which reasons Modal Shift. There was a case that Modal Shift to ferry ships between Kanto Area and Kyushu Area succeed in reduction of 60% CO2 emission. ("Proving experiment to aim at establishment of best transportation mode to the environment", Oceantrans Ltd./Ocean Tokyu Ferry [2]).

According to the statistics on transportation energy directory by Ministry of Land, Infrastructure, Transport and Tourism in 2006 [3], energy consumption of Truck is 2,257KJ/ton-km while Trains and Ships are 528KJ/ton-km and 494 KJ/ton-km, respectively, which means that Trains and Ships need amazingly less energy consumption that Truck, and therefore are more effective transportation mode.

At the same time, CO2 emission of Truck is 0,15kg-CO2/ton-km while domestic shipping and trains are 0,04 kg-CO2/ton-km and 0,02 kg-CO2/ton-km respectively according to some material disclosed by Ministry of the Environment [4]. That means Trains and Ships are also better than Trucks in terms of environmental load.

Modal Shift rate, however, was 55% in 1975, which gradually going down to 35% by 1980, then 40% currently. This stagnation of Modal Shift rate has so many reasons such as traits of each transportation mode, infrastructure, distribution system, industrial structure and so on. Among them, one of the biggest reason is the rapid increase of transportation amount by Truck, which has become four to five times as it was in 1975, going through last thirty years because of enhancement of expressway network and convenience of high frequency retail transportation and delivery service to house. During the thirty years, transportation amount by Train and Ship become just twice.

When it comes to Modal Shift to domestic shipping, main problems are slower transporting and uncertain arrival time. In terms of uncertain arrival time, it is considerably affected by weather and hydrographic conditions. Therefore, heavy weather should be taken into account for operation control. For example, in response to expected weather or hydrographic conditions, you can change speed and route of ships in order to minimize the gap between estimated arrival time and actual arrival time. Additionally, service related to weather and hydrographic information can support coordination between sea and land transportation. Of course, they should be provided in a balanced manner in light both of less environmental load and of certainty of cargo arrival.

To strongly drive Modal Shift, the cargo owners should have the notion of "strategic commercial logistics" by their initiative. Looking back, the suggestions of Modal Shift are from Trains or Shipping industry insisting that they aim at energy saving or gas emission reduction. However, it feels that they end up with fighting for transportation mode alternation for one's favor, without having a view of environmental well-being. To realize the concept of Modal Shift into firm business model, the cargo owners should not be limited to fixed transportation mode. It would rather be expected more flexible and dynamic transportation mode that they choose the best transportation mode in each case by taking into situations (sea, road, airway) consideration while coordinating with several transportation modes, having the viewpoints of achieving business goals and environmental load. That is "strategic commercial logistics." Under the

concept of holistic optimization, the cargo owners, each transportation mode and all relevant people should try to reduce environmental load while dealing with dynamic and transient business environment in order to achieve business goals more efficiently. We need a base for sharing necessary information and for supporting dynamic information sharing, which we call "ECO operations," so that such flexible and quick transportation scheme.

If we look at Modal Shift from the viewpoint of weather-related service, Transportation Weather has almost surpassed the stage to support each transportation mode, and is reaching the stage to realize total optimized logistics by coordinating every possible transportation mode. Not to say decision-making support on transportation mode choice, a lot more service will be needed such as evaluation report on fuel saving or gas emission reduction. I am pretty confident that Logistics Weather service will be established based on Transportation Weather service in the near future.

I can not stop expecting that a new environment-oriented service and therefore a new transportation scheme will be born from many discussions among the cargo owners and relevant people.

3.3. The Northern Sea Route (The new route discovery with the new vehicle)

As a result of recent sharp retreat of sea ice in the Arctic Ocean in summer, feasibility of the Northern Sea Route through the Arctic Sea is getting higher. In response to this, we have established Global Ice Center to monitor sea ice in the Arctic Ocean as a first step to realize the Northern Sea Route.

Due to global warming, an amount of sea ice coverage in the Arctic Ocean records the minimum in 2007, summer. Notably, Canada-side route (Northeast route) and Russia-side route (Northwest route) have been open for the first time ever in the history in 2008. Also, IPCC estimates that there would be no ice in the Arctic Ocean in summer by the end of this century, thus meaning possibility of the Northern Sea Route is getting feasible. In shipping industry, development of the Northern Sea Route would be the second revolutionary incident behind containerization. If the route developed, it would drastically shorten the distance between Asia and Europe by 40%, the distance between Asia and the Atlantic side of North America by 30%. The optimization of sea routes would reduce CO2 emission, thus resulting in counter global warming.

Global Ice Center, which integrates all the information on sea ice in the Arctic Ocean generated by each country under one's jurisdiction, takes on a role to lay out the framework to let a ship safely pass through the Northern Sea Route anytime. We would like to support the voyages by "Ice Routeing," a service for Voyage Planning. More concretely, Global Ice Center collects and integrates information on sea ice in the Arctic Ocean and keeps track of current sea ice conditions, and then anticipation of future sea ice conditions by "I-SEE engine."

Additionally, we are planning to monitor sea ice in the Arctic Ocean from the outer space by a compact satellite whose launch is scheduled for 2010. Beginning from Global Ice Center and the mission specific micro satellite, we are going to challenge the development of the whole new sea route.

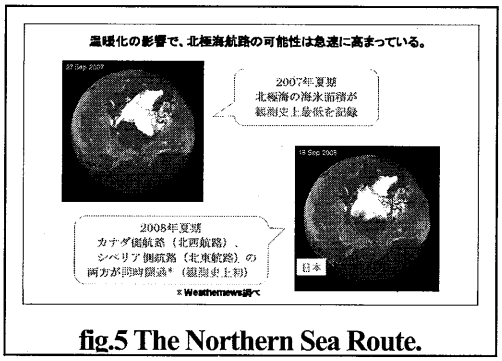

fig.5 The Northern Sea Route.

References

1) "The GHGs Emissions Data of Japan (1990-2006)", Greenhouse Gas Inventory Office of Japan, National Institute for Environmental Studies. (http://www-gio.nies.go.jp/aboutghg/nir/nir-j.htm)
2) The corporate site of Ocean Tokyu Ferry, Ocean Tokyu Ferry Co. Ltd. (http://www.otf.jp/environment/)
3) "The Survey on Transport Energy 2007", Ministry of Land, Infrastructure, Transport and Tourism. (http://www.mlit.go.jp/toukeijouhou/energy/h19_energy.pdf)
4) "Greenhouse Gas Emissions in FY 2006", Ministry of the Environment. (http://www.env.go.jp/earth/ondanka/ghg/2006yoin.ppt)

Estimation of sugar beet yield based on soil type through analysis of satellite data

Chiharu Hongo[1] and Katsuhisa Niwa[2]

[1] *Center for Environmental Remote Sensing, Chiba University, hongo@faculty.chiba-u.jp*

[2] *Zukosha co Ltd., niwa@zukosha.co.jp*

Abstract

In order to assess the feasibility of developing an efficient sugar beet cultivation support system to effectively reduce the costs of beet cultivation, beet collection and sugar production using an agricultural spatial information, and also to predict the root yield of sugar beet three months before the harvesting season, an analysis of satellite data and meteorological data was carried out in this study.

For predicting the root yield of sugar beet, the analysis of the growth was conducted around the town of Memuro, Hokkaido, Japan. The cumulative temperature (T), cumulative rainfall (P) and cumulative solar radiation (R) from the end of April to the middle of July were selected as the predictors of the root yield (RY) prediction formula.

$$RY=0.043675R+0.02783T-1.09513P-39.634(r^2=0.87^{**})$$

The predictive error was 3.8t/ha, that was the result calculated by the farmers group, after weighted to the predicted root yield using NDVI which was derived from SPOT5 satellite data. The results suggest that it was possible to predict the root yield before three months of harvesting season. By providing such result to sugar companies in much earlier before harvesting, the sugar beet collection and sugar production efficiency will be increased.

Keywords **:** root yield prediction, precision agriculture, cost reduction

1. Introduction

The production of beet sugar in Hokkaido is about 640,000 tons, which is 3/4 of the total national production (Ministry of Agriculture, Forestry and Fisheries, Japan 2006). The Japanese government is implementing a "New policy on sugar beet crops and other sweet resources" policy, through which it aims to reduce the cost of the production and manufacturing processes.

In order to assess the feasibility of developing an efficient sugar beet cultivation support system to effectively reduce the costs of beet cultivation, beet collection and sugar production using an agricultural spatial information, and also to predict the root yield of sugar beet three months before the harvesting season, an analysis of satellite data and meteorological data was carried out in this study.

2. Methods

2.1 Study site

This study was conducted around the town of Memuro located in the middle west of the Tokachi plain, Hokkaido, Japan (longitude 143.1°E, latitude 42.9°N) (Fig. 1). The area of the test site in this study is 22.6km from east to west and 35.4km from north to south, in which large-scale agricultural management is performed. The acreage of sugar beet cultivation is 3,505ha in Memuro, and the average cultivation area of sugar beet per farmer is 6.9ha(Ministry of Agriculture, Forestry and Fisheries, Japan 2007). The test site can be divided into three geographical types: lowland, low, middle and high terraces (Koji Kikuchi 1981).

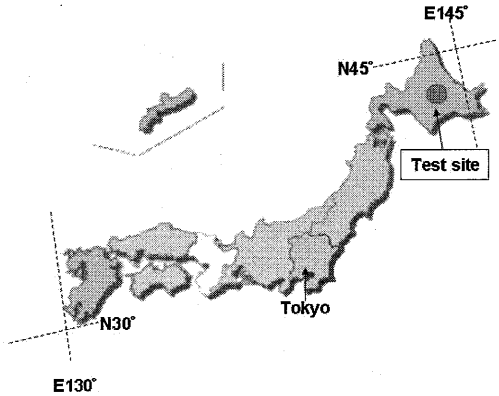

Fig1. Study site

2.2 Ground truth data

Sugar beet field observation data was prepared to analyze the relationship between beet tops and root yield. To measure the plant height, leaf color (SPAD: Soil & Plant Analyzer Development), root yield and sugar concentration, investigation points were set in 56 different locations each with an area of 3 rows×7 plants (Fig 2). The field survey was performed from June to October in 2006 and 2007. In addition to these data, the annual average root yield in Memuro from 1990 to 2007 were prepared, which was compiled by Hokkaido Government Tokachi Subprefectural Office.

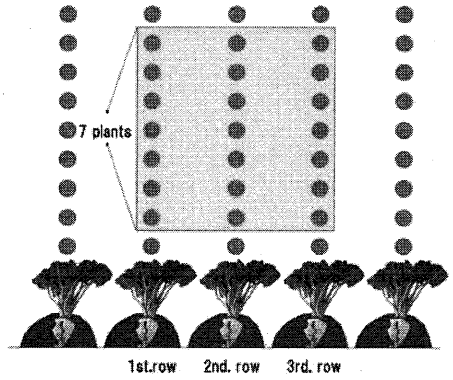

Fig .2 Outline of a ground observation point

2.3 Meteorological data

Data on cumulative temperature, cumulative rainfall and cumulative solar radiation from the end of April to the middle of July was collected from Obihiro meteorological observatory and Memuro observation site.

2.4 Satellite data and GIS data

SPOT data was acquired on July 27, 2006 and July 27, 2007. GIS data of 2006 and 2007 was used to identify sugar beet fields from the satellite data.

2.5 Procedure

The procedure for predicting the root yield is described in Figure 3.

To derive the root yield prediction equation, multiple linear regression analysis was executed using the data on cumulative temperature, cumulative rainfall and cumulative solar radiation from the end of April to the middle of July from 1990 to 2005. The average root yields of Memuro town in 2006 and 2007 were predicted using the yield prediction equation.

Secondly, the digital values of sugar beet fields derived from the satellite data were converted to surface radiance values, and the majority value of the NDVI was calculated from the radiance values of all sugar beet fields in Memuro.

The predicted yield obtained from the meteorological data and the majority value of NDVI are presumed to be equal, and the NDVI values of whole sugar beet fields were transformed into absolute root yield value after calculating the predicted yield value in proportion to the NDVI value.

Finally, to validate the root yield prediction results of 2006 and 2007, the predicted root yields of the farmers' groups were compared with the observed root yields by calculating RMSE.

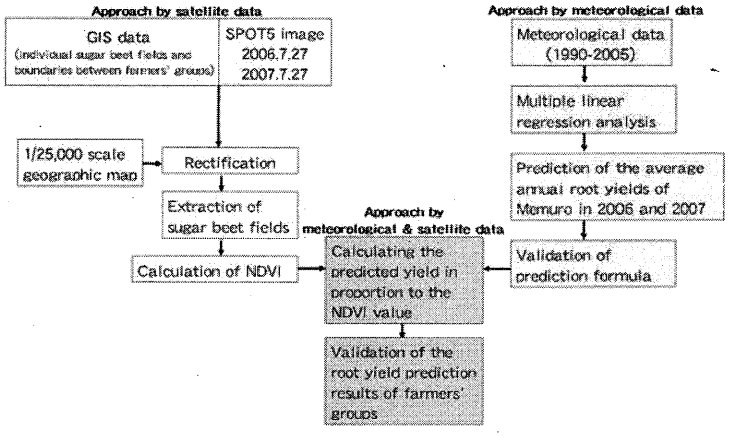

Fig. 3 Procedure of image analysis

3. Results and discussion

The relationship between SPAD×plant height and the root yield was investigated. There is positive correlation between [SPAD×plant height] on July 12 and the root yield on October 4, 2007. The coefficient of determination is 0.64.

The result shows that sugar beet with a larger amount of leaf and stem in July has a higher root yield in the harvesting season, and it is also suggested that the root yield in the harvesting season is determined by the growth status of beet tops in July. Moreover, there is positive correlation between [SPAD×plant height] and NDVI on July 27, 2007 (r^2=0.6). Through these results, it may be possible to estimate the root yield of sugar beet about three months before the harvesting season.

For predicting the root yield of sugar beet, the analysis of the growth was conducted around the town of Memuro, Hokkaido, Japan. The cumulative temperature (T), cumulative rainfall (P) and cumulative solar radiation (R) from the end of April to the middle of July were selected as the predictors of the root yield (RY) prediction formula. The root prediction formula derived from these predictors is as follows:

RY=0.043675R+0.02783T-1.09513P-39.634(r2=0.87**)

The coefficient of determination of the prediction formula is 0.87, which is significant at the 1% level. RMSE is 3.2t/ha, which is calculated from the predicted root yield and observed root yield.

In our previous research, we reported that there was a positive correlation between the root yield at the harvesting season and the amount of beet top in July and that was possible to estimate the root yield by analyzing the SPOT5 satellite data acquired in July(Chiharu Hongo et al. 2006a), 2006b), 2008,).

However, the absolute root yield value cannot be obtained before the harvesting season even if the satellite data in July is applied to this prediction approach because it is necessary to know the ground observation root yield data of October, which is input into the prediction formula to derive the absolute root yield value. Thus, we focused on the relationships between the beet top biomass and NDVI in July and root yield in October, and the absolute root yield value was derived using the following prediction procedure.

The root yield predicted using the formula is replaced by the majority NDVI value of the beet fields cultivated in the study site. The predicted average root yield is converted to the root yield of individual sugar beet fields in proportion to the NDVI value. Finally, the average root yield of each farmers' groups was calculated from the yields of individual sugar beet fields.

The scatter graph in Figure 4 shows the relationship between the prediction root yield and the observed root yield in 2007. The ground observed root yield data was collected from the observation points on farmers' fields, each of which consisted of three rows of 7 plants. The RMSE of the predicted value relative to the observed root yield was 4.8t/ha, corresponding to an error of about 6.8% against the observed value of 70.54t/ha. However, the RMS error of the predicted value was 3.8t/ha after eliminating the fields with the brown lowland soils.

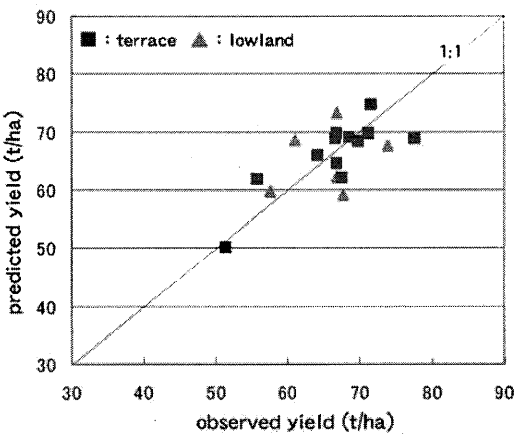

Fig.4 Relationship between predicted yield and observed yield of the field observation points (2007)

4. Conclusion

To assess the feasibility of developing an efficient sugar beet cultivation support system to effectively reduce the costs of beet cultivation, beet collection and sugar production using agricultural spatial information, and also to predict the root yield of sugar beet three months before harvesting season, analysis of satellite data and meteorological data was carried out in this study.

The results show that it is possible to predict the root yield with high accuracy using the meteorological data and satellite data. In this study, we have constructed a new

yield prediction method using the average root yield in region predicted from meteorological data replaced by the majority of NDVI value of the beet fields.

By providing such results to sugar companies much earlier before the harvesting, the efficiency of sugar beet collection and sugar production is expected to increase substantially, which will lead to economic and environmental benefits.

Acknowledgements

This study was funded by the Ministry of Agriculture, Forestry and Fisheries, Japan as part of Research on Advanced Technologies in Agriculture, Forestry and Fisheries (assignment number: 18083). The authors would like to express our deepest gratitude to Dr. Roji Samejima, Dr. Ryutaro Yamada, Dr. Masato Kuwahara, Dr. Jun Yokobri and Dr. Akira Nishimune whose comments and suggestions made enormous contribution to our research. We would also like to acknowledge the Agricultural Cooperative Association of Memuro, Nippon Beet Sugar Manufacturing Co.Ltd., and Hokkaido Sugar Beet Association for providing yield data and GIS data.

References

1) Chiharu Hongo, Takanori Suzuki, Yukinobu Hiramitsu, Takashi Miyamoto, 2006a),Development of an efficient sugar beet cultivation support system using the agricultural spatial information – Part1-Growth analysis of sugar beet using a satellite image and GIS ,Proceedings of the 41 th autumn conference of the remote sensing society of Japan, 41, 291-292

2) Chiharu Hongo, Katsuhisa Niwa, Ryutaro Yamada, Ryoji Samejima, Yashishi Hiramitsu,Masato Kuwahara, Takanori Suzuki, 2006b), Development of an efficient sugar beet cultivation support system using the agricultural spatial information –Part2-Estimation of root yield and growth analysis based on soil type, Proceedings of the 42 th spring conference of the remote sensing society of Japan, 42 , 155-156

3) Chiharu Hongo, Katsuhisa Niwa , Jun Yokobori , Ryutaro Yamada , Masato Kuwahara,2008, Development of an efficient sugar beet cultivation support system using the agricultural spatial information – Part3-Prediction of root yield using meteorological data and satellite data, Proceedings of the 45th autumn conference of the remote sensing society of Japan, 45, 115-116

4) Koji Kikuchi, 1981, Interpretative classification of soil in the Tokachi district, and their mapping and practical application for soil improvement, Report Hokkaido Prefect. Agric. Exp. Stn., 34, 1-118

5) Ministry of Agriculture, Forestry and Fisheries, Japan, 2006, The present state of and issue on the policy of sugar and sweetness-resource crops.
URL:http://www.maff.go.jp/www/counsil/counsil_cont/kanbou/kanmi/h17-1/siryou3.pdf

6) Ministry of Agriculture, Forestry and Fisheries, Japan, 2007, The Statistical Year Book (2005-2006) of MAFF, Hokkaido, Norin Tokei Kyokai, Sapporo

Estimation of Radiation budget using Geostationary Satellites

- Formation of a virtual laboratory for diagnosing the Earth's climate system -

Hideaki Takenaka, Munehisa K. Yamamoto, Masamitsu Hayasaki, Atsushi Higuchi, Fumihiko Nishio, Hiroaki Kuze, and Tamio Takamura (1)

[1]*Center for Environmental Remote Sensing (CEReS), Chiba University, Japan*

Arata Okuyama, Yuki Kosaka, Ryuichiro Nakayama, Hiromi Owada, Kenji Date, and Tomoaki Ono (2)

[2]*Meteorological Satellite Center, Japan Meteorological Agency (MSC/JMA)*

Abstract

In this study, we develop a vicarious calibration technique and estimation algorithm of radiation budget for the global analysis. The vicarious calibration technique using three components (clear sky sea surface, clear sky land surface, uniform cloud top) is applied to the geostationary satellites. This vicarious calibration technique is based on radiative transfer calculations and it has each optical properties (aerosol, cloud, surface BRDF/albedo) in three components. The quality of three geostationary satellites (GMS-5, GOES-10, GOES-8) visible channel fixed accurately for global analysis. An accurate calibrated data set propose the better accuracy for analysis of cloud and radiation budget. Thus, cloud and radiation budget analysis algorithm are applied to new calibrated data set for global analysis. This is first result of trial for global analysis.

Keywords :Radiation budget, Vicarious calibration, Geostationary satellite.

1. Introduction

Clouds have a strong influence on the solar energy budget and on the Earth climate as discussed in several studies [Manabe 1967, Schneider 1972]. Clouds can cool the Earth by reflecting solar radiation and also can keep the Earth warm by absorbing and emitting terrestrial radiation. They are important in the energy balance at the Earth surface and the Top of the Atmosphere (TOA) and are connected complexly into the Earth system as well as other feedback processes. Szilder and Lozowski [Szilder and Lozowski 1995] and Szilder et al. [Szilder et al. 1998] discussed cloud feedback processes using zero-dimensional time-dependent climate models including three climate feedbacks. They showed that a drastic environmental change was caused by the change of cloud water amount. However, their model has an uncertainty in the optical characteristics of clouds. Wetherald and Manabe [Wetherald and Manabe 1988] discuss the cloud feedback process using a General Circulation Model (GCM). Tsushima and Manabe [Tsushima and Manabe 2001] tested cloud feedback sensitivity to global mean surface temperature based on explicit definition of cloud feedback processes. They estimated the difference of the global mean surface temperature between the model and the observation. GCMs have strong cloud feedback sensitivity to global mean surface temperature. Based on observations, the global mean surface temperature showed that it was unrelated to the cloud feedback process. Therefore it is necessary to estimate the influence of the clouds on radiation budget from observations accurately. Accurate estimates of the large scale radiation budget is an urgent need for improved model parameterization and for a better understanding of the Earth system.

Geostationary satellite observations are useful for estimating the upward and downward solar radiation at the surface and the TOA over wide regions and at high temporal resolution. One of the key factors in the estimation is a sensor calibration. Geostationary satellites have some issues in the calibration procedures. In this study, we developed a vicarious calibration technique for global analysis. vicarious calibration technique using three components is applied to three geostationary satellites (GMS-5, GOES-10, GOES-8). It is based on radiative transfer

calculations and it has each optical properties (aerosol, cloud, surface BRDF/albedo) in three components. The optical characteristics of atmospheric particles were supplied in the analysis by Terra/MODIS data for aerosol and cloud using Retrieval of Aerosol optical Properties (REAP) [Higurashi and Nakajima 1999, 2002] and Comprehensive Analysis Program for Cloud Optical Measurement (CAPCOM) algorithm [Nakajima and Nakajima 1995, Kawamoto et al. 2001], respectively, and by objective analysis data Japanese Re-Analysis 25 years (JRA-25) for temperature, pressure, water vapor and data set of EarthProbe/Total Ozone Mapping Spectrometer (EarthProbe/TOMS). The albedo in the sea surface was decided from the wind velocity of sea surface, and land surface albedo is used a MODIS standard product of Bidirectional Reflectance Distribution Function (BRDF) 16 day mean product fixed by each spectral response function.

In addition, radiation budget analysis is applied to new calibrated data set (September 2002). We apply the Extreme speed and Approximation module Multiple drive System (EXAM SYSTEM) that construct by Neural network solver. The solver for solar radiation budget built by the NN is based on radiative transfer calculation using radiative transfer code. NN traces the radiative transfer code that is approximated by learning algorithm. This manuscript shows the first result of trial for global analysis.

2. Vicarious calibration

Vicarious calibration is one of the effective calibration method for satellite sensor. It correct the degradation of sensor sensitivity using Top Of Atmosphere (TOA) radiance based on some atmospheric and surface components. As a radiative transfer code, Remote sensing System for Transfer of Atmospheric Radiation (RSTAR) is used [Nakajima 1986, Nakajima 1988] in this study. It simulate the GMS-5/VISSR radiance using three components (Ocean, Land surface, and Cloud targets). There are selected by a strict quality control for conciliation of radiance between observed and radiative transfer calculation.

The vicarious calibration is adjust of TOA radiance for satellite sensor, it is conciliation of observed radiance and radiative transfer calculation output. Generally, pre-launch calibration is done by the integrating sphere measurement or filtered clear sky solar irradiance. The long-term degradation or the sensitivity error of just after launching is corrected by radiative transfer calculation on orbit. The concept of vicarious calibration using TOA radiances is as follows:

$$L_{TOA}^{(correct)} = L_{TOA}^{(pre-launch)} \times a + b$$

where, $L_{TOA}^{(pre-launch)}$ and $L_{TOA}^{(correct)}$ are TOA radiance based on pre-launch calibration and corrected one. a and b are calibration coefficients decided by TOA radiance adjustment. TOA radiance with simplification are as follows :

$$\begin{aligned} L_{TOA}(\lambda;\theta,\phi;\theta_0,\phi_0) &= L_{ray}(\lambda;\theta,\phi;\theta_0,\phi_0) \\ &+ L_{par}(\lambda;\theta,\phi;\theta_0,\phi_0) + L_{ray|par}(\lambda;\theta,\phi;\theta_0,\phi_0) \\ &+ t(\lambda;\theta) \times L_{suf}(\lambda;\theta,\phi;\theta_0,\phi_0) + L_{suf|atm}(\lambda;\theta,\phi;\theta_0,\phi_0) \end{aligned} \quad (1)$$

where, λ is a wavelength. θ and ϕ are satellite zenith angle and satellite azimuthal angle, θ_0 and ϕ_0 are solar zenith angle and solar azimuthul angle respectively. L_{ray} is a rayleigh scattering by air molecules and L_{par} is scattering by aerosol particles. $L_{ray|par}$ is the interaction between air molecules and aerosol particles scattering. Each elements are including multiple scattering. t is an atmospheric transmittance of assumed plane parallel atmosphere and L_{suf} is a radiance reflected by surface (land and ocean surface), it contains the consideration of Bidirectional Reflectance Distribution Function (BRDF). $L_{suf|atm}$ is a interaction between surface reflection and atmosphere. The simulated sensor radiance is converted by each wavelength radiance as follwos:

$$L_{TOA} = \frac{\int w(\lambda) L_{TOA}(\lambda) d\lambda}{\int w(\lambda) d\lambda}$$

$w(\lambda)$ is a weighting function of sensor response. Generally, it is a discrete value that obtain from measurement using integrating sphere. Therefore, L_{TOA} is can be simulated by radiative transfer code with atmosphere and surface condition in vicarious calibration. It needs each paremeters: the atmospheric pressure and the absorption gasses profiles for L_{ray}, the particle optical characteristics for L_{par}, the sea surface wind speed or the land surface BRDF parameters for L_{suf} respectively. Each interactions and atmospheric transmittance are decided by total. All parameters must be independent from target satellite data for the calibration.

2.2 Target selection

The surface and atmospheric parameters are required for vicarious calibration. It must be based on condition to minimize the error of radiance between calculation and observation. For example, cloud and white cap contamination is a big uncertain element for match-up of clear-sky radiance over ocean. Thus it must add the filters for quality control. Three components are used for vicarious calibration in this study; dark target is clear-sky ocean surface, bright target is liquid cloud top, and middle bright target is land surface, respectively. Each sumples are selected on the condition. The satellite veiwing angle θ and the solar zenith angle θ_0 are first select condition that inhibit three-dimensional effect by inhomogeneity. Deep angle causes illumination and shadow by the three-dimensional structure. Basically, the samples that are larger than 60 degree are rejected. This is a common condition in all components.

Clear-sky ocean surface

Ocean surface is used as dark target that consists atmospheric profiles, aerosol optical characteristics, and sea surface albedo. Cloud contamination is rejected by historical reflectance and split window method [Inoue 1987]. Equation 1 is updated as follows:

$$L_{TOA}(\lambda;\theta,\phi;\theta_0,\phi_0)=L_{ray}(\lambda;\theta,\phi;\theta_0,\phi_0)$$
$$+L_{aer}(\lambda;\theta,\phi;\theta_0,\phi_0)+L_{ray|aer}(\lambda;\theta,\phi;\theta_0,\phi_0)$$
$$+t(\lambda;\theta)\times L_{sea}(\lambda;\theta,\phi;\theta_0,\phi_0)+L_{sea|atm}(\lambda;\theta,\phi;\theta_0,\phi_0)$$

where, L_{aer} and $L_{ray|aer}$ are scattering by aerosol in clear-sky ocean surface and interanction between rayliegh and aerosol scattering respectively. The aerosol optical characteristics (refractive index, size distribution) is largest uncertainty in the radiance of ocean surface. It changes L_{aer} by absorption and scattering, and its properties depends on wavelength. Thus L_{aer} and L_{aer} variability is very large. In this study, aerosol optical characteristics is retrieved from MODIS L1B data set using Retrieval of Aerosol optical Properties (REAP) algorithm [Higurashi1999, Higurashi2002]. The sensor observed radiance is simulated using retrieved aerosol optical properties. In addition, the sample points only with very thin optical thickness of retrieved aerosol is used for calibration $(\tau_{aer} \ll 0.1)$. It inhibit the L_{aer} and L_{aer}, thus these are enough small. L_{sea} and $L_{sea|atm}$ are sea surface reflection and interaction between sea surface reflection and atmosphere. The sea surface albedo decided by sea surface wind velocity. It is used only under 10m/s samples that reject the white-cap contamination. Thus, the sea surface albedo is low and $L_{sea|atm}$ is enough small. L_{ray} and L_{sea} are predominant and other uncertainty is inhibited by these filters.

Uniform liquid water cloud top

Liquid cloud top is used as bright target that consists atmospheric profiles, cloud optical characteristics, and sea surface albedo. Uniform cloud top is searched using VIS and IR1 bands data spatial variance and select the liquid water cloud (Tbb > 273K) with sprit window method. It reject dense cirrus and ice crystal contamination. Equation 1 is updated as follows:

$$L_{TOA}(\lambda;\theta,\phi;\theta_0,\phi_0)=L_{ray}(\lambda;\theta,\phi;\theta_0,\phi_0)$$
$$+L_{cld}(\lambda;\theta,\phi;\theta_0,\phi_0)+L_{ray|cld}(\lambda;\theta,\phi;\theta_0,\phi_0)$$
$$+t(\lambda;\theta)\times L_{sea}(\lambda;\theta,\phi;\theta_0,\phi_0)+L_{sea|atm}(\lambda;\theta,\phi;\theta_0,\phi_0)$$

where, L_{cld} and $L_{ray|cld}$ are cloud scattering and interanction between cloud particle scattering and atmosphere respectively. Also the cloud optical properties (optical thickness, cloud droplet effective radius) is retrieved from MODIS L1B data set using Comprehensive Analysis Program for Cloud Optical Measurement (CAPCOM) algorithm in this study. Cloud with strong reflection is hardly has optical characteristics sensitivity. The crux in vicarious calibration is to simulate a sensor signal using optical properties based on the observation. It can follow the cloud change in long term climate. A change of the size distribution causes the change of cloud reflectance, similarly, absorption aerosol contamination decreases the cloud nominal reflectance. Long term cloud change in Earth climate system is unknown yet. The calculation of radiance not depends on the observation has the big risk, it does not follow the cloud change. Because the liquid water cloud is spherical, the optical parameter can be obtained from satellite observation. The samples with sensitivity in the optical characteristics are used in this study $(20<\tau_{cld}<40)$. Thus because cloud optical thickness is thick, L_{cld} is predominant. L_{sea} and $L_{sea|atm}$ are enough small. These filters inhibit the uncertainty.

Land surface with BRDF

Land surface is used as middle bright target that

consists atmospheric profiles, land surface aerosol, and surface BRDF/albedo. Cloud contamination is rejected by historical reflectance and split window method as well as the ocean surface. BRDF/albedo is used from MODIS 16 days product MOD43, it is predominant in clear-sky land surface. MOD43 is based on Ross ThickLiSparse-Reciprocal BRDF/albedo model that is consists three parameters f_{iso} , f_{vol} , f_{geo} : isotropic, volumetric, geometric. Black-sky albedo is used in this study. The wavelength dependency based on land-cover classification is important factor in surface albedo. Thus, BRDF/albedo is fixed by each spectral response function.

3. Estimation algorithm

Three geostationary satellites (GMS-5, GOES-10, GOES-8) were calibrated at September 2002. Cloud and radiation budget analysis is applied to new calibrated data set.

Cloud optical thickness

We used the Comprehensive Analysis Program for Cloud Optical Measurement (CAPCOM) [Nakajima and Nakajima 1995, Kawamoto et al. 2001] to retrieve cloud optical thickness. This algorithm was also adopted as one of the standard algorithms for the Advanced Earth Observing Satellite II/Global Imager (ADEOS-II/GLI) products [Nakajima et al. 1999]. The original CAPCOM estimated the cloud optical thickness, effective particle radius, and cloud-top temperature from visible, near-infrared, and thermal infrared channels using a LUT calculated from radiative transfer [Nakajima and Tanaka 1986, 1988] under a plane-parallel and single-layer cloud model. However, we applied CAPCOM to geostationary satellites data to retrieve only the cloud optical thickness using the VIS channel because water absorbing channel is does not exist. Briefly, cloud optical thickness is obtained as follows. First, each pixel is classified using the IR1 and IR2 split-window technique. Second, cloud optical thickness is retrieved from the VIS channel with corresponding atmospheric model profile data and scan geometries at the observation point, such as satellite and solar zenith angles and their azimuth angles. In the inversion process, multiple scattering components due to bright surfaces are corrected by the following:

$$L_{obs}(\tau;\mu,\mu_0,\phi)=L(\tau;\mu,\mu_0,\phi) + t(\tau;\mu)\frac{A_g}{1-\bar{r}A_g}t(\tau;\mu_0)\frac{\mu_0 F_0}{\pi}$$

where, τ is cloud optical thickness, μ and μ_0 are cos(satellite viewing angle) and cos(solar zenith angle), respectively, ϕ is the Sun-satellite azimuthal angle, $\bar{r}$ is spherical albedo in the channel, and Ag is surface albedo in the channel. F_0 is solar irradiance outside the atmosphere weighted by the sensor response function. The function of t is atmospheric transmittance. The first term on the right side of the formula is cloud scattering, and the second term is interaction at the ground surface. albedo was estimated from each geostationary satellite data by a simple statistical method with a clear-sky condition.

Estimation of radiation budget

We applied the Extreme Speed and Approximation Module Multiple Drive System (EXAM SYSTEM) that controls Neural Network solvers by multi-threading. EXAM SYSTEM can drive NN solvers at the same time according to the number of central processing unit (CPU) cores and the capacity. The main advantages of the NN approach are computation speed and the ability to consider multiple parameters, as large data sets are not required. Highly accurate radiative transfer codes can calculate solar radiation, including the effect of gasses and particles. However, researchers have had to deal with the trade-off between calculation speed and accuracy. In general, satellite-based estimation methods have used lookup tables (LUTs). Because pre-calculated values are used, the LUT method is effective when processing large amounts of data. However, if the effects of absorbing gasses and the optical characteristics of particles are incorporated precisely, the LUT volume becomes too large and slows computations. Including many values for numerous parameters not only increases the LUT volume but also requires complex interpolation / extrapolation procedures [Sauer 1995, Gasca 2000]. Calculation speed falls markedly when a complex interpolation / extrapolation procedure such as Lagrangian interpolation is needed. The NN approach is one solution to these problems, allowing for high-speed calculation and multi-parameter problems. The simple structure of a NN and that fact that it needs neither a large database nor complex interpolation / extrapolation techniques make NNs appropriate for

approximating radiative transfer code. High-speed calculation allows for more rapid analysis, and the ability to handle numerous parameters will allow more options for advanced analysis of atmospheric radiation.

4. Result

A part of the result is shown. Figure 1: Downward shortwave flux at the surface, Upward shortwave flux at the TOA. Three geostationary satellites (GMS-5, GOES-10, GOES-8) VIS channel is fixed accurately by vicarious calibration technique. Thus, gap is not found in each satellite. Estimated flux product is accurately connected. Each satellite flux products are only displayed (the overlap area is not averaged, it was simple paste at a midway point in each satellite). These products are available for validation of the GCM.

- Formation of a Virtual Laboratory for Diagnosing the Earth's Climate System -

In order to diagnose the earth's climate system under severe stress such as a global warming, the cooperative research centers (CCSR, HyARC, CAOS, and CEReS) construct "Virtual Laboratory", and research climate and environmental studies cooperatively with properties of each center. CEReS activities are Geostationary satellites global data archives and construction of Satellite information data base. Moreover, development of atmospheric radiation budget product. We aim at the contribution to a climate model and the better understanding of the climate system.

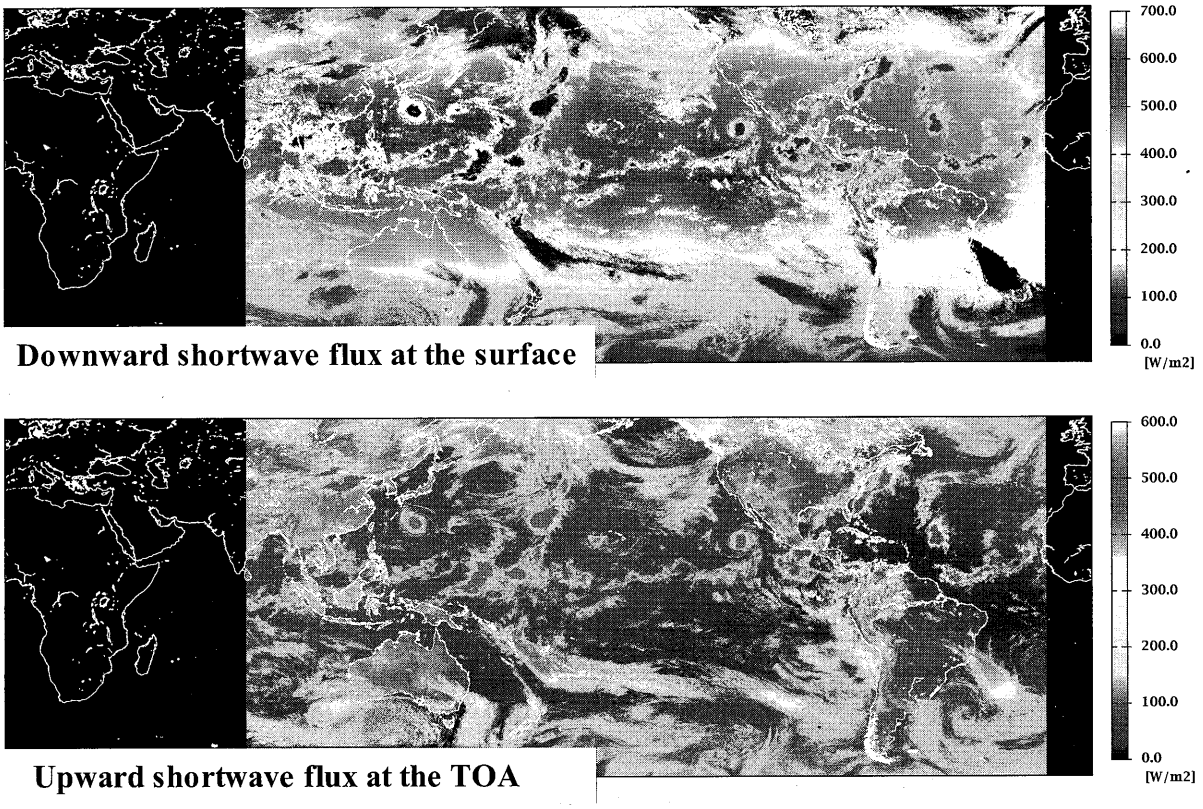

Figure 1: A part of the result of shortwave radiation budget analysis. Day time averaged image. Upper side: Downward shortwave flux at the surface. Lower side: Upward shortwave flux at the TOA. GMS-5, GOES-10, GOES-8, each satellite flux product 15 hours / five data is used.

GMS-5: 2002/09/02/20:31-2002/09/03/08:31 UTC
GOES-10: 2002/09/02/15:00-2002/09/03/03:00 UTC
GOES-8: 2002/09/02/11:45-2002/09/02/23:45 UTC

References

Gasca, M., and T. Sauer, (2000), Polynomial interpolation in several variables, Adv. Comput. Math., 12, 377-410.

Higurashi, A., and T. Nakajima, (1999), Development of a two channel aerosol retrieval algorithm on global scale using NOAA / AVHRR, J. Atmos. Sci., 56, 924-941.

Higurashi, A., and T. Nakajima, (2002), Detection of aerosol types over the East China Sea near Japan from four-channel satellite data., Geophys. Res. Lett., 29(17), 1836, doi:10.1029/2002GL015357.

Inoue, T., (1987), A cloud type classification with NOAA-7 split-window measurements, J. Geophys. Res., 92, 3991-4000.

Kawamoto, K., T. Nakajima, and T.Y. Nakajima, (2001), A global determination of cloud microphysics with AVHRR remote sensing, J. Climate, 14, 2054-2068.

Manabe, S. and R. T. Wetherald (1967), Thermal Equilibrium of the Atmosphere with a Given Distribution of Relative , J. Atmos. Sci., 24, 241-259.

Nakajima, T. Y., and T. Nakajima (1995), Wide-area determination of cloud microphysical properties from NOAA AVHRR measurements for FIRE and ASTEX regions, J. Atmos. Sci., 52, 4043-4059.

Nakajima, T., T. Y. Nakajima, M. Nakajima, and the GLI Algorithm Integration Team (GAIT), (1999), Development of ADEOS-II/GLI operational algorithm for earth observation, SPIE, 3870, 314-322.

Nakajima, T., and M. Tanaka (1986), Matrix formulations for the transfer of solar radiation in a plane-parallel scattering atmosphere, J. Quant. Spectrosc. Radiat. Transfer, 35, 13-21.

Nakajima, T., and M. Tanaka (1988), Algorithms for radiative intensity calculations in moderately thick atmospheres using a truncation approximation, J. Quant. Spectrosc. Radiat. Transfer, 40, 51-69.

Sauer, T., Xu Yuan, (1995), On multivariate Lagrange interpolation, Math. Comput., 64, 11471170.

Schneider, S. H. (1972), Cloudiness as a Global Climate Feedback Mechanism: The Effects on the Radiation Balance and Surface Temperature of Variations in Cloudiness, J. Atmos. Sci., 29, 1413-1422.

Szilder, K. and Lozowski, E.P., (1995), Cloud feedback examined using a two-component time-dependent climate model , Beitr. Phys. Atmos., 68, 43-57.

Tsushima, Y. and S. Manabe (2001), Influence of cloud feedback on annual variation of global mean surface temperature, J. Geophys. Res., 106(D19), 22,635-22,646.

Wetherald, R. T. and S. Manabe (1988), Cloud feedback processes in a general circulation model, J. Atmos. Sci., 45(8), 1397-1415.

Analysis of rice production and irrigation system in Cianjur, Indonesia

Masashi Kasuya[1], Chiharu Hongo[2]

[1] *Department of Earth Sciences, Faculty of Science, Chiba University*
[2] *Center for Environmental Remote Sensing, Chiba University*

Abstract

It is necessary to supply food and manage water in Indonesia because of increasing population and climate variations. In this study, relationships between rice production and weather condition or water management are analyzed using GIS data in Cianjur, Indonesia. North area is more rice production than south area in Cianjur, and both areas are stable. But precipitation fluctuates each year. We research the relationship between total production and irrigation that include total irrigation, technical irrigation (TI) and rain-fed rice cultivation.

Keywords **:** Indonesia, irrigation, GIS, rice production

1. Introduction

In Indonesia about 18% of th e pop ulation is farmer , and they have been suffering from their crucial conditions such as (1) considerable rice production decrease in the last 5 years due to m any unsuccessful program s and disasters (inse ct diseases, flood, e tc) (2) change of la nd use, fr om rice fie ld i nto o ther la nd use, i .e. set tlement, industrial area s, t ourism (3) when rice price is low , farmers are not inte rested in the rice cultivation a nd they prefer to c ultivate other c ash cro ps. And now, t he population is growing year by year and it is predicted that the population in 2050 will be 1.3 times larger than that in 2006. I t has misgi vings ab out the issues of fo od s upply issues. In addition, this area has the rainy season and the dry season clearly, and when the climate change happens, the rice p roduction am ount will be als o a ffected. It is concerned that a downpour an d a lo ng-term water shortage may occur more frequently in the future and the food production will be influenced remarkably. Recently, in the p eriod o f 1997-1998 an d 2 002-2003, the drought happened because of El N iño, and it ha d a big influence on the production of rice.

To resolve these problems, it is necessary to maintain an infrastructure to supply food and manage water resources. So in this study, rice production data in the study site was compared with elem ents of w eather c ondition a nd water management in formation to und erstand the sp atial and the yearly fluctuation of rice in each year.

2. Methodology

2.1 Study site

The study was carried out in the Cia njur dictrict, Indonesia (Fi g. 1). The test site is located i n the central part of West Java, where t he lo ngitude is 106°42'~107°25'E an d th e latitude is 6 °21'~7°25'S. In the st udy site, there are 17 vi llages i n t he northern a rea and 13 villages in the southern area.

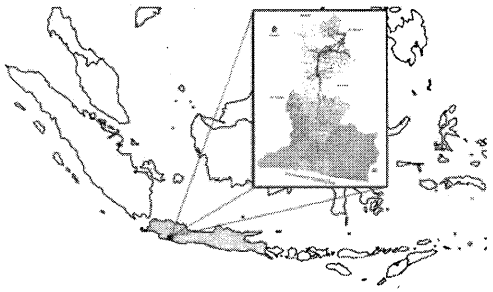

Fig. 1 Cianjur, West Java, Indonesia

2.2 Data sources

The so urce of stat istical data fr om 20 00 to 2006 was published by Cianjur Central Bureau of S tatics. The data included the rice production, precipitation, total irrigation number an d i rrigation data having f ive different le vels. Irrigation le vels are divided into Irr igasi T eknis (technical irrigation: TI), I rrigasi 1/2 T eknis, Irr igasi Seder-hana, I rrigasi No n-PU and T adah H ujan (rain-fed cultivation). In this study, TI and rain-fed cultivation data were used to avoid the ambiguity.

Because of lack of precipitation data of Cianjur in 2005, the data was s ubstituted for observing in Cilacap where longitude is 109°21'E and latitude is 7°73'S .

2.3 Procedure

After developing the dataset of rice production, irrigation and precipitation, it was unified on ArcGIS.

Based on it , relationships between total ri ce pr oduction and annual preci pitation, tota l pr oduction and total irrigation, a verage rice production a nd TI an d yearly change of number of farmers are analyzed.

3. Results and discussion

The total rice production and precipitation from 2000 to 2006 are shown in Fig.2. Average annual production of rice in Cianjur is 611,459t. It is stable except for 2003 and the rice production in northern area is higher than in the southern area. Precipitation changed every year and much decreased in 2003. The production of rice this year decreased by 100,000t compared with the annual average production. This shows that the rice production is affected not only by weather condition, and then other factors were compared with rice production.

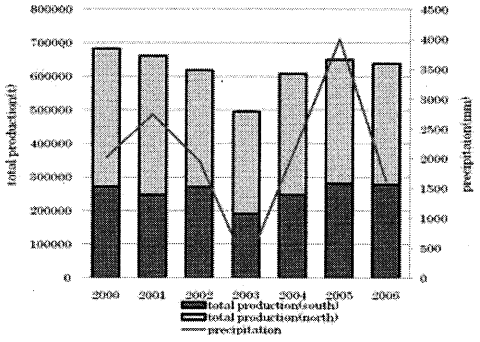

Fig. 3 Rice total production and precipitation in Cianjur

Table 1 shows the yearly change of number of farmers and rain-fed cultivation. Number of farmers in 2006 increased by 5 thousand compare with in 2000. And number of rain-fed cultivation increased. Number of total irrigation also increased.

Table 1 Rice total production and number of farmers and rain-fed cultivation

	2000	2001	2002	2003	2004	2005	2006
Rice total production(t)	681757	659916	617886	493399	606971	582248	638039
Number of farmers	58301	58585	58823	58819	61771	62894	63509
Rain-fed cultivation	9191	9714	10031	12415	12316	14124	14165

The production increases as the number of irrigation increases. It shows tendency that the change greatly every year in the region having a lot of irrigation farmers(Fig.3).

Average rice production greatly decreases since 2003. The ratio of technical irrigation system against the total irrigation system in northern area of the test site was higher than that of southern area. Total rice production amount increases according to the number of irrigation and higher the number of farmer using technical irrigation system is the bigger change of annual production. However, average rice production per hector in three regions of the southern area, where technical irrigation system is lower than that in the northern area. Moreover, the number of rain-fed cultivation system in the southern area is higher than the northern area. Only three regions adopt TI in southern area. But in the northern area have more average rice production in the same proportion of TI since 2003(Fig.4,5).

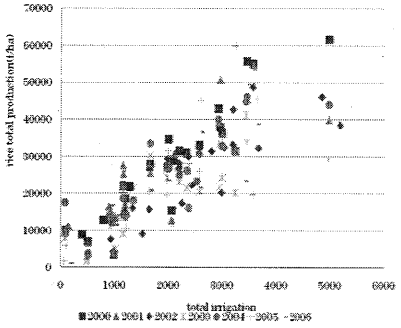

Fig. 2 Relationship between total irrigation and rice total production

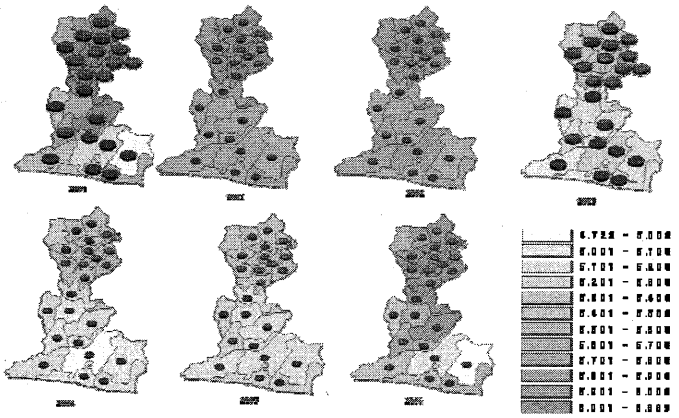

Fig. 4 Rice average production map and proportion of water management (red: TI blue :rain-fed cultivation)

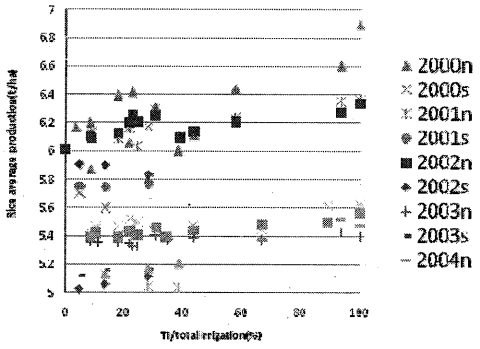

Fig. 5 Relationship between TI and rice average production

These results show that the irrigation level different in each area and especially villages of southern area mainly adopt rain-fed cultivation and it is considered that they are susceptible to soil and weather factors.

References

1) BADAN PUSAT STATISTIK KABUPATEN CIANJUR, KABUPATEN CIANJUR DALAM ANGKA 2000~2006
2) Japan Meteorological Agency
http://www.jma.go.jp/jma/index.html

Estimation of beet top yield using satellite data

Tomoyuki Wakamatsu[1], Chiharu Hongo[2]

[1]*Department of Earth Sciences, Faculty of Science, Chiba University*

[2]*Center for Environmental Remote Sensing, Chiba University*

Abstract **:**

In this study, the estimation of beet top yield using satellite data was conducted in Memuro, Hokkaido. The test site can be divided into four main geographical types which are lowlands, low, middle and high terraces. To derive the beet top yield estimation equation, the multiple linear regressions analysis was executed using the surface radiance value of SPOT5 image acquired in September 21, 2006 and ground observation data of beet top weight acquired on October 4, 2006. The accuracy of predictive error was affected by geographical types. Moreover, the yield of beet top was overestimated compared with ground observation data. The result suggests that the estimation accuracy can be improved by considering weather condition such as precipitation in the future.

Keywords **:** sugar beet, estimation equation of beet top

1. Introduction

Sugar beet is suited to cool weather, and Hokkaido is the only place where it is grown in Japan. To produce a beet sugar, root of sugar beet which is raw material of sugar is squeezed. Beet pulp is used for animal feed. After harvesting the root of sugar beet, beet top is plowing-in soil. This is one of effective method to reduce the cost of beet top disposal and the fertilizer application amount. On the other hand, the concentration of nitric acid in beet leaf and stem is higher than any other crops. After harvesting the root of sugar beet, beet top is plowing-in soil to keep fertility of upland field.

However, beet top is resolved and is the source of nitric oxide gas. Also, sometimes nitrogen in soil is overstock to product crop. In this area, fertilizer management is important to rotate. Information of the amount of nitrogen in soil is basic to manage fertilizer.

In this study, it is the purpose that satellite data which continuous can research wide area use to construct the way to management fertilizer. To acquire basic information, ground observation is practiced in 2006 and 2007 at Memuro, Hokkaido. We make estimate expressions using field data and ground observation data.

2. Methodology

2.1 Study area

This study was conducted around the town of Memuro located in the middle west of the Tokachi plain, Hokkaido, Japan (longitude 143.02°E, latitude 42.54°N).

The cultivation area of Memuro town is 19,720ha, and the acreage for beet planting is 3550ha in 2005.

2.2 Data

SPOT satellite data were acquired on September 21, 2006 (SPOT2) and September 23, 2007(SPOT5). There are three bands in the SPOT2 imagery, with the observation wavelengths including green band, red band, near infrared band with a 20m image resolution. There are fore bands in the SPOT5 imagery, with the observation wavelengths including the green band, red band, near infrared band and short-wavelength infrared band, with a 10m image resolution for the visible bands and near-infrared band and a 20m image resolution for the short-wavelength infrared band.

A geographic map drawn at a scale of 1 to 25,000 published by Geographical Survey Institute, Japan was prepared to rectify the satellite data.

Ground observation data of beet top weight were measured at about 40 points in October 4, 2006 and 2007. To measure the plant height and beet top weight, investigation points were set in 40 different locations each with an area of 3 rows×7 plants. The field survey was performed from June to October in 2006 and 2007.The beet top weight of the observation point was transformed into the weight of hectare using planting density value.

2.3 Procedure

Digital numbers at the ground observation points were extracted from satellite image of 2006 and 2007 which is corrected geometrically beforehand. Digital numbers were transformed to radiance value. Estimation formula of beet top weight was developed using five predictors, green band, red band, near infrared band, NDVI and GNDVI in 2006. In this study, the short-wavelength infrared band was not used as a predictor because SPOT2 does not have a sensor for the short-wavelength infrared wavelength. NDVI was derived from red (R) and near-infrared (NIR) spectral bands, which are calculated using the following formula:

$$NDVI=(NIR-R)/(NIR+R).$$

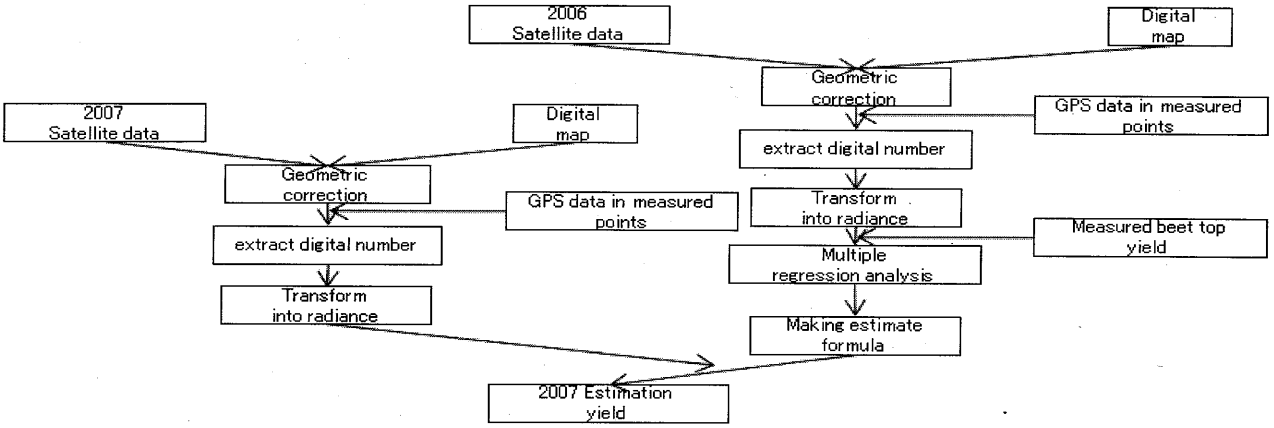

GNDVI was derived from green (G) and near-infrared (NIR) spectral bands, which are calculated using the following formula:

$$GNDVI=(NIR-G)/(NIR+G).$$

Finally, beet top weight in 2007 was calculated using the estimate formula derived from data of 2006, and comparison was performed between estimation data and the ground observation data in 2007.

3. Results and discussion

Ground observation data in 2006 shows that plant height of each geological type (low land, low terrace, middle and high terrace) is different in each month from June to October as shown in Fig 2. There is little difference in the height until the beginning of July and then the difference gets bigger gradually. After that, growing pattern of plant height was different in each geological type. So, estimation formula of beet top was developed for three different geological types.

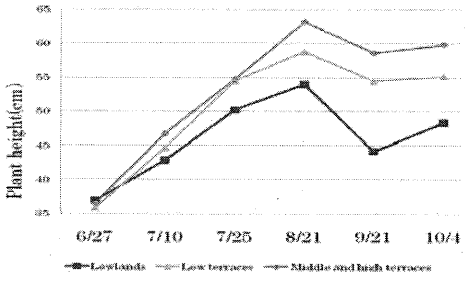

Fig.2 Transition of plant height in 2006

As a result, the green band and NDVI were selected as the predictors of beet top. The correlation coefficient of estimation equation of lowland soil is 0.207. In this area, October plant height is the second in all geological types.

Beet top weight was the highest value which is grown in lowland (Table 2).

Table 2 Beet top weight and plant height in October 2006

Geological type	Plant length (cm)	Beet top weight (kg)
Lowlands	48.35	0.700
Low terraces	55.19	0.969
Middle and high terraces	59.82	0.932

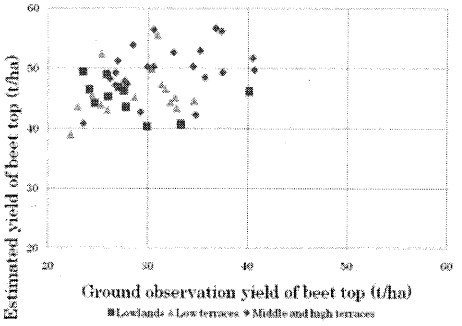

Fig.3 Comparison with observation data and estimated data of beet top in 2007

Beet top weight was the highest value which is grown in lowland (Table 2). In this area, it is suggested that the beet grows more horizontally in such a way where number of leaves increases, when compared with growth pattern of other areas. This growth pattern difference is considered to give big difference over to the reflection property.

Fig 3 shows the comparison of yield between 2 cases where calculation is made with use of the observation data and the estimated data of beet top in 2007., which indicates that the yield based on the estimated data is higher than that of the observation data.

References

1) Keiko KATO: Estimation of sugar beet yield using satellite and weather data, Graduation thesis of Department of Earth Sciences, Faculty of Science, Chiba University, 2009

Monitoring land subsidence in Semarang City Indonesia using Multiple Acquisition Radar Interferometry (MARI)

Ashar Muda Lubis[1)], Toshinori Sato[1)], Isezaki Nobuhiro[1)]
Nobuhiro Tomiyama[2)] and Tsutomu Yamanokuchi[2)]

[1)]Graduate School of Science, Chiba University
1-33, Yayoi-cho, Inage-ku, Chiba-shi, Chiba, 263-8522, Japan
E-mail: *asharml@graduate.chiba-u.jp*, Tel: +81-43-290-2854, Fax: +81-43-290-2859
[2)] Remote Sensing Technology Center of Japan,
1-9-9 Roppongi Minato-ku, First Building 12F, Tokyo

Abstract

Based on field observation, it was reported that the ground subsidence associated with groundwater extraction became one of environmental problems in Semarang Indonesia. In order to understand time and spatial distribution of land subsidence in Semarang city Indonesia, we performed Multiple Acquisition Radar Interferometry (MARI) of ALOS-PALSAR satellites data. We created 20 interfrogram images from 13 scans SAR data and removed topography phase using DEM three-arcsec (90 m) from each initial interferograms. We performed precision baseline estimation of each pairs to vanish the fringes derived by baseline between master and slave data. The improved phase unwrapping image shows land subsidence about 5-12 cm/y, which mainly caused by groundwater extraction and landuse changing from agriculture and cultivation purposes to industrial estates and house in Semarang. The fringe patterns are detected very clearly in center of Semarang city and northern part of city where the number of pump of groundwater concentrated in this area and large amount of water supply for the communities and industries. Our results are comparable to our previous work and shows the centre of the city was subsided continually after March 2008. The pattern of land subsidence in Semarang city derived by MARI is good relationship with past result obtained by both leveling data and digital elevation modeling (DEM) interpolated and benchmark points.

Key words: Radar Interferometry, subsidence, groundwater, landuse,

1. Introduction

It was reported that in Semarang, located on the northern part of Central Java Province in Indonesia at latitudes 6°58'S and longitude 110°25'E (Fig. 1), surface water and groundwater became mainly water supply for the communities and industries [1]. When groundwater levels decline sufficiently so that stress on the aquitards becomes greater than the maximum previous stress, then the aquitards compact and the land surface subsides permanently. Many buildings in Semarang city are severely affected by land subsidence (Fig. 2) which is mainly due to excessive groundwater extraction and natural consolidation of alluvium soil.

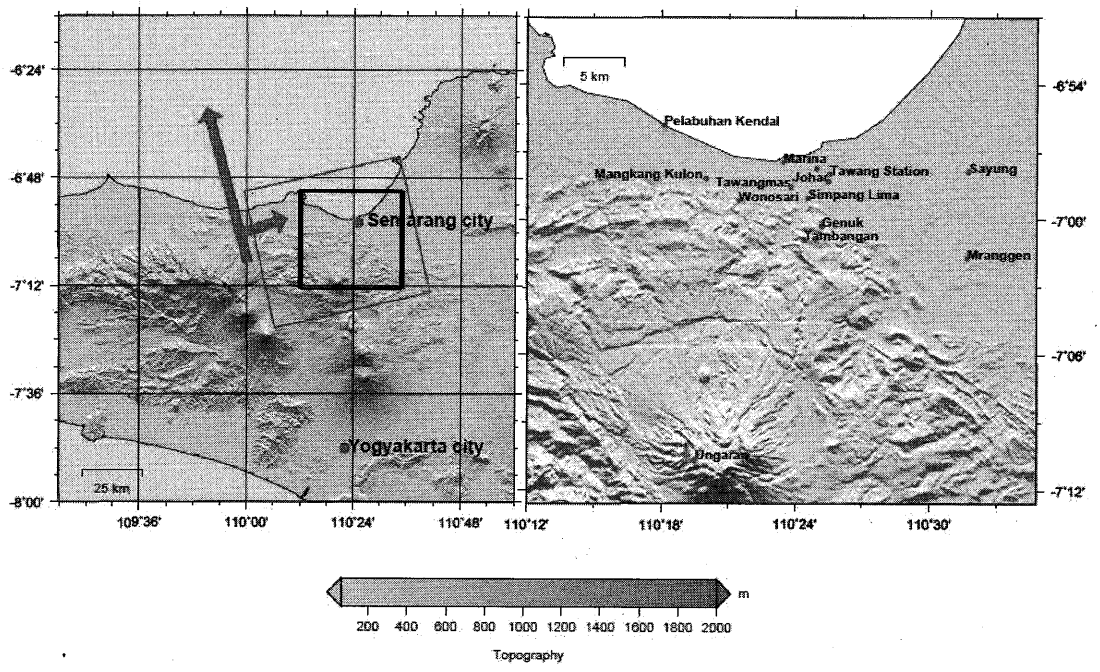

Figure 1. Map of Semarang city, shaded digital elevation model data shown in the figure. Red rectangular is location of PALSAR acquisition.

In this study, we performed Multiple Acquisition Radar Interferometry (MARI) of ALOS-PALSAR satellites data to access land subsidence in Semarang city Indonesia.

Figure 2. Impact of land subsidence in Semarang city [2].

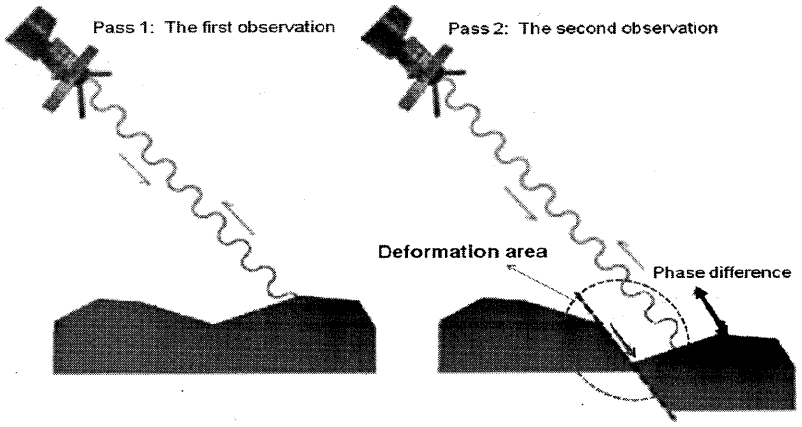

Figure 3. Carton of InSAR observation

2. Method and Result

In this research we used row data from two passes of ALOS PALSAR satellite (Tables 1). All of our data cover area around Semarang city (Fig 1). The principal measurement for Synthetic Aperture Radar Interferometry (InSAR) for monitoring land deformation in target area is shown by Fig 3. Two satellites send radar waves to the same point on the ground at different times. If the earth moves between passes, the wave will return at a different phase. Knowing the length of the wave, it is possible to calculate the precise amount of deformation.

The total differential of the phase difference is represented by three kinds of fringes which are caused by orbital fringe, topographic fringe and fringe land displacement due to earthquake, volcano eruption, oil, gas and water extraction, and landslides. To remove fringe related to topographic effect we mosaiced conventional digital elevation data a 3-arcsecond SRTM digital elevation model. e performed precision baseline estimation to vanish the fringes from baseline between master and slave data, and improved signal to- noise ratio of each differential interferogram using a weighted power spectrum filter as discussed in [3]. The minimum cost flow (MCF) was applied for unwarping process since the interferometry phase is wrapped modulo 2π, and an integer number of 2π must be added to recover the absolute phase difference.

Table 1. Row data of ALOS PALSAR satellite used in this study.

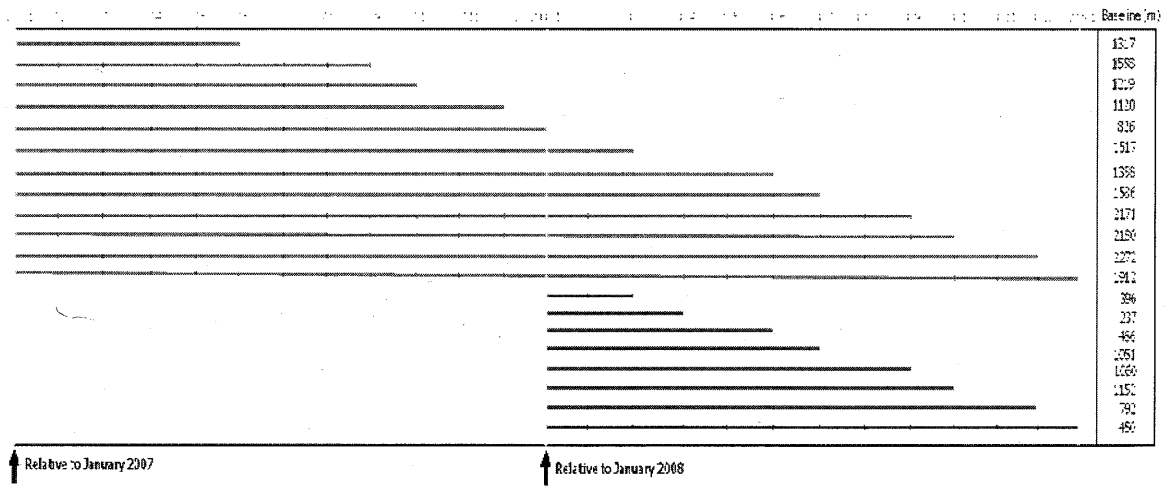

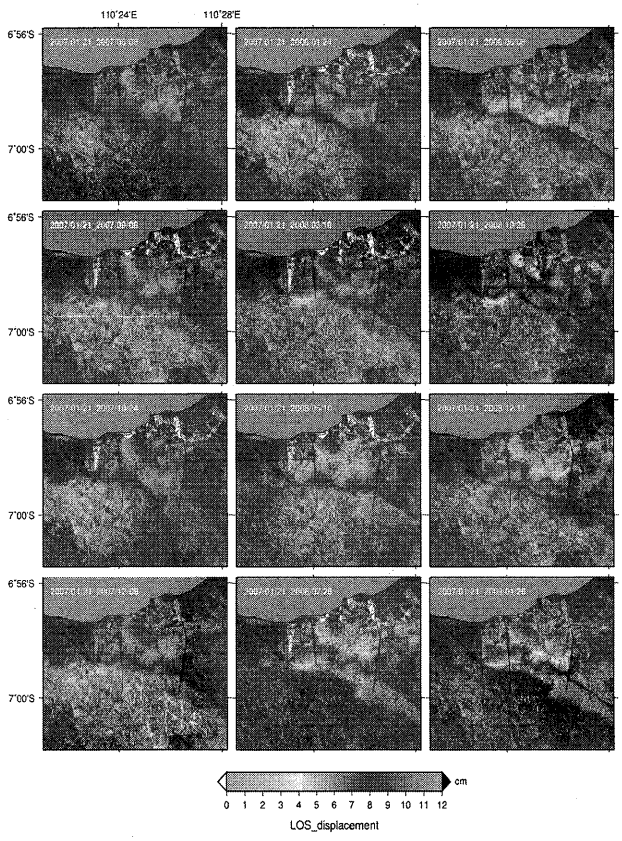

Figure 4. Land deformation images during 2007-2009 relative to January 2007.

In Both pair relative to January 2007 A (Fig. 4) and pair relative to January 2008 B (Fig. 5), the fringe patterns are detected very clearly in center of Semarang city and we can also see that high-subsidence rate occurred especially along the coastal area where in these areas the groundwater became mainly water supply for the communities and industries.

We estimated land deformation about 5-12 cm/y during January, 2007 to January 2009. The images of deformation show that the pattern of land displacement is increasing with extending time span observation. It can be noticed the significant difference from each pair with increasing time evolution of observation. Result of deformation during 2007-2009 and 2008-2009 observation shows similar pattern where fringe patterns of 2007-2008 are almost the same in comparison to 2008-2009 InSAR data which revealed

that the subsidence was continue after 1 years (2007-2008) time period of observation. Our results in general are similar pattern of land subsidence with Fig 6 derived from Envisat *Persistent Scattered Interferometry* [3] and ldeformation in Semarang city from Leveling data (Fig. 7)

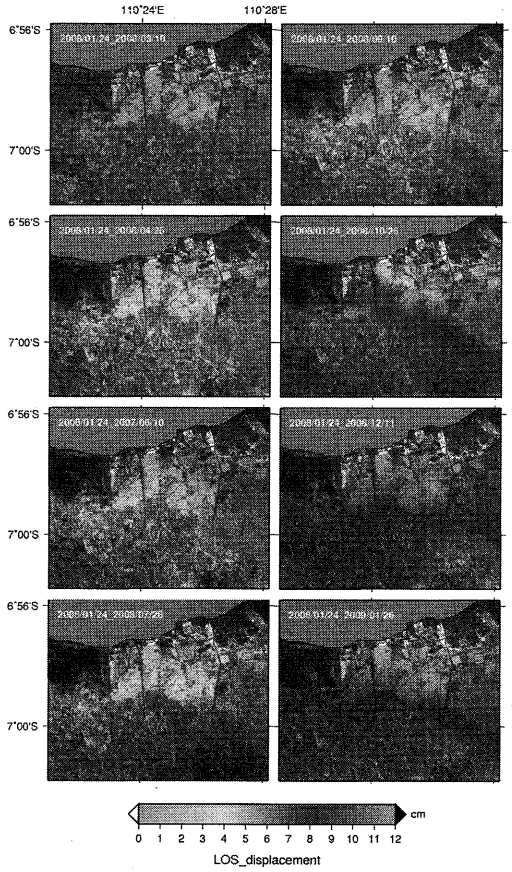

Figure 5. Land deformation images during 2008-2009 relative to January 2008.

The Semarang city can be divided into two major landscapes, namely, lowland and coastal area on the northern part and hill area on the southern part (Fig. 1). The city centre is situated on the lowland area, and landuse was changed rapidly from agriculture and cultivation purposes to industrial estates and house because the population is growing rapidly [1]. According to land deformation distribution from our result, past leveling data and Envisat *Persistent Scattered Interferometry* result, it can be noticed that

land subsidence mostly occurred on the lowland and coastal area of Semarang where in this region increasing populated area and land changing purpose are concentrated since 1990.

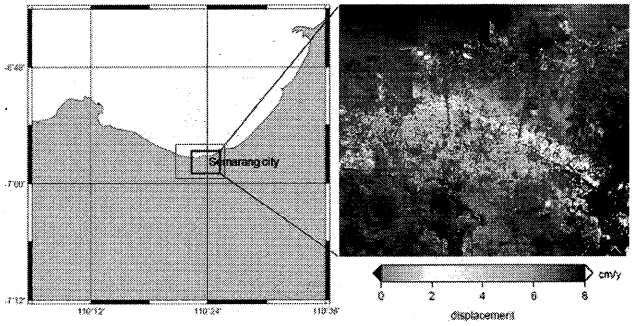

Figure 6. Land deformation in Semarang city from Envisat data [3].

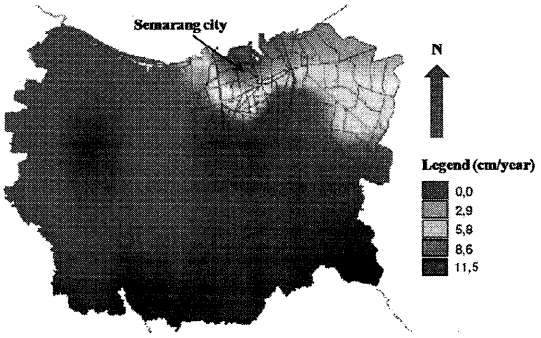

Figure 7. Land deformation in Semarang city from Leveling data [4].

3. Conclusion and Recommendation

We investigated land deformation in Semarang city using PALSAR data interferometry and estimated max. land subsidence 5-12 cm/year. We concluded that ground water extraction combined with landuse change incorporating with house development due to increased urbanization caused land subsidence in Semarang city. To achieve a better understanding and modeling of land subsidence phenomena in the Semarang city, the land subsidence information derived by InSAR method should be integrated with the land subsidence information obtained by geodetic techniques (e.g., leveling, and GPS) by incorporating by geohydrological and geotechnical

measurements (e.g., using automatic water level recorder, piezometer, and drilling). The reliable and best of information of land subsidence will help government, planners, regulators, and administrators to manage landuse and groundwater resources in Semarang city.

References

1. Marfai & King, (2007).
2. Kobayashi, (2003).
3. Friedrich et al., (2009).
4. Sutanta, (2002)

Accuracy improvement of the Needleleaf evergreen forest and the Needleleaf deciduous forest in the GLCNMO

Gegen Tana[1], Ryutaro Tateishi[2]

[1]Graduate Schools of Science, Chiba University, 1-33 Yayoi-cho, Inage-ku, Chiba, Japan, 263-8522,gegentana@graduate.chiba-u.jp

[2]Centre for Environmental Remote Sensing (CEReS), Chiba University, 1-33 Yayoi-cho, Inage-ku, Chiba, Japan, 263-8522, tateishi@faculty.chiba-u.jp

Abstract

The Global Land Cover by National Mapping Organizations (GLCNMO) is the product of the Global Mapping Project organized by International Steering Committee for Global Mapping (ISCGM). The data are produced by 16-day composite MODIS data observed in 2003. In this study, the accuracy improvement of GLCNMO was realized. The accuracy was mainly improved by decreasing the error caused by the classification method. According to the result of the accuracy assessment, Needleleaf evergreen forest and Needleleaf deciduous forest were selected for reclassification. In the new classification process, the MODIS data of October 16 were selected and the threshold of NDVI patterns was set again. Finally, by comparing the new classification result with ground truth data, the GLCNMO with improved accuracy was produced.

Keywords: MODIS data, GLCNMO, NDVI patterns

1. Introduction

Global land cover maps are used in the numerical models that estimate ecosystem behavior, water cycle and climate at the global scale. Within the past decades, large volumes of global land cover maps were produced, such as IGBP DISCover product, the MODIS land cover product, UMD land cover product, and Global Land Cover 2000. They were all derived from remotely sensed data with moderate resolution. Although there are several global land cover data, it is also necessary to develop a land cover database more up-to-date and with high accuracy.

Global Mapping Project has produced a 1km global land cover map called Global Land Cover by National Mapping Organizations (GLCNMO). In the GLCNMO, 16-day composite MODIS data of 2003 were used as source data. The GLCNMO is composed of comprehensive global land cover data and ground truth database. As a new global land cover map, the accuracy assessment of GLCNMO was completed. To derive a quantitative description of the accuracy of GLCNMO, a stratified random sampling method was used for accuracy analysis. The purpose of this study is by decreasing the errors caused by the classification methods to improve the accuracy of GLCNMO. The result of the accuracy assessment shows that Needleleaf deciduous forest has a lowest user's accuracy and 6 sampling pixels out of 27 sampling pixels are misclassified into Needleleaf evergreen forest. The reasons that make the accuracy low are considered to be the seasonal affection, the threshold of NDVI. 3 training sites for Needleleaf evergreen forest and 4 training sites for Needleleaf deciduous forest were collected by using Forest Cover of the USSR for the year 1990. Finally, a new GLCNMO with improved accuracy was derived.

2. Global land cover product-GLCNMO

2.1 Source data

The main source data used for GLCNMO is MODIS/TERRA Nadir BRDF- Adjusted Reflectance 16-DAY L3 Global 1 KM SIN Grid Product (MOD43B4 NBAR). This is the data with 1km resolution. And the data are composed of 7 spectral bands.

2.1 Legend and classification methods

GLCNMO consists of 20 land cover classes defined by Land Cover Classification System (LCCS). Land cover legend of the GLCNMO is shown in the Table 1. 7 spectral bands and NDVI patterns of MODIS 2003 were used for classification. Maximum likelihood method, which is one of the supervised classification techniques, was mainly used for GLCNMO. 14 classes out of 20 classes were classified by Maximum likelihood method. The rest of 6 classes that are Water, Snow/ ice, Urban, Wetland, Mangrove and Tree open were classified independently because of the complicated characteristics of the data.

Table 1. Land cover legend of the GLCNMO

GLCNMO code	Class name
1	Broadleaf evergreen forest
2	Broadleaf deciduous forest
3	Needleleaf evergreen forest
4	Needleleaf deciduous forest
5	Mixed forest
6	Tree open
7	Shrub
8	Herbaceous
9	Herbaceous with sparse tree / shrub
10	Sparse vegetation
11	Cropland
12	Paddy field
13	Cropland / other vegetation mosaic
14	Mangrove
15	Wetland
16	Bare Area, consolidated (gravel, rock)
17	Bare Area, unconsolidated (sand)
18	Urban
19	Snow / ice
20	Water bodies

3. Accuracy improvement of GLCNMO

3.1 Methodology

There are several reasons that lead to the errors of the map. From the instrument and orbits points of view, the errors may be influenced by spectral data quality or geolocation. From the classified map point of view, the errors may be influenced by legends definition, mixed pixels or classification methods. In this study, the accuracy of GLCNMO was improved by decreasing the error caused by the classification methods. Needleleaf deciduous forest has a lowest user's accuracy of 44.4% and 6 sampling pixels out of 27 sampling pixels are misclassified into Needleleaf evergreen forest. The reasons that make the accuracy low are considered to be the seasonal affection, the threshold of NDVI and the band used for the classification. 3 training sites for Needleleaf evergreen forest and 4 training sites for Needleleaf deciduous forest were collected by using Forest Cover of the USSR for the year 1990 (Fig. 1). In the Fig. 1, training sites for Needleleaf deciduous forest were marked from 1 to 4 and training sites for Needleleaf evergreen forest were marked from 5 to 7.

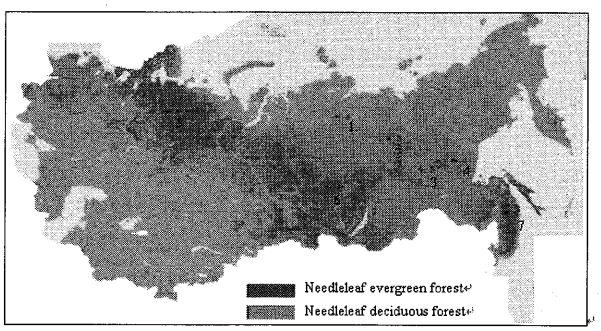

Fig. 1. Training sites for Needleleaf evergreen forest and Needleleaf deciduous forest

The parameters that make the user's accuracies of needleleaf evergreen forest and needleleaf deciduous forest low are considered to be the seasonal affection and the threshold of NDVI selected for classification. For this reason, MODIS NDVI monthly changed patterns were made for all the 7 pure training sites (Fig. 2). From the NDVI patterns MODIS data of October 16 were chosen in both areas.

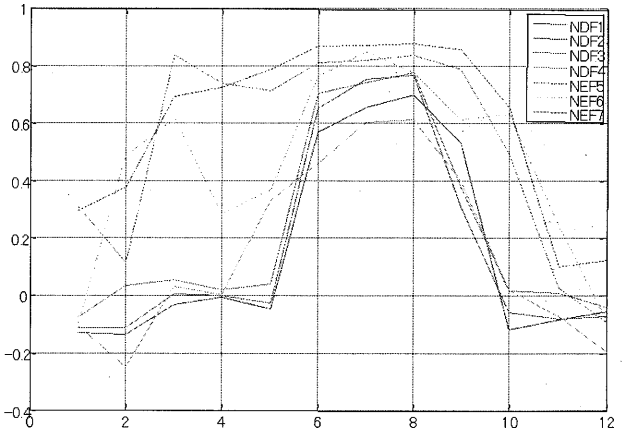

Fig. 2. NDVI patterns for 7 training sites

3.2 Results

MODIS data of October 16 were chosen because the difference of needleleaf evergreen forest and needleleaf deciduous forest is the biggest. According to the difference, the NDVI thresholds were set for classification in North America and Eurasia respectively. After several times validation the best two thresholds were selected for classification. That is when the threshold of NDVI pattern is 0.31 in North America and the threshold of NDVI pattern is 0.36 in Eurasia. Finally the new GLCNMO with improved accuracy of needleleaf evergreen forest and needleleaf deciduous forest was derived.

4. Conclusions

Land cover maps derived from the remote sensing data are simple attempts to represent what actually exists in the world,

but they are never completely accurate. There are many reasons lead to errors. It is difficult to modify the errors caused by the data itself. However, it is possible to do some technical improvements in the classification process. This study concentrates the errors caused by the classification methods. The results proved that this is just one part of the improvement for the map. For further study, it is necessary to improve the overall accuracy of the map. In order to achieve this purpose, the heterogeneous classes should be the focus of consideration.

References

1) T. R. Loveland, B. C. Reed, J. F. Brown, D. O. Ohlen, Z. Zhu, L. Yang, and J. W. Merchant, "Development of a global land cover characteristics database and IGBP DISCover from 1 km AVHRR data," *International Journal of Remote Sensing*, Taylor & Francis, Vol. 83 (1-2), pp. 1303–1330, 2000.

2) M. A. Friedl, D. K. McIver, J. C. F. Hodges, X. Y. Zhang, D. Muchoney, A. H. Strahler, C. E. Woodcock, S. Gopal, A. Schneider, A. Cooper, A. Baccini, F. Gao, and C. Schaaf, "Global land cover mapping from MODIS: Algorithms and early results, *Remote Sensing of Environment*, ELSEVIER, Vol. 83, pp. 287–302, 2002.

3) E. Bartholomé and A. S. Belward, "GLC2000: A new approach to global land cover mapping from Earth Observation data," *International Journal of Remote Sensing*, Taylor & Francis, Vol. 26, pp. 1959–1977, 2005.

4) S. Sakabe, H. Maruyama, J. Kisanuki, T. Nagayama, H. Koshimizu, S. Kayaba, M. Abe, and T. Ubukawa, "Global Mapping Project By National Mapping Organizations On The Globe," GSDI-9 Conference proceedings, 6-10 November, 2006.

5) M. Philippe, E.Hugh, G. Javier, A. H. Strahler, Member, IEEE, H. Martin, Student Member, IEEE, A. Shefali, N. Sergey, E. D. M. Evaristo, M. D. B. Carlos, O. Callan, K. Yuri, and P. S. Roy, "Validation of the Global Land Cover 2000 Map," *IEEE Transactions on Geoscience and Remote Sensing*, IEEE, Vol. 44 (7), 1728-1739, 2006.

6) Y. Ohtani, Y. Mizoguchi, T. Watanabe, Y. Yasuda, and M.Toda, "Carbon dioxide flux above an evergreen needle leaf forest in a temperature region of Japan, " Sixth International Carbon Dioxide Conference, pp. 469-472, 1-5 October, 2001.

7) R. Tateishi., Bayaer., M. A. Ghar., H. Al-Bilbisi., J. Tsendayush., A. Shalaby., Alimujiang Kasimu., N. T. Hoan., T. Kobayashi., B. Alsaaideh., Md. M. Rahman., E. Tsevengee., Y. Yamada. and S. Kajikawa., "A new global land cover map, GLCNMO," The International Archives of the Photogrammetry, Remote Sensing and Spatial Information Sciences, Vol. XXXVII, Part B7, 3-11 July, 2008

8) M. Herold, P. Mayaux, C. E. Woodcock, A. Baccini, and C. Schmullius, "Some challenges in global land cover mapping: An assessment of agreement and accuracy in existing 1 km datasets," *Remote Sensing of Environment*, ELSEVIER, Vol. 112, pp. 2538–2556, 2008.

9) M. C. Hansen, and B. Reed, "A comparison of the IGBP DISCover and University of Maryland 1 km global land cover products," *International Journal of Remote Sensing*, Taylor & Francis, Vol. 216-7, pp. 1365–1373, 2000.

Structures of Explosively Developing Extratropical Cyclones in Northwestern Pacific by Satellite Data

Munehisa K. Yamamoto[1], Masamitsu Hayasaki[2] and Atsushi Higuchi[3]

[1]*Center for Environmental Remote Sensing, Chiba University, Japan,mkyamamoto@faculty.chiba-u.jp*

[2]*Center for Environmental Remote Sensing, Chiba University, Japan,m_hayasaki@faculty.chiba-u.jp*

[3]*Center for Environmental Remote Sensing, Chiba University, Japan,higu@faculty.chiba-u.jp*

Abstract

Horizontal distributions of explosively developing extratropical cyclone formed and developed in Northwestern Pacific Ocean in precipitation, water vapor, cloud liquid water, and surface wind fields are analyzed using the Advanced Microwave Scanning Radiometer for EOS (AMSR-E) on Aqua Satellite dataset in recent 7 winter seasons. Cyclone center-relative compositing mean fields are constructed for four life stages: 1) developing, 2) maximum deepening, 3) minimum center sea level pressure (SLP), and 4) decaying. These stages are distinguished by a value and a kind of differentiation in center SLP using a database of cyclone tracking derived from a reanalysis dataset. The developing processes of the composited cyclone are documented.

In developing stage, the water vapor pass (WVP) has south-north (high-low) contrast corresponding to the temperature distribution. Corresponding to the cold-dry air mass advections, WVP concentration starts from western part of the cyclone center in the maximum deepening stage. The concentration is distinct along the cold front in the minimum SLP stage. The horizontal distributions at the maximum deepening stage agree with the previous study using global objectively analyzed dataset (GANAL). As the deepening rate is larger, the value and concentration is higher and stronger. Precipitation appears around the root of front corresponding to large cloud liquid water, while there is no precipitation near the cyclone center in minimum center SLP and decaying stages regardless of the strength.

Keywords: Extratropical cyclone, winter precipitation, satellite observation

1. Introduction

Extratropical cyclone is one of sources to supply heat and moisture from mid-latitude to high-latitude regions, so that it plays an important role for energy and material transportations. Explosively developing extratropical cyclones particularly form and develop frequently in northwestern Pacific and Atlantic in winter[1].

Development mechanisms of extratropical cyclones have been studied using numerical models and re-analysis data mainly in the Atlantic Ocean. On the other hand, Yoshida and Asuma[2] mention the characteristics of explosive cyclones in northwestern Pacific. They classified the cyclones into three types depending on cyclogenesis and rapid development, and suggested that the each type of cyclone has favorable terms of frequent appearance and atmospheric conditions such as jet stream and baroclinicity.

Satellite data enables us to investigate global vertical and horizontal structure in moisture, wind, and precipitation/clouds of the systems regardless of land and ocean. The heights of the cyclones and frontal precipitation over northwestern Pacific are concentrated around 3 km of echo top height and 6 km of cloud top height observed by the Tropical Rainfall Measuring Mission (TRMM) Precipitation Radar (PR) and infrared imager[3]. Field and Wood[4] showed that surface speed and/or water vapor path cause response a variability of cyclone-mean rain rate, cloud fraction, etc. derived from categorized cyclone relative composited using

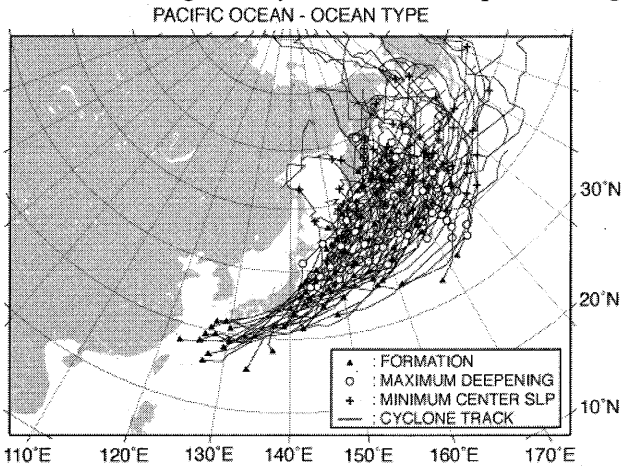

Fig. 1. Cyclone tracks investigated in this study. They correspond to PO-O cyclones defined by Yoshida and Asuma (2004). Triangles show positions of formation, circles show positions of maximum deepening rate, and crosses show positions of minimum center SLP.

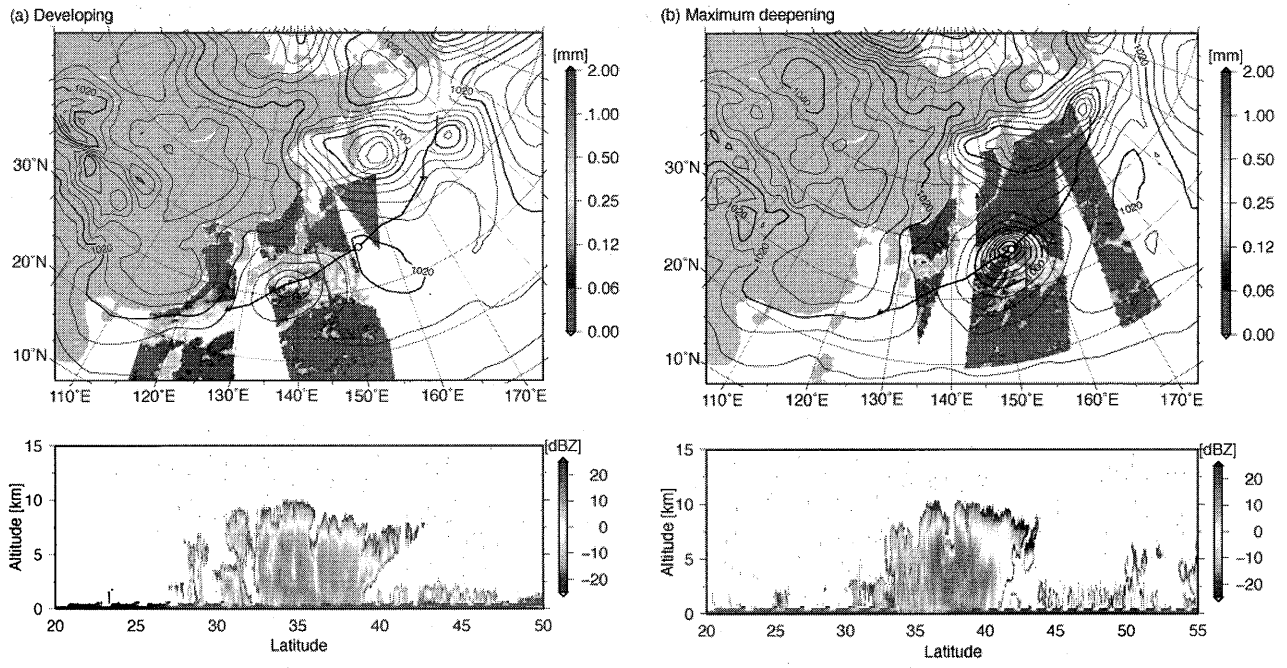

Fig. 2. AMSR-E estimated cloud liquid water (upper color image) and vertical distributions of radar reflectivity factor observed by Cloudsat CPR (under color image) with orbit (red line on the upper image) for (a) developing and (b) maximum deepening stages. Sea level pressure (contour) and cyclone track (solid line) are illustrated on the upper image.

the Moderate Resolution Imaging Spectroradiometer (MODIS) and the Advanced Microwave Scanning Radiometer-EOS (AMSR-E) onboard the Aqua satellite. They concluded that the systemwide mean rainfall rates and composite structure are broadly agree with satellite estimates. However, the spatial distributions largely depend on the life stages the cyclones[5]. Except for some case studies, there are few studies using composite analysis to focus on developing process of extratropical cyclones.

This study presents the developing processes of vertical and horizontal structure in the extratropical cyclones using satellite observation data.

2. Data and Method

This study investigates explosively extratropical cyclones which form and had rapidly developed in 20°N–65°N and 100°E–180° in 7 winter seasons (2002/2003–2008/2009 from October to March). The cyclone identification and tracking algorithms are based on Serreze[6]. We applies to SLP data installed in the Japanese 25-year Reanalysis (JRA-25) and the Japanese Meteorological Agency (JMA) Climate Data Assimilation System (JCDAS) products provided by the JMA[7]. At first, the JRA25/JCDAS longitude-latitude grids in northern hemisphere were converted to the Equal-Area Scalable Earth (EASE) grid about 125 km square area. For the SLP in EASE grids, a cyclone center was detected at the grid point less than 0.5 hPa next to 8 grid points. When the cyclone center existed less than 4 grid points (~ 500 km) from the previous 6 hours, the cyclone identified as the same. The definition of explosively developing cyclones and their classification method were applied to Yoshida and Asuma[2]. For this study we just use PO-O type cyclones (Fig. 1) because the AMSR-E products do not retrieve any hydrospheric products on the most of track over land for the rest of two-types. In order to identify for life stages for the every explosive cyclones selected in this study, we defined four life stages; 1) developing stage at the intermediate time between formation and maximum developing, 2) maximum developing stage at maximum deepening rate, 3) minimum center SLP stage, and 4) decaying stage at the intermediate time between minimum center SLP and cyclolysis.

We used some satellite observation data which form the constellation satellites named A-Train. The AMSR-E Ocean Products version 5[8] provides 0.25° × 0.25° grid data. The CPR is a spaceborne cloud profiling radar. The 2B-GEOPROF product provides cloud geometric profile expressed in terms of occurrence and reflectivity. The minimum detectable signal has −28 dBZ that enable to detect cloud top height.

3. Results

3.1 Case study for a typical explosive cyclone developed in 3-5 February 2008

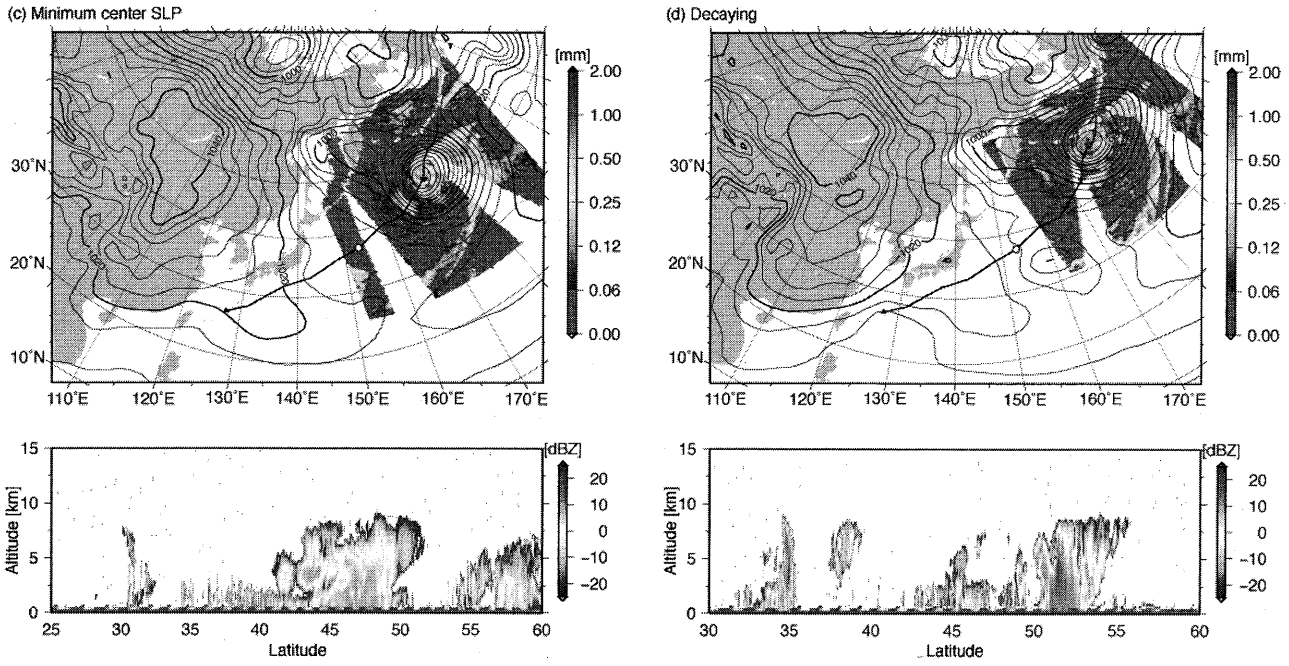

Fig. 3. The same as Fig. 2 except for (c) minimum center SLP and (d) decaying stages.

3.1.1 Synoptic Conditions

Figures 2 and 3 show a track of the explosive cyclone developed in 3–5 February 2008 and SLP fields at the four-life stages. The incipient cyclone was formed at 27°N and 127°E at 2 February 0600 UTC. The cyclone moved to ENE with 18 m s^{-1} speed in average along the southern Japan Island. After the developing stage the cyclone increased its speed more than 23 m s^{-1} with rapid depression, the cyclone has maximum deepening stages with 1.1 Bergeron at 3 February1800 UTC. The cyclone continued both fast moving and depression until 961 hPa of the minimum center SLP stage at which 5 February 0000 UTC. At last, the cyclone disappeared at 6 February 1200 UTC with slow down (8 m s^{-1}) and system intensity.

3.1.2 Cloud liquid water (CLW)

At the developing stage CLW distributes widely from the west to east part of the cyclone, the CLW concentrated around the root of the front until the maximum deepening stage. A line of CLW formed and strengthened along to the cold front at the minimum center SLP and decaying stages, which seems to be a distinct frontal T-borne shape. At these stages, there is relatively weak CLW near the cyclone center with warm-core seclusion.

3.1.3 Vertical distributions of cloud

At the developing stage, the cloud top height near the cyclone center (35°N) reaches almost 10 km. A strong echo from precipitation (> 20 dBZ) also can be found at 7.5 km. While the southern edge of the cyclone cloud appears to be vertical, there are slope as going to top of the cloud. At the maximum deepening stage, the eastern side at the cyclone center also passed. The height of echo top does not have large difference. The CPR captured the cyclone center and cold front at the minimum center SLP stage. After the maximum deepening stage, the cloud top height keeps around 10 km although the cloud echoes were relatively weak over the cyclone center. In contrast, a narrow cloud radar pattern appears around the cold front compared to the horizontal distributions of CLW (30° and 35° N at the rest of two stages). This difference implies that cloud/precipitation is not well formed in spite of concentration of water vapor due to cold-dry advection from the backward of the cyclone.

3.2 Composite analysis

In order to check the possible factors to cause the strength of the explosive cyclones, we carried out a composite analysis for above mentioned parameters. The explosive cyclones for CO-O types (52 cyclones) are classified into strong (ST, ≥ 1.3 Bergeron) and weak (WE, < 1.3 Bergeron) patterns. The sample numbers of ST and WE are 17 and 35 cyclones, respectively. Atmospheric water vapor increases toward southward for both ST and WE patterns at the developing stage (Fig. 4). The slope for ST is steeper than that for WE, particularly the north part of the cyclone for ST is drier. Surface wind pattern (Fig. 5) also do not have remarkable difference of the distributions relative to the cyclone center, the northwestern dry advection are stronger for ST.

Compared to the results in Field and Wood[4], the most different parameter of composite map is surface rain rate (not

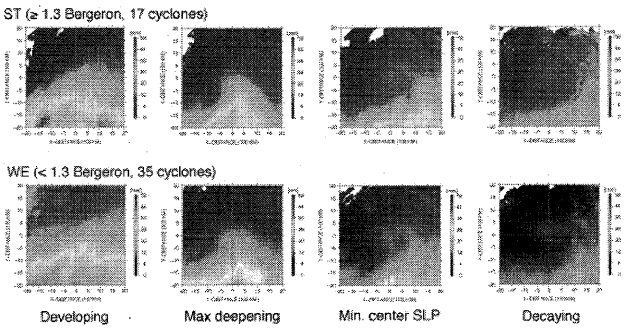

Fig. 4 Cyclone center-relative composite map for AMSR-E for estimated atmospheric water vapor for strong pattern (more than 1.3 Bergeron) and moderate deepening pattern (less than 1.3 Bergeron).

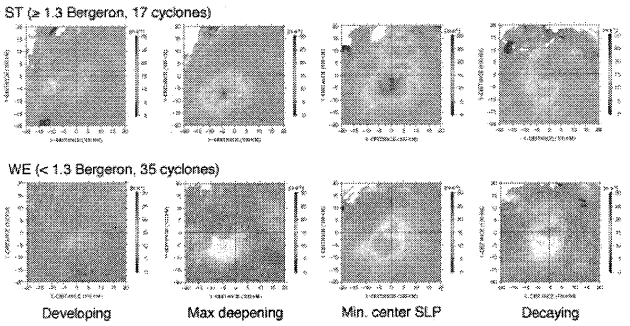

Fig. 5 The same as Fig. 4 except for surface wind speed.

shown). Precipitation about 4 mm h^{-1} appears from the center of the cyclone to the south-eastward at the maximum deepening stage. Although some precipitation bands derived from cold fronts are also observed for ST patterns at the minimum center SLP and the decaying stages, there is little precipitation around the center and eastward from a warm front. This difference may be because the precipitation could be the solid phase. Yamamoto et al.[3] pointed out almost all precipitation did not estimated by TMI for the cold outbreak type from the comparison between TRMM PR and TMI. Precipitation retrieval algorithm for microwave radiometer are generally tuned to the tropical regions and are less suitable for the weak rain in mid-latitude regions[9]

4. Concluding remarks

In order to better understand the vertical and horizontal structure of explosively developing extratropical cyclones depending on their life stage. Cloud liquid water, precipitation, and surface wind are concentrated around the center of the cyclone at the developing stage. Atmospheric water vapor increase latitudinally. At the maximum deepening stage, dry-cold air advection occurs from north-west of the cyclone center, which corresponds to the surface wind and atmospheric water vapor. The cold-dry advection, the concentrated area of the gale wind and atmospheric water vapor, moves south to south- east part of the cyclone center at the minimum center SLP and decaying stage. However, these changes depending on the life stages in precipitation do not appears maybe due to retrieval problem of microwave radiometer. There are not significant spatial differences from separately composited by deepening rate, but those contrast are distinct for all parameters except for precipitation. According to the case study, cloud echo-top height reaches around 10 km in the developing stages of an explosive cyclone, while significant echo pattern does not appear at the cold front for mature and decaying stage.

Acknowledgements

This study was supported by "Formation of a Virtual Laboratory for Diagnosing the Earth's Climate System", the Ministry of Education, Culture, Sports, Science and Technology Japan.

References

1) Sanders, F. and J. R. Gyakum, 1980: Synoptic-dynamic climatology of the "bomb". Mon. Wea. Rev., 108, 1589–1606.
2) Yoshida, A. and Y. Asuma, 2004: . Structures and environment of explosively developing extratropical cyclones in the northwestern pacific region. Mon. Wea. Rev., 132, 1121– 1142.
3) Yamamoto, M. K., A. Higuchi, and K. Nakamura, 2006: Vertical and horizontal structure of winter precipitation systems over the western pacific around japan using TRMM data. J. Geophys. Res., 111, D13108, doi:10:1029/2005JD006412.
4) Field, P. R., A. Gettelman, R. B. Neale, R. Wood, P. J. Rasch, and H. Morrison, 2008: Midlatitude cyclone compositing to constrain climate model behavior using satellite ob- servations. J. Climate, 21, 5887–5903.
5) Bjerknes, J., 1919: On the structure of moving cyclones. Mon. Wea. Rev., 47, 95–99.
6) Serreze, M. C., 1995: Climatological aspects of cyclone development and decay in the Arctic. Atmos.-Ocean, 33, 1–23.
7) Onogi, K. and Coauthors, 2007: The JRA-25 Reanalysis. J. Meteor. Soc. Japan, 85, 369–432.
8) Wentz, F. J. and T. Meissner, 2000: AMSR Ocean Algorithm. Algorithm Theoretical Basis Document. Tech. rep., Remote Sensing Systems, 59 pp., Santa Rosa, CA.
9) Negri, A. J., E. J. Nelkin, R. F. Adler, G. J. Huffman, and C. Kummerow, 1995: Evaluation of passive microwave precipitation algorithms in wintertime midlatitude situations. J. Atmos. Oceanic Technol., 12, 20–32.

CUDA/GPU Technology : Parallel Programming For High Performance Scientific Computing

Yuhendra[1], Hiroaki Kuze[2],Josaphat Tetuko Sri Sumantyo[3]

[1] *Center for Environmental Remote Sensing, Chiba University ,yuhendrat@graduate.chiba-u.jp, JAPAN*
[1]*Infornatic Engineering Department, Padang Institute of Technology, yuhendra_st@yahoo.com, West-Sumatra*
[2] *Center for Environmental Remote Sensing , Chiba University ,hkuze@faculty.chiba-u.jp, JAPAN*
[3]*Center for Environmental Remote Sensing , Chiba University ,hkuze@faculty.chiba-u.jp, JAPAN*

Abstract

Graphics processing units (GPUs) originally designed for computer video cards have emerged as the most powerful chip in a high-performance workstation. In the high performance computation capabilities, graphic processing units (GPU) lead to much more powerful performance than conventional CPUs by means of parallel processing. In 2007, the birth of Compute Unified Device Architecture (CUDA) and CUDA-enabled GPUs by NVIDIA Corporation brought a revolution in the general purpose GPU area. The NVIDIA CUDA technology is a novel computing architecture that enables the GPU to solve complex computational problems in image processing applications. CUDA also provides orders of magnitude more performance and simplifies software development by using the standard C language. We describe the CUDA programming model and motivate its use in the remote sensing imaging community.

Keywords **:** Graphic Processing Units, Compute Unified Device Architecture, Image Processing

1. Motivation

GPU computing, or the use of graphics processors for general-purpose computing, began in earnest several years ago [1]. In recent years, the computation speed of graphics processing unit (GPU) has increased rapidly. We only take the float-point operation as an example, and GPU's computation speed is several times faster than CPU's. The Flops of NVIDIA Ge80 series has gotten 520G in late 2006 [2], whereas Intel 64-bit dual-core CPU has only 32 GFlops.

Over the past few years, the performance of GPU has been improving at a much faster rate than the performance of CPUs. In 2007, NVIDIA's most advanced GPU provided six times the peak performance of Intel's most advanced CPU [3]. GPU has evolved from special-purpose processor to programmable processor, and meanwhile the programmability has been the most important feature. Compared to the previous GPU, CUDA GPU has the following advantages:

- *General programming environment:* CUDA uses C programming tools and C compiler, which make programs have better compatibility and portability.
- *More powerful parallel computing capability:* CUDA graphics card applied more transistors to computing, not to data cache or flow control [1]. GeForce 8800 has 128 1.35GHz stream processors, 512 bit DDR3,and 768M device memory, far bigger than the L1 cache of CPU.
- *Higher bandwidth:* Take the GeForce

8800 as an example, its bandwidth gets to 86.4GB/s between GPU and device memory, and 4GB/s between host memory and device memory via PCI-E x16 bus.

- *Instruction operation*: CUDA GPU supports integer and bit operation.

How much can GPU computing speed up a real-world science or engineering code? Researchers and companies are achieving speedups ranging from 10× to 100× (and sometimes more!) by using CUDA application in image processing, across domains ranging from computational parallel image[4], fast color image balancing [5], Processing SAR Data [6], Real-Time 3D Computed Tomographic Reconstruction[7] and etc.

2. THE CUDA PROGRAMMING MODEL

The fundamental strength of the GPU is its extremely parallel nature. The new hardware architecture exposed to programmers is shown in Figure 1. The CUDA programming model allows developers to exploit that parallelism by writing natural, straightforward C code that will then run in thousands or millions of parallel invocations, or *threads*. To utilize the GPU, CUDA provides an extended C-like programming language and compiling, Figure 3 and 4.

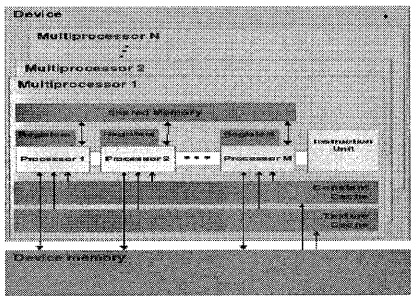

Fig 1. Hardware Model

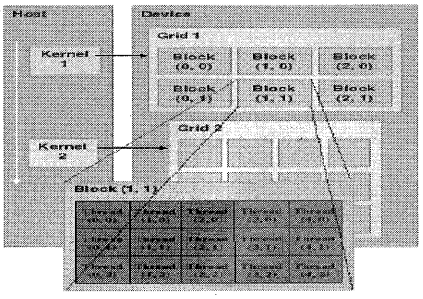

Fig 2. Execution Model

Any call to a global function is said to issue a kernel to run on the GPU and must first specify the dimension of the grid and the blocks that will be used to execute the function on GPU. The execution model is shown in Figure 2. Matrix addition will serve as a simple example. To add two N×N matrices on the CPU in C, one would write a doubly-nested *for* loop:

```
// add 2 matrices on the CPU:
void addMatrix(float *a, float *b,
float *c, int N)
{
int i, j, index;
for (i = 0; i < N; i++) {
for (j = 0; j < N; j++) {
index = i + j * N;
c[index]=a[index] + b[index];
}
}
void main()
{
.....
addMatrix(a, b, c, N);
}
```

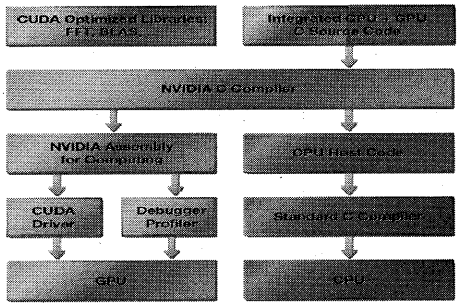

Fig 3. CUDA Software

In CUDA, one writes a C function, called a *kernel*, to compute one element in the matrix, and invokes as many threads to run that function as the matrix has elements. In each thread the kernel runs with a predefined structure**threadIdx** indicating which of the many threads is running:

```
// add 2 matrices on the GPU (simplified)
__global__ void addMatrix(float *a,float
*b,
float *c, int N)
{
int i= threadIdx.x;
int j= threadIdx.y;
int index= i + j * N;
c[index]= a[index] + b[index];
}
void main()
{
// run addMatrix in 1 block of NxN
threads:
dim3 blocksize(N, N),
addMatrix<<<1, blocksize>>>(a, b, c, N);
}
```

Here the **__global__** declaration specifier indicates a kernel function that will run on the GPU, and the **<<<N, N>>>** syntax indicates that the **addMatrix()** function will be invoked across a group of threads run in parallel, called a *thread block*. Thread blocks may be one-, two-, or three-dimensional, providing a natural way to invoke computation across the elements in a domain such as a vector, matrix, or field. CUDA makes three key refinements to the core concept of running kernel functions across many parallel threads: hierarchical thread blocks, shared memory, and barrier synchronization.

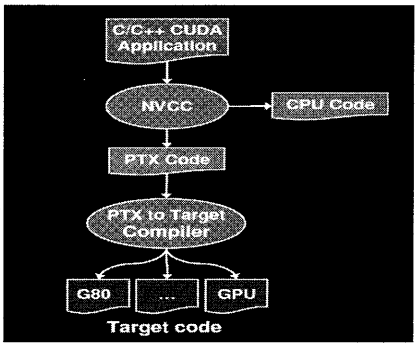

Fig.4 Compiling Process

2.1. Hierarchical thread blocks

Thread blocks may contain up to 512 threads on an NVIDIA Tesla architecture GPU, but kernels are invoked on a *grid* consisting of many thread blocks that are scheduled independently. All the threads in all the blocks in a grid execute the kernel and then exit. Thus the CUDA code given above needs to be extended slightly:

```
// add 2 matrices on the GPU (scalable)
__global__ void addMatrix(float *a,float
*b,
float *c, int N)
{
int
i=blockIdx.x*blockDim.x+threadIdx.x;
int
j=blockIdx.y*blockDim.y+threadIdx.y;
int index = i + j * N;
if ( i < N && j < N)
c[index]= a[index] + b[index];
}
```

The most important and widely used numerical algorithms, computational physics and general signal processing, CUDA has offer package CUFFT, shown in fig.4. This Package fine tune the algorithm for the GPU memory structure, in order to minimize data accesses.

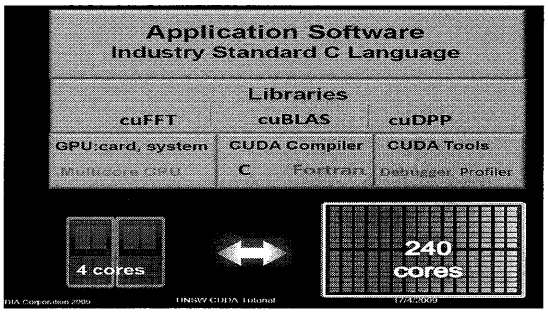

Fig.4 CUFFT Libraries

2.2. Shared memory

In our simple matrix addition example, threads can efficiently run independently: no thread needs to know the elements being accessed by other threads. Often however many threads can solve a problem more efficiently by cooperating, sharing the results of computations or memory fetches. CUDA enables this cooperation by providing *shared memory* where kernels can store data – e.g. variables or arrays – that are visible to all threads in a thread block. For example, the threads in a block could compute the sum of the elements in an array by each placing one element into an array in shared memory, then adding the element next to it, then the element located four array slots away, then eight, and so on. All the other threads in the block are doing the same thing in parallel – they are cooperating by computing partial sums through shared memory. Shared memory is on chip and thus small (16K on NVIDIA's current GPUs) but extremely fast, so exploiting shared memory makes this summing operation dramatically faster.

3. Summary & Future Work

NVIDIA GPUs provide massive computation resources, with up to hundreds of cores running thousands of threads. CUDA makes that raw computational power accessible and easy to program by allowing the user to write natural C code which is then run by thousands or millions of threads. Threads are organized in a two-level hierarchy of blocks and grids. Threads run in parallel with other threads in their thread block and can intercommunicate via shared memory, with simple barriers to synchronize. Researchers around the world and across all scientific and engineering disciplines are successfully using CUDA and NVIDIA GPUs to speed their codes up by one to two orders of magnitude. We have attempted to motivate the use of GPU computing in image processing and provide a brief overview of the "feel" of CUDA programming. In this future, the advantage of CUDA will be fully implemented by applying the technique to remote sensing fields where huge volume of image data are generated and consequently, near real-time or very fast analysis is indispensable. Because the Center for Environmental Remote Sensing (CEReS) is accumulating a variety of satellite datasets, there are many potential application of the CUDA methodology.

REFERENCES

[1] See *http://gpgpu.org*.
[2] NVIDIA Corporation, CUDA Programming Guide 1.0, http://www.nvidia.com,2007.
[3]Michael Boyer, Kevin Skadron, Westley Weimer. "Automated Dynamic Analysis of CUDA Programs", STMCS 2008, Boston, Massachusetts, Apr 06, 2008.
[4] Zhiyi Yang, Yating Zhu, Yong Pu,. "Parallel Image Processing Based on CUDA", International Conference on Computer Science and Software Engineering, 2008.
[5] Yong Kiat Alln Tan, Wee Juan Tan, Leong Keong, " Fast Colour Balance Adjustment of IKONOS Imagery Using CUDA", IEEE Journal, 2008.
[6] C. Clemente, M. Bisceglie, M. Santo, N. Ranaldo, M. Spinelli, "Processing of SAR Data with GPGPU", NVIDIA 2009.

[7] F. Xu and K. Mueller. "Real-Time 3D Computed Tomographic Reconstruction Using Commodity Graphics Hardware," Physics in Medicine and Biology, vol. 52, pp. 3405–3419, 2007. [6] NVIDIA. 2007. CUDA Programming Guide 1.1; see *http://developer.download.nvidia.com/compute/cuda/1_1/NVIDIA_CUDA_Programming_Guide_1.1.pdf.*

Development of a spectroradiometer system for observing UV-VIS-NIR skylight

Kenji Kuriyama, Naohiro Manago , Yasuto Kaba, Syuuji Miyazawa Ippei Harada, Hiroaki Kuze
CEReS, Chiba University, tskmasu@graduate.chiba-u.jp

Abstract

Images observed with satellite sensors are affected by Earth's atmospheric layers. In order to evaluate the intrinsic reflectivity of various surface targets, satellite images should be corrected for atmospheric effects. If sensors operated in the spectral regions of UV, VIS, and NIR are considered, extinction (i.e. the sum of absorption and scattering) of aerosol particles are important in addition to the Rayleigh scattering due to air molecules and absorption due to various molecular species such as water vapor, oxygen, ozone, carbon dioxide, etc. In this paper, we report recent results of long-term measurement using a VIS differential optical absorption (DOAS) spectrometer at CEReS. Also we describe a ground-based, wide-spectral-range sensor that derives molecular absorption signatures and aerosol scattering properties from simultaneous skylight observations in UV, VIS and NIR spectral regions. Three compact spectroradiometers operated in the wavelength range of 200-800 nm, 700-1100 nm, and 1100- 2200 nm are employed to measure the spectral intensities under clear-sky conditions. Both HITRAN and MODTRAN database/codes are used to derive column amount of absorbing molecular species including carbon dioxide and to characterize aerosol particles.

Keywords **:** DOAS; Air pollution distribution; Absorption cross section; UV, VIS and NIR spectral InGaAs photodiode

1. Introduction

In satellite measurement in the visible (VIS) spectral range, significant influence is exerted on the resulting images by aerosol distributions in the lower troposphere [1]. The scattering and absorption characteristics of aerosols play an important role also in the Earth' s radiation budget. Generally clouds and aerosols tend to reflect the solar radiation back to space, thus contributing to the cooling of the Earth's atmosphere system, though some of them absorb radiation and contributing to the warming effect [2]. The infrared and near-infrared (NIR) absorption of molecules is the main cause of the global warming (greenhouse) effect. Absorption due to carbon dioxide (CO_2), methane (CH_4), and other trace molecular species is of crucial importance, in addition to the large and variable effect of water vapor absorption. Since most of the sources/sinks of these molecules are located in the lower troposphere, it is beneficial if the NIR absorption of these so-called greenhouse gases can be monitored simultaneously with the gases and SPM that mainly interacts with radiation in the ultraviolet (UV) and visible spectral regions.

The method of differential optical absorption spectroscopy (DOAS) provides a useful tool for the measurement of atmospheric pollutants by measuring optical extinction (absorption and scattering) over a light path having a length of a few kilometers [3-6]. A novel DOAS approach has been proposed by the CEReS group on the basis of white flashlights installed at tall constructions such as buildings, bridges, and smokestacks [6]. Such flashlights, known as aviation obstruction lights, are mandatory under regulations in Japan. Since Xe lamps give flashes every 1.5 s that covers the whole VIS spectral range, a simple setup consisting of an astronomical telescope and a compact spectroradiometer enables the measurement of nitrogen dioxide using the original DOAS technique. Also, the stable intensity of the light source makes it possible to retrieve aerosol (SPM) concentrations in the lower troposphere, since the intensity variation of the detected light is mostly ascribable to the aerosol extinction over the light path [6,7]. An extension of the DOAS methodology is the multi-axis (MAX) DOAS approach, in which the spectral measurements of skylight (i.e. scattered solar radiation) in various elevation angles provide information on molecular absorption [8, 9]. Mostly an UV-VIS spectrometer is employed to retrieve the column amount of target species.

In this paper, we describe an extended form of DOAS and MAX-DOAS measurement. Result of a long-term measurement at CEReS, Chiba University is described in terms of the simultaneous NO_2 and aerosol concentration measurements. Molecular absorption signatures and aerosol scattering properties are derived from simultaneous MAX-DOAS (skylight) observations in UV, VIS and NIR

spectral regions. Both HITRAN and MODTRAN database/codes are used to derive column amount of absorbing molecular species including carbon dioxide and to characterize aerosol particles.

2. Instruments

2.1 DOAS in the visible spectral range

Figure 1 shows the schematic of DOAS measurement based on an aviation obstruction light, situated at 5.5 km away from the CEReS observatory. The light source is equipped at the top of a smokestack (130 m tall) of a municipal garbage incinerator. The average height of the light path is approximately 80 m above the ground level (100 m above sea level). A commercially available astronomical telescope (115 mm diameter, 910 mm focal length) is employed to focus the image of a Xe flashlamp at the location of the eyepiece. Instead of an eyepiece, the entrance of an optical fiber (400 μm core diameter) is placed and the other end of this fiber is connected to the slit (5 μm width) of a compact spectro-radiometer (Ocean Optics USB2000). The wavelength range of 200-800 nm is detected using a CCD array (2048 channels), resulting in a nominal wavelength resolution of 0.3 nm. After averaging 100 flashing events (with 300 background events), one DOAS spectrum can be obtained in every 5 min. The wavelength range of 430-450 nm is used here to retrieve the NO_2 concentration. The same wavelength range is employed to detect the aerosol effect from the variation of the intensity of the DOAS spectra.

In order to compare with the DOAS-retrieved concentrations, the hourly data from a ground sampling station (Miyanogi), operated by the environmental section of the municipal government, are obtained from a website of the Ministry of Environment (Atmospheric Environmental Regional Observation System (AEROS), http://www.nies.go.jp). It should be noted, however, that while the DOAS concentrations are resulting from the average over a light path (5.5 km), the ground sampling is carried out only at a point that is below the light path. Thus, the comparison is not necessarily to seek for complete agreement between the two different datasets, but to examine the similarity in the temporal variation of the relevant data.

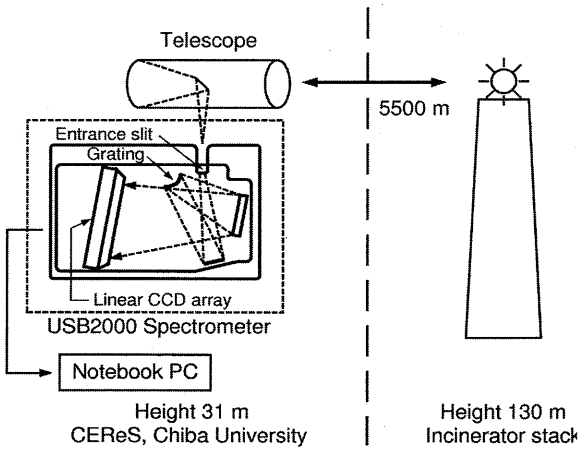

Fig. 1 Schematic of DOAS measurement

2.2 Sunphotometer

The result of DOAS measurement is compared with the data taken using a sunphotometer (Pride PSF-100), an instrument that measures the direct solar radiation. The measurement is carried out automatically, and values of aerosol optical thickness (AOT, τ_a) are measured at the wavelengths of 368, 500, 675, and 778 nm with wavelength width of 5nm each. The wavelength dependence of AOT is analyzed with a formula

$$\tau_a(\lambda) = B(\lambda/\lambda_0)^{-A} \quad (1)$$

to obtain the angstrom exponent $A=\alpha_{ang}$ (the coefficient B is called the turbidity constant at the reference wavelength λ_0= 550 nm.) The typical value of this parameter is unity. The value becomes smaller when coarse particles (with diameter larger than 2 m) are dominant, whereas it becomes larger when fine particles (with diameter larger than 2 μm) are dominant. Thus, the value of α_{ang} =2, for instance, indicates the existence of anthropogenic fine particles such as nitric and sulfuric aerosols, while α_{ang} =0.5, for instance, suggests the dominance of larger particles such as sea salt and soil.

2.3. UV-VIS-NIR MAX-DOAS system

Three compact spectroradiometers operated in the wavelength range of 200-800 nm (Ocean Optics USB4000), 700-1100 nm (Ocean Optics HR2000), and 1100- 2200 nm (Hamamatsu C9914GB), respectively, are employed to measure the spectral intensities from four directions (North, East, South, West) and six elevation angles (15, 30, 45, 60, 75, and 90 deg) under clear-sky conditions. Although each of fiber cables for these spectroradiometers has an intrinsic acceptance field-of-view (FOV) angle of approximately 120 deg, it is reduced to 5 deg to ensure better homogeneity in the sky radiance (scattered solar radiation, SSR) measurement. Homemade adaptors with shadow rings have been manufactured for this purpose, the inside of each adaptor (including the surface of rings) being covered with non-reflecting material. In order to achieve the simultaneous measurement in a combined, wide wavelength range, the three tubes are bound together and placed on a tripod. The exposure duration is typically 100 ms for USB4000, 300 ms

for HR2000, and 1 s for C9914GB. After relevant averaging, a set of data points can normally be obtained in a time period of 10 min.

3. Theory

The analysis of the DOAS spectra is based on the Beer-Lambert's law expressed as

$$I(\lambda) = kI_0(\lambda)e^{-L\sigma(\lambda)n}, \quad (2)$$

where $I(\lambda)$ is the measured intensity, k is the system constant, $I_0(\lambda)$ is the unattenuated reference intensity, L is the path length, $\sigma(\lambda)$ is the wavelength-dependent absorption cross section, and n is the number density of the species averaged over the path length. The dimensionless quantity $L\sigma(\lambda)n$ represents the optical thickness, denoted as τ .

Here we describe the algorithm developed for the retrieval of both the NO_2 concentration and the aerosol optical thickness. After the background subtraction, the observed light intensity $I_{obs}(\lambda)$ can be expressed as

$$I_{obs}(\lambda) = kI_0(\lambda)T_m(\lambda)T_a(\lambda)T_{NO_2}(\lambda) \quad (3)$$

Here k is an empirically determined coefficient, $I_0(\lambda)$ is the spectrum of the light source observed at a location close to the light source, $T_m(\lambda) = \exp[-\tau_m(\lambda)]$ is the transmittance of air molecules (Rayleigh scattering) [$\tau_m(\lambda)$ is the molecular optical thickness], $T_a(\lambda) = \exp[-\tau_a(\lambda)]$ is the transmittance of air molecules (Mie scattering) [$\tau_a(\lambda)$ is the aerosol optical thickness], and $T_{NO2}(\lambda)$ is the transmittance representing the NO_2 absorption. By dividing $\tau_a(\lambda)$ with the path length L, it is possible to estimate the average value of aerosol extinction coefficient, $\alpha_a(\lambda)$. In the present algorithm involving both the NO_2 and the aerosol retrieval, we first correct the observed spectrum $I_{obs}(\lambda)$ for the first three factors on the right-hand side of Eq. (3):

$$I_{obs}'(\lambda) = \frac{I_{obs}(\lambda)}{kI_0(\lambda)T_m(\lambda)}. \quad (4)$$

Combining Eqs. (3) and (4), we obtain

$$I_{obs}'(\lambda) = \exp[-\tau_a(\lambda) - \sigma(\lambda)C], \quad (5)$$

where $C = Nl$ is the column amount of NO_2. Moreover, if it is assumed that the aerosol optical thickness exhibits wavelength dependence as given by the Angstrom exponent, we obtain

$$-\ln I_{obs}'(\lambda) = B(\lambda/\lambda_0)^{-A} + \sigma(\lambda)C . \quad (6)$$

Removing the slowly varying contribution from Eq. (5),

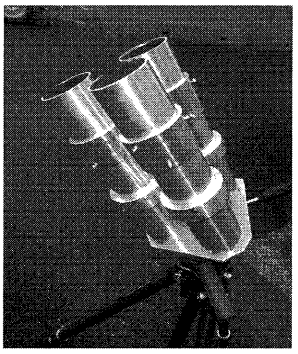

Fig. 2 Adaptor tubes for UV-VIS-NIR MAX-DAOS measurement

and applying the spectral matching to the rapidly varying part with the laboratory cross-sectional data, we obtain the value of C. Then, substituting C into Eq. (5) leads to the value of $(\lambda/\lambda_0)^{-A}$. In the actual data analysis, this process has to be operated in an iterative way. When simultaneous observation is made with a sunphotometer, the resulting information on the Angstrom exponent can be employed for aerosol retrieval from DOAS data. Alternatively, it is possible to employ DOAS data taken on a very clear day, and by using this as a reference spectrum (assumed to be mostly aerosol free), the spectra taken on other turbid days can be analyzed to obtain the aerosol quantity.

4. Results and discussion

4.1 Results of DOAS and sunphotometer measurements

At the CEReS, Chiba University (35.62°N, 140.12°E, 30 km southeast of Tokyo), long-term observation has been made in terms of the concentrations of nitric dioxide and aerosol. The monthly observation result of NO_2 and aerosol concentration measurement in February 2009 is shown in Fig. 3. Generally the region is relatively dry in this winter season with small precipitation. The urban air-pollution tends to exacerbate because of the formation of ground inversion layer. Figure 3(a) shows the monthly variation of NO_2 concentration, comparing the DOAS and ground sampling data. Since the DOAS light source is available only during the daytime (red, blinking lights are used during nighttime), the DOAS data are shown only for daytime. The diurnal variation from the ground sampling data clearly indicates that the NO_2 concentration tends to increase during the nighttime, due probably to the strong inversion layer. The ground sampling data are generally higher than the DOAS result: this can be ascribed mainly to the vertical distribution of the pollutants, higher near the ground level (the intake height of ground sampling is about 3 m), decreasing toward higher altitude (the average height of the DOAS light path,

80 m). Also, it is known that the UV fluorescence method is sensitive not only to NO_2, but also to other chemical species existing together. Figure 3(b) compares the temporal variation of aerosol extinction coefficient from DOAS [$\alpha_a(\lambda)$ with λ= 425 nm] and the SPM concentration from the ground sampling. Obviously a good correlation is found between the two quantities. The regression between the DOAS optical parameter (in units of m^{-1}) and SPM mass parameter (in units of g/m^3) leads to the mass extinction efficiency (MEE, in units of m^2/g). The MEE is an important parameter connecting the optical and mass properties and aerosol particles [10]. In the case of Fig. 3(b), the MEE value can be determined to be 6.0 ± 0.8 m^2/g, a reasonable value for urban aerosols under dry conditions.

Figure 3(c) shows AOT variations from DOAS and sunphotometer measurements. The DOAS values are generally larger than the sunphotometer values because of the difference in the light path directions, horizontal for DOAS and vertical for sunphotometer. Nevertheless, a reasonable temporal correlation is found between the DOAS and sunphotometer results in Fig. 3(c). Figure 3(d) shows the temperature and wind speed data observed at the CEReS site (on the rooftop of a 4 story building). It is seen that the change of wind speed becomes more significant when the diurnal change of the temperature is larger. Comparison with Fig. 3(a) suggests that the NO_2 concentration tends to become larger when the wind speed is lower (0-2 m/s). This tendency can also be found for aerosol particles: higher SPM concentrations are found during nighttime when the wind speed is generally lower. It is noteworthy, however, that occasionally increasing aerosol concentration is found with higher wind speed during the daytime, as seen the data on 10and 23 February 2009. This is likely to be caused from local dust (or sea salt) aerosol sources.

Nighttime increase in air pollutants was observed from the night on 12 February to the morning on 13 February (Fig. 4). Temporal behavior of temperature and wind speed shows the onset of ground inversion layer. Nocturnal increase in the aerosol concentration can be seen in Fig. 4(b), which lasted until the noon of the following day. High concentration of NO_2 is seen in Fig. 4(a), but more fluctuating in the range of 20-60 ppb.

4.2 Spectral radiance of scattered solar radiation

Molecular absorption spectra observed with spectro-radiometers are shown in Fig. 6: (a) 300-730 nm (USB4000) and (b) 700-1100 nm (HR2000). These clear-sky, skylight spectra (raw spectra, not calibrated) were observed near the

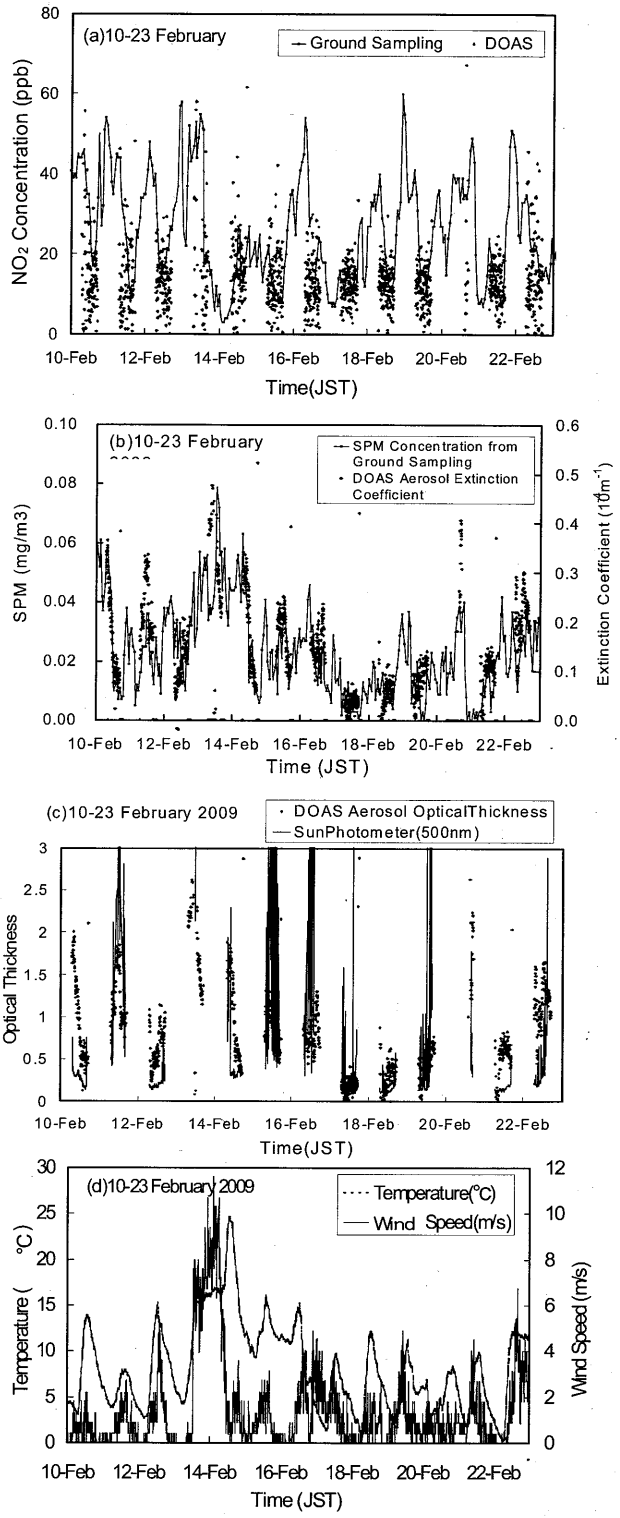

Fig. 3 Observation results during 10-23 February 2009. (a) NO2 concentration from DOAS and ground sampling, (b) extinction coefficient from DOAS and concentration of SPM from ground measurement, (c) aerosol optical thickness (AOT) from DOAS and sunphotometer measurements, and (d) temperature and wind speed.

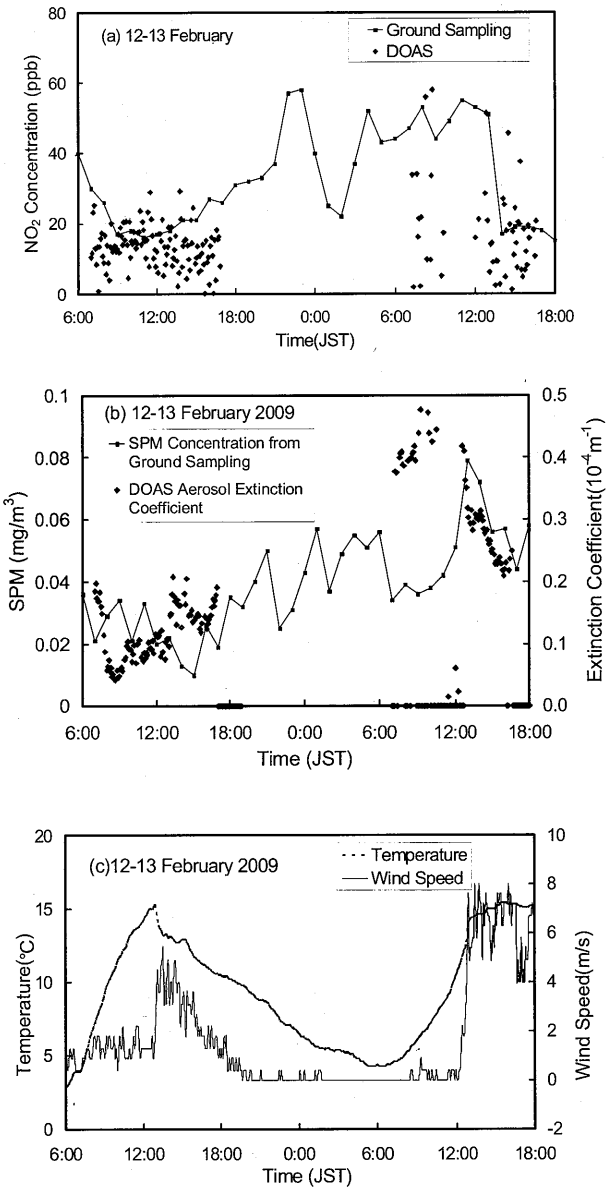

(a) NO_2 concentration from DOAS and ground sampling measurements, (b) aerosol extinction coefficient from DOAS and SPM concentration from ground sampling, and (c) temperature and wind speed.

solar direction on 10 and 11 June 2009 (45° elevation, 58° eastward direction) at Hamamatsu (34.43°N, 137.43°E). In Fig. 5(a), ozone (O_3) absorption feature is seen in the UV part, in addition to several features due to Fraunhofer structures intrinsic to the solar spectra. In Fig. 5(b), NIR absorption features of O_2 (A band) and water vapor bands are clearly seen. The calibration and quantitative determination of molecular column amounts are discussed in a separate presentation [11]. A NIR spectroradiometer based on an InGaAs photodetector can be used to observe absorption bands of CO_2, a major molecular species

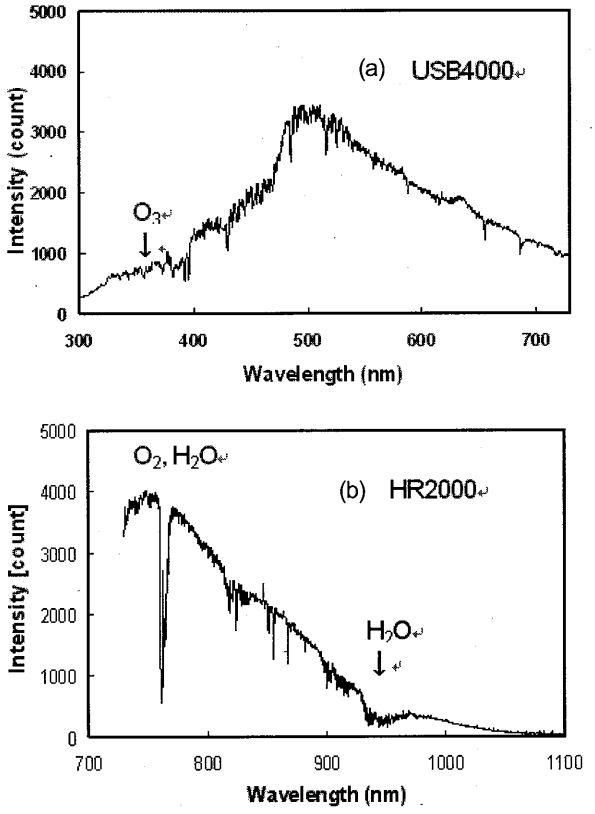

Fig. 5 Molecular absorption observed with Spectroradiometers: (a) 300-730 nm (USB4000) and (b) 700-1100 nm (HR2000)

responsible for the global warming.

Figure 6 shows (a) observed spectrum (11:45 JST on 10 June 2009) and (b) simulated spectrum. The simulation is based on MODTRAN and HITRAN calculations. In the MAX-DOAS approach, the analysis of SSR spectra taken at various observation directions (elevation angles) is carried out by means of radiative transfer calculations. Recently, we have demonstrated that the combination of VIS spectra for direct solar radiation, aureole and SSR enables the retrieval of aerosol optical characterization as well as column amounts of water vapor and ozone [12]. The present combination of three spectroradiometers covers wider spectral ranges, and more comprehensive analysis of atmospheric conditions will become feasible using the MAX-DOAS approach.

5. Conclusion

In this work, we have reported recent achievement in our activities in DOAS and MAX-DOAS measurements. In the DOAS measurement of NO_2 and aerosol (SPM), the data observed at CEReS have been employed to investigate

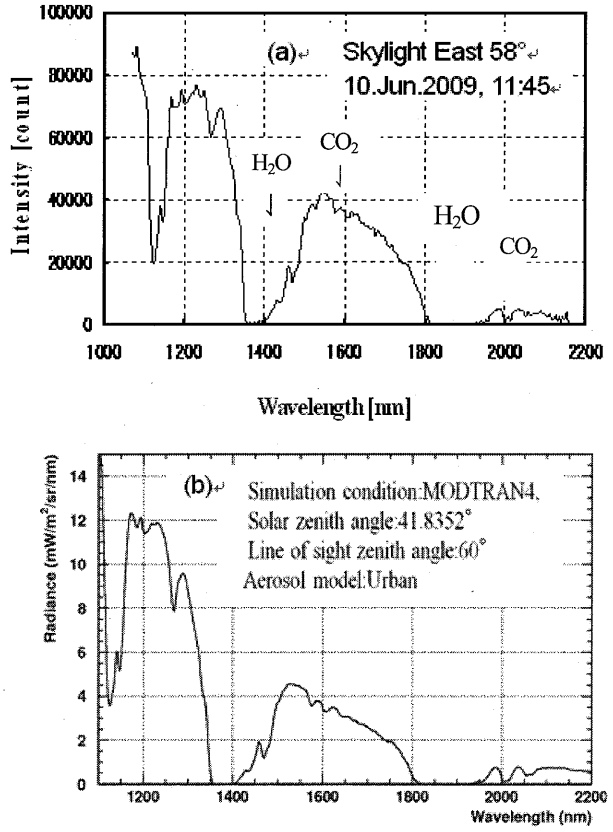

Fig. 6 Near-infrared measurement including CO_2 absorption: (a) observed spectrum (with a NIR spectroradiometer), and (b) simulated spectrum.

long-term variations of urban air-pollution in the lower troposphere. The results of DOAS measurements are compared with those from sunphotometer and point sampling at a nearby ground station. As an extension of visible measurement of direct/scattered solar radiation, we have constructed an instrument that enables MAX-DOAS measurements covering a wide wavelength range of 300-2200 nm. The instrumental calibration and related improvement of the radiative transfer calculation is ongoing.

References

[1] W.G.Rees, Physical Principles of Remote Sensing , 2nd. Ed. (2001)

[2] The Fourth Assessment Report (AR4) IPCC (2007)

[3] A. Fraser, C. Adams, J.R. Drummond, F. Goutail, G. Manney, K. Strong (2009): The polar environment atmospheric research laboratory UV–visible ground-based spectrometer: first measurements of O_3, NO_2, BrO, and Ocl Ocolumns. Journal of Quantitative Spectroscopy Radiative Transfer 110 , 986–1004.

[4] Zuo Hao-yi, Zhu Shi-fu , Wang Jie-yu , Luo Shi-rong, (2008): Retrieval of the vertical column density of the atmospheric pollution gases by using the scattered solar radiation. Journal of Quantitative Spectroscopy & Radiative Transfer 109 , 2628- 2634.

[5] G. Bagtasa, N. Takeuchi, S. Fukagawa, H. Kuze, S. Naito,(2007):Correction in aerosol mass concentration measurements with humidity difference between ambient and instrumental conditions. Atmospheric Environment 41, 1616-1626.

[6] Y. Yoshii, H. Kuze, N. Takeuchi, (2003): Long-path measurement of atmospheric NO_2 with an obstruction flashlight and a charge coupled device spectrometer, Applied Optics, 42, 4362-4368.

[7] F. Si, H. Kuze, Y. Yoshii, M. Nemoto, N. Takeuchi, T. Kimura, T. Umekawa, T. Yoshida, T. Hioki, T. Tsutsui, and M. Kawasaki, (2005): Measurement of regional distribution of atmospheric NO_2 and aerosol particles with flashlight long-path optical monitoring, Atmospheric Environment, 39, 4959-4968.

[8] F. Wittrock, H. Oetjen, A. Richter, S. Fietkau, T. Medeke, A. Rozanov, and J. P. BurrowsF., (2004): MAX-DOAS measurements of atmospheric trace gases in Ny-A° lesund - Radiative transfer studies and their application , Atmos.Chem.Phys., 4, 955-966 .

[9] H. Irie, Y. Kanaya, H. kimoto, H. Iwabuchi, A. Shimizu, and K. Aoki,(2008): First retrieval of tropospheric aerosol profiles using MAX-DOAS and comparison with lidar and sky radiometer measurements.,: Atmos. Chem. Phys., 8, 341–350

[10] G. Bagtasa, N. Takeuchi, S. Fukagawa, H. Kuze, and S. Naito, Correction in aerosol mass concentration measurements with humidity difference between ambient and instrumental conditions. Atmospheric Environment, 41 (8), 1616-1626.

[11] N. Manago, K. Kuriyama, Y. Kaba, S. Miyazawa, H. Kuze, (2009): Analysis of skylight spectra for aerosol characterization and its application to multi-axis differential optical absorption spectroscopy.15th CEReS symposium P20

[12] N. Manago, H. Kuze, Determination of tropospheric aerosol characteristics by spectral measurements of solar radiation using a compact, stand-alone spectroradiometer. (submitted)

Study on microwave remote sensing applications to snow and ice monitoring for the winter road maintenance

Kohei OSA[1,2], Josaphat Tetuko Sri Sumantyo[1,3], Fumihiko Nishio[1,4]

[1]*Center for Environmental Remote Sensing, Chiba University,*
1-33 Yayoi-cho Inage-ku chiba-shi (Japan),
[2] *k-osa@faculty.chiba-u.jp,* [3] *jtetukoss@faculty.chiba-u.jp,* [4] *fnishio@faculty.chiba-u.jp*

Abstract

The purpose of this research program is to investigate and clarify the microwave response from snow and ice in order to apply the results to development microwave sensor for road-surface condition monitoring of winter road maintenance operation. This paper introduces the outline of this research program briefly and summarizes the dielectric measurement of snow, one of the topics of this research, which was conducted in this November.

Keywords **:** Microwave remote sensing, Winter road maintenance, Dielectric measurement of snow and ice

1. Introduction

In Japan, the road maintenance in winter is very important for the safety and the effectiveness of the traffic, because approximately half of the highways are located in the cold and snowy areas. The essential monitoring activities are namely road surface conditions monitoring, as well as the ice and snow cover monitoring.

By utilizing the remote sensing technologies, the information of the road surface conditions over a wide area can be obtained without having any staffs on the road locations. Furthermore, by investigating "transmission", one of the characteristics of the electromagnetic wave, internal conditions of snow cover, volume distribution, structures of layers and snow-buried road surface conditions can be monitored. Microwave sensor, with its "transmission" properties, will complement the optical sensor in foggy or snowy situations, and the combination of both sensors will create a more powerful system.

The purpose of this research program is to investigate and clarify the microwave response from snow and ice in order to apply the results to development of microwave sensor for the road-surface condition monitoring of winter road maintenance operations.

2. Outline of research program

This research program consists of the following topics.

1) Fundamental research on microwave response from snow and ice. (See section 3.)
2) Development of a microwave sensor system to detect the snow and ice on road surface.
3) Development of a SAR data processing method to detect the snow and ice on road surface.
4) Designing practical applications of remote sensing to the winter road maintenance operations.

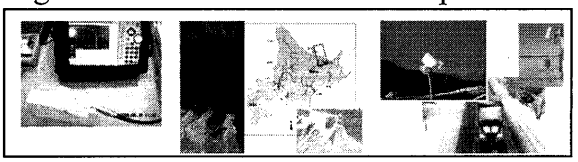

3. Topics: Dielectric measurements of snow with microwave free-space method

3.1. Introduction

To investigate the microwave response to snow, the dielectric measurements of snow by using microwave free-space method were conducted from 9th Nov. to 13th Nov. 2009 at the Snow and Ice Research Center (Shinjo, Yamagata), NIED. The measurements of artificial dry snow were made in the 4 to 6 GHz range. A linearly polarized wave obliquely incident on a surface was used. The incident angle of θ_i was 30 to 60 deg. Polarization mode were selected TE-mode and TM-mode. The temperature in the room was kept at -20C.

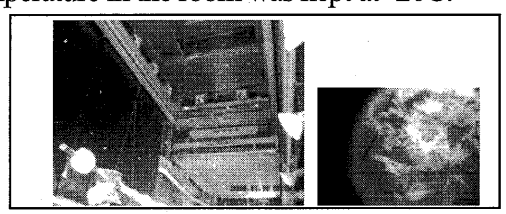

3.2. Methods

A permittivity value for a sample is estimated by comparing with the measured value of the reflection coefficient by network analyzer and the calculated value theoretically. The permittivity is the value which minimizes the delta calculated by following equation.

$$\Delta = \Sigma(\Gamma_{meas} - \Gamma(\varepsilon_r))^2 \qquad (1)$$

where Γ_{meas} is the measured value of reflection coefficient, Γ is the theoretical value and ε_r is the estimated value of permittivity of the snow sample.

This time, the reflection at upper surface of a sample is considered, and the theoretical value of the reflection coefficient is calculated the following equations.

The refection coefficient for TE-mode (HH) :

$$\Gamma_{TE} = \frac{cos\theta_i - \sqrt{\varepsilon_r - sin^2\theta_i}}{cos\theta_i + \sqrt{\varepsilon_r - sin^2\theta_i}}$$

The refection coefficient for TM-mode (VV) :

$$\Gamma_{TM} = \frac{\sqrt{\varepsilon_r - sin^2\theta_i} - \varepsilon_r cos\theta_i}{\sqrt{\varepsilon_r - sin^2\theta_i} + \varepsilon_r cos\theta_i}$$

where ε_r is relative permittivity of snow, θ_i is angle of incidence.

The density of sample was estimated by the following equation of an empirical model [1].

$$\varepsilon_r = \varepsilon'_r = 1.0 + 1.9\,\rho_s \quad \text{for } \rho_s < 0.5\ [g/cm^3] \quad (4)$$

where ε_r is relative permittivity of snow, ρ_s is density of snow [g/cm^3].

3.3. Measurement System

The measurement system consists of a network analyzer, by which reflection coefficients are measured as S11 and S11, and two antenna systems, horn antenna and dielectric lens, which emits microwave and receives. The block diagram of the system is shown in the following figure.

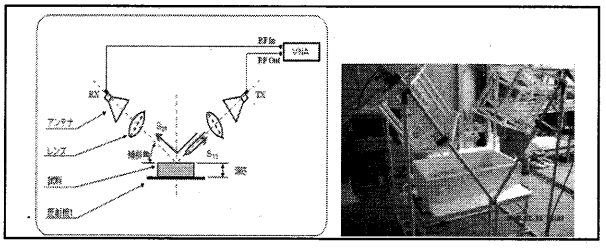

3.4. Example of measurement result

An example of the measurement result is shown in this section. The measured data of the reflection coefficients are shown in the following figure. Blue color means TE-mode and red means TH-mode. The dashed curves are theoretical values when the relative permittivity is 1.1 and the density of snow calculated by the empirical model is 0.053 [g/cm3]. It seems to give good estimation because that the average measured density of the sample was 0.065 [g/cm^3].

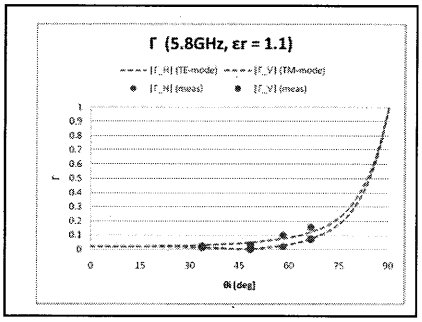

4. Conclusion

This year, the following items have been conducted:

1) A number of experimental researches on the characteristics of propagation and scattering of microwave against snow and ice, e.g. measurements of reflection from snow and ice.

2) The performance evaluations of the C-band antenna designed for the sensor.

3) Examination and discussion of the method (multi-polarization SAR) applied for detecting the snow and ice.

Acknowledgements

The authors would like to thank Dr. Kenji Kosugi, NIED, Ms Mayuko Yoshikawa, Chiba University, and Dr. Kazuhiro Naoki, JAXA, for their help with the measurements. The dielectric measurements of this project were conducted by a joint research with the Snow and Ice Research Center (Shinjo, Yamagata), NIED.

References

1) M.T. Hallikainen et al., "Dielectric Properties of Snow in the 3 to 37 GHz Range".

Estimation of percent tree cover in Eurasia using simulation data

Kobayashi Toshiyuki[1], Tsend-Ayush Javzandulam[2], Tateishi Ryutaro[3]

[1]*Graduate School of Science, Chiba University*

Tateishi laboratory, Geosystem and Biological Sciences Division, Graduate School of Science, Chiba University, 1-33 Yayoi-cho, Inage, Chiba 263-8522, Japan

E-mail: kobayashit@graduate.chiba-u.jp

[2]*School of Computer and Information Technology, Mongolian State University of Education*

[3]*Center for Environmental Remote Sensing, Chiba University*

Abstract

Global percent tree cover is an important parameter to understand global environment. It can be used for deriving carbon cycle models as one of the environmental parameters in it, deciding environmental policies and understanding the present environmental situation on school education. Some attempts to produce global percent tree cover maps have been made so far. But previous maps of global tree cover percentage are not so accurate. In this study, simulated training data were created by combining a lot of ground truth data consisting of various land cover types to improve the accuracy of the estimate of percent tree cover. QuickBird images and Google Earth images were used for getting training data. Percent tree cover was estimated by regression tree method using MODIS data.

Keywords **:** Global MODIS 2003 data, Google Earth, decision tree.

1. Introduction

Forests provide foundations for life on earth. They serve as habitats for it and regulate the climate and water resources. But they have recently been converted or degraded to unsustainable forms of land use, because of urbanization and deforestation by expanding human populations [1)2)]. Trees are important structural members of forests. They remove carbon dioxide from the atmosphere when they grow, and emit it when they decay or burn. Some attempts to produce global percent tree cover maps have been made so far [3)4)5)]. These maps can be used for deriving carbon cycle models as one of the environmental parameters in it, deciding environmental policies and understanding the present environmental situation on school education. However, these maps of global tree cover percentage produced by some organizations or researchers are not so accurate. The final goal of our study is to produce a precise global percent tree cover map in a certain year and to investigate the change of tree cover.

In this study, percent tree cover was estimated for some sites in Eurasia as a preliminary research. It was estimated by regression tree method using MODIS data. The original MODIS dataset (Global MODIS 2003 data processed by CEReS Chiba University [6)]) was converted into the annual predictor variables, such as yearly maximum band values, yearly maximum NDVI value and yearly average band values. The produced predictor variables were used for constructing regression tree model and estimating the percent tree cover. QuickBird images and Google Earth images were used for getting training data. Because the actual land covers are very complicated, various land cover types of training data are needed to make more precise estimate. For instance, cropland, urban area and many kinds of trees and soils are there in one pixel (1km x 1km). To deal with this problem, simulated training data were created by combining a lot of ground truth data.

The definition of "tree" and "percent tree cover (or tree canopy cover)" are a little bit different by the research [4)7)8)]. In botany, tree is defined from following aspects, that is, it is perennial or not, it has a self-supporting stem or not, the thickness of secondary tissues is increasing or not, it repeatedly flowers and fruits or not, the girth of its stem increases or not, or by height [9)10)]. But it is difficult to distinguish trees well by satellite remote sensing technique. In this study, the percent tree cover meant the percentage of the ground surface area covered by a vertical projection of the foliage and branches of trees at the time when trees have grown thick. Small openings inside the crown and small gaps between crowns are included. The definition of a tree is a woody perennial with a single self-supporting main stem, and its minimum height is approximately 3-6m. Trees for agricultural production or in gardens, and trees on

plantations are included. Bamboos were also included in trees.

2. Study area

In this study, percent tree cover was estimated for 9 areas in Eurasia. 7 areas were in Asia, which ranged from West Siberia to Indonesia, and 2 areas were in Europe, which were part of Iberia peninsula and part of Scandinavia peninsula (Fig. 1). These areas cover various land cover types from tropical zone to arctic zone. Training data were obtained from only 7 Asian areas to examine whether these training data were enough to estimate the tree cover percentage at global areas.

3. Data

3.1 MODIS data

Global MODIS 2003 data processed by CEReS Chiba University were used for estimation of percent tree cover. The summary of this dataset is given in Table 1. This dataset was made from MODIS/TERRA Nadir BRDF-Adjusted Reflectance 16-day L3 Global 1km SIN grid product (MOD43B4 NBAR) [11)12)]. This product is corrected surface reflectance to a nadir view geometry at the mean solar zenith angle during the observation period using BRDF model. It is a product of 16-day composites. It was mosaicked and re-projected to geographic map projection at CEReS, Chiba University. Furthermore cloud-contaminated pixels were linearly interpolated using 2002 and 2004 data to make it cloud-free.

Table 1 Summary of global MODIS 2003 data processed by CEReS Chiba University

Spatial resolution	Temporal resolution	Spectral bands
32.3748 seconds	16 days	Band1-Band7

3.2 Google Earth imagery

Google Earth™ images were used for producing training data set and validating the result. Training data were collected from only the areas where percent tree cover was almost 100% or 0% because it was difficult to estimate the true percentage of tree cover from Google Earth™ images. They were obtained to include various land cover types from tropical zone to arctic zone (Fig. 2, Table 2). Training data of percent tree cover from 0% to 100% were produced by simulation using linear equation.

Google Earth™ images have some problem for science. One of the problems of the use of Google Earth™ images is that they might be intentionally falsified. To partially deal with this problem, all collected training data were checked by comparing with MODIS 2003 data.

3.3 QuickBird imagery

Six pan-sharpened QuickBird images were also acquired for use in validating the result. Percent tree cover of those images was estimated by unsupervised clustering. In case the estimation result was not good, on-screen digitizing method, which was manual extraction of trees according to visual interpretation, was performed.

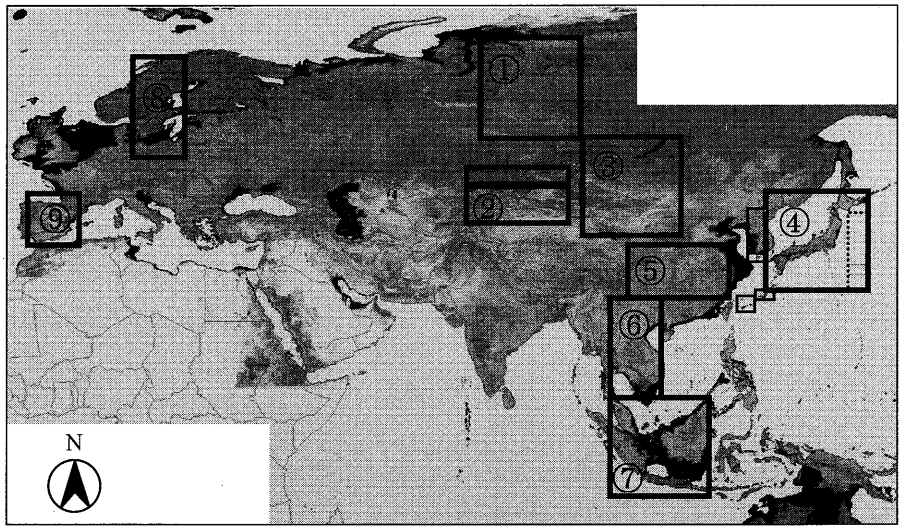

Fig. 1. Location map of the study area. Boxes represent areas where percent tree cover were estimated in this study.

Table 2 Site locations and the number of collected training sites, and their dominant land cover types. The "Area" corresponds to that of Fig. 2.

Area	Number of collected training sites		
	Forests	Grasslands or agricultural areas	Urban and bare areas
West Siberia	19	40	7
Around Kazakhstan	1	10	3
Around Mongol	3	5	10
Japan and Korea	25	18	8
China	4	11	2
Indochina peninsula	6	12	1
Indonesia and Malaya	6	11	2

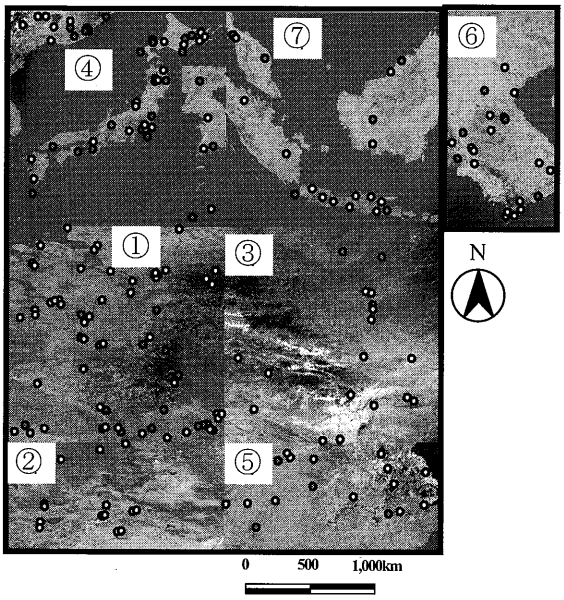

①West Siberia ②Around Kazakhstan ③Around Mongol
④Japan and Korea ⑤China ⑥Indochina peninsula
⑦Indonesia and Malaya

Fig. 2. Distribution of collected training sites.

4. Methods

4.1 Creation of simulated training data

Training data ranging from 0% to 100% in tree cover percentage were created by the equation:

$$S_i = \sum_{j=1}^{n} a_j V_{ij} \quad (1)$$

where S_i is simulated MODIS 2003 value of band i, V_{ij} is original MODIS 2003 value of band i at collected ground truth site j, and a_j is area ratio of site j. S_i was calculated at 5% intervals of a_j.

204 training data in total collected from Google Earth™ images were grouped into 53 types, according to its area, land cover type and predictor variables. S_i was calculated for combinations of these groups. In this study, impossible combinations, for example combination of forest in Siberia and grassland in Indonesia, were not considered.

4.2 Predictor variables

The selection of predictor variables to estimate percent tree cover is difficult for estimating percent tree cover using regression tree method. In previous researches, a lot of annual variables were used such as maximum value of NDVI (normalized difference vegetation index), average band 1-7 reflectance at three or seven highest NDVI periods, minimum band 1 reflectance, maximum band 2 reflectance, average reflectance in four darkest reflectance periods and amplitude for minimum and maximum reflectance [4)5)13)]. The best variables were selected among them.

In this study, MODIS 2003 values in whole study area and simulated training data were converted to only 10 predictor variables. They were average NDVI value at periods with three highest NDVI values from period 9 to 18, average band 1-7 values at periods with three highest NDVI values from period 9 to 18 and minimum NDSI (normalized difference soil index) value and average SI (shadow index) value at periods with three highest NDVI values from period 9 to 18. *NDVI*, *NDSI* and *SI*[14)] were calculated from equations:

$$NDVI = \frac{band2 - band1}{band2 + band1}, \quad (2)$$

$$NDSI = \frac{band6 - band2}{band6 + band2}, \quad (3)$$

and

$$SI = \{(band1_{\max} - band1) \times (band3_{\max} - band3) \times (band4_{\max} - band4)\}^{1/3} \quad (4)$$

where *band i* is MODIS 2003 reflectance of band *i* and *band i* $_{\max}$ is maximum band *i* reflectance in the images.

4.3 Decision tree model

Regression tree analysis is used well for estimating percent tree cover. In this study, regression tree models were produced from predictor variables made from simulated training data using Cubist, which is a commercial software for constructing regression tree model by RuleQuest Research Pty. The models were constructed to minimize the number of rules unless the mean absolute error on training data was larger than 5%, in order to avoid overfitting the data and keep the stability of constructed models. Band 3, band 4 and SI of predictor variables were used only in case the mean absolute error of constructed model on training data was larger than 5%, because these bands had some noises in the images.

4.4 Estimation of percent tree cover

Percent tree cover was estimated pixel by pixel. Regression tree models to apply to each pixel were chosen by comparing predictor variables of the pixel and unbiased estimator of mean value and standard deviation of predictor variables on grouped training data. The average percentage among tree models to fit each pixel was adopted as its estimated percent tree cover.

4.5 Refinement of percent tree cover estimation

There were some cases where trees could not be clearly distinguished from grasses or agricultural areas. For this reason, new decision tree models were created using MOSIS 2003 band reflectance and NDVI values of 23 periods directly as predictor variables. In these models, only pixels fitted to seasonal changes of training data were chosen for tree cover estimation. The accuracy of these new models was higher, but pixels to fit with these models were fewer.

5. Results

The percent tree cover map created on this study is shown in Fig. 3. The mean absolute error compared with validation data in 71 Asian sites was 10%, and that in 24 European sites was 19% (Fig. 4).

6. Discussions

The accuracy of the estimation improved by the use of simulated training data with the mean absolute error of 10%. But the majority of improvement was in areas where training data were collected. In areas where training data were not collected, the number of pixels whose absolute error was larger than 30% became smaller, though mean absolute error was not improved. The areas where the estimation result was bad were the south of Vietnam and high latitude areas. One of the reasons is that agricultural fields in Southeast Asia consist of a lot of types in intensity and cropping season. Another reason is that we did not use any training data in water area.

These results suggest that we have to collect more training data throughout continental or global area for estimating the tree cover percentage in global or continental scale. More accurate validation and the comparison with previous researches will be necessary.

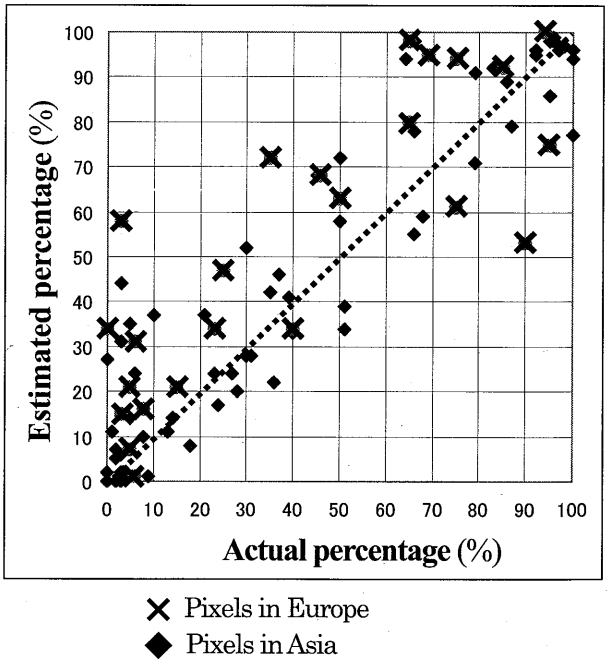

Fig. 4 Comparison between estimated tree cover percentage and the actual percentage extracted from Google Earth™ images and QuickBird images. The mean absolute error of the estimated percentage in Asia and Europe was 10% and 19% respectively.

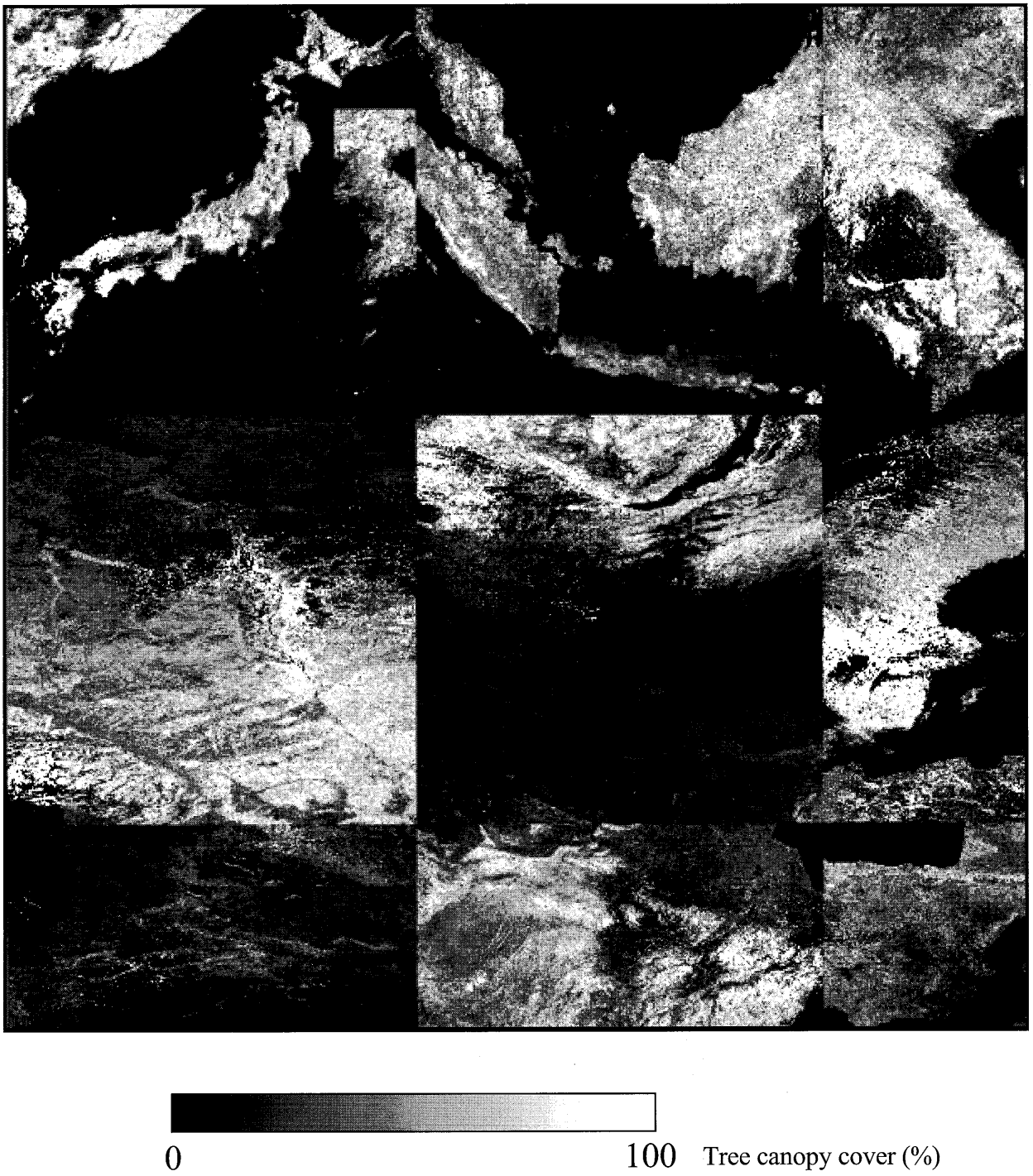

Fig. 3 Percent tree cover estimation map for this study area. This map was produced by regression tree method using MODIS data. Training data were created by simulation to combine a lot of ground truth data consisting of various land cover types.

References

1) FAO (Food and Agriculture Organization of the United Nations), 2000. FRA 2000 on definitions of forest and forest change, Forest Resources Assessment Working Paper 33. Rome, FAO, (14 pp.).

2) FAO (Food and Agriculture Organization of the United Nations), 2001. Global forest resources assessment 2000 Main report. Rome, FAO, (512 pp.).

3) Defries, R. S., Hansen, M.C., and Townshend, J. R. G., 2000. Global continuous fields of vegetation characteristics: a linear mixture model applied to multi-year 8km AVHRR data. *International Journal of Remote Sensing*, 21, 6-7, 1389-1414.

4) Hansen, M. C., Defries, R. S., Townshend, J. R. G., Carroll, M., Dimiceli, C., and Sohlberg, R. A., 2003. Global Percent Tree Cover at a Spatial Resolution of 500 Meters: First Results of the MODIS Vegetation Continuous Fields Algorithm. *Earth Interactions*, 7, 10, 1-15.

5) Rokhmatuloh, Nitto D., Al-Bilbisi, H., Arihara, K., and Tateishi, R., 2007. Estimating percent tree cover using regression tree method with very-high-resolution QuickBird images as training data. *Journal of the remote sensing society of Japan*, 27, 1, 1-12.

6) Al-Bilbisi, H., and Tateishi, R., 2007. Global MODIS 2003 data Version 3. Chiba Unversity, (122 pp.).

7) FAO (Food and Agriculture Organization of the United Nations), 2004. Global forest resources Assessment update 2005 Terms and definitions, Forest Resources Assessment Working Paper 83. Rome, FAO, (35 pp.).

8) Heiskanen, and Kivinen, S., 2008. Assessment of multispectral, –temporal and –angular MODIS data for tree cover mapping in the tundra-taiga transition zone. *Remote Sensing of Environment*, 112, 2367-2380.

9) Thomas, P., 2000. Trees: Their natural history. Cambridge Unversity press, (286 pp.).

10) Rushforth, K., 1999. Trees of Britain and Europe. Collins.

11) Strahler, A. H., Muller, J. P., and MODIS Science Team Members, 1999. MODIS BRDF/Albedo Product: Algorithm Theoretical Basis Document Version 5.0. Bostpn Unversity, (53 pp.).

12) MODIS BRDF/Albedo Product (MOD43B) User's Guide. Available online at: http://www-modis.bu.edu/brdf/userguide/intro.html (accessed November 2009).

13) Hansen, M. C., Defries, R. S., Townshend, J. R. G., Sohlberg, R., Dimiceli, C., and Carroll, M., 2002. Towards an operational MODIS continuous field of percent tree cover algorithm: examples using AVHRR and MODIS data. *Remote Sensing of Environment*, 83, 303-319.

14) Rikimaru, A., Roy, P. S., and Miyatake, S., 2002. Tropical forest cover density mapping. *Tropical Ecology*, 43, 1, 39-47.

Improving Tropical Forest Mapping using Combination of Optical and Microwave Data of ALOS

Nguyen Thanh Hoan, Ryutaro Tateishi

Tateishi-Lab., Centre for Environmental Remote Sensing (CEReS), Chiba University,
1-33 Yayoi-cho, Inage-ku, Chiba, 263-6522, Japan
Email: hoanrs@gmail.com

Abstract

Optical remote sensing usually has not enough multi-temporal high resolution images to describe phenology of objects for forest mapping in local scale. This paper presents a possibility to improve accuracy of tropical forest mapping by combination of optical and microwave images. Study area is located in the southern part of Vietnam. The first, ALOS/AVNIR-2 images were used to create the forest map, then ALOS/PALSAR single-polarized and dual-polarized images were used to improve the accuracy of the classification result by a combination model. ALOS/PRISM images were also used to make Pan-sharpen images for collecting training data and validation data. Discrimination of Planted Forest and Natural Forest is one of the most important purposes of this study. The overall accuracy of ALOS/AVNIR-2 classification result is 77.0%, while after combining with ALOS/PALSAR, it is increased up to 88.2%. The accuracy is higher than 90% for main forest classes.

Keywords **:** ALOS/AVNIR-2, ALOS/PALSAR, Combination model, Planted Forest, Natural Forest

1. Introduction

Tropical forests cover large parts of the Earth's land surface. These forests hold an enormous biodiversity, and they are disappearing at an alarming rate (Nugroho 2006). Deforestation is occurring at an alarming rate in developing countries, which are the main location of tropical forests. For example, according to 2005 report conducted by the Food and Agriculture Organization of the United Nations (FAO), Vietnam has the second highest rate of deforestation of primary forests in the world, second only to Nigeria (Butler and Rhett 2005). Meanwhile, forest mapping in the developing countries like Vietnam has many problems. The most recent official forest map of Vietnam is the Vietnam Forest map 2005. This map was produced for the Ministry of Resource and Environment by the Forest Inventory and Planning Institute (FIPI) of Vietnam in 2008 using Landsat ETM+ images 2005. However, this map includes many mistakes that are easy to find by visually.

Monitoring tropical forest frequently on the ground is very difficult related to its existence in the complex terrains, large areas. Therefore, remote sensing images have been widely applied as an important tool for mapping and monitoring tropical forest. Forest mapping by remote sensing data already has been known by many programs that cover global scale, such as FRA 2000 by FAO using SPOT Vegetation data, Global Forest Mapping (GRFM/GBFM) Program by JAXA using JERS-1 SAR data and others. Moreover, the broad categories mapped by these programs fail to deliver valuable and useful information on the variation within the tropical forest environment (Tottrup 2004). Many other studies of forest mapping using high resolution images have been presented in several works, some of them used multi-temporal optical images (Rahman et al. 2005, Tottrup 2004, Foody et al. 2003, Helmer et al. 2000). But, collecting good multi-temporal images of high-resolution satellites for tropical regions in one year cycle is very difficult or impossible because of the presence of the cloud and long repeat cycle of satellites. E.g. of using microwave data for forest mapping (Almeida-Filho et al. 2009, Ling et al. 2008, Cloude et al. 2007, Fransson et al. 2007, Sgrenzaroli et al. 2002, Takeuchi et al., 2000), microwave data can be used to analyze some characters of forest, specially that microwave data is very useful for studies about forest cover change detection and forest fire, due to its effective characteristics that can penetrate the surface in different conditions of the weather. In spite of that using only microwave data to make a complete forest map has many limitations. The principal uses of radar will be to map forest structure and moisture, this information is largely complementary to that obtained by optical techniques (Dobson and Craig 2000). However, the studies about combination of optical and radar images for forest mapping is not so many, some of them about using synergism of SAR and optical data for land use classification, including some forest types in categories table with limited number of forest classes (Kuplich 2000, Juha et al. 2000).

ALOS satellite of Japan was launched successfully on

January 24 2006. It has both microwave and optical sensor. With high resolution (~10m), this data will be very useful for land studies including forest studies in local scale. The study of combination between optical and microwave data also becomes more feasible. Therefore, this study presents a possibility to improve accuracy of tropical forest mapping by combination of optical and microwave images of ALOS. To support for managing reforestation activities and preserving existing natural forest, discrimination of Planted Forest and Natural Forest is one of the most important purposes of this study. This study will not discuss biomass estimation and wood volume estimation, due to the lack of ground truth measurement data.

2. Data acquisition

The study area of this study is located in the southern part of Vietnam. It is covered fully by four scenes of ALOS/AVNIR-2 or six scenes of ALOS/PALSAR. The ALOS/PALSAR single-polarized images were selected closest to ALOS/AVNIR-2 images as possible about time (there are no dual-polarized images around that time). This selection can reduce effects of land cover change when combine them together to remove clouds (Hoan and Tateishi 2009) and to separate between forests and growing paddy/croplands. Table 1 shows the information of data acquisition used in this study.

Table 1. Information of data acquisition

Data names	Information	Spatial resolution
ALOS/AVNIR-2	Four images, date 2007/01/19, 2007/01/19, 2008/02/05, 2007/02/05	10m
ALOS/PRISM	Three images in date 2009/03/28, 2009/03/31, 2009/03/31	2.5m
ALOS/PALSAR single-polarization	Six images, three images in date 2007/06/20, the others in date 2007/02/19	6.25m
ALOS/PALSAR dual-polarization	Six images, three images in date 2007/06/20 and the others in date 2007/07/07	12.5m
Vietnam forest map 2005	Produced in 2008 by Forest Inventory and Planning Institute of Vietnam using Lansat ETM+ images in 2005	50m
Local topographic map 2005	Nine pieces in vector format, scale 1:50.000	

3. Methodology

In whole the 2007 year, only one-time good quality images of ALOS/AVNIR-2 were found in the study area. These images are not enough to describe phenology of land cover objects for forest mapping. They cannot separate between forests and growing paddy/croplands and others. This section will present a method for combination of single-temporal ALOS/AVNIR-2 images and multi-temporal ALOS/PALSAR images for tropical forest mapping.

3.1. Forest classes definition

The forest classes were mainly determined after visual interpretation of the ALOS/PRISM sharpen image, 2.5m spatial resolution. In addition, other concerned documents were used as references including: National Forest Inventory - Field Manual (FAO 2004), Vegetation and Special Vegetation of Forest (Vietnamese, Chan and Dung 1992), and the Vietnam Forest Map 2005. The initial number of categories visually discriminated was 16, but some classes were found very similar in digital processing products (by unsupervised classification - Kmean method). Finally, 11 classes were used for tropical forest classification in the study area, in which, there are 5 classes of forest as shown in Table 2.

Table 2: Legend table for tropical forest mapping of the study area in southern part of Vietnam

Class name	Color (R, G, B)
1. Primary forest	(0,60,0)
2. Degraded forest	(60,160,0)
3. Bamboo	(230,230,0)
4. Mixed forest	(0,120,0)
5. Planted forest	(60,190,130)
6. Shrub & Grass	(255,127,80)
7. Mosaic	(130,130,70)
8. Paddy/Cropland	(120,70,130)
9. Built-up	(200,0,0)
10. Wetland	(100,100,200)
11. Water	(0,100,250)

3.2. ALOS/AVNIR-2 classification

In normal, forest mapping and land cover mapping from remote sensing images are usually performed using either supervised or unsupervised techniques. In classification, there are two types of classes that need to be distinguished: user classes and spectral classes. User classes are those categories of interest that the analysis is actually trying to identify in the imagery. In contrast spectral classes are groups of pixels that are uniform with respect to their brightness values in the different spectral channels of the data. Actually, rarely there is a simple one-to-one match between these two types of classes. Spectral classes are always more detail than user classes. In this study, to determine ability of ALOS/AVNIR-2 images in tropical forest mapping, all main spectral classes were used as training data to estimate user classes. The first step, unsupervised classification

(K_mean) method was used to divide image to 60 spectral classes. Each class of the spectral classes was compared with PRISM-sharpen image and other reference data like local forest map 2005 and Tree-Height map to determine that belong in which user class name. Only main spectral classes that are easy to determine user class name and cover large areas were used. Subsequently, 30 spectral classes were already chosen.

One of the most important purposes of this study is to discriminate planted forest and natural forest. However, clustering spectral classes of ALOS/AVNIR-2 image using K_mean method was not successful for this purpose. Thus, discrimination will be tried one more time by supervised techniques. To separate planted forest and natural forest in training data, one simple mask was drawn manually for the main locations of natural forest. All planted forests inside of this mask were deleted while natural forests outside of this mask were converted to a new planted forest class. Single pixel is usually error of classification result. In this study, every single pixels in training data were removed. Therefore, total of 31 classes were used as training data for supervised classification by Maximum Likelihood (ML) method to represent for 9 user classes as shown in Table 2 without paddy/cropland and built-up area. Because paddy/cropland and built-up area are confused totally with forests and other land cover types in ALOS/AVNIR-2 image, so they have no training data for supervised classification, they will be estimated later by ALOS/PALSAR data.

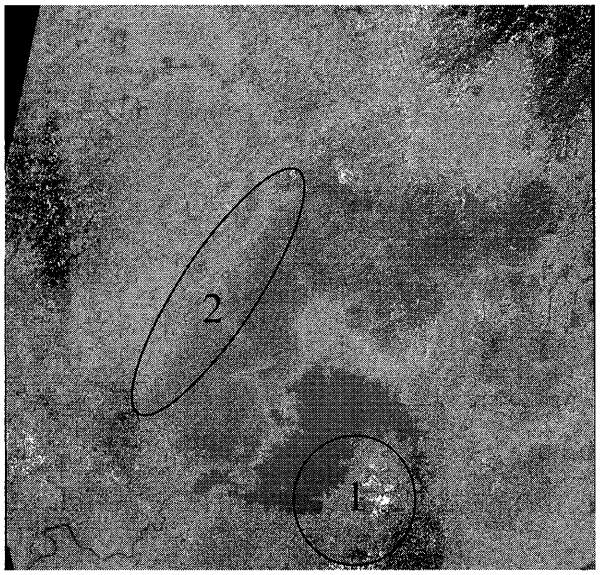

Figure 1: ML classification result of ALOS/AVNIR-2

Figure 1 shows some examples that Maximum Likelihood method also cannot discriminate between planted forest and natural forest from the ALOS/AVNIR-2 image. The region (1) is a location of planted forests but there are many natural forests in the classification result. On the other hand in the region (2), many natural forests was misclassified to planted forest.

The observed time of the ALOS/AVNIR-2 images is in the growing season of paddy/croplands in the study area. The single-temporal ALOS/AVNIR-2 image also cannot separate between forests and growing paddy/croplands as shown in Figure 2.

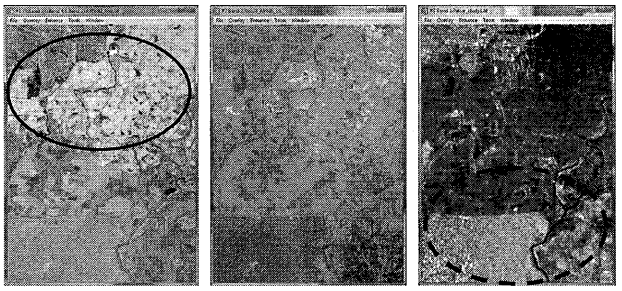

(*a*) (*b*) (*c*)

Figure 2. Confusion of paddy/croplands and forests in AVNIR-2 classification result, but that can be separated clearly in PALSAR visually, (*a*) AVNIR-2 image (R-red, G-NIR, B-green), (*b*) classification result, and (*c*) PALSAR image

In Figure 2( ), the black ellipse is a place of paddy/cropland, but in the classification result from ALOS/AVNIR-2 (figure 2(*b*)), the paddy/cropland almost was misclassified to planted forest, bamboo or other forest types. At the same time in figure 2(*c*), the black ellipse (dashed line) is location of forests in PALSAR image, they are easy to be separated with the paddy/cropland area in the radar image by visually. In addition, some other land cover types like built-up area also cannot be discriminated from others by ALOS/VNIR-2 image, but it can be separated easily by ALOS/PALSAR image.

From the analyses above, it can be concluded that using ALOS/AVNIR-2 image (single-temporal) cannot separate between planted forest and natural forest, between forest and growing paddy/cropland, between built-up area and some other land cover types. ALOS/PALSAR data will be used to solve these problems.

3.3. ALOS/PALSAR analysis

The interest in using radar remote sensing for monitoring forest cover raises from the two assets of radar data. The first, radar can provide information related to the canopy volume, which cannot be collected by other means. The other advantage of radars is the possibility to acquire data over areas with frequent cloud or haze coverage as tropical regions (Toan et al. 2001). In this study, radar data was used for two main purposes: the first one is to separate forests and growing paddy/cropland that cannot be separated by single-temporal optical image; and the second one is to discriminate planted forest and natural forest by analyzing structure of forest.

According to Alvin Wong (Wong et al. 1997), there are four

main scattering mechanisms of radar including: "Smooth Surface", "Rough Surface", "Double-bounce" and "Vegetation Layers". Where, backscatter in the scattering mechanism of "Smooth Surface" is the weakest and backscatter in the scattering mechanism of "Double-bounce" is the strongest. These scattering mechanisms will be used to analyze the differences of the interested objects in the next sections.

3.3.1. Discrimination of planted forest and natural forest

The main difference of tropical planted forest and tropical natural forest is their structure. Tropical planted forest normally has only one layer of wood tree and the density of the tree is not very high. Conversely tropical natural forest always has more than one layer of wood tree, density of the tree is usually very high and there are many branches and lianas. According to Thuy Le Toan (Toan et al. 2001), main scatterers of tropical natural forest are shown in table 3.

Table 3. Main scatterers of tropical natural forest

Frequency band	X	C	L	P	VHF
Main scatterers	Leaves, Twigs	Leaves, Small branches	Branches	Branches & Trunk	Trunk

Using ALOS/PALSAR (L-band), in forest, the scattering is affected mainly by branches of tree. Meanwhile, number of branches is one of the main differences between tropical planted forest and tropical natural forest. It means that tropical planted forest and tropical natural forest can be discriminated together by ALOS/PALSAR images in theory.

Based on the scattering mechanisms, backscatter of tropical natural forest with many branches and lianas is affected mainly by the scattering mechanism of "Vegetation Layer". Backscatter of tropical planted forest should be stronger with a significant amount of the "Double-bounce" scattering mechanism, because some radar signals can go through the forest canopy to ground and be affected by backscatter of ground and trunks.

In ALOS images, differences of planted forest and natural forest are shown in Figure 3.

AVNIR-2 PALSAR - HH PALSAR - HV

Figure 3: Differences of natural forest and planted forest in ALOS images: region (1) is natural forests, region (2) is planted forests

Planted forest and natural forest cannot be separated in AVNIR-2 images, but boundary of them can be determined in PALSAR images visually. Natural forest looks darker and planted forest looks lighter. The boundary of them in HH polarization image is clearer than in HV polarization image (Figure 3). In this study, both polarization HH and HV were used to separate between planted forest and natural forest.

When planted forest or natural forest areas in PALSAR images are zoomed in, they are become visible not homogeneous regions. They are mixtures of many different dots (pixels), in that case, darker dots (for natural forest) or lighter dots (for planted forest) is dominated. Consequently, these images cannot be used to classify forest types directly. To solve this problem, one filtering method is necessary to get mean values of objects and at the same time, still keep their boundaries well as possible. FROST filtering method - the best suitable -, window size 15x15 was chosen (Lopes et al. 1993, Zhenghao and Fung 1994). Then, the dual-polarized image (including HH and HV) of PALSAR was classified by unsupervised classification Kmean method to 20 classes. These classes were labeled to two user classes: natural forest and others. After that, every natural forest region that is smaller than 500 pixels (~5 hectares) was deleted. Finally, natural forest mask was completed as shown in Figure 4.

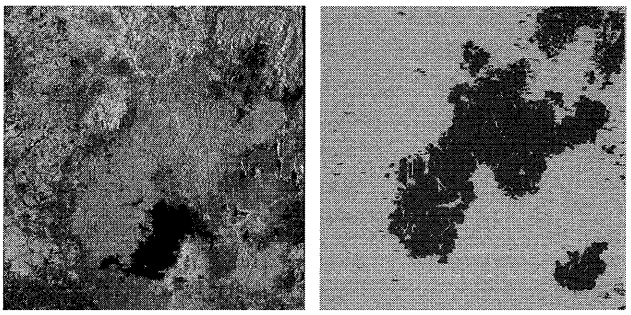

Figure 4. Natural forest mask (right) derived from ALOS/PALSAR dual-polarized images (right), color composite: R-HH, G-HV, B-HH

The mistakes of planted forest and natural forest as mentioned in Figure 1 do not appeared in the natural forest mask. This mask will be used in combination model to make final tropical forest map in the next section.

3.3.2. Discrimination of forests and growing paddy/croplands

ALOS/PALSAR is SAR of L band, long wavelength. Paddy/cropland is considered like quite smooth surface by L band SAR in any season (Ishitsuka 2007), in this case backscatter of paddy/cropland is almost affected by the "Smooth surface" scattering mechanism. This reason is due to the weakness of backscattering of paddy/croplands in ALOS/PALSAR images. Backscatters of forests are in "Vegetation Layer" and "Double-bounce" scattering

mechanisms as presented in the section 3.3.1. Therefore, backscatters of forests should be higher than that of paddy/croplands. In this study, ALOS/PALSAR single-polarized (HH) images were used to extract the paddy/cropland mask because the observed time of the single-polarized images are close to the received optical images and also it is enough to separate between forests and paddy/croplands. Level slicing method was applied to divide the PALSAR images to four layers. The built-up class is also one of them. Final result is shown in Figure 5, where, blue color is water and no-data, green-yellow color is paddy/croplands, red color is built-up area and grey color is other.

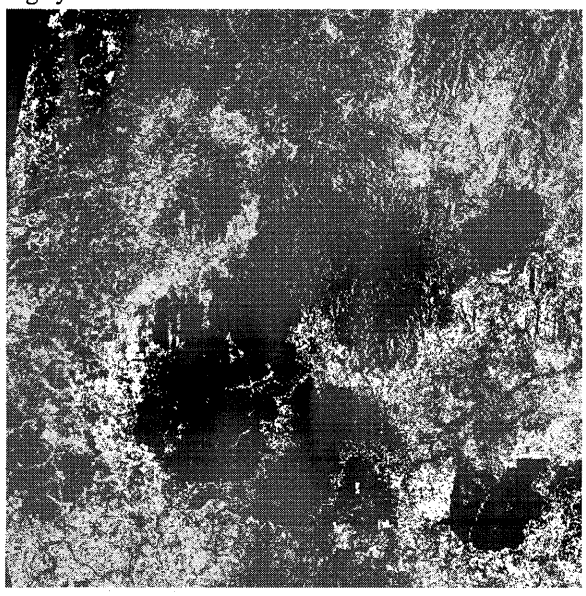

Figure 5. Paddy/Cropland mask and Built-up derived from ALOS/PALSAS single HH polarization images

The paddy/cropland and built-up layers will be used as masks in the combination model to make final forest map.

3.4. Combination model

The result classified from ALOS/AVNIR-2 images was used as a background image to combine with the natural forest mask, paddy/cropland mask and built-up mask derived from ALOS/PALSAR images for producing the final tropical forest map. This combination was summarized in one combination model as shown in Figure 6.

According to Feilong Ling (Ling et al. 2008), multi-temporal ALOS/PALSAR dual-polarization data can create accurate maps for forest in flat areas. The capability to map forest in hilly regions is still limited. Furthermore, the analyses in this study showed a similar result. Therefore, the slope map developed from DEM 10m resolution was used to remove high slope areas. In this model, the areas that have slope higher than 10° will be kept as ALOS/AVNIR-2 classification result.

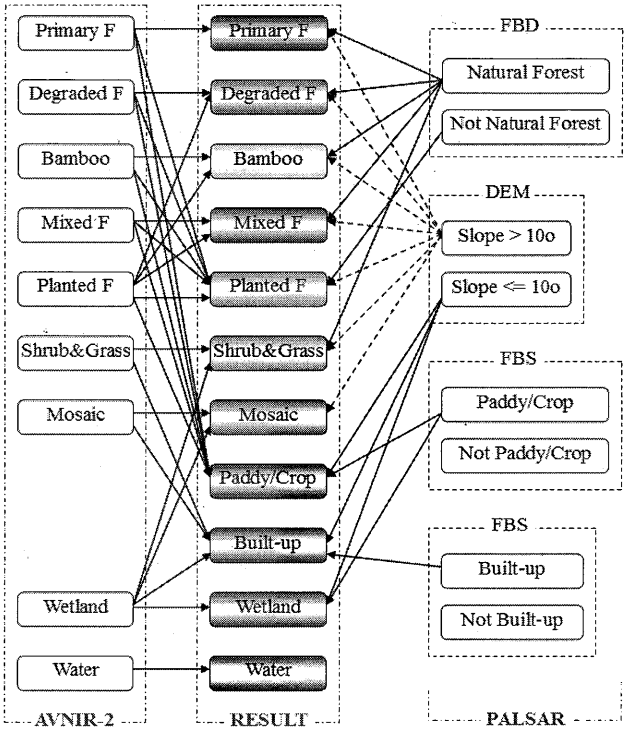

Figure 6. The combination model of ALOS/AVNIR-2 and ALOS/PALSAR images for tropical forest mapping

In Figure 6, the continuous vectors present for AND condition. That means, the parameters at begin of the vectors will be used AND function to combine with other parameters. The dashed vectors present for OR condition. The parameters at begin of the vectors will be used OR function to combine with other parameters. The dashed vectors will be used in direct conversions only. That means, the parameters at begin of the vectors will be used to combine with other parameters only when destination has the same class name with original class, e.g. converting from Primary F of AVNIR-2 box to Primary F of RESULT box, from Bamboo of AVNIR-2 box to Bamboo of RESULT box, and so on.

One example to explain the combination model, from original Primary Forest as shown in the box of AVNIR-2 will have three destinations presented in the RESULT box: to Primary F when the pixel is in natural forest mask OR slope is higher than 10°; to Planted F when the pixel is not in natural forest mask; and to Paddy/Crop when the pixel is in paddy/crop mask AND slope is lower or equal 10°. The order of priority functions is from up to down. Other classes were done by similar ways. Figure 7 shows the final tropical forest map.

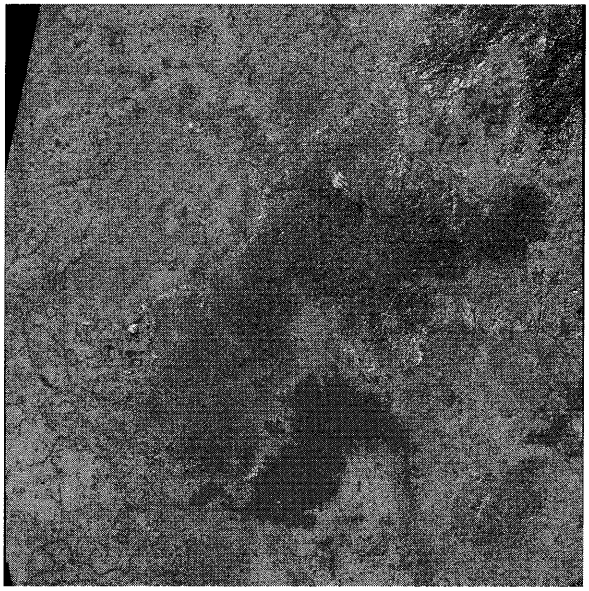

Figure 7. The final tropical forest map 2007

4. Validation and Discussions

Accuracy assessment always is an important step of forest mapping to verify the quality of information that resultant from remotely sensed data. In this study, 330 random points were selected by PCI software version 9.1 to validate for 11 classes of the categories, averagely, 30 random points for one class. The distribution of these points was shown in Figure 8.

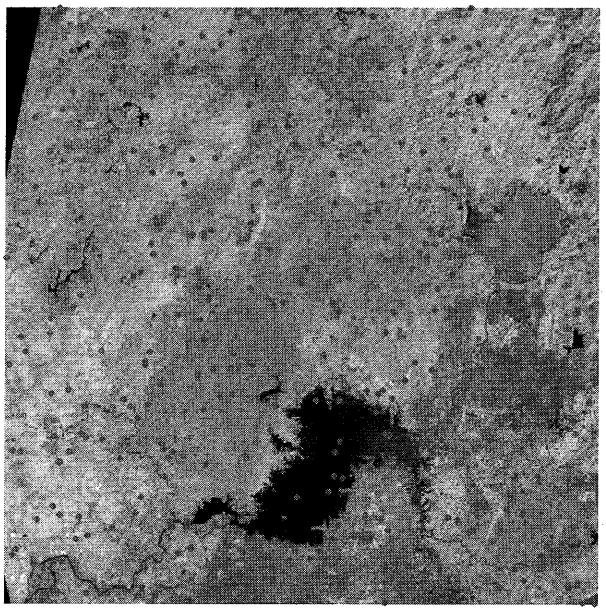

Figure 8. Distribution of 330 random points for validation

Currently, the random points are in vector format, but the required database is polygons that cover pixel by pixel of the final tropical forest map. To build this database, the first, the random points were converted to raster pixels based on the pixel size and image size of the final tropical forest map. Then, these raster pixels were converted again to polygons in vector format.

To set the attributes for the polygons of database, each random point (pixel) was compared carefully with PRISM-sharpen image and some other maps like local forest map 2005 and Tree-Height map to determine class name which was already mentioned in the categories (Table 2). This work was done independently with classification steps. This validation database was used to assess accuracy for both classification result derived from ALOS/AVNIR-2 image and the final combination result.

To imagine the difference easily, user's accuracy and producer's accuracy of the classification result derived from ALOS/AVNIR-2 images and the combination result were compared together in Table 4 and Table 5.

Table 4. Comparison table of User's accuracy before and after combining with PALSAR

Class name	AVNIR-2 only	AVNIR-2 + PALSAR
[1] Primary forest	91.7%	91.7%
[2] Degraded Forest	78.7%	88.4%
[3] Bamboo	50.0%	72.7%
[4] Mixed forest	86.2%	87.5%
[5] Planted forest	72.0%	91.7%
[6] Shrub & Grass	87.8%	91.5%
[7] Mosaic	81.6%	84.2%
[8] Paddy & Crop	0.0%	81.3%
[9] Built-up	0.0%	100.0%
[10] Wetland	27.8%	62.5%
[11] Water	100.0%	100.0%

Table 5. Comparison table of Producer's accuracy before and after combining with PALSAR

Class name	AVNIR-2 only	AVNIR-2 + PALSAR
[1] Primary forest	78.6%	78.6%
[2] Degraded Forest	90.2%	92.7%
[3] Bamboo	50.0%	80.0%
[4] Mixed forest	69.4%	77.8%
[5] Planted forest	88.9%	95.1%
[6] Shrub & Grass	86.0%	86.0%
[7] Mosaic	69.0%	82.8%
[8] Paddy & Crop	0.0%	86.7%
[9] Built-up	0.0%	100.0%
[10] Wetland	100.0%	100.0%
[11] Water	100.0%	100.0%

The results showed that the overall accuracy before combination is 77.0%, after combination overall accuracy is increased up to 88.2%.

Planted forest almost has only one layer of wood tree and it looks smooth in ALOS/AVNIR-2 images, also Bamboo has only one layer, and it looks smooth and light in ALOS/AVNIR-2 images. Actually, planted forest and bamboo are confused together totally in optical data. That is why the accuracy of

bamboo is increased more than that of other forest classes after combination, from 50% to 72.7% for user's accuracy and from 50% to 80% for producer's accuracy. Outside of confused with bamboo, planted forest is also confused very much with other types of forest like degraded forest and mixed forest. In addition, many paddy/cropland fields become planted forest in ALOS/AVNIR-2 classification result. Therefore, accuracy of planted forest also increased much after combination, from 72% to 91.7% for user's accuracy and from 88.9% to 95.1% for producer's accuracy. Accuracies of paddy/cropland and built-up increased very much because they have no training data for ALOS/AVNIR-2 classification. Final accuracies of built-up area and wetland maybe not correct because number of validation points distributed in these classes is very few, only 4 points for built-up and 5 points for wetland. Any way, this problem doesn't affect so much to purpose of this study.

Primary forest, degraded forest and mixed forest are natural forest, which are usually confused together. Some time, it is very difficult to separate between of them even by visual interpretation using very high resolution images like PRISM sharpen images. For forest management purposes, they could be merged together to become one natural forest class only. In this case, error matrices of main forest classes are shown in Table 6 and Table 7.

Table 6. Error matrix of main forest classes before combining with PALSAR

	Reference data				
Classified	Natural forest	Planted forest	Bamboo	Total	User's accuracy
Natural forest	81	5	2	88	92.0%
Planted forest	7	72	3	100	72.0%
Bamboo	3	2	5	10	50.0%
Total	91	81	10	182	
Producer's Accuracy	89.0%	88.9%	50.0%		

Overall accuracy of the main forest classes before combination is 86.8%.

Table 7. Error matrix of main forest classes after combining with PALSAR

	Reference data				
Classified	Natural forest	Planted forest	Bamboo	Total	User's accuracy
Natural forest	87	0	0	87	100.0%
Planted forest	0	77	2	84	91.7%
Bamboo	2	0	8	11	72.7%
Total	91	81	10	182	
Producer's Accuracy	95.6%	95.1%	80.0%		

Overall accuracy of the main forest classes after combination is 94.5%.

Accuracies of natural forest and planted forest become very high after combination. That means, combination of ALOS/AVNIR-2 and ALOS/PALSAR images in order to separate between natural forest and planted forest shows a good result, in the other hand ALOS/AVNIR-2 image has some limitations in discrimination of primary forest, degraded forest and mixed forest together. The accuracy of bamboo is still not high after combination. Actually, bamboo includes natural bamboo and planted bamboo, but they are almost similar together. Validation result shows that some time bamboo is confused with natural forest, but in some other places it is confused with planted forest. So, separating bamboo from other forest types is a very difficult work. In any case, accuracy of bamboo was already increased after combination so much more than before combination. That is also a success, however, not very perfect.

5. Conclusions

Using single-temporal optical data like ALOS/AVNIR-2 is not adequate to separate between forests and growing paddy/croplands, between planted forests and natural forests. However, using ALOS/PALSAR single-polarized image are sufficient to discriminate between forests and growing paddy/croplands, between built-up and others. On the other hand, using ALOS/PALSAR dual-polarized images can separate between planted forests and natural forests.

In whole the 2007 year, only one-time good quality images of ALOS/AVNIR-2 were found for the study area because of the presence of the cloud and the long repeat cycle of satellite. Collecting multi-temporal optical images of high-resolution satellites for tropical regions in one-year cycle to describe phenology of objects for forest mapping is usually very difficult. ALOS/PALSAR is not affected by cloud, in one year, it has many images. Therefore, combination of single-temporal image of ALOS/AVNIR-2 and multi-temporal images of ALOS/PALSAR for tropical forest mapping is a feasible way for every year. Tropical forest mapping annually by high resolution images becomes possible with ALOS data.

Combination of optical and microwave data of ALOS by a combination model can improve the accuracy of tropical forest mapping. The accuracy was increased up so much after the combination. The final tropical forest map has a high accuracy,

especially for forest classes.

Acknowledgements

ALOS data is provided by JAXA in the framework of ALOS program as a Principal Investigator (PI) member. We warmly give thanks to JAXA provided ALOS images for this study.

References

1) ALMEIDA-FILHO, R., SHIMABUKURO, Y.E., ROSENQVIST, A., SANCHEZ, G.A., 2009, Using dual-polarized ALOS PALSAR data for detecting new fronts of deforestation in the Brazillian Amazonia. *International Journal of Remote Sensing*, **30**, pp. 3735-3743.
2) BUTLER and RHETT, A., 2005, Nigeria has worst deforestation rate, FAO revises figures. Available online at: Mongabay.com (accessed 14 September 2009).
3) CLOUDE, S., VIERGERVER, K., WOODHOUSE, I.H., 2007, Forest Stucture Estimation using POLInSAR. *CD Proceedings of the first joint PI symposium of ALOS data nodes for ALOS science program* in Kyoto, JAXA, Nov. 2007.
4) DOBSON and CRAIG, M., 2000, Forest information from Synthetic Aperture Radar. *Journal of Forestry*, **98**, pp. 41-43.
5) FAO (Food and Agriculture Organization), 2004, National Forest Inventory - Field Manual Template. Forestry Department, FAO. Available online at: http://www.fao.org/documents/pub_dett.asp?pub_id=191385&lang=en (accessed 29 August 2009).
6) FOODY, G.M., BOYD, D.S., CUTLER, M.E.J., 2003, Predictive relations of tropical forest biomass from Landsat TM data and their transferability between regions. *Remote Sensing of Environment*, **85**, 463-474.
7) FRANSSON, J.E.S., MAGNUSSON, M., OLSSON, H., ERIKSSON, L.E.B., SANDBERG, G., SMITH-JONFORSEN, G., ULANDER, L.M.H., 2007, Detection of forest changes using ALOS PALSAR satellite images. *CD Proceedings of Geoscience and Remote Sensing Symposim (IGARSS)*, Barcelona, July 23-27, 2007.
8) HELMER, E.H., BROWN, S., COHEN, W.B., 2000, Mapping montane tropical forest successional stage and land use with multi-date Landsat imagery. *International Journal of Remote Sensing*, **21**, pp. 2163-2183.
9) HOAN, N.T., and TATEISHI, R., 2009, Cloud Removal of Optical Image Using SAR Data for ALOS Applications - Experimenting on Simulated ALOS Data. *Journal of The Remote Sensing Society of Japan*, **29**, pp. 410-417.
10) ISHITSUKA, N., 2007, The scatter characteristic of rice paddy fields using L band multi polarimetric satellite SAR observation. *CD Proceedings of the first joint PI symposium of ALOS data nodes for ALOS science program* in Kyoto, JAXA, Nov. 2007.
11) KUPLICH, T.M., 2000, The study of ERS-1 SAR and Landsat TM synergism for land use classification. *International Journal of Remote Sensing*, **21**, pp. 2101-2111.
12) LING, F., LI, Z., CHEN, E., WANG, Q., 2008, Forest mapping with multi-temporal dual polarization ALOS PALSAR data. *Procedings of SPIE*, Vol. 7285, 728517 (2008).
13) LOPES, A., NEZRY, E., TOUZI, R., LAUR, H., 1993, Structure detection and statistical adaptive speckle filtering in SAR images. *International Journal of Remote Sensing*, **14**, pp. 1735-1758.
14) NUGROHO, M., 2006, Integration of Multi Remotely Sensed Data and Geodatabases for Forestry Management in Indonesia. PhD thesis, Wageningen University, The Netherlands.
15) RAHMAN, M.M., CSAPLOVICS, E., KOCH, B., 2005, An efficient regression strategy for extracting forest biomass information from satellite sensor data. *International Journal of Remote Sensing*, **26**, 1511-1519.
16) SGRENZAROLI, M., DE-GRANDI, G.F., EVA, H., ACHARD, F., 2002, Tropical forest cover monitoring estimates from the GRFM JERS-1 radar mosaics using wavelet zooming techniques and validation. *International Journal of Remote Sensing*, **23**, pp. 1329-1355.
17) TAKEUCHI, S., SUGA, Y., OGURO, Y., KONISHI, T., 2000, Monitoring of new plantation development in tropical rain forests using JERS-1 SAR data. *Advances in Space Research*, **26**, pp. 1151-1154.
18) TOAN, T.L., PICARD, G., MARTINEZ, J.M., MELON, P., DAVIDSON, M., 2001, On the relationships between RADAR measurements and forest structure and biomass. *CD Proceedings of the 3rd International Symposium, "Retrieval of Bio- and Geophysical Parameters from SAR Data for Land Applications"*, Sheffield, UK, Sep. 2001.
19) TOTTRUP, C., 2004, Improving tropical forest mapping using multi-date Landsat TM data and pre-classification image smoothing. *International Journal of Remote Sensing*, **25**, pp. 717-730.
20) VIETNAMESE, CHAN, L.M., and DUNG, V.V., 1992, *Th·c v·t và th·c v·t đ·c s·n r·ng*, N.T. HOAN (Vegetation and special vegetation of forest). Forestry University of Vietnam, Hanoi 1992, pp. 294-302.
21) WONG, A., CHAPMAN, B., RICHARDSON, A., FREEMAN, A., 1997, SIR-C EDucation #03 (SIRCED03-B) CD-ROM, PC Special Edition, California Institute of Technology, Pasadena, California, USA. Available online at: http://southport.jpl.nasa.gov/cdrom/sirced03/cdrom/DOCUMENT/HTML/TEACHERS/MODULE02/MOD2SECE.HTM (accessed 10 September 2009)
22) ZHENGHAO, S., and FUNG, K.B., 1994, A Comparison of Digital Speckle Filters. *Proceedings of International Geoscience and Remote Sensing Symposium (IGARSS)*, California, August 8-12, 1994, pp. 2129-2133.

Development of the cropland mapping in the Selenge aimag of Mongolia using Remote sensing/GIS

B.Erdenee[1] Ryutaro Tateishi[1]

1 Center for Environmental Remote Sensing (CEReS), Chiba University, 1-33 Yayoi-cho, Inage-ku, Chiba 263-8522, Japan, E-mail erdene@graduate.chiba-u.jp

Abstract

Agriculture is one of the major economic sectors of Mongolia and the country's economy is very much dependent on the development of agricultural production.
Agricultural sustainability has the highest priority in all countries, whether developed or developing. Remote Sensing and GIS technology are gaining importance as useful tools in sustainable agricultural management and development. Maps, photographs and satellite images were used to build an area-sampling frame in order to further improve the agricultural statistics system in Mongolia.
This paper discusses the integrated use of Remote Sensing and GIS technology in particular cropland areas for sustainable agricultural development and management in Mongolia, with case examples.
We were developed agricultural cadastral map and create the vector coverage of the study site, the vector field boundaries were built and digitized from the ground truth data using with ARCMAP software. In this study, maximum likelihood supervised classification was applied to Landsat TM and ETM images acquired in 1989 and 2000, respectively, to map cropland area cover changes in the Selenge aimag of Mongolia. A supervised classification was carried out on the six reflective bands (bands 1-5 and band 7) for the two images individually with the aid of ground based agricultural monitoring data. Results were then tested using ground check data.

Keywords: Mongolian agriculture, land-cover/use change, remote sensing, GIS

1.Introduction

Agriculture is one of the major economic sectors of Mongolia and the country's economy is very much dependent on the development of agricultural production. From 1990s, Mongolia entered a period of transition from a central-based planned economy to a market economy. The change to a market-oriented economy had also an impact on the natural resources and their management, not only due to privatizations, but also because of the strong land fragmentation as a result of the land distribution and increased urbanization.
Mongolian agriculture had developed slowly. In the 1950s, agriculture began to adopt its present structure and modern techniques, based in part on material and technical assistance from the Soviet Union and East European countries. Mongolia has also began receiving large-scale agricultural assistance from the Soviet Union and other East European countries after Mongolia's 1962 entry into Comecon /an economic association of Communist countries, established in 1949, to facilitate trade and development/. In the late 1980s, several changes in governmental organization occurred to facilitate agricultural development. When Mongolia began to report statistics on arable land in 1960, there were 532,000 hectares of arable land, and sown crops covered 265,000 hectares of the 477,000 hectares of plough land.
Land reclamation started in the late 1950s and the early 1960s, when 530,000 hectares were developed, and it continued throughout each five-year plan. During the Seventh Plan, 250,000 hectares were assimilated, and the Eighth Plan called for an additional 120,000 to 130,000 hectares to be reclaimed.
Mechanization of the farm operations commenced on a large scale in the 1950s with the Soviet assistance. The Soviet Union provided most agricultural machines, as well as advice and expertise in mechanization. State farms were more highly mechanized than cooperatives.
Mongolia's staple crops were wheat, barley, oats, potatoes, vegetables, hay, and silage crops.
The objective of this study is to develop techniques for assessing and analyzing agricultural land cover land use in Selenge aimag of Mongolia, as a typical monitoring region through of the use of remotely sensed data and GIS.
The availability of remotely sensed images and the advances in digital processing and analysis

techniques have enabled research scientists to have information about the type, condition, area estimation, and the modeling growth of agricultural crops and agricultural product.

2. Study areas and data description

The selected study area Selenge aimag is prime cropland region and located in the Northeastern part of the Mongolia, measuring approximately 41,152.63 sq. km and covers mostly forest-steppe, steppe and is rich in chernozem soil. The geographic boundaries of the area are 49° 45′ 0″-49° 75′ 0″ N, 106° 30′ 0″-106° 50′ 0″ E (Figure1).

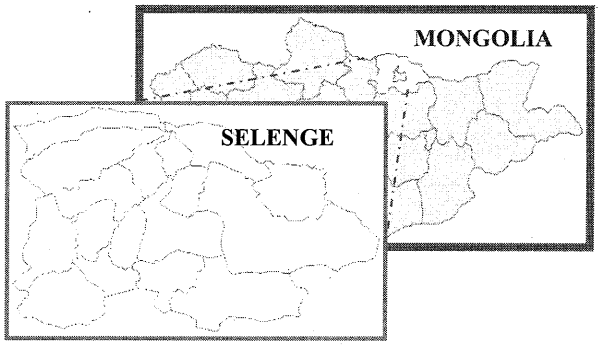

Figure 1. The study area

Selenge aimag is produces 60 percent of grain of the country. The climate of the region is semi-arid and arid; and the mean annual precipitation is 250-301 mm.

The main crops being grown in this region are wheat, fodder crops, potato, and some vegetables. Except for wheat, all other crops are rain fed. The planting dates of wheat and fodder crops are mostly planted in from the mid of May to October period. For vegetables planting starts in the end of May and continues until the end of August and mid-September. Almost all the crops present an important vegetative development in the June–August period. The wheat is harvested between September and early October. Vegetables are harvested gradually from late July to September.

Landsat Thematic Mapper (TM) and Enhanced Thematic Mapper (ETM+) images (with path/row132/25-27, 133/25, and 131/26-27) acquired on 1989 and 2000, respectively. All images were cloud free and of good quality.

3. Data pre-processing

Data processing and analysis operations were carried out using ENVI 4.3 and PCI GEOMATICA Image Analysis software.

The preliminary data processing was performed in this study using development of vector datasets. To create the vector coverage of the study site, the vector field boundaries were built and digitized from the ground truth data using with ARCMAP software. After that the each polygon points was then registered to Geographic lat/Long (Zone-48 WGS84 using) projection and the evenly distributed. The registration was based on first-degree polynomial and nearest neighbour resampling techniques.

Each polygon was assigned a numeric code, owner's name, polygon measurement, geographical location and the crop types of the ground-visited fields were recorded as attribute information. The polygon topology was then created and the attribute database was linked to the polygons to make polygon selection possible through a database query. This map was used to validation of classification result.

4. The methodology

The methodology is outlined in figure 2.

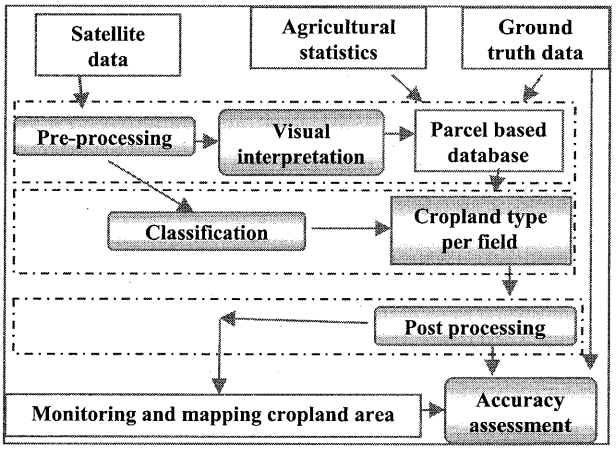

Figure2. Methodology

All pre-processed scenes can be superimposed to form a "multivariate image set", which contains two types of information: spectro-temporal and spatio-contextual. The spectro-emporal information is extracted by the supervised classification, which results in a first raster: the per-pixel classification. The segmentation extracts the spatio-contextual information contents and creates a map (in raster or vector format) with the delineation of all uniform image zones (segments). In the best case, these segments should correspond with parcels on the ground. The post-classification per field filter combines both results, and creates a segment-based (or field-based) map with enhanced accuracy. In practice, the per-pixel classification was created with the Maximum Likelihood algorithm.

Generally, land cover classifications with a limited number of broad categories (water body, forests, cropland, bare land…), the required training pixels can easily be defined and delineated by photo-interpretation of the pre-processed imagery.

In this study using the Landsat geometrically corrected multispectral map, test areas, and containing different type of classes such as cropland area (wheat and fodder crops, vegetables), water body, forest, and open space area (grassland and bare land) in the Selenge aimag have been selected. For classification, we have used Landsat 5 TM and ETM data taken on August 1989 and September 2000.

Three TM bands (band 1, band 4 and band 5) have been used for the study area. Upon completing the classification, the integrated analysis of the classified images and the vector field data was carried out.

After this operation, the reduced class trainings were used to mask out methodology.

After completing the classification procedure, the classified outputs were combined to make a single classified image such as cropland area and unused area.

To design the classification procedure, we analyzed the producer's and user's accuracies of cropland area and unused area and determined those classes with high accuracy. The thresholds of approximately 82% and 77% were defined for producer's and user's accuracies respectively.

The individual class accuracies and the producer's and user's accuracy were illustrated in an error matrix in Figure 5. The result of the masking classification is illustrated in figure 2 and figure 3.

4. Results and Conclusion

Supervised (ML) classification using six reflective bands of the images acquired on 1989 and on 2000, spectively was carried out using maximum likelihood classifier. Figures. 3 and 4 show the result of the classification.

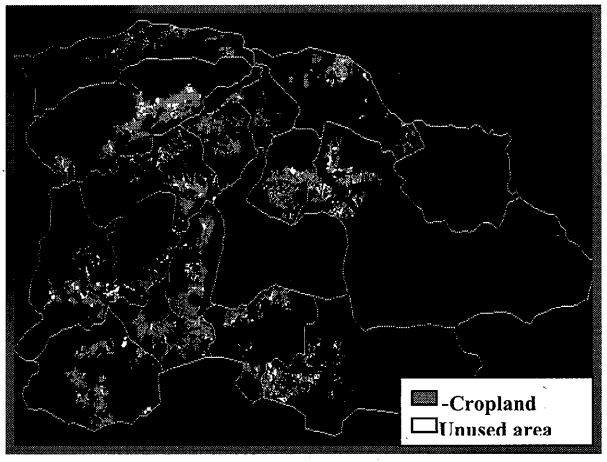

Figure3. Croplands use/cover classification map in Selenge aimag of Mongolia, using Landsat TM 1989.

Figure4. Croplands use/cover classification map in

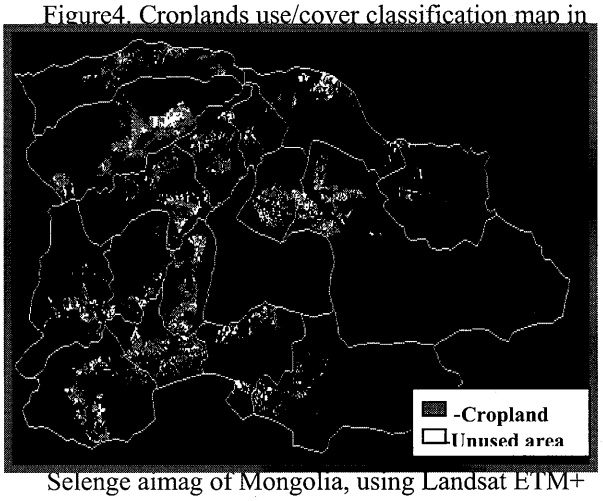

Selenge aimag of Mongolia, using Landsat ETM+ 2000

The results at aggregated land cover land use change show that the type classes (Table 1).

The classified areas change dynamics are the cropland area-1.64% and bare land-0.09% was expanded and forest area reduced 1.7%.

/by hectares/

-	Cropland	Water body	Open space	Forest
TM5, 1989	68944.84	480316.16	204437.15	112182.85
ETM 2000	81761.33	483575.88	206325.63	98472.64
Change LULC	12816.49	3259.72	1888.48	-13710.21

Table 1. Land cover classification result of the Landsat TM-1989 and ETM-2000 images

To analyze this classification, the overall accuracy percentage, user's and producer's accuracy that provide the statistical evaluation of these accuracy values were calculated.

Table 2 and 3 show the supervised classification accuracy results of the ETM and TM of agricultural land area of the Selenge aimag.

Classified images	Reference image				
	Class name	Cropland	Unused	Σ	**User's accuracy**
	Cropland	89	11	100	89.0%
	Unused	12	88	100	88.0%
	Σ	101	99	200	
	Producer's Accuracy	93.7%	88.9%		

Table 2. Supervised classification confusion matrices ETM-2000

Classified images	Reference image				
	Class name	Cropland	Unused	Σ	**User's accuracy**
	Cropland	91	9	100	91.0%
	Unused	12	88	100	88.0%
	Σ	103	94	200	
	Producer's Accuracy	88.3%	93.6%		

Table3. Supervised classification confusion matrices TM-1989

Privatisations of agricultural land have changed agricultural production considerably. Changes in the intensity of use, functioning of cropland fragmentation should be considered when analyzing changes at the level of land-use. However, these factors cannot be measured with remote sensing. Combination of the present study results with socio-economic data may provide more conclusive evidence.

Land-cover/use changes do not always occur in a progressive or gradual manner, but they may show periods of rapid and abrupt change followed either by a quick recovery of ecosystems or a non-equilibrium trajectory (Lambin *et al.*, 2001). In the present study only two years are available: 1989 describing the land-cover/use situation under the centralized government and 2000 in a market-oriented economy. The mid 1990s are not represented but stand for the moment in which the land was distributed to rural households and registration as private property took place.

Considering the above-described limitations of remote sensing for analysis of land-cover/use dynamics, one could state that the present results are more likely an underestimation of change than an overestimation. If more land-use aspects and information would be integrated into the study, the area subject to change would be likely to be more extensive.

References

1) Ince, F., 1986, Maximum likelihood classification optimal or problematic? A comparison with KNN classification. International Journal of Remote Sensing, 8(12), 1829–1838.

2)Janssen, L.L.F., M.N. Jaarsma and E.T.M. van der Linden, 1990. Integrating topographic data with remote sensing for land-cover classification. Photogrammetric Engineering and Remote Sensing, 56(11), pp. 1503-1506.

3)Conese,C., and Maselli, F., 1991. Use of multi-temporal information to improve classification performance of TM scenes in complex terrain. ISPRS Journal of Photogrammetry and Remote Sensing, 46, pp. 187-197.

4)Ram, B., & Kolarkar, A. S. (1993). Remote sensing application in monitoring land-use changes in arid Rajasthan. International Journal of Remote Sensing, 14(17), 3191–3220.

5)Lins, K. S., & Kleckner, R. L. (1996). Land cover mapping: An overview and history of the concepts. In J. M. Scott, T. H. Tear, & F. Davis (Eds.), Gap analysis: A landscape approach to biodiversity planning (pp. 57–65). Bethesda, MD: American Society for Photogrammetry and Remote Sensing.

6)Kurosu, T., Fujita, M., and Chiba, K., 1997. The identification of rice fields using multi-temporal ERS-1 C band SAR data. International Journal of Remote Sensing. 18, pp. 2953-2965.

7)Panigrahy, S., and Sharma, S. A., 1997. Mapping of crop rotation using multidate Indian Remote Sensing Satellite data. ISPRS Journal of Photogrammetry and Remote Sensing, 52, pp. 85-91.

8)Khorram, S., Biging, G. S., Chrisman, N. R., Congalton, R. G., Dobson, J. E., Ferguson, R. L., et al. (1999). Accuracy assessment of remote sensing-derived change detection. Bethesda: American Society of Photogrammetry and Remote Sensing

9)Lambin E F, Turner B L, Geist H J, Agbola S B, Angelsen A, Bruce J W, Coomes O T, Dirzo R, Fischer G U, Folke C, et al., 2001. The causes of land-use and land-cover change: moving beyond the myths. Global Environmental Change, 11, 261-269.1)

10)Murakami, T., Ogawa, S., Ishitsuka, N., Kumagai, K. and Saito, G., 2001. Crop discrimination with multitemporal SPOT/HRV data in the Saga Plains, Japan. International Journal of Remote Sensing, 22, pp. 1335-1348.

Acknowledgements

We want to express our sincere gratefulness to Mr.Badarch officer of Selenge aimag, for technical support for fieldwork.

Microwave and Multispectal Remote Sensing data for Monitoring Urban dynamics in Urumqi, China

Alimujiang Kasimu[1, 2], Nguyen Thanh Hoan[1] and R. Tateishi[1]

1.Center for Environmental Remote Sensing (CEReS), Chiba University 1-33, Yayoi-cho, Inage-ku, Chiba 263-8522 Japan
2. Institute of Geographic Sciences and Tourism Xinjiang Normal University Urumqi, China 830054
E-mail: Alimkasim@gmail.com

Abstract

Multispectal remote sensing data has been widely used for land cover mapping as well as urban study. The mechanism of ground object recognition is based mainly on its spectral reflectance characteristics. However, in most cases, it has certain limitation of accuracy in ground objects recognition. SAR remote sensing data on the other hand supplies information on surface structure, texture patterns. To achieve the best result it is strongly required to combine both these data for the analysis.

The study area Urumqi is located in the northwest region of China. The used dataset is composed of Landsat TM, ETM+, and JERS-1, PALSAR. At first the maximum likelihood classification was used to extract urban area. The classification images were then combined with microwave data to segment out different land cover categories. By combination of both Multispectal and microwave data, the accuracy the classification is increased a lot. Some errors caused by misclassification of ALOS/AVNIR-2 data were corrected by using ALOS/PALSAR.

Key word: ALOS/AVNIR-2, ALOS PALSAR, Multispectal data, Urban, mapping

1. Introduction

In order to conduct thorough analyses using any RS data sets, one should use a sophisticated interpretation method or apply a well-known and reliable mapping technique. Thematic information can be extracted in different ways, including manual, automatic and knowledge-based approaches. However, in most cases, users of spatial information like to apply sophisticated and easy to use automatic method for high quality urban mapping.

Optical remote sensing data such as LANDSAT TM, ETM, ASTER, and SPOT have been widely used in urban study. The mechanism of ground object recognition of these sensors is based on spectral reflectance characteristics of land cover categories that are, in general, independent on their surface roughness and texture patterns. This limits in certain way classification capability of these data types.

The microwave remote sensing data, on the other hand, provides information mostly on surface roughness or texture that have no correlation to material composition of the ground object. In recent years, Advanced Land Observation Satellite (ALOS) Phase Array L-type Synthetic Aperture Radar (PALSAR) data sets have been successfully used for different environmental and socio-economic studies. Unlike the traditional single frequency and single polarization SAR, the PALSAR has a number of advantages, because some objects, which are not seen in one polarization, can be seen in another polarization, thus improving the interpretation and analysis of the images. Separate use of both multispectal and microwave data has brought fruitful results in thematic mapping, however, a combination of both data types for land cover mapping in general and urban study

in particular could be one of the way to improve accuracy of classification.

In this paper, the author presents preliminary result on combination of multispectal and microwave remote sensing data in urban study.

2. MATERIALS AND METHODS

2.1 Descriptions of Study Area

The study area is located in Northwest China (Fig. 1) between the range of 86◦37′ E–88◦58′ E and 43◦01′ N–44◦06′ N, with an area of around 169 km^2. The topography mainly is hilly area and the basins in mountains. The southwestern and northeastern parts are higher than the middle part and the northwestern part. It has a dry continental climate in the mid-temperate zone. The average annual temperature is 6.2 degree Celsius and the average annual precipitation is 250mm. Urumqi abounds in coal, oil shale, the salt in Dabancheng Salt Lake and so on.

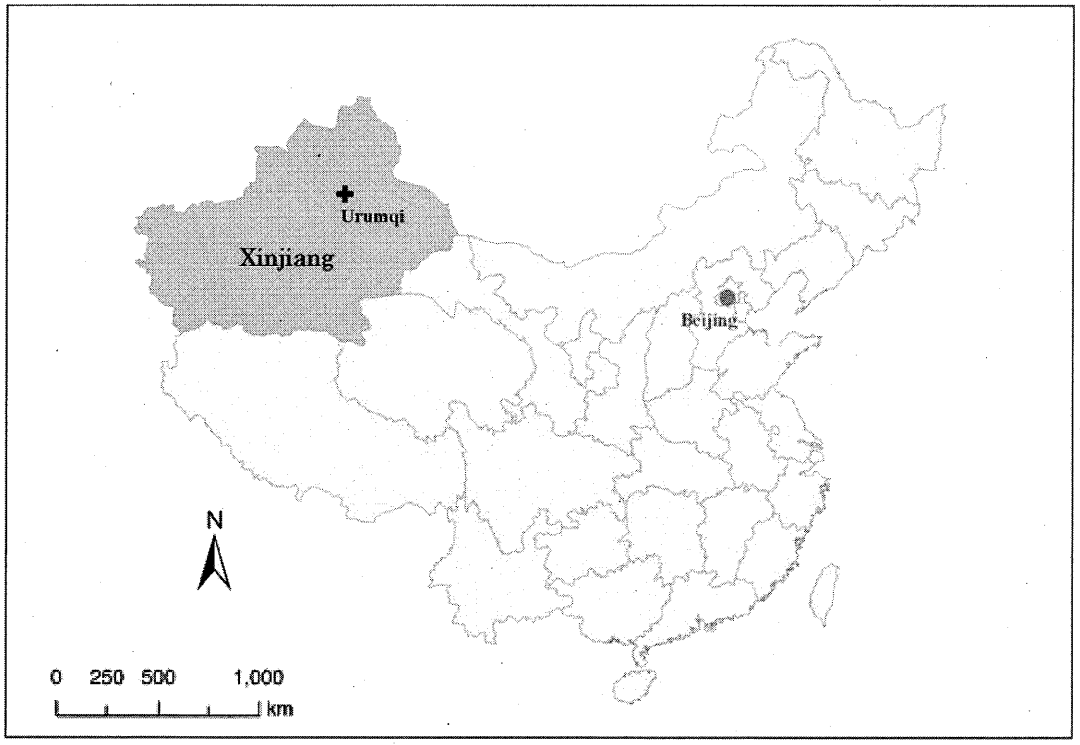

Fig.1 the position of Urumqi in Mainland China

Urumqi is the capital and the largest city in the Xinjiang and is important as the center of administration, culture, economy and transportation. The current population is around 1.8 million. In the early 1884s, it was just a small city. The construction of the Lan-Xin railway line (Lanzhou to Xinjiang) and Hotan line, Tu-Wu high-way (Turpan to Urumqi), Wu-kui high-way (Urumqi to Kuitun) and provided it a good opportunity for development. Especially in the last 20 years of economic reform, urban expansion in Urumqi has been very significant (Alimujiang, et al., 2006).

2.2 Data Sets

The materials used in this study are listed in Table 1

The study area is covered by two scenes of ALOS/AVNIR-2 and two scenes of ALOS/PALSAR. Table 1 shows the information of data acquisition used in this study. Reference data for training data collection and accuracy assessment includes local maps and google earth.

Table 1. Information of data acquisition

Data names	Observation date	Spatial resolution	Path/Frame	Provider
ALOS/AVNIR-2	20th Aug 2008	10m	170/2710	JAXA
	20th Aug 2008	10m	170/2720	JAXA
ALOS/PALSAR dual-polarization	16th Jun 2008	12.5m	499/860	JAXA
	16th Jun 2008	12.5m	499/870	JAXA
SRTM-DEM		90m		NASA

2.3 Data processing

Processing level of the received ALOS/AVNIR-2, and ALOS/PALSAR is 1.5. All of them are geo-coded images (CEOS format) and in the same coordinate system. However, when overlay together, objects in these images have not same position. ALOS/PALSAR data was geometric corrected using ALOS/AVNIR-2 image (Figure 2).

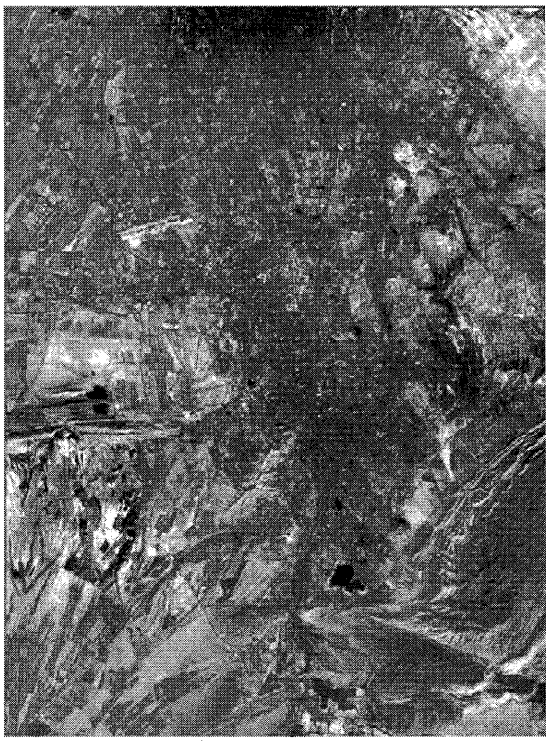

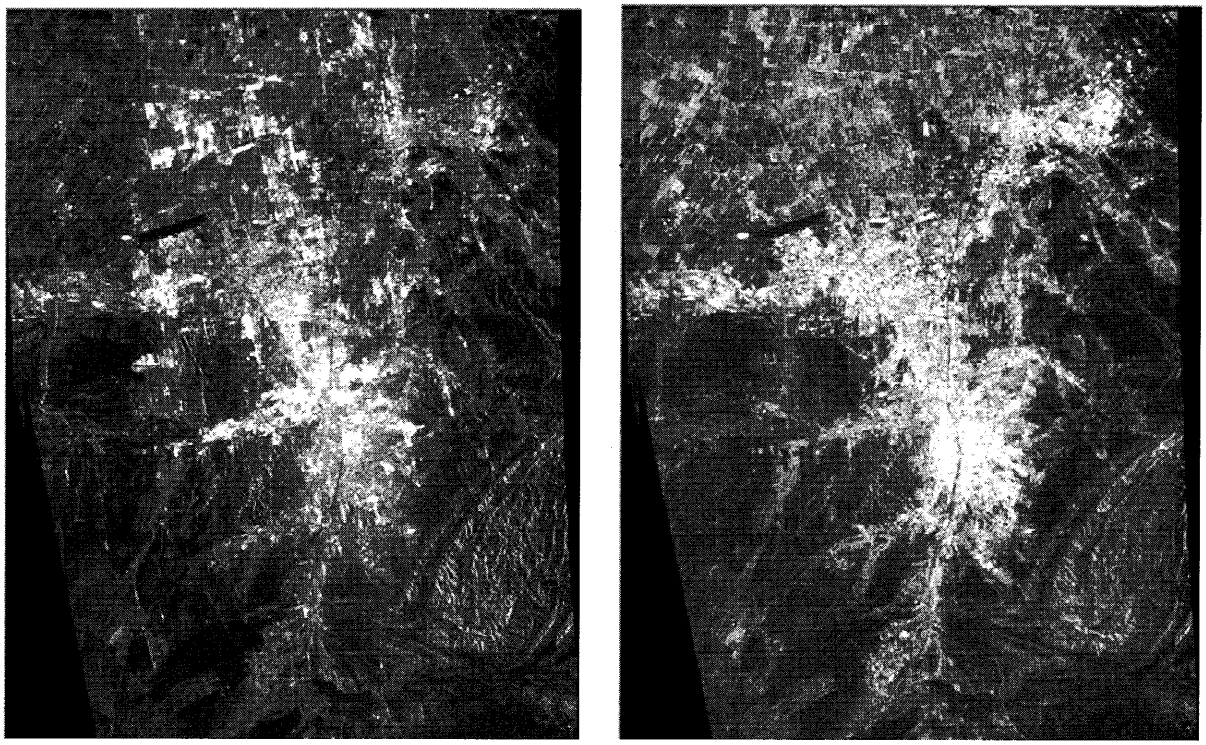

Figure 2 Color composite of ALOS/AVNIR-2 (up) and ALOS/PALSAR data after geometric correct (down) HH band (down right) HV band (down left)

3. Urban extraction using multispectral and microwave data

ALOS/AVNIR-2 and ALOS/PALSAR were collected for analyzing urban monitoring. The classification schemes include:(1) water (rivers, lakes, ponds and reservoirs) (2) urban land (the largely continuous area covered by urban constructions and urban facilities), (3) barren land, (4) crop land, (5) Forest. On figure.3 is shown classification of Urumqi city by maximum likelihood method (Murai, 1996). Training site data were collected by means of on-screen selection of the polygon training data method. A total of 100 training sites were chosen for each image to ensure that all spectral classes constituting each land use category were adequately represented in the training statistics. The accuracy of the classified maps was checked with a stratified random sampling method, by which 60 samples were selected for each land use category. The reference data were collected from field surveys and existing land use maps that have been field-checked. Global positioning systems were used to assist in the identification of field data on images. Large-scale aerial photos were also employed as reference data for the assessment of classification and accuracy.

Figure.3 Urumqi classification in 2008

4. RESULTS AND DISCUSSION

The overall accuracies of the classification is 79.84% in 2008; Conventional pixel-wise classification algorithms have some difficulties in it detection and especially in separation of urban area from bare land: forest land from cropland. The PALSAR data as known provides mostly information of surface roughness and therefore texture

of land cover categories. PALSAR data display built up area, tree coverage and crop in different brightness which is in proportion to backscatter level and therefore their surface roughness. On figure.4 is shown color composite of PALSAR data band HH, band HV, band HH assigned to color red, green and blue respectively. On this image, crop field is shown in different color shades, water bodies appear in black color, gray shades show distribution of various unchanged objects such as housing and built up area, evergreen tree coverage (parks and zoo).

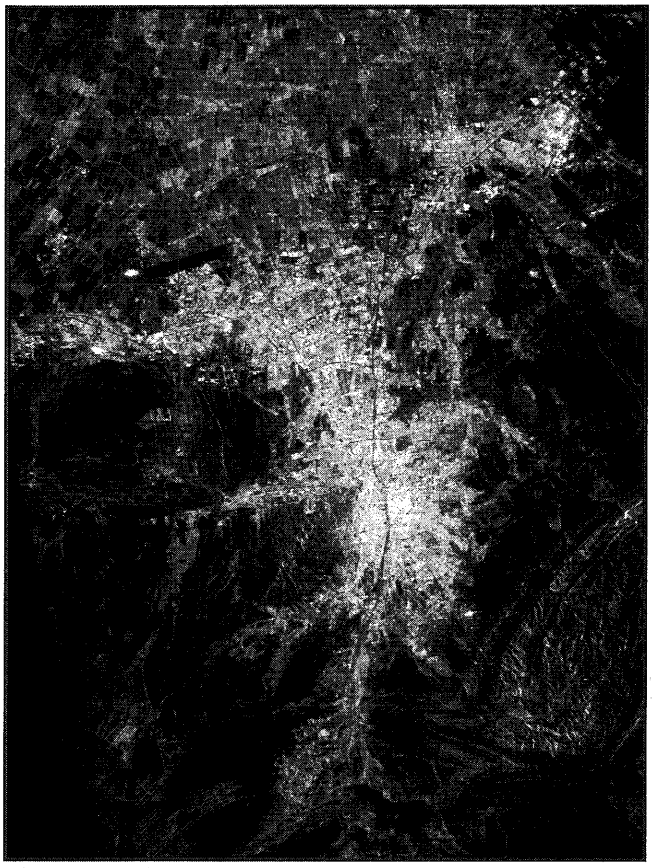

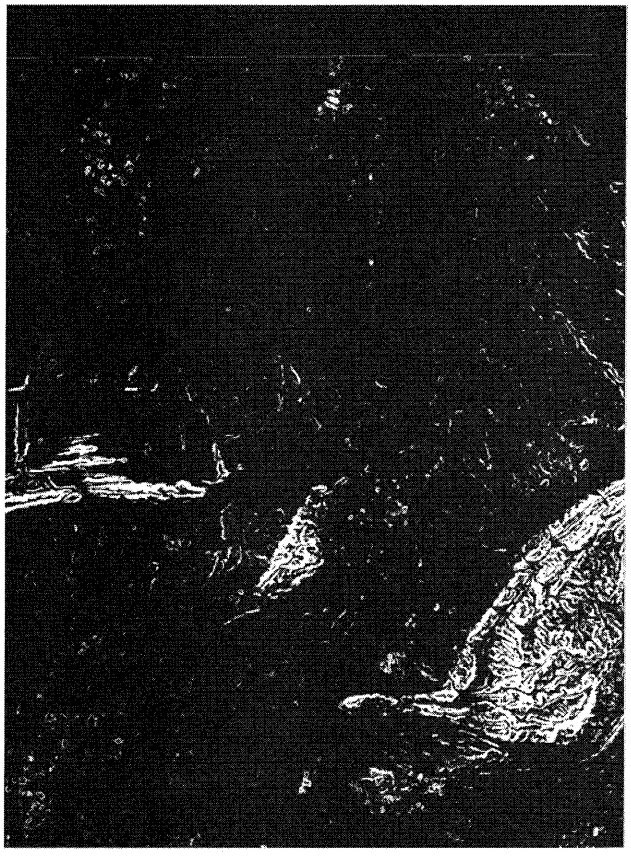

Figure.4 Color composite images of PALSARFigure.5 Urumqi high slope map
(HH=R, HV=G, HH=B)

The results in Figures.6 showed that the overall accuracy after combination is increased up to 88.2%. The final classification map was produced by combining the classification result of ALOS/AVNIR-2 with the results derived from ALOS/PALSAR images and the high slope map in Figure.5.

5. CONCLUSION

This is a preliminary result on study of combination of ALOS/AVNIR-2 and ALOS/PALSAR data for urban study. The approach used in this study seems to be simple but quite effective. By using ALOS/AVNIR-2 and ALOS/PALSAR data has been refined to achieve more accurate classification result. The time difference between ALOS/AVNIR-2 and ALOS/PALSAR is three months, in ideal case both data should be acquired at the same time.

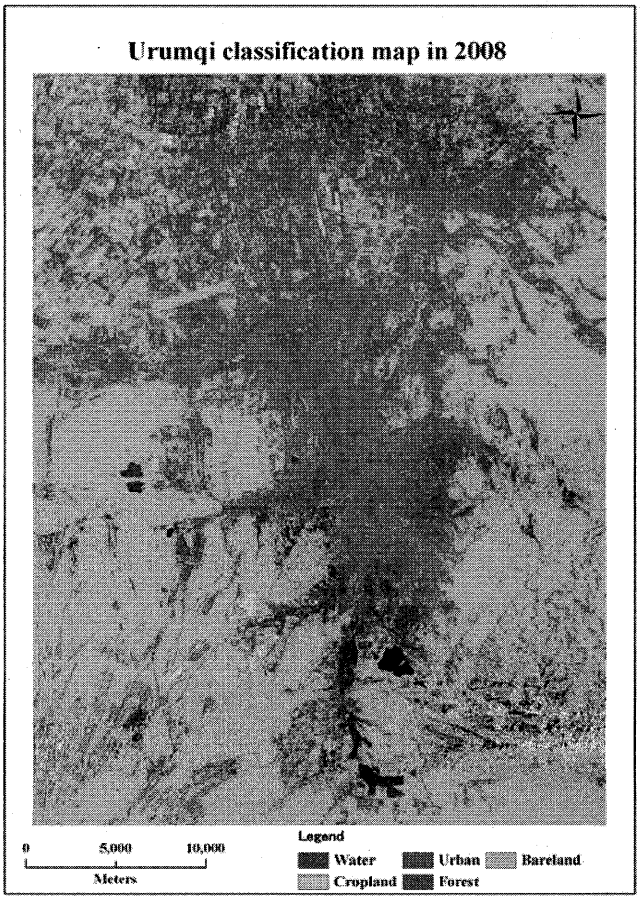

Figure.6 Classification map after combining ALOS/AVNIR-2 and ALOS/PALSAR

6. REFERENCE

Alimujiang. Kasimu, Anwaer, Ryutaro Tateishi 2006 Evaluating urban expansion and land use change in Urumqi, China, by using GIS and remote sensing, Arid Land Geography Vol.35 No.4: pp 12-22, (In Uyghur).

Murai, S., 1996. Remote Sensing Note, second ed. Nihon Printing Co. Ltd., Tokyo, pp. 220–221.

HUANG Yue, CHEN Xi, BAO An-ming, MA Yong-gang, Urban Sprawl Pattern and Spatial Features of Urumqi City during the Last 15 Years; Journal of Glaciology and Geocryology; 2006-03

Acknowledgments

We warmly give thanks to JAXA provided ALOS images for this study. This work is supported by National Natural Science Foundation of China (Grant No.40761008) and Doctoral Start Fund of Xinjiang Normal University (Grant No XJNUBS0907).

Application of Remote Sensing for Urban area change analysis in Bangladesh. (A case study of Khulna City)

Md. Mijanur Rahman[1], Md. Rahmat Ullah[2], Mi Lan[3], Josaphat Tetuko Sri Sumantyo[4], Hiroaki Kuze[5], Ryutaro Tateishi[6]

[1,3,4,5,6] *Center for Environmental Remote Sensing (CEReS), Chiba University, 1-33 Yayoi-cho, Inage-ku, Chiba 263-8522, Japan.*

[2]*Department of Electrical & Electronics Engineering, Atish Diponker University, Dhanmondi Dhaka 1207, Bangladesh.*

[1]*E-mail: Mijan@graduate.chiba-u.jp*

[2]*E-mail: dipu_ykk@yahoo.com*

[3]*E-mail: Miran@graduate.chiba-u.jp*

[4]*E-mail: jtetukoss@faculty.chiba-u.jp*

[5]*E-mail: hkuze@faculty.chiba-u.jp*

[6]*E-mail: Tateishi@faculty.chiba-u.jp*

Abstract

Bangladesh is still a relatively low urbanized country compared to other Asian countries. However, the country experienced a remarkable rate of urban growth both in terms of urban population and urban centers immediately after it's independence in 1971. Information on land use and land cover is required in many aspects of land use planning and policy development, as a prerequisite for monitoring and modeling.

The main objectives of this research is to analyze the major urban centers land use/cover change of Bangladesh between 1989 and 2006 using multi sensor images data. But the present study gives emphasis on Khulna city the third largest city of Bangladesh as a partial study of the whole research. This study employed Landsat TM and ETM+ & ASTER images and land use/cover changes were quantified using a supervised classification algorithm with Maximum Likelihood decision rule. For Training area selection, Google Earth and photograph had been considered and common training areas used for Landsat TM and ETM+& ASTER image of specific urban center. After performing the classification method statistical analysis of all land cover class had been done to find out the change of major urban area in Bangladesh.

Keywords: Remote sensing; image classification; land use and land cover; urban expansion.

1. Introduction

Urbanization is one the most widespread anthropogenic causes of the loss of arable land (Lopez, Bocco, Mendoza, & Duhau, 2001), habitat destruction (Alphan, 2003), and the decline in natural vegetation cover. The conversion of rural areas into urban areas through development is currently occurring at an unprecedented rate in recent human history and is having a marked effect on the natural functioning of ecosystems (Turner, 1994). Rapid urban expansion through infilling of low-lying areas and clearing of vegetation resulted in a wide range of environmental impacts, including habitat quality.

Remote sensing can provide frequent land cover of an area which can be a great tool to monitor urban land use pattern and change for physical planning of an urban area. Khulna as a divisional head quarter and a metropolitan city has a distinctive land use pattern but entire city is not yet developed.

2. Growth trend of Urban centers in Bangladesh

According to the 1991 Population census of Bangladesh, following three statistical criteria were set to test how 'urban' the urban centers in Bangladesh are:

i) a density of not less than 1,000 per sq. kms.

ii) a population of at least 5,000

iii) a literacy rate of not less than 50 %.

Considering the above criteria the growth trend of urban centers from 1901-1991 are given in the following figure 1.

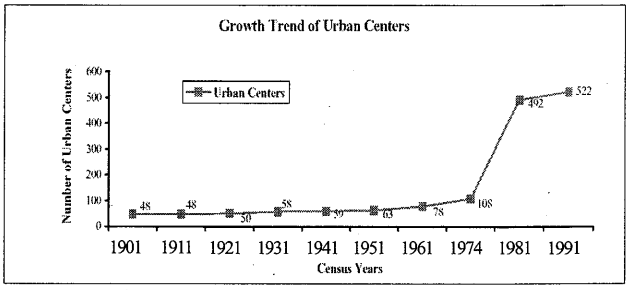

Figure 1: Growth Trend of Urban Centers

3. Study area

The study area for this study was Khulna City of Bangladesh. Geographically, Khulna lies at 22° 49′north latitude and 89° 34′east longitudes. Its mean elevation is 7 feet above Mean Sea Level (MSL). The area of Khulna City is about 60 km^2 with population of 855,650. Khulna City has not yet grown enough though it is a divisional head quarter. But in the last few years its growth rate is noticeable.

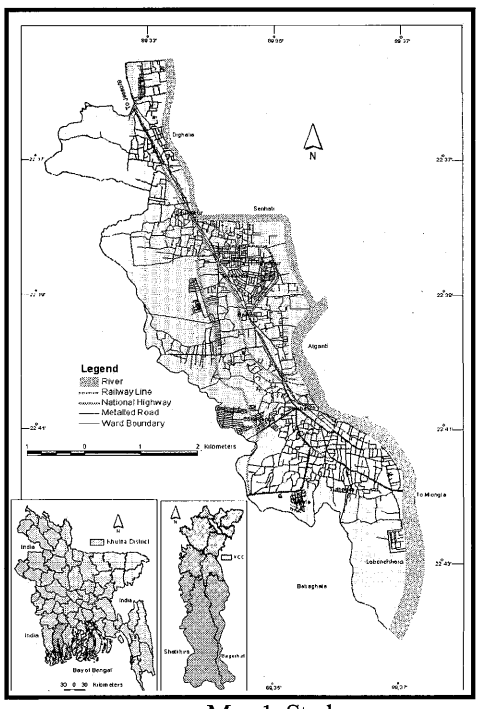

Map 1: Study area

4. Objectives of this study

This research evaluates land use/cover changes and major urban area/centers expansion in Bangladesh using satellite images data. Specific objectives of this research are--

1) To predict the urban land use and land cover of Bangladesh.
2) To compare the Major urban centers/area expansion trend and rate.

5. Data & Methodology

This study used Landsat TM, ETM from 1990-2006 & ASTER (VNIR) of 2006 and other ancillary data, information from published unpublished document. Landsat TM & ETM+ images were downloaded from Global Land Cover Facility with University of Maryland in USA website. Landsat images with band 1, 2, 3, 4, 5, 7 were used for this study. For Training area selection, Google Earth and photograph had been considered. For accuracy assessment, reference maps (Survey of Bangladesh topo-sheets) as well as local knowledge (Field survey) are used.

Table 1: Information of Landsat ETM+ images

Sensor Name	Path (p) & Row(r)	Accusation Date
ASTER	VNIR	2006/02/28
Landsat TM	p137r044	2006/12/05
Landsat TM	p138r044	2004/11/04
Landsat ETM+	p138r044	2000/11/17
Landsat TM	p137r044	1989/11/04

Methodology of this study is schematically shown in figure 2. Image Normalization, Filtering technique were applied for improving data quality or removing different noises from Landsat image. Supervised classification using maximum likelihood decision rule applied for urban land cover classification and accuracy assessment also performed and preparation of final map.

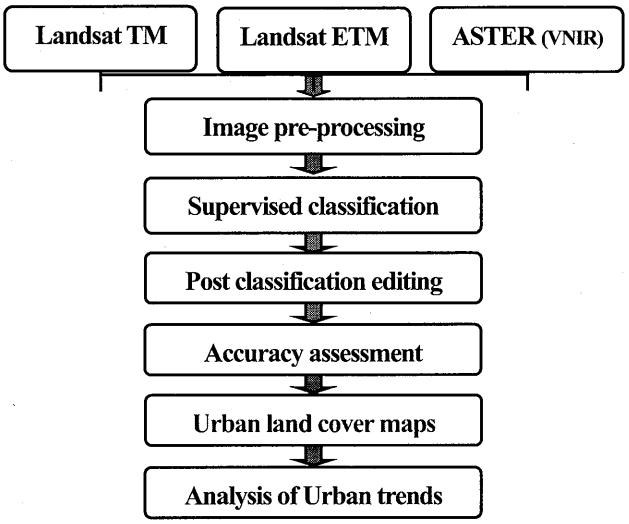

Figure 2: Flow of Methodology

6. Image classification

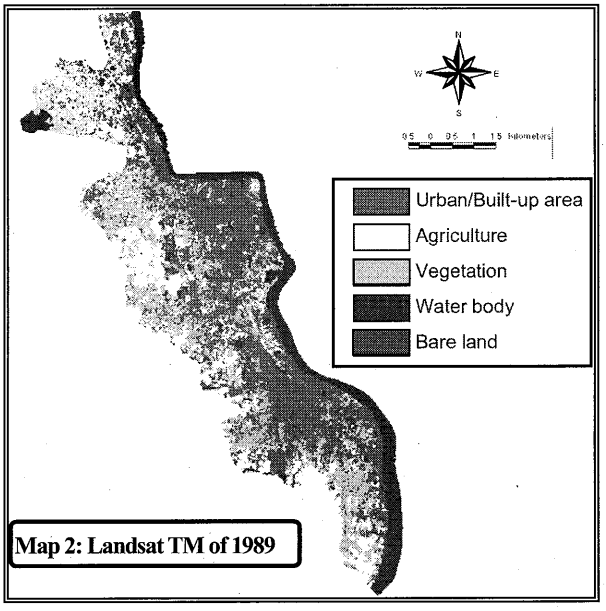

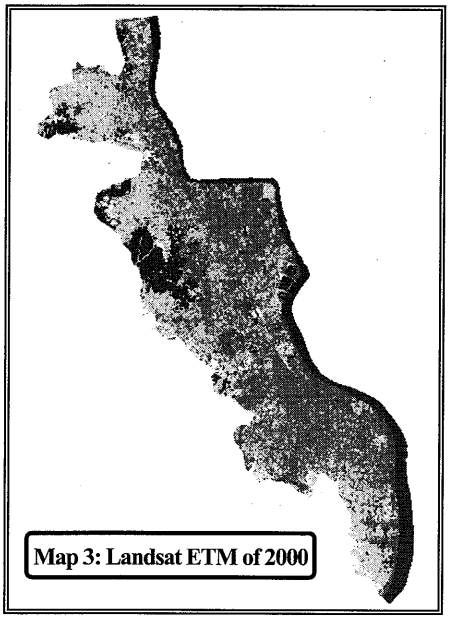

Map 3: Landsat ETM of 2000

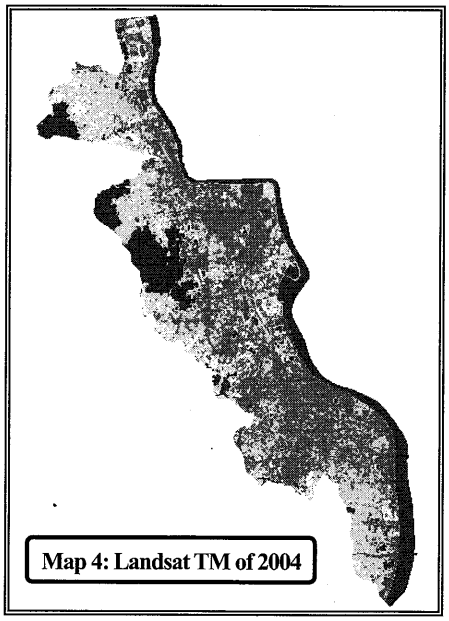

Map 4: Landsat TM of 2004

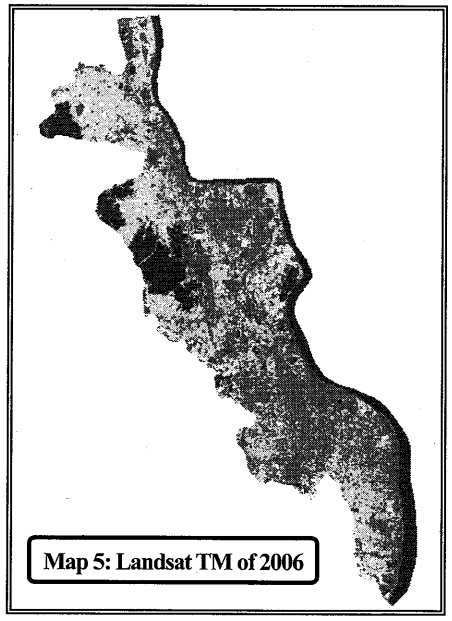

Map 5: Landsat TM of 2006

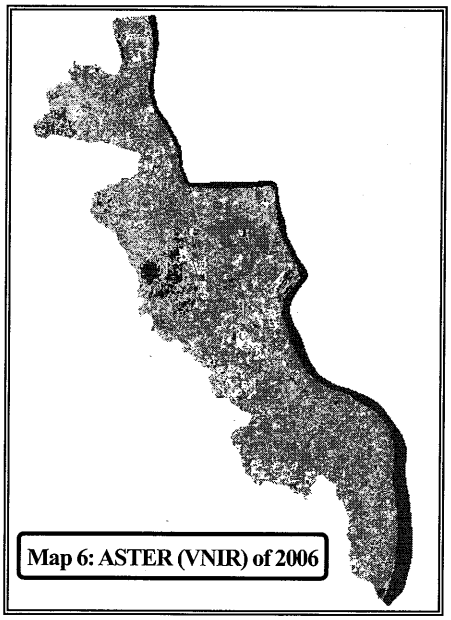

Map 6: ASTER (VNIR) of 2006

7. Statistical analysis of Landsat TM 1989 & Landsat ETM 2000

Landsat TM of 1989/11/04		Landsat ETM of 2000/11/17		Types of land use/cover
Area in km^2	% of Area	Area in km^2	% of Area	
14.592	30.319	17.871	37.132	Build-up area
13.474	27.996	14.772	30.693	Vegetation
9.055	18.814	2.059	4.278	Agri. Land
6.597	13.707	9.676	20.104	Water body
4.404	9.1505	3.750	7.791	Bare land
48.122	**100**	**48.122**	**100**	**Total area**

8. Statistical analysis of Landsat TM 2004 & 2006

Landsat TM of 2004/11/04		Landsat ETM of 2006/12/05		Types of land use/cover
Area in km^2	% of Area	Area in km^2	% of Area	
19.723	40.985	20.934	43.501	Build-up area
14.450	30.027	13.311	27.660	Vegetation
3.6999	7.688	3.283	6.822	Agri. Land
7.828	16.266	6.972	14.488	Water body
2.417	5.022	2.702	5.614	Bare land
48.122	**100**	**48.122**	**100**	**Total area**

9. Statistical analysis of Landsat TM 2006 & ASTER (VNIR) of 2006

Landsat TM of 2006/12/05		ASTER (VNIR) of 2006/02/28		Types of land use/cover
Area in km^2	% of Area	Area in km^2	% of Area	
20.934	43.501	21.789	45.278	Build-up area
13.311	27.660	12.252	25.460	Vegetation
3.283	6.822	4.477	9.303	Agri. Land
6.972	14.488	6.613	13.742	Water body
2.702	5.614	2.997	6.227	Bare land
48.122	**100**	**48.122**	**100**	**Total area**

10. Accuracy assessment

Before accuracy assessment, the classified images were checked visually and further ensured by Google earth and then selected sampling points/pixels arbitrary by random sampling method. This study considered (50x6) 300 sampling points as random basis for accuracy assessment. After completing the accuracy assessment work a report has been produced that contains error matrix, producers and user's accuracy, kappa statistics and overall accuracy are shown in figure 3.

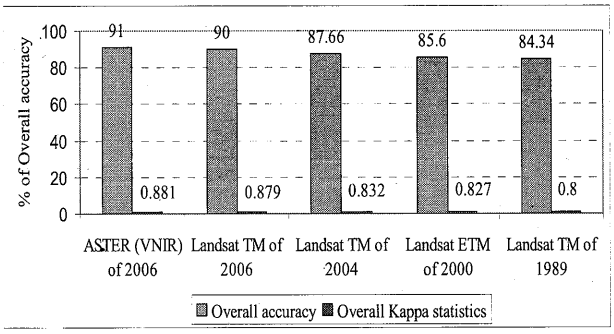

Figure 3: Overall accuracy and kappa statistics

The standard accuracy of 85–90% for LULC mapping studies as recommended by Anderson et al. (1976).

11. Conclusions

This study has assessed urban LULC changes and the dynamics of urban expansion in Khulna City, Bangladesh using RS data. Urban expansion was quantified for the last 16 years using the post-classification comparison technique. Khulna City was found to have experienced rapid changes in LULC, particularly in urban/built-up areas. Analysis revealed that urban areas increased by 3.279 km^2 during 1989-2000 and 1.852 km^2 from 2000 to 2004, and 1.211 km^2 from 2004 to 2006, which resulted in a substantial reduction in the area of water bodies, vegetation, agricultural areas and bare land. The dramatic expansion of the urban areas of Khulna City from1989-2000 exhibited clear spatio-temporal differences. The conversion of water bodies, vegetation and bare land areas to urban land has caused extensive and varied environmental degradation in the study area, and the vulnerability to flooding and the growth of slums have been the main negative outcomes associated with the rapid urban development.

The interpretation and classification of RS data were useful for estimating the rate and spatial pattern of the urban expansion in Khulna City of Bangladesh. As reliable and current data are lacking for Bangladesh, the land use maps produced in this study will contribute to both the development of sustainable urban land use planning decisions and also for forecasting possible future changes in growth patterns.

Acknowledgements

The author would like to thank Professor Dr. Tateishi Ryutaro of Center for Environmental Remote Sensing (CEReS), Chiba University for providing ASTER data and his helpful suggestions and advice. The author also grateful to Professor Dr. Hiroaki Kuze and Professor Dr. Josaphat Tetuko Sri Sumantyo for their critical comments and suggestion.

References

1) BBS (1997), *Bangladesh Population Census 1991,* Vol. 3, (Urban Area Report). Dhaka: Statistics Division, Ministry of Planning, Government of People's Republic of Bangladesh.
2) Howarth, P. J., & Wickware, G. M. (1981). Procedures for change detection using Landsat digital data. International Journal of Remote Sensing, 2(3), 277–291
3) Johnson, R. D., & Kasischke, E. S. (1998). Change vector analysis: a technique for the multi-temporal monitoring of land cover and condition. International Journal of Remote Sensing, 19, 411–426
4) Lu, D., Mausel, P., Brondiozio, E., & Moran, E. (2004). Change detection techniques. International Journal of Remote Sensing, 25(12), 2365–2407.
5) Lu, Q., & Weng, D. (2005). Urban classification using full spectral information of Landsat ETM imagery in Marion County, Indiana. Photogrammetric Engineering & Remote Sensing, 71(11), 1275–1284.
6) Lu, D., Mausel, P., Brondiozio, E., & Moran, E. (2004). Change detection techniques. International Journal of Remote Sensing, 25(12), 2365–2407.

Estimation Surface Energy Balance components relate with Land Use and Land Cover in the Indonesian big city (case study: Surabaya) by using Remote Sensing and GIS

Laras Tursilowati[1,2], Josaphat Tetuko Sri Sumantyo[1], Hiroaki Kuze[1], Erna Sri Adiningsih[2]

[1]*CEReS, Chiba University-Japan,1-33 Yayoi-cho, Inage-ku, Chiba-shi, Japan 263-8522*

[2]*LAPAN, Jl. dr. Junjunan 133, Bandung. 40173, Indonesia*

E-mail: laras@restaff.chiba-u.jp, jtetukoss@faculty-chiba.u.jp, hkuze@faculty-chiba.u.jp, ernasri@yahoo.com

Abstract

Recent development technologies have demonstrated an increasing capability to estimate the spatial distribution of surface fluxes for very large areas with remote sensing techniques. The current state of progress in utilizing satellite-based remote sensing data to estimate various surface energy balance parameters. Remote sensing reflectance and emittance data can be used to estimate parameters needed to characterize Rn, G, and H, leaving LE to defined mathematically. In this research used Landsat ETM satellite data to extrapolate Surface Energy Balance (SEB) estimates in the Indonesian big city (case study: Surabaya) and characterizing the partitioning of fluxes among the different soil and lancover types found in the study area with tools ErMapper and Arcview GIS. The general equation of SEB can be summarized as Rn= H + LE + G, (Rn is net radiation absorbed at the surface, G the flux of heat into the soil, H and LE are the sensible and latent heat fluxes into the atmosphere). The result is representation difference of energy balance components (Rn, G, H, and LE) in the land cover types. Net radiation and latent heat fluxes (Rn and LE) in urban region less then in vegetation region and water body. On the contrary, sensible heat flux and soil heat flux in urban land cover (open land, reseidence, and industries) higher than vegetation area (plantation, forest, paddy field) and water body (water and embankment). The proporsional of SEB components also determined in this paper.

Keywords **:** Surface Energy Balance, Land Use Land Cover, Remote Sensing

1. Introduction

Shortwave radiation from the sun enters the surface-atmosphere system of the Earth and is ultimately returned to space as longwave radiation (because the Earth is cooler than the sun). A basic necessity of this energy interchange is that incoming solar insolation and outgoing radiation be equal in quantity. Three main losses of solar radiation back to space occur in the Earth's shortwave radiation cascade. 4 units of sunlight are returned to space from surface reflection. Cloud reflection returns another 20 units of solar radiation. Back scattering of sunlight returns 6 units to space. The total loss of shortwave radiation from these processes is 30 units. The term used to describe the combined effect of all of these shortwave losses is earth albedo (Pidwirny 2004).

Clouds, the atmosphere, and the Earth's surface reflect about 30% of the incoming solar radiation back into space. Therefore, the Earth's albedo is 0.30. The remaining 70% of the radiation is absorbed or thermalized to heat the Earth's surface; it evaporates water (latent heat), or causes convection (sensible heat) (Figure 1).

The absorbed energy is eventually reemitted as longwave (or infrared) radiation, with 6% coming from the surface and 64% from the clouds and atmosphere. This whole process is known as the Earth's heat engine. The calculation or measurement of the various paths for the radiation and energy flows are the Earth's radiation and energy budgets, respectively (Hoyt 1997).

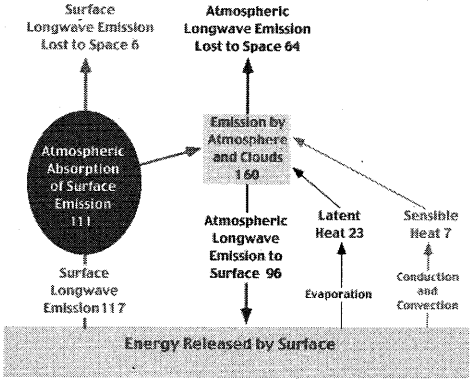

Fig 1. Global longwave radiation cascade (Pidwirny 2004)

Many controversies and ironies exist in the sun/climate field. One additional irony worth mentioning is the claim by Dove and Maury (oceanographers) in the last century that the sun's radiant output remains constant and therefore plays no role in climate change. Solar physicists have never been highly confident about the sun's constancy, since the sun shows some variability wherever it is observed (Hoyt 1977). The net radiation balance at the earth's surface determines the amount of energy which can be transformed into the remaining components of the energy balance, i.e. the sensible, the latent, and the soild heat flux (Kalthoff et al. 2006). Partitioning into these fluxes determines the local and regional climate.

In this paper talk about advantage of surface energy budget estimation from satellite data in the big city (case study in Surabaya as capital of West Java province, as improvement from recent result about evapotranspiration estimation from satellite data (Tursilowati et al. 2009).

Figure 2 show the diurnal radiant temperature cycles for surface materials in equatorial.

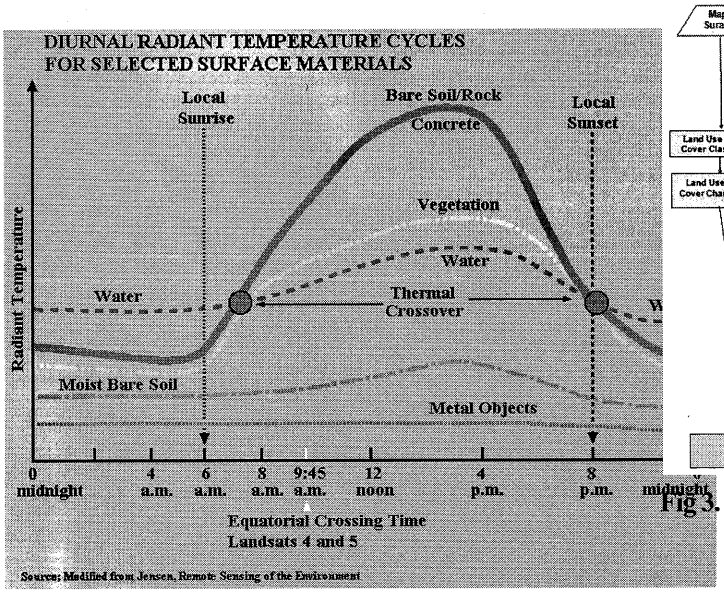

Fig 2. Diurnal radiant temperature cycles for seleted surface materials.

In the figure 2 show that difference of diurnal radiant temperature cycles in the surface material types. The radiant temperature reach maxmimum intensity after midday (around 3 p.m.), the highest value of radiant temperature in land type of Bare Soil Rock and concrete, afterwards vegetation, water, moist bare soil and metal object. On the equatorial crossing time Landsat (around 9:45 am) the diurnal temperatur is starting reach.

2. Methods

2.1. Data

We use Landsat ETM satellite data (acquisition data : 23 August 2002) for principal data, and the other data are RBI from Bakosurtanal, and observational data from BMG. For case study is in Surabaya city (capital of East Java-Indonesia).

2.2. Methodology

The basic method use surface energy balance equation that represent by equation 1:

$$Rn = LE + G + H \quad (1)$$

Rn = radiation net, LE = latent heat flux, G = soil heat flux, and H = sensible heat flux.

Figure 3 represent methodology shceme for estimation of surface enery balance and land cover classification from Landsat satellite data. Land cover classification by using unsupervised classification method.

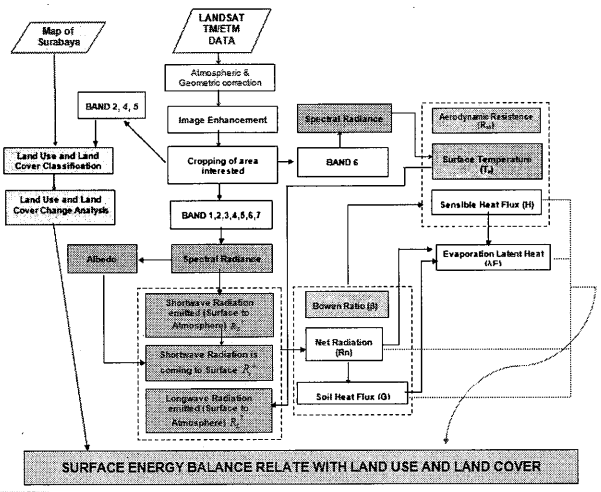

Fig 3. Methodology scheme for estimation SEB components and land classification.

3. Result & analysis

3.1. Landcover

Land cover classification using unsupervised classification is represented by figure 4.

Fig 4. Land cover classification of Surabaya.

In the figure 4 show the land cover of Surabaya as 8 types, there are water body, forest, industry, residence, plantation, paddy field and embankment. The dominant land cover in Surabaya is residence and industries (9083 ha and 8062 ha respectively), then paddy field (5678 ha), embankment (3335 ha), open land (3196 ha), plantation (2338 ha), and water body (122 ha).

3.2. Net radiation

Estimation of net radiation in Surabaya from Landsat satellite data is represented by figure 5 as below:

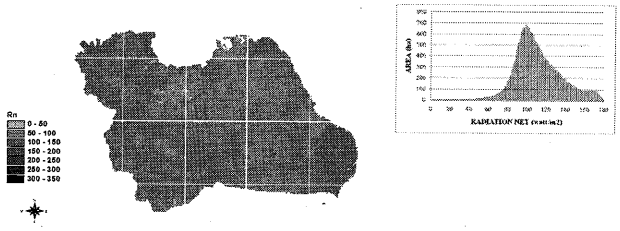

Fig 5. Net radiation of Surabaya in watt/m^2.

In the figure 5 show that the net radiation in residence area is less than area that dominated by water or vegetation. Lowest net radiation is in residence region, paddy field, and industry, however highest net radiation in embankment and plantation. The net radiation value in urban area, paddy field, and industry are not significantly difference, then it can be concluded that net radiation in this land cover is similar. The same case also was represented in embankment region and plantation, that is not significant real.

3.3. Latent heat flux

Figure 6 represent spreading of latent heat flux (LE) that was estimated from satellite data.

Fig 6. Latent heat flux (LE) of Surabaya in watt/m^2.

In the figure 6 show that latent heat flux (LE) as energy for evapotranspiration in water body and embankment are higher than the other land cover types. The lowest value of LE is in residence and industry (urban area). Land cover that dominated by vegetation will have value between these two land cover types (water area and urban area). LE is variate in land cover types, in residence lower than the other land cover types, and embankment have highest LE.

3.4. Soil heat flux

Spreading of soil heat flux (G) was represent by figure 7.

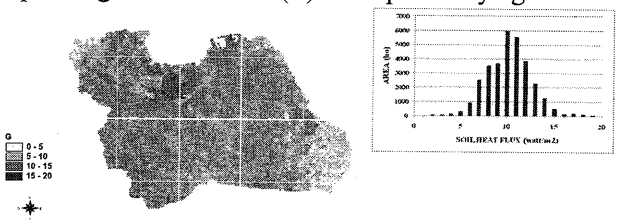

Fig 7. Soil heat flux (G) of Surabaya in watt/m^2.

In figure 7 show that soil heat flux in Surabaya. Estimation of soil heat flux need surface temperature, albedo, net radiation and NDVI. In this equation soil heat flux proportional with surface temperature, can be estimate that soil heat flux in urban area will be higher than in land cover that dominated by water (wet area). Figure 7 also represent soil heat flux in residence higher than the other land cover types. Soil heat flux in embankment is lowest if we compare with the other land cover types. Also the case for embankment and plantation soil heat flux lower than the other land cover types.

3.5. Sensible heat flux

The spasial of sensible heat flux spreading in Surabaya was represented by figure 8.

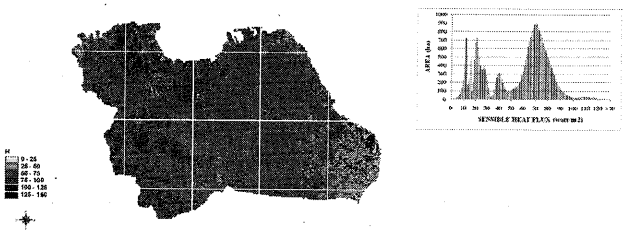

Fig 8. Sensible heat flux (H) of Surabaya in watt/m^2.

In the figure 8 show that the spasial distribution of sensible heat flux that represent of air temperature. The difference of H in land cover residence in the urban and non urban area especially in sunny day is very large. Otherwise for region dominated by water, difference of H is very small, moreover surface temperature in land cover dominated by water in the morning and night will be less than air temperature. This means that sensible hat flux in residence is larger then water body i.e. embankment. Sensible heat flux in residence larger than in embankment and wet paddy field.

3.5. Composition of surface energy balance in land cover types.

The composition of surface energy balance in land cover types is represented by figure 9.

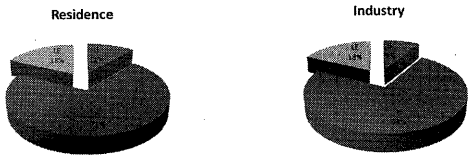

Fig 9 (a). Composition of Surface Energy Balance in Urban area (residence and industry).

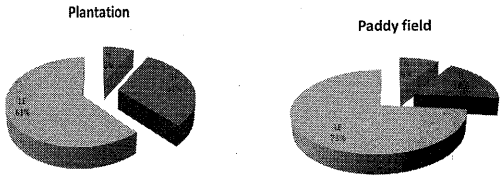

Fig 9 (b). Composition of Surface Energy Balance in vegetation area (plantation and paddy field).

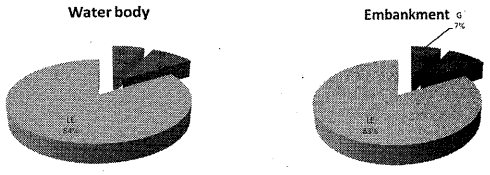

Fig 9 (c). Composition of Surface Energy Balance in water area (water body and embankment).

Figure 9 (a) show that net radiation in the surface of urban region (residence and industry) dominantly by energy for heating air (sensible heat flux/H) around 71% for residence and 73% for industry, afterwards energy for evapotranspiration (latent heat flux/LE) around 18% residence and industry. The energy for heating soil is smallest (11% for residence and 9% for industry). In urban area that dry land cover, priority of net radiation is for heating air and land surface, and the residu for evaporate water, this mean that is why air temperature in urban area hotter (higher) than non urban area.

Figure 9 (b) represent proportion of energy in vegetation area (plantation and paddy field). The energy for evapotranspiration is highest (61% for plantation and 73% for paddy field), then sensibel heat flux in plantation (31%) and in paddy field (18%), soil heat flux in vegetation is the smallest proportion (plantation 8% and paddy field 9%).

In the wet area (water body and embankment) that represent in figure 9 (c) is contrary in urban area. Similar with in vegetation area, the highest energy is energy for evapotranspiration (LE water body 84% and embankment 83%), afterwards H in water (9%) and embankment (10), and the samllest is energy for heating soil (G water body and embankment same as 7%). The contrary proportion in the urban air, in wet area net radiation was used for evaporate more than fifty percent, then air tempearture in mid day colder then air temperature in urban area.

Figure 9 (a) (b) and (c) could be explain by Fourier law (Holman and White, 1992) whose found heat transfer formulation through conduction per unit of land area as:

$$\frac{q}{A} = -k\frac{dT}{dx} \qquad (2)$$

q/A is surface heat flux through conduction per area ($w\ m^2$), dT/dx is temperature gradient ($K\ m^{-1}$) and k is heat conductitity ($wm^{-1}K^{-1}$). Negative symbol represent direction of heat moving from high temperature region to low temperature region. k value for three land cover types are: 0.76 (urban area), 0.56 (water body), and 0.12 (vegetation region), ((Holman and White, 1992).

The same of temperature gradient for three land cover types, q/A is defined by *k* (heat conductivity). In the result G value for three land cover types are 10% (urban), 7% (water body), and 8.5% (vegetation) respectively. However H and LE depend on surface condition, in dry land (urban), LE very small, then domination of net radiation of H as indicator of air temperature in urban area high in the midday. In vegetation area and water body, most of energy is used for evaporation, then H smaller and air temperature in vegetation area and water body in the midday smaller than nightime.

4. Summary

Classification of Surabaya land cover with unsupervised classification method and overlay matrix show that land cover significance change from vegetation region to non vegetation region in city central.

Impact of land use land cover change in the big city especially in Surabaya as a capital of province is change in surface energy balance.

Base on difference energy balance, net radiation and evapotranspiration in urban land cover smaller than vegetation area or embankment. Otherwise, sensible heat flux and soil heat flux in urban area larger than vegetation area or embankment. Any changes in land use from

vegetation area to urban area (non vegetation) will decrease evapotranspiration and net radiation, and increase sensible heat flux and soil heat flux.

Surface energy balance variable i.e. Radiation net (Rn), latent heat flux (LE), sensible heat flux (H) and soil heat flux (G).

Acknowledgements

The project is partly funded by the National Institute of Aeronautics and Space (LAPAN)-Indonesia and JSPS Ronpaku-Japan.

References

1) Holman, J.P and White, P.R.S. 1992. Heat Transfer. (7^{th} edition in SI unit). McGraw-Hill Inc. UK. 713pp.

2) Hoyt, D.V., K.H. Schatten, 1997, The role of the Sun in Climate Change, pp. 288, New York, Oxfor University Press.

3) Kalthoffa, N., M. Fiebig-Wittmaackb, C. MeiXnera, M. Kohlera, M. Uriartea, I.Bischoff-GauX, E. Gonzales, 2006, The energy balance, evapo-transpiration and nocturnal dew depositiion of an arid valley in the Andes, Journal of Arid Environments, 65, pp. 420-443.

4) Pidwirny, M., 2004, Fundamentals of Physical Geography, chapter 7, Depart.of Geography, Okanagan Univ. College.

5) Rapp, D., 2008, Assessing Climate Change: Temperatures, Solar Radiation, and Heat Balance, pp. 392, Springer, UK.

6) Tursilowati, L., J.T.S. Sumantyo, H. Kuze, E.S. Adiningsih, 2009, Comparison Evaluation of Evapotranspiration Estimation between Satellite data and Observation data, Proceeding of Workshop on Ground – Based Atmosphere Observation Network in Equatorial Asia, pp. 174-185.

The comprehensive use of existing global land cover data

*Naijia Zhang,[1] and Ryutaro Tateishi[2]
Center for Environmental Remote Sensing (CEReS), Chiba University 1-33, Yayoi-cho, Inage-ku,
Chiba 263-8522 Japan
E-mail: Z_N_J@graduate.chiba-u.jp

Abstract

A global land cover project always costs a long time, and its accuracy is not so high (70%, or a little higher). Until now, six global land cover projects have been produced: the University of Maryland global land cover product (UMD), the International GeosphereBiosphere Programme Data and Information System Cover (IGBP-DISCover), the MODerate resolution Imaging Spectrometer global land cover product (MODIS), the Global Land Cover 2000 (GLC2000), Global Land Cover by National Mapping Organizations (GLCNMO), and Global Land Cover Map for the year 2005 by ESA (GLOBCOVER). This study aimed to make the hierarchical reliable area in global scale, by comparing these six existing global land cover maps. There are two main problems that we have to deal with. First, the global cover maps with different resolutions. Actually, GLOBCOVER with resolution of 300m, is different with others. Second, these global cover maps have different legends. And, for comparing them, it is necessary to know the relationship between all the legends of each map.

Keywords **:** global land cover, LCCS, relatively reliable area

1. Introduction

In 2008, two new global land cover maps had become available: GLOBCOVER, and GLCNMO. Until now, six global land cover projects have been available (IGBP-DISCover, UMd, MODIS, GLC2000). A global land cover project always costs a long time, and its accuracy is not so high (70%, or a little higher). For improve the accuracy, a lot of devices have been done. For example, using different classification methods, using multiple data sources (special maps, Google Earth, and so on) to select the training data, etc. As a new idea, this study is trying to compare these existing global land cover maps. Appropriately, we aim to make the relative reliable area map.

2. Data

We used six global land cover maps as follows.

IGBP-DISCover(v2.0): 1 km resolution global land cover product, derived using the data from the Advanced Very High Resolution Radiometer (AVHRR) from 1992 to 1993, distinguished 17 classes , and produced by the U.S. Geological Survey for the International Geosphere– Biosphere Programme.

UMd: 1 km resolution global land cover product, derived using the same data from AVHRR, distinguished 14 classes, produced by the University of Maryland.

MODIS(V004): 1 km resolution global land cover product, derived using 2001 data from Moderate Resolution Imaging Spectrometer (MODIS), generated by Boston University

GLC2000(v1.1): 1 km resolution global land cover product, derived using the data from SPOT-VEGETATION data from November 1999 to December 2000, with 22 classes, implemented by The Joint Research Center (JRC) of the European produced by the Global Mapping Project of National Mapping Organizations Commission (EC), and in partnership with more than 30 partner institutions around the world.

GLOBCOVER(v2.0): 300m resolution global land cover product, derived using the data from an automatic and regionally-tuned classification of a MERIS FR time series from December 2004 to June 2006, with 22 classes, was an ESA initiative in partnership with JRC, EEA, FAO, UNEP, GOFC-GOLD and IGBP.

GLCNMO: 1 km resolution global land cover product, derived using 2003 data from MODIS, with 20 classes.

3. Problems

i) The six global cover maps with different resolutions. Actually, GLOBCOVER with 300m resolution, that is different with others. Second, these maps have different classification systems (both the number of classes and the definition of the classes are different).

ii) More complex, the classification system. There're mainly two kinds of classifications: IGBP classification and LCCS (Land Cover Classification

System, by by Food and Agriculture Organization (FAO) and the United Nations Environment Programme (UNEP)). In fact, The IGBP DISCover classes are of the IGBP classification scheme. MODIS primarily used the IGBP classification system (Loveland et al., 2000). And, the UMd classes largely conform to the IGBP scheme (HANSEN, 2000).While, the GLC-2000, GLOBCOVER, and GLCNMO used a classification system based on LCCS.

4. Methodology

The GLOBCOVER has resolution of 300m. There' re 129600 × 43200 pixels in the GLOBCOVER, while other fives have 43200×21600 pixels. So, we increase the number of pixels of five maps to three times. In other words, we resampled five maps to make 300m resolution.

Another problem, these maps have different classification systems. The work of the LCCS translation process has been done. In detail, use LCCS software to translate the legends (see [1]). However, the translation is not straightforward, because that the definition of the class of IGBP is not perfectly match with that of LCCS. Moreover, for example, in GLCNMO, the class 'Wetland' (Lcc formula: A1A20B1-R1 // A1A20B1-R2 // A2A20B4), corresponds to both class 'Closed to open (>15%) herbaceous vegetation (grassland, savannas or lichens/mosses)' (Lcc formula: A2A20B4) and 'Closed to open (>15%) grassland or woody vegetation on regularly flooded or waterlogged soil - Fresh, brackish or saline water' (Lcc formula: A4A20B3C1 // A4A20B3C2 // A2A20B4C3 // A2A20B4C1 // A2A20B4C2 // A4A20B3C3), which is in GLOBCOVER. So, we make the agreement with that one class may corresponds two or more classes, which in another map. And, comparative lists between the six maps' legends have been built (see [2]).

According to the comparative lists, we make the pixel-by-pixel comparison of six maps which are in same size. Finally, a relative reliable area map was completed (Fig. 1).

5. Conclusion

According to these hierarchical areas, both data producer and users may use the relative 'high reliable area' to select training data in future work, validation data, etc; and pay more attention to 'different area'. A reclassification for a certain region or a special class from analyzing the 'different area' will also be considered.

References

[1] M.Herold, R.Hubald, and A.Di Gregororio, 2009. Translating and evaluating land cover legends using the UN Land Cover Classification System (LCCS), GOFC-GOLD Report No. 43, June 2009.

[2] Global Map Version 1.3 Specifiations, Revised at 14th ISCGM meeting Cambridge, 14 July 2007

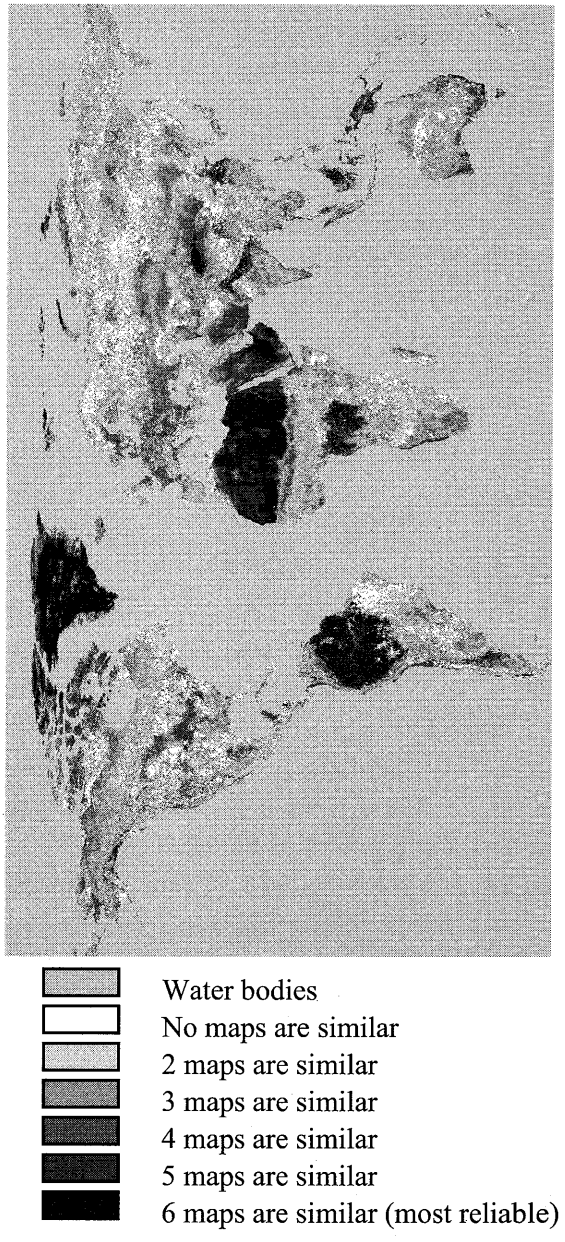

Fig. 1 Agreement in six global land cover maps

Characteristics of Backscattering Coefficients over Different Vegetation Land Covers Derived from TRMM/PR

Junichi NAGAOKA[1], Munehisa K. YAMAMOTO[2], and Atsushi HIGUCHI[3]

[1]*Graduate School of Science, Chiba University*
(1-33, Yayoi-cho, Inage-ku, Chiba, 263-8522, Japan), nagaoka@graduate.chiba-u.jp
[2]*Center for Environmental Remote Sensing (CEReS), Chiba University*
(1-33, Yayoi-cho, Inage-ku, Chiba, 263-8522, Japan), mkyamamoto@faculty.chiba-u.jp
[3]*CEReS, Chiba University (1-33, Yayoi-cho, Inage-ku, Chiba, 263-8522, Japan), higu@faculty.chiba-u.jp*

Abstract

The characteristics of backscattering coefficients (σ^0) observed by the Tropical Rainfall Measuring Mission (TRMM) / Precipitation Radar (PR) were investigated for different vegetation covers; evergreen broadleaf forests (ebf), woody savannas, savannas, open shrublands, and grasslands in Africa. For ebf, σ^0 decreases rapidly from nadir to 3°, then the rest of the angles are constant. On the other hand, σ^0 gradually decreases from nadir to 17° for savannas, open shrublands, and grasslands. For woody savannas, σ^0 value for each angle bin in the dry season is similar to that for savannas, but the characteristics of σ^0 in the rainy season is similar to that for ebf. The maximum monthly mean precipitation corresponds to that of σ^0 at nadir and 17° for grasslands and savannas. For grasslands, σ^0 at 3° does not increase that is likely to be saturated from the dry season to the rainy season when Leaf Are Index (LAI) is more than 0.5. Seasonal variations of σ^0 do not clearly correspond to that of precipitation for ebf where LAI is more than 3. It implies that σ^0 at 3° is susceptible to vegetation canopy. It suggests that the combination of 3° and 17° of σ^0 enable to classify vegetation land covers.

Keywords **:** TRMM/PR, backscattering coefficients, vegetation land covers, incident angle dependency, seasonal variation

1. Introduction

Satellite microwave remote sensing has attracted a lot of attention as one of methods for collecting global information on land surface. The Tropical Rainfall Measuring Mission (TRMM) has on board Precipitation Radar (PR) that is the first spaceborne rain radar. The TRMM PR observes backscattering not only from rain particles but also from surface to estimate path integrated attenuation (PIA) by a surface reference technique (SRT) [1]. Thus, it is possible to monitor land surface from surface backscattering coefficient (σ^0) by PR. Some previous studies applied TRMM PR signals for monitoring land surfaces. Seto et al. [2] investigated characteristics of σ^0 by TRMM PR as a basic of soil moisture estimation. Hirabayashi et al. [3] produced a land cover map from σ^0 observed by TRMM PR. Satake and Hanado[4] showed a diurnal variation in σ^0 over the Amazon rain forest, and they concluded that the increase of σ^0 in the early morning is probably caused by dewdrops on leaves. The characteristics of σ^0 over vegetation land covers are however still far from fully understood. The objective of this study is to reveal the characteristics of σ^0 over different vegetation land covers.

2. Data

2.1 TRMM/PR

The TRMM PR employs 13.8 GHz (Ku band) microwave with Horizontal transmit-Horizontal receive polarization[5]. The PR antenna beam scans in the cross-track direction over ±17° that has 220 km swath width. The antenna width of the PR is 0.71° and there are 49 observation angle bins within the scanning angle of ±17° (e.g., the angle bins 1, 25, and 49 correspond to -17°, 0°, and +17°, respectively). The horizontal resolution (footprint size) is 4.3 km at nadir and about 5 km at the scan edge in initial orbit altitude (350 km).

In this study, σ^0 from 2A25 standard product (Ver. 6) were used. In addition, σ^0 under no rain were used if rain flag from 2A23 standard product (Ver. 6) shows "no rain" or "rain possible". The analyzed periods were from 1998 to 2007.

2.2 Precipitation and Leaf Area Index (LAI)

Precipitation data from 3B43 product[6] (monthly 0.25° merged TRMM and other satellites estimation) were used. The Moderate Resolution Imaging Spectroradiometer (MODIS) LAI product (MOD15A2; Version 5) [7] were used. The LAI in MOD15A2 is defined as one sided green leaf

area per area (unit: m^2/m^2). The product is 8-days composite with 1 km resolution. The data were converted from 1 km to 0.25° grid to set the same resolution of the precipitation data.

2.3 Land Cover (IGBP.EcoMap)

The One-Minute Land Ecosystem Classification Product is a global (static map) data set provided by the International Geosphere-Biosphere Programme (IGBP) with an equal-angle rectangular grid at 1-minute resolution. IGBP.EcoMap classifies land covers into 17 categories. The targets in this study are evergreen broadleaf forest (ebf), woody savannas, savannas, open shrublands, and grasslands in Africa. The 5-biomes Africa map is shown in Fig. 1.

2.4 Uniform σ^0

Previous study[4] pointed out that σ^0 mixed both forest and river in the Instantaneous Field Of View (IFOV) of PR is higher than σ^0 that in just forest area. In order to obtain pure σ^0 of land covers such as ebf and grasslands, mixed areas in land covers using IGBP.EcoMap in 5 × 5 pixels (about 5 km × 5 km) was excluded

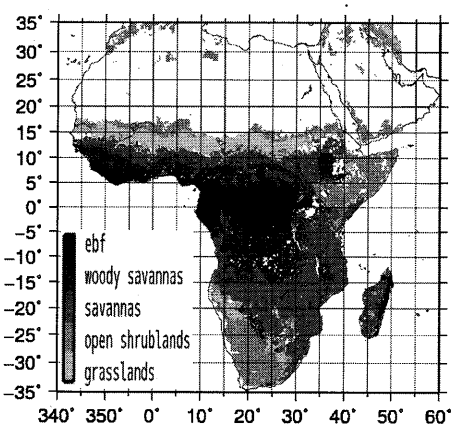

Fig. 1. 0.25° grid 5-biomes map used by IGBP.EcoMap. White pixels display other land covers such as barren and water.

3. Results and Discussion

3.1 Incident Angle Dependency of σ^0 and Seasonal Variations

In order to compare the differences in surface conditions between in the wet and dry seasons, σ^0 every incident angles are investigated. Seasonal variations of σ^0 for different incident angles are also compared to those in precipitation and LAI for 3 vegetation land covers.

3.1.1 ebf (0-5°S, 20-25°E)

σ^0 rapidly decreases from nadir to 3°, then is almost constant (about -2 dB) regardless of the seasons (Fig. 2. (a)). The seasonal variation of σ^0 for all angles is very small (Fig. 2. (b)). σ^0 does not have clear relation both precipitation and LAI.

3.1.2 grasslands (10-15°N, 5-15°E)

σ^0 in dry month decreases from nadir to 5°, and is almost constant from 7° to 10°, then decreases to 17° (Fig. 3. (a)). In contrast, σ^0 in rainy month gradually decreases from nadir to 17°. σ^0 at nadir in grasslands is higher than that in ebf, but σ^0 at more than 10° in grasslands is lower than that in ebf.

The phase at seasonal variation of σ^0 at nadir and 17° is similar to that of precipitation (Fig. 3. (b)). The higher precipitation, the higher soil moisture. This implies that σ^0 is affected by soil moisture depends on precipitation. On the other hand, the month of maximum σ^0 at 3° does not correspond to that of precipitation, when LAI is more than 0.5. It implies that σ^0 at 3° is susceptible to vegetation canopy. In addition, the seasonal variation of σ^0 at 12° is very small.

3.1.3 woody savannas (5-10°S, 20-25°E)

There is the largest difference between σ^0 at more than 10° in the rainy month and those in the dry month in the other vegetation covers (Fig. 4. (a)). The incident angle dependency of σ^0 in the dry month is similar to that for savannas (not shown), but that in the rainy month is similar to that for ebf. Comparing to savannas, land surface in woody savannas in the rainy season are covered by leaves of forests and grass. It shows land surface in the rainy month became rough. There is not clear relation between σ^0 at nadir and both precipitation and LAI (Fig. 4. (b)). However, the seasonal variation of σ^0 at 17° corresponds to precipitation. It implies that σ^0 is affected by soil moisture.

3.2 Cluster Analysis

Figure 5 shows a scatter diagram (feature space) between annual mean σ^0 at 3° and annual mean σ^0 at 17° and the distribution in Africa after the k-means cluster analysis. The dynamic range of σ^0 at 3° is larger than that of σ^0 at 17°, but the most of data of σ^0 at 3° distributes from -2 to 2 dB. As a result, ebfs such as Congo, the West Africa coast, and Madagascar are classified in class 4 (σ^0 at 3° is low and σ^0 at 17° is high). The west sides in Sahel (11-13°N, 5-10°E) are classified in class 3. In contrast, the east sides in Sahel (12-14°N, 15-20°E) are classified in class 2. σ^0 at 17° in the west sides is higher than that in the east sides (not shown). In addition, precipitation in the west sides is higher than that in the east sides (not shown). It implies that soil moisture in the west sides is higher than that in the east sides.

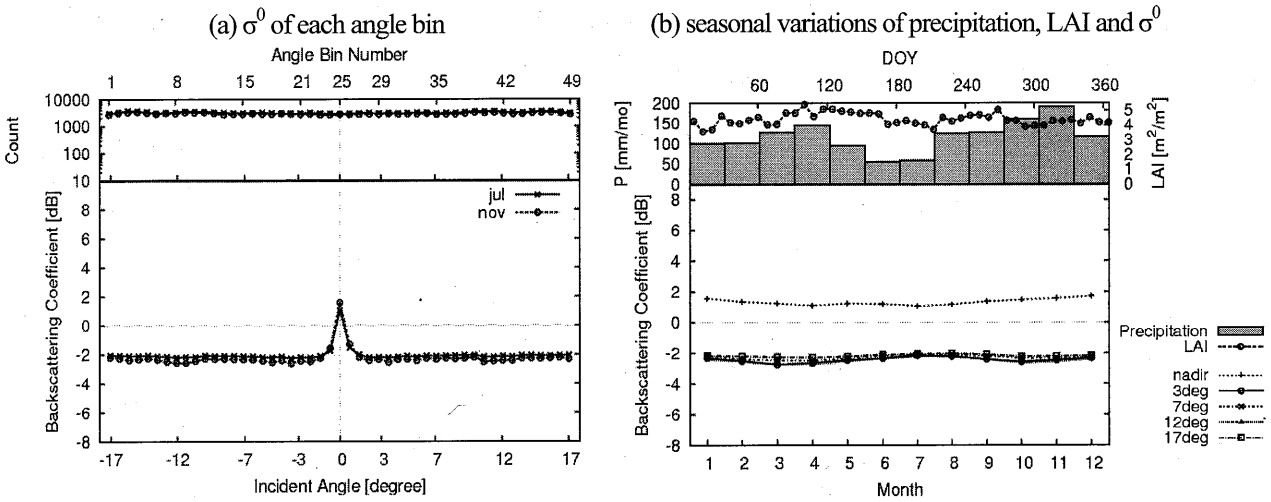

Fig. 2. σ^0 of each angle bin and seasonal variations of precipitation, LAI, and σ^0 for 5 angles for ebf.

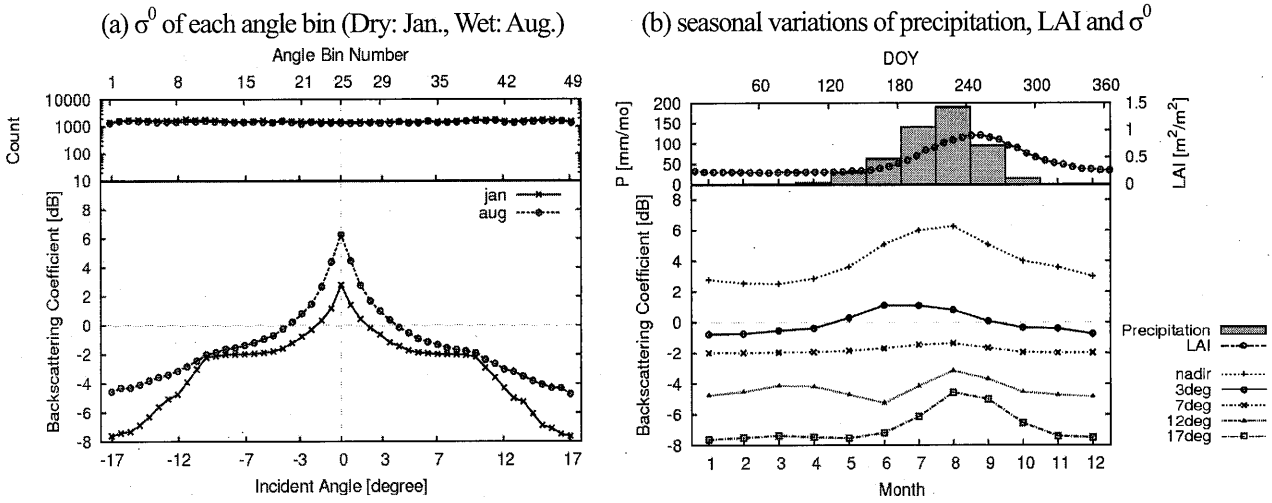

Fig. 3. The same as Fig. 2 but for grassland.

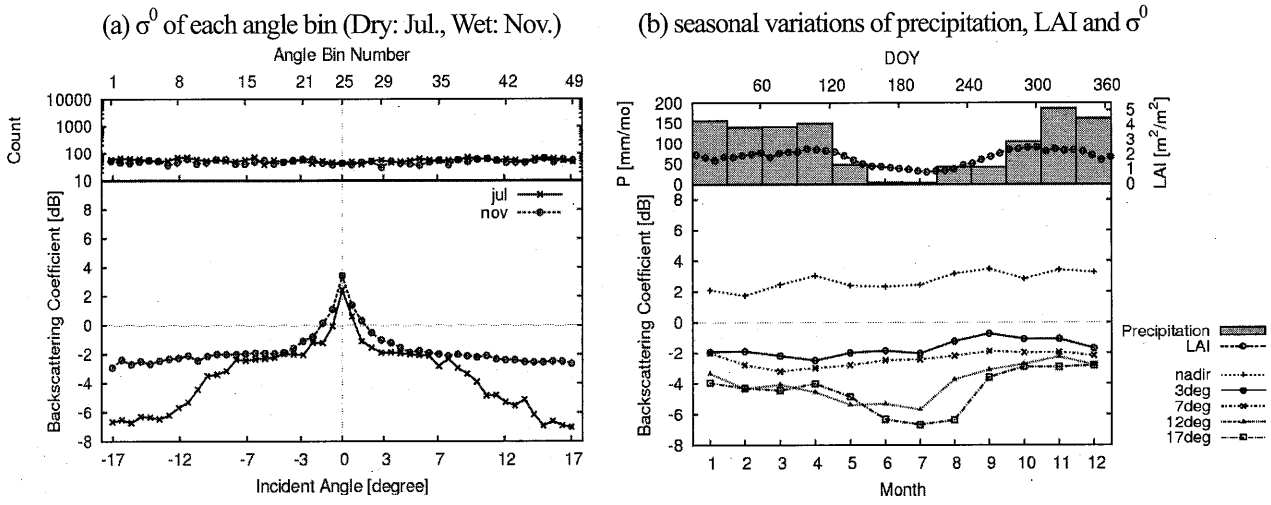

Fig. 4. The same as Fig. 2 but for woody savannas.

(a) Feature space

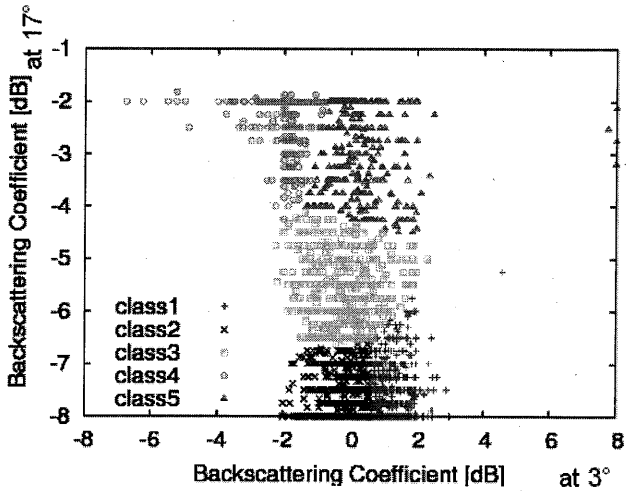

(b) Classification map by k-mean method

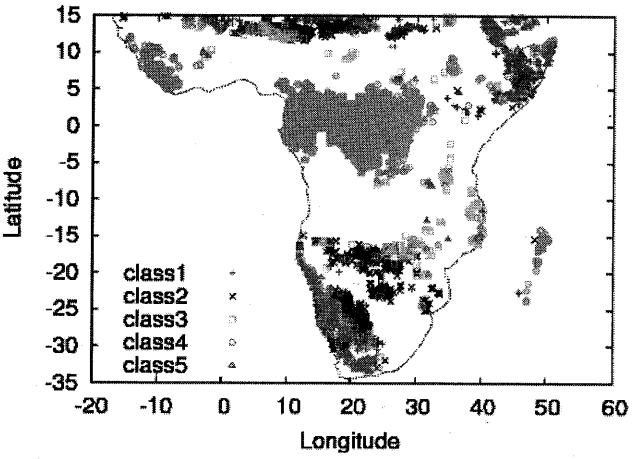

Fig. 5. Classification results using annual mean σ^0 at 3° and 17°. (a) feature space (the abscissa is σ^0 at 3°, the ordinate is σ^0 at 17°.), and (b) Classification map by k-mean method, k=5.

4. Conclusions

The incident angle dependency of σ^0 for woody savannas in the dry month is similar to that for savannas, but that in the rainy month is similar to that for ebf. The month of maximum σ^0 at nadir and 17° corresponds to that of precipitation. It implies that σ^0 is affected by soil moisture. On the other hand, the month of maximum ^{0} at 3° does not correspond to that of precipitation. It implies that σ^0 at 3° is susceptible to vegetation canopy. It suggests that the combination of 3° and 17° of σ^0 enable to classify vegetation land covers.

Acknowledgements

TRMM products were provided by the National Aeronautics and Space Administration (NASA) and the Japan Aerospace Exploration Agency (JAXA). MODIS products were provided by NASA.

References

1) T. Iguchi, T. Kozu, R. Meneghini, J. Awaka, and K. Okamoto: Rain-profiling algorithm for TRMM precipitation radar, J. Appl. Meteor., 39, pp. 2038-2052, 2000.

2) S. Seto, T. Nakaegawa, T. Oki, and K. Musiake: Characteristics of backscattering coefficients at different land covers observed by TRMM-PR, Annual Journal of Hydraulic Engineering, 43, pp. 223-226, 1999 (written in Japanese).

3) Y. Hirabayashi, S. Seto, S. Kanae, T. Oki, and K. Musiake: Analyses of global land cover information using backscattering coefficients by TRMM-PR, Annual Journal of Hydraulic Engineering, 44, pp. 259-264, 2000, (written in Japanese).

4) M. Satake and H. Hanado: Diurnal change of Amazon rain forest σ^0 observed by Ku-band spaceborne radar, IEEE Trans. Geosci. Remote Sens., 42 (6), pp. 1127-1134, 2004.

5) T. Kozu, T. Kawanishi, H. Kuroiwa, M. Kojima, K. Oikawa, H. Kumagai, K. Okamoto, M. Okumura, H. Nakatsuka, and K. Nishikawa: Development of precipitation radar onboard the Tropical Rainfall Measuring Mission (TRMM) satellite, IEEE Trans. Geosci. Remote Sens., 39 (1), pp. 102-116, 2001.

6) G. J. Huffman, R. F. Adler, D. T. Bolvin, G. Gu, E. J. Nelkin, K. P. Bowman, Y. Hong, E. F. Stocker, and D. B. Wolff: The TRMM multisatellite precipitation analysis (TMPA): Quasi-global, multiyear, combined-sensor precipitation estimates at fine scales, J. Hydrometeor., 8, pp. 38-55, 2006.

7) R. B. Myneni, S. Hoffman, Y. Knyazikhin, J. L. Privette, J. Glassy, Y. Tian, Y. Wang, X. Song, Y. Zhang, G. R. Smith, A. Lotsch, M. Friedl, J. T. Morisett, P. Votava, R. R. Nemani, and S. W. Running: Global products of vegetation leaf area and fraction absorbed PAR from year one of MODIS data, Remote Sens. Environ., 83, pp. 214-231, 2002.

Cropland area extraction in Northern Asia using MODIS 250 m data

Ts.Enkhzaya and R.Tateishi

Center for Environmental Remote Sensing, Chiba University,
1-33, Yayoi-cho, Inage-ku, Chiba, 263-8522, Japan
E-mail: tse_enkhzaya@graduate.chiba-u.jp

Abstract

Accurate identification of cropland from natural vegetated cover is important task in semi-arid area, however the identification of cropland from natural vegetated area is not easy because of their similar characteristics.

This research tried to examine the potential of the MODIS 16-day composite 250 m time-series data (MOD13Q1) to dryland cropping phenology and discriminate the cropland from natural vegetated area throughout the northern part of Asia. Phenology based NDVI results indicate that the consequence of MODIS images have high potential for large scale monitoring.

Keywords **:** cropland, semi-arid area, cropping phenology, MODIS data

1. Introduction

Identification of cropland distribution from natural vegetated cover is important task to agricultural management, land degradation therefore to making social and economic decisions. But in semi-arid area, the identification of cropland from natural vegetated area is not easy because of their similar characteristics in the growing season. Past large scale mapping efforts have developed mostly at low spatial resolution and have low accuracy in some similar classes. The development of a large-scale crop mapping methodology is challenging because it requires remotely sensed data that have large geographic coverage, high temporal resolution, adequate spatial resolution relative to the typical field size, and minimal cost.

Recent studies have indicated that the time series MODIS NDVI data has high potential for mapping crops and estimation of seasonal biophysical changes of vegetation at a moderate spatial resolution and high temporal resolution attributes that corresponding to relatively homogeneous land cover types and major phonological events.

This study aims to evaluate the ability to discriminate the cropland from natural vegetated area based on their growth phenological information with MODIS NDVI data.

2. Study area

The study area covers northern part of Asia for 40N to 60N at latitude, 62d15E to 141d35E at longitude. It incorporates full territory of Mongolia and some parts of few countries such as: Russia, Kazakhstan, China, and North Korea. The geographic location and climate variables throughout the study site show large variance.

Climatically this region belongs from continental temperate zone to arid and semiarid zone that characterized by cold winter and hot summers have large daily and seasonal temperature ranges. Amount of rainfall is also different in each zone. Major land cover types are forest, cropland, urban, water, steppe, sparse vegetated and desert. Growing season lasts from May until September. Cropping systems are mostly characterized as rain-fed cultivation, single crop per year that cultivating wheat, barley, cotton, vegetables, fodder and rice.

3. Data description and preprocessing

3.1. MODIS NDVI images

For this study, we selected multi-temporal images from NAS Terra/MODIS (AM-1) satellite. MODIS images are acquired from Land Processes Distributed Active Archive Center (LP DAAC) located at the USGS Earth Resources Observation and Science (EROS) Center at free of charge. Acquired MODIS data (MOD13Q1) are validated at stage 2 and it covers 12 tiles for h21v03, h27-v04, and h22 to h26, v03 to v04. The tiles are mosaicked and resampled from integerized sinusoidal grid projection (SIN) to geographic projection using nearest neighbor method.

Quality analysis (QA) data included in the VI product indicate the quality of the input data. In a first step, we used

this data to identify less clouded or snow covered periods by visual and statistical examinations. Most area is covered by snow in winter season, thus this study selected the images of May to October. Cloud covered area masked out in selected periods. Noise and poor quality pixels that are determined by quality information and not detected anomalous high and low values are smoothed using median filter algorithm.

3.2. MODIS land water mask

Newly released MODIS 250 m land-water mask (MOD44W) data used to extract water area.

3.3. Landsat images and existing maps

Landsat ETM+ images acquired from the EROS Data Center's Global Land Cover Facility and cropland maps at a country and regional level are used as the reference for identifying training sites for each class. Global land cover maps of IGBP DIScover, Boston University and university of Maryland are used to extract training area for natural vegetated classes.

4. Methodology

Training data is divided into two main groups: cropland and non-cropland. For cropland area, existing maps of country and regional level and 30 m resolution LANDSAT ETM+ images are used. After identification of cropland on the existing maps, 30 m LANDSAT ETM+ images downloaded and used to draw polygons. For collection of non-cropland area, filtered MODIS NDVI and global scale existing maps are used. Composite images of NDVI from May to October are classified using K-means clustering method and divided it into 50 classes. Extracted classes are grouped into two classes of forest and natural vegetated class using common area of above three global maps. All training data for cropland and non-cropland are then divided more classes based on their NDVI profiles.

Water is masked out using MODIS mask image while bare land is eliminated using MODIS NDVI images with thresholds lower than 0.3 for whole period.

5. Analysis

Seasonal profiles of NDVI in selected classes give more detailed information. Training area of all cropland is finally grouped into seven types based on their temporal profiles. For forest cover, 25 types are distinguished, while non-forest and natural vegetated classes grouped into 79 types.

Using multi-temporal profile of NDVI, we identified the important phenological parameters such as start of greenness, end of greenness and length of growing season to differentiate the selected classes.

Forest covers have distinct characteristics compare to other classes that greenness start from April, end September to October and growing season continues 4.5 - 6 months.

Natural vegetated classes have large variation in these parameters and show very similar sign with cropland. Vegetation greenness starts from April-May and ends in August-September and continues 3-6 months. Main difference of these two classes was length of the growing season. The cropland is plowed for planting in the last week of May and it greens up later than natural vegetated area and have 3-4 months length.

6. Results and conclusions

In this study, we attempt to differentiate rain-fed cropland and natural vegetated classes at phenological growth stages using spectral characteristic information extracted from remote sensing based variables. A time-series profile of NDVI is a good reflector to vegetation growing regularity. Phenology based results indicate that the consequence MODIS images have potential for large scale monitoring over short growing season.

7. References

1) Brian D. Wardlow, Jude H. Kastens and Stephen L. Egbert. Using USDA Crop Progress Data for the Evaluation of Greenup Onset Date Calculated from MODIS 250-Meter Data. Photogrammetric Engineering & Remote Sensing Vol. 72, No. 11, November 2006, pp. 1225–1234

2) Huete,A., Didan, T.Miura, E.P.Rodriues X. Gao and L.G. Ferreira. Overview of the radiometric and biophysical performance of the MODIS vegetation indices, Remote Sensing of Environment 83, pp. 195–213

3) Jonsson, P., and L. Eklundh, 2002. Seasonality extraction by function fitting to time-series of satellite sensor data. IEEE Transactions on Geoscience and Remote Sensing 40, pp.1824–1832.

4) Jonsson, P and Eklundh. L, 2004. TIMESAT - a program for analyzing time-series of satellite sensor data. Computers & Geosciences 30, pp 833-845

5) Knight, J.F., R.L. Lunetta, J. Ediriwickrema, and S. Khorram, 2006. Regional scale land-cover characterization using MODIS-NDVI 250 m multi-temporal imagery: A phenology based approach. GIScience and Remote Sensing, 43 (1), 1-23.

Analysis of skylight spectra for aerosol characterization and its application to multi-axis differential optical absorption spectroscopy

Naohiro Manago, Kenji Kuriyama, Yasuto Kaba, Shuji Miyazawa, Hiroaki Kuze
Center for Environmental Remote Sensing, Chiba University, Japan

Abstract

Skylight spectra reflect optical properties of aerosols as well as those of molecular species, and these properties can be retrieved by comparing observed and simulated spectra. Using the scheme of multi-axis differential optical absorption spectroscopy (MAX-DOAS), we can obtain skylight spectra using compact spectroradiometers. The data are analyzed by means of our recent method based on calculation with the radiative transfer code MODTRAN4. In this report, we describe a method to calculate effects of aerosols and molecular absorption using MODTRAN4 and its application to analyze spectral data obtained from MAX-DOAS measurements.

Keywords **:** skylight, radiation transfer, aerosol extinction, molecular absorption

1. Introduction

Tropospheric aerosols have significant influence on the Earth's radiation budget both directly and indirectly [1]. In urban areas, aerosols in the atmospheric boundary layer occasionally cause health problems. Remote sensing data obtained from satellites are often subject to uncertainties of atmospheric conditions. It is important to measure the characteristics of tropospheric aerosols globally all the time, since they show significant variations both spatially and temporally. Direct solar radiation (DSR) as well as scattered solar radiation (SSR) reflect optical properties of molecules and aerosols, and they have been widely measured with instruments such as sunphotometers and skyradiometers [2,3]. Recently, we have developed a method for characterizing atmospheric properties using a compact, stand-alone spectroradiometer [4]. In this report, first we give a brief description of the method, and then, apply the method to analyze the data obtained by the multi-axis differential optical absorption (MAX-DOAS) schemes.

2. Methods

A portable spectroradiometer (EKO, MS-720) is used to measure the spectra of solar radiation. This instrument is capable of measuring both DSR and SSR in the wavelength range of 350 - 1050 nm. We also measure the aureole (AUR), the scattered light just around the sun. This AUR component is useful for the aerosol optical characterization, since it reinforces information on the forward scattering. Home-made baffle tubes are used to limit the field of view (FOV) of the instrument: 5 deg for DSR, 20 deg for SSR, and between 5-20 deg for aureole.

Measured spectra are reproduced by the radiative transfer code MODTRAN4 [5]. Since often small intensity changes due to aerosol extinction have to be measured with high accuracy, we make corrections for the characteristics of the instrument such as spectral sensitivity, temperature dependence, and optical resolution. Non-uniformity of the SSR and background light of the DSR inside the FOV are also corrected.

Input parameters for the simulation are modified iteratively so that simulated spectra match well with the measured spectra. The aerosol parameters that should be optimized through the fitting are (i) the aerosol optical depth (AOD) τ_{550} at wavelength 550 nm, (ii) wavelength dependence of the aerosol extinction coefficient $\alpha_{ext}(\lambda)$ (normalized against the value at 550 nm), (iii) wavelength dependence of the aerosol scattering coefficient $\alpha_{scat}(\lambda)$ (normalized against the extinction coefficient at 550 nm), and (iv) the phase function $f(\lambda, \chi)$ as a function of wavelength λ and scattering angle χ.

It is unacceptable to have too many or too few parameters for optimizing the matching result. After some trial and improvement, we have decided to introduce the three component aerosol model (TCAM), which is composed of 3 types of aerosol species, each having its own complex refractive index dependent on wavelength and its own mono-modal lognormal size distribution. The three species correspond to water soluble (component 1), sea salt (component 2), and soot (component 3) aerosol types, chosen from the aerosol database compiled by Levoni et al. [6]. Although the actual aerosol mixture is usually more complex, TCAM forms a "quasi-complete" basis for aerosol parameterization, in that optical parameters of most aerosols can be reproduced by linear combinations of the basis. Figure

1 (a-b) show the real and imaginary parts of the refractive index of the three basic components, and (c-e) show the possible range of optical parameters covered by the TCAM parameterization. Optical parameters of each component are calculated with the Mie-scattering code developed by Wiscombe [7], with the assumption of spherical shapes. Alternatively, they are calculated assuming randomly oriented spheroids with a fixed aspect ratio using the code developed by Dubovik et al. [8]. Optical parameters of the total mixture are calculated assuming external mixing.

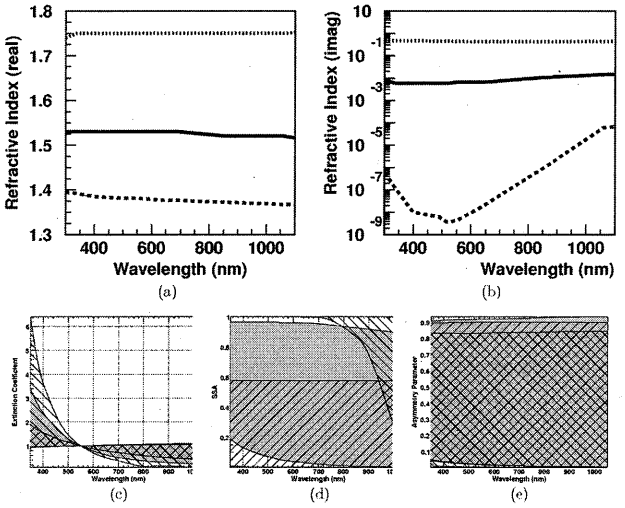

Fig. 1 Aerosol models assumed in the scheme of three-component aerosol model (TCAM). (a) Real part and (b) imaginary part of the complex refractive index as a function of wavelength; component 1 (water soluble, solid line), component 2 (oceanic, dotted line), and component 3 (soot, broken line). (c-e) Possible range of aerosol optical parameters calculated from each component of TCAM (gray area: component 1, 45◦ lines: component 2, 135◦ lines: component 3) assuming that the particle size changes between $10^{-2.5}$ and $10^{+1.5}$ μm: (c) extinction coefficient normalized at 550 nm, (d) single scattering albedo, and (e) asymmetry parameter.

Water vapor exhibits absorption bands with significant intensity in the measurement range of the spectroradiometer. Figure 2 shows an example of measured and simulated DSR spectra around 725 nm. In the simulation, water vapor column amount can be adjusted by modifying the water scale factor (WSF) S_w to scale the default column amount (2.92231 g/cm^2 for the mid-latitude summer model, and 0.85170 g/cm^2 for the mid-latitude winter model). The value of S_w can be optimized by fitting simulated DSR spectra

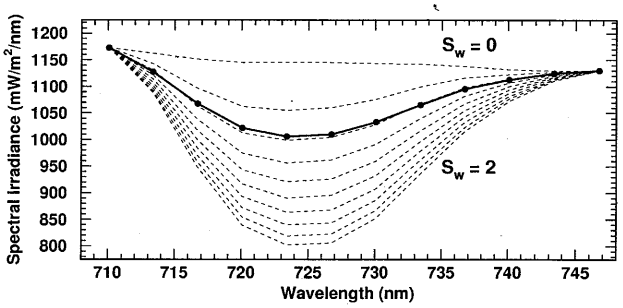

Fig. 2 Variation of spectral irradiance around 725 nm water absorption band for various values of the water scale factor S_w. Solid and dotted lines represent observed and simulated spectra, respectively. The 12 channels marked with filled circles were used for the analysis.

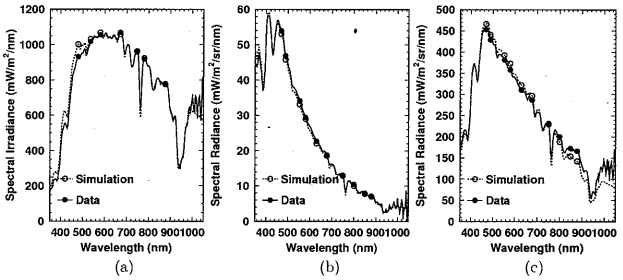

Fig. 3 Spectral matching for the spectra observed at 12:30 on December 30, 2008: (a) DSR, (b) SSR, and (c) AUR. The channels marked with circles were used for the analysis.

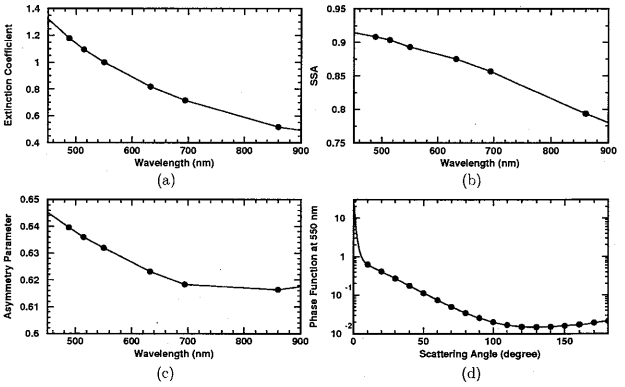

Fig. 4 Aerosol optical parameters derived from the DSR, SSR, and AUR observations on December 30, 2008: (a) extinction coefficient normalized at 550 nm, (b) single scattering albedo, (c) asymmetry parameter, and (d) phase function at 550 nm. Meteorological data at the observation site were: temperature 13.7 ◦C, relative humidity 47 %, pressure 1002.6 hPa, and wind speed 1.3 m/s.

to the measured ones. Prior to the fitting, simulated spectra are scaled to match with the measured ones at both ends of the absorption band. In this process, differences of the linear slopes due to, for example, disagreement of the aerosol model are removed. Note that optical resolution of the spectroradiometer must be correctly incorporated.

We applied the spectral matching method using the TCAM to the data taken at the Center for Environmental Remote Sensing (CEReS, 35.62° N, 140.10° E), Chiba University from 12:25 to 12:58 JST on December 30, 2008. Figure 3 shows the spectral matching between the observed and simulated spectra. We measured the aerosol optical depth (AOD) and water vapor column amount to be 0.190 ± 0.001, 0.80 ± 0.02 g/m^2, respectively.

3. Application to MAX-DOAS data

In the scheme of MAX-DOAS, we obtain skylight spectra from which we can retrieve column amount of molecules just like the way we retrieve water vapor column amount from DSR spectrum. Figure 5 shows the instrument developed for the MAX-DOAS measurement. Figure 6 shows an example spectrum taken at the CEReS site on May 5, 2009 (zenith/azimuth angle of the sun and that of the line of sight were 42°/195° and 32°/190°, respectively). Three spectroradiometers (Ocean Optics, USB2000: 280 - 740 nm, Ocean Optics, HR2000: 720 - 1080 nm, Hamamatsu, C9914GB: 1080 - 2100 nm) were used to obtain continuous spectra from 280 to 2100 nm. Optical resolutions of USB2000 and HR2000 are about 1 nm (FWHM), while that of the near-infrared (NIR) spectrometer (C9914GB) is about 8 nm. They are sensitive enough to get sufficient amount of light within 1 s exposure duration.

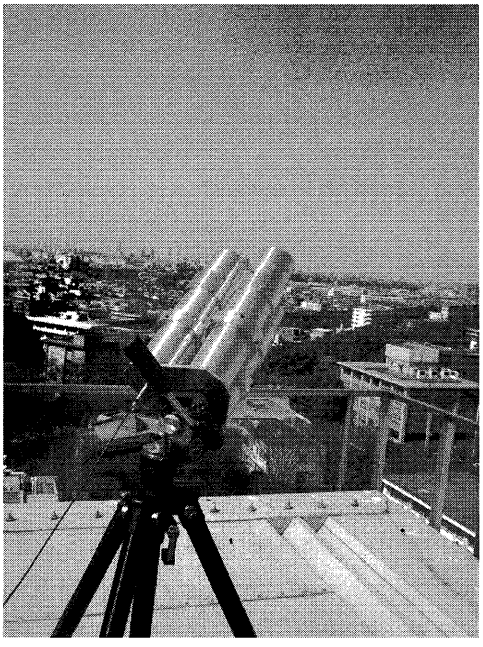

Fig. 5 MAX-DOAS instrument looking toward the sky. Incident lights are taken from the baffle tubes and transferred into the spectroradiometers through the optical fibers.

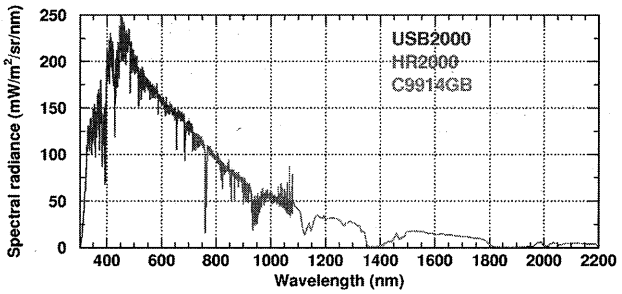

Fig. 6 Hyper-spectral measurement of scattered solar radiation using 3 spectroradiometers (USB2000, HR2000, and C9914GB) at 12:30 on May 5, 2009.

In this case, the spectrum to be simulated is not DSR but SSR, and it takes longer calculation time than DSR. If the DISORT algorithm [9] is used to evaluate multiple scattering contributions in the fitting procedure, it would take too much time. Fortunately, since simulated spectra are scaled to match with the measured spectrum at the ends of the absorption band, we can use a faster algorithm, i.e., Isaacs algorithm [10], without any significant errors. As is the case for DSR, the optical resolution should be matched between the two spectra before the comparison is carried out.

We retrieved column amount of H_2O, O_3, CO_2, and CH_4 from the spectra as shown in Fig. 6. The results of spectrum matching for these molecules are shown in Figures 7-10, respectively. We obtained column amount as follows. H_2O: $0.45 \pm 4 \times 10^{-5}$ g/cm^2, O_3: $389 \pm 3 \times 10^{-2}$ DU, CO_2: $331 \pm 6 \times 10^{-2}$ ppm, CH_4: $1.9 \pm 8 \times 10^{-2}$ atm · cm. Here the error values are fitting errors only, and other systematic errors are

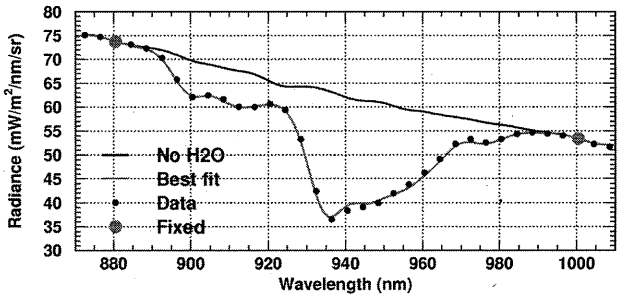

Fig. 7 Spectrum matching at the H_2O absorption band around 940 nm. Optical resolutions of both simulated and measured spectra are degraded to 8 nm.

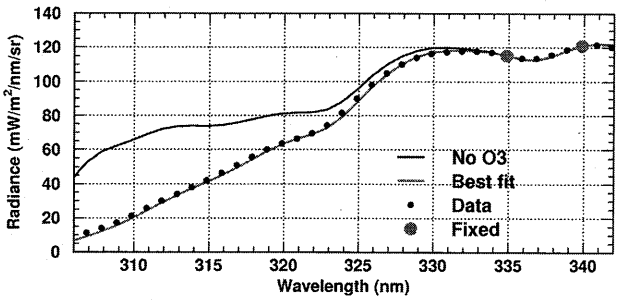

Fig. 8 Spectrum matching at the O_3 absorption band around 310 nm. Optical resolutions of both simulated and measured spectra are degraded to 4 nm.

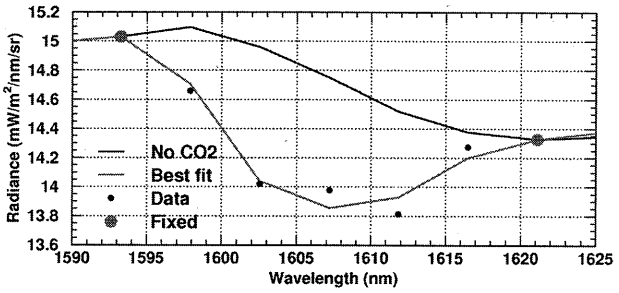

Fig. 9 Spectrum matching at the CO_2 absorption band around 1607 nm. Optical resolution of simulated spectrum is degraded to 8 nm.

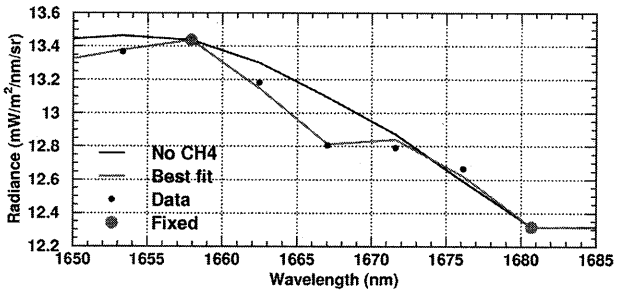

Fig. 10 Spectrum matching at the CH_4 absorption band around 1667 nm. Optical resolution of simulated spectrum is degraded to 8 nm.

not included. Obviously, the obtained value of CO_2 is too small. This is due to the lack of precise calibration of the NIR spectrometer at the present situation; besides, systematic errors cannot be avoided in the readings. Since strong signals are observed for the molecular species investigated here, it is expected that reliable values of column amounts can be retrieved after suitable calibration procedure.

4. Conclusion

We have explained the method to retrieve optical parameters of aerosols from sky-radiance measurements using radiative simulation code MODTRAN4. Similar method is applicable to retrieve column amount of atmospheric constituents from skylight spectra obtained in the scheme of MAX-DOAS measurement. We demonstrated the feasibility of retrieving column amount of H_2O, O_3, CO_2, and CH_4 from a continuous skylight spectrum between 280 and 2100 nm.

References

1) IPCC, Climate Change 2007: The Physical Science Basis (Cambridge University Press, Cambridge, United Kingdom, 2007).

2) T. Nakajima, et al., "Use of sky brightness measurements from ground for remote sensing of particulate polydispersions," Appl. Opt. 35, 2672–2686 (1996).

3) B. N. Holben, et al., "Aeronet – a federated instrument network and data archive for aerosol characterization," Remote Sensing of Environment 66, 1–16 (1998).

4) N. Manago and H. Kuze, "Determination of tropospheric aerosol characteristics by spectral measurements of solar radiation using a compact, stand-alone spectroradiometer," submitted to Applied Optics.

5) G P. Anderson, et al., "MODTRAN4 version 2: radiative transfer modeling," in "Proc. SPIE vol.4381," , S. S. Shen & M. R. Descour, ed. (2001), pp. 455–459.

6) C. Levoni, M. Cervino, R. Guzzi, and F. Torricella, "Atmospheric aerosol optical properties: a database of radiative characteristics for different components and classes," Appl. Opt. 36, 8031–8041 (1997).

7) W. J. Wiscombe, "Improved mie scattering algorithms," Appl. Opt. 19, 1505–1509 (1980).

8) O. Dubovik, et al., "Application of spheroid models to account for aerosol particle nonsphericity in remote sensing of desert dust," J. Geophys. Res. 111 (2006).

9) K. Stamnes, S.-C. Tsay, W. Wiscombe, and K. Jayaweera, "Numerically stable algorithm for discrete-ordinate-method radiative transfer in multiple scattering and emitting layered media," Appl. Opt. 27, 2502–2509 (1988).

10) R. G Isaacs, W.-C. Wang, R. D. Worsham, and S. Goldenberg, "Multiple scattering lowtran and fascode models," Appl. Opt. 26, 1272–1281 (1987).

Preliminary Remote Sensing Investigation towards Geological Mapping in Northwest Libya

N. M. Saadi, K. Watanabe and H. Mizunaga

Department of Earth Resources Engineering, Kyushu University, 744 Motooka, Nishi-Ku, Fukuoka 819-0395, Japan, Saadi-n@mine.kyushu-u.ac.jp

Abstract

This study presents a detailed analysis based on digital process of optical Landsat Enhanced Thematic Mapper Plus (ETM+) and radar (C-band Synthetic Aperture Radar (ERS-2 SAR)) remote sensing data, and digital elevation model (DEM) extracted from topographic maps (1:50,000) to evaluate their efficiency for geological mapping in the Jifara Plain of northwest Libya. Lithological and structural units were distinguishable based on their topographic form and spectral properties. GIS and remote sensing-based methods were used to integrate all raster and vector results extracted from multiple geoscientific data types. The results discriminated eighteen lithological units were plotted in the geological map defined by the new boundaries. The dominant extracted lineaments tend to run in the NW-SE direction. Analysis and interpretation of the extracted lineaments provided information about the tectonic evolution of the study area. Field work was done for ground-based verification of remote sensing data.

Keywords : ETM+, DEM, ERS-2 SAR, Image processing, Geological mapping

1. Introduction

The sensors of remote sensing satellites can image geological features based on their spatial and spectral resolution (Masoud and Koike, 2006 ; Yang et al., 2007; Saadi and Watanabe, 2008). Several analysis and image processes were implemented in this study to enhance the visual interpretation and discrimination of different lithological units and the extraction of geological lineaments in the Jifara Plain of northwest Libya. The Jifara Plain has been the subject of numerous geological studies by different geologists in the 1940s, 1960s, and 1970s (Lipparini, 1940; Jordi and Lonfat, 1963; Christie, 1966 ; El Hinnawy and Cheshitev, 1975; Antonovic, 1977).

In this study, an attempt has been made to use diverse data sets such as Landsat ETM+ image, ERS-2 SAR, and DEM data for further geological investigations. Remote sensing data processing and interpretation was applied in this study in three phases. During the first phase, distinguishing the spatial distribution of basalt flows, basalt cones and pholonite intrusions by integrating ETM+ thermal infrared (TIR) and visible-near infrared (VNIR) bands and ERS-2 SAR C-band (Leech et al., 2003; Cengiz et al., 2006; Pereira et al., 2008). The Intensity-Hue-Saturation (IHS) transformation was used to fuse the optical and radar data (Mather, 2004). Basically, data fusion techniques used to improve the spatial and spectral resolution of remote sensing data by combining multi-satellite images (Jensen, 1996; Solberg, 2006). In the second phase, a series of landform interpretation experiments was conducted on the ETM+ images by using different False Color Composites (FCC) (Gibson and Power, 2000; Hoffman and Markman, 2001) and Principal Component Analysis (PCA) (Chen , 2006) for further lithological units recognition. In the third phase, extracting and mapping geological lineaments using DEM data extracted from topographic maps (1:50,000). The DEM were used to overcome the obscuring effects of artificial features in order to extract geological lineaments (Gloaguen et al., 2007 ; Demirkesen, 2008). Calculating and interpreting DEM derivatives including shaded relief maps and slope maps. The manual extraction criteria for the lineaments were based on photographic characteristics, including shape and geomorphologic features.

Field work was done to confirm the remote sensing implications by identifying lithological boundaries and determining the artificial lines, which could eventually generate edges on the remote sensing data.

The results discriminated eighteen rock units and sediments. These units were identified and plotted in the new geological map defined by new boundaries. More than six hundred geological lineaments were discriminated in the study area. The segregation of extracted lineaments into groups based on the age of the geological formations provided information about the tectonic structure of the study area.

2. Geological Setting

The study area lies in the northwestern part of Libya, bounded by longitudes 12°10′ E to 13°55′ E and latitudes

31°50′ N to 32°55′ N. It covers a surface area of approximately 20000 km2. It can be distinguished into three main Geomorphological units. These units are known as the Jifara Plain, the Scarp, and the Plateau. The Jifara Plain is bounded from the north by the Mediterranean Sea and from the south by the scarp of Jabal Nafusah (Conant and Goudarzi, 1967). The Jabal Nafusah runs approximately in an east-west direction from the Mediterranean Sea and westwards to beyond the Libyan border. It overlooks the Jifara Plain and rises above sea level for an elevation ranges from 500 to 700 meters (El Hinnawy and Cheshitev, 1975). The Plateau is a Questa made mainly of hard and resistant dolomitic limestone of Upper Cretaceous age. The southeast area is covered by basalt sheets with scattered black hills made of phonolite and basalt (Antonovic, 1977; Zivanovic, 1977).

The study area contains exposures of sedimentary rocks ranging in age from Triassic to Quaternary. The study area is characterized by uplifts, subsidences and block faulting (Miller, 1971; El Hinnawy and Cheshitev, 1975; Saadi et al., 2009).

3. Data Processing

The south region of the study area covered by basalt sheets with scattered black hills made of phonolite and basalt. The ETM+ TIR band was tested to discriminate multi volcanic rocks on the basis of an expected difference in emissivity with VNIR band-ratio (NIR/G) because of their higher spatial resolution and ERS-2 C band for discriminating different volcanic rocks on the basis of their surface roughness. For fusing images, the IHS–RGB transformation was used to display spectral variations in a single RGB color combination image. The hue defines the color based on the dominant wavelength; the saturation defines the purity of the color; the intensity defines the brightness (Mather, 2004). Hence, the multi-spectral information in the ETM+ data is used to define the hue and saturation while the radar data are used to define the intensity (Fig. 1).

Several false color composite (FCC) images using Landsat ETM+ were created to improve the visual interpretation. These band combinations included RGB-742, RGB-234, RGB-456, RGB-467, and RGB-367. The optimum index factor (OIF) method (Chavez et al., 1982) was used to calculate the variance of different band combinations. The VNIR bands have the advantage of preserving morphological features and displaying different lithological units in vivid different colors. Mid infrared band can be used to distinguish clay units because clay minerals have a significant absorption feature within this band (Sabins, 1997). Near infrared band is effective in mapping iron oxides because these minerals have high reflectance within this band (Abdelsalam et al. 2000). The bands MIR-NIR-G are effective in geological mapping in arid regions because of lack of vegetation (Fig. 2). Additionally, the first three PCA of ETM+ band-combinations were used to show the lithological units with vivid colors.

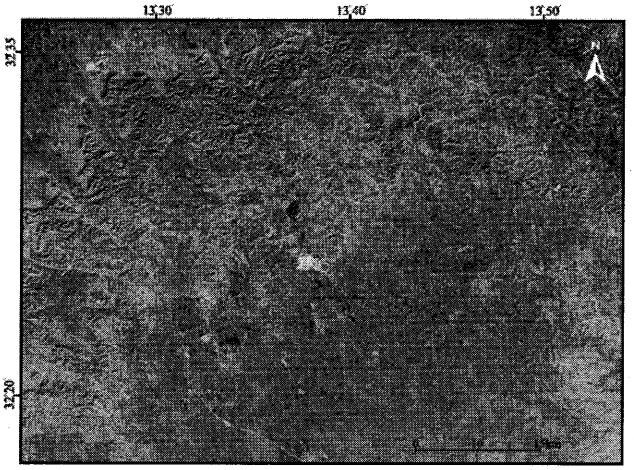

Fig. 1. Partial frame of RGB-IHS

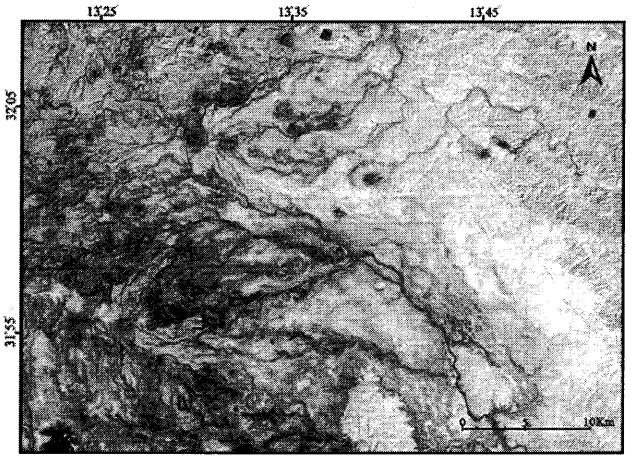

Fig. 2. Partial frame of FCC MIR-NIR-G

DEM constructed from topographic contour maps (1:50,000) (S.P.L.A.J., 1979). The contour interval of the topographic maps was 20 m, with supplementary contours at 10 m intervals. The produced DEM has a horizontal resolution of 20 m and a vertical resolution of 5 m. DEM data have been used to detect and map geological lineaments by calculating and interpreting DEM derivatives, including shaded relief maps and slope maps. In shaded relief maps, we experimented with the evaluation of an incoming illumination that is perpendicular to the prevailing trend of lineaments in the study area. According to the old geologic map of the study area, the prevailing lineaments trend in the NW-SE directions (I.R.C., 1975). Therefore, low incoming

solar r adiation from th e NE- NNE w as t ested to m itigate azimuth-biasing effects and enh ance th e vi sual det ection of linear features in t he dom inant tr end. A low sun-elevation angle (20° t o 30°) was u sed for lineament de tection in all directions (Fig. 3). Slope map was created using a quadratic fitted to a 3×3 kernel. The output image contains slope values that range from 0° (flat terrain) to 90° (vertical terrain) (Fig. 4). T opographic lin eaments can be di stinguished b y their elevation difference fro m the su rrounding terrain. These elevation changes can be represented as cha nges in colors in the slope map.

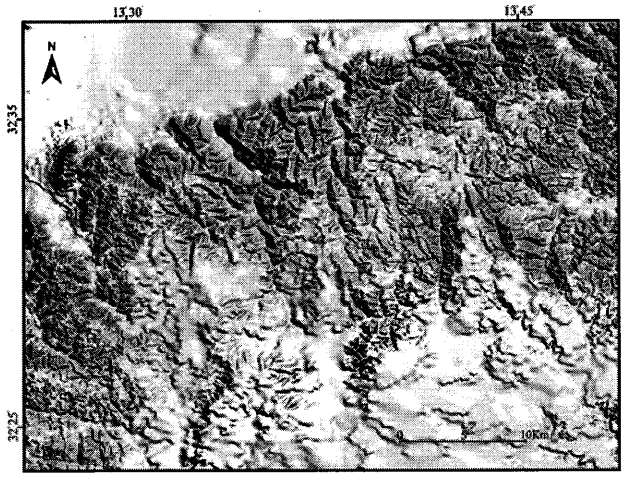

Fig. 3. Partial frame shaded relief map

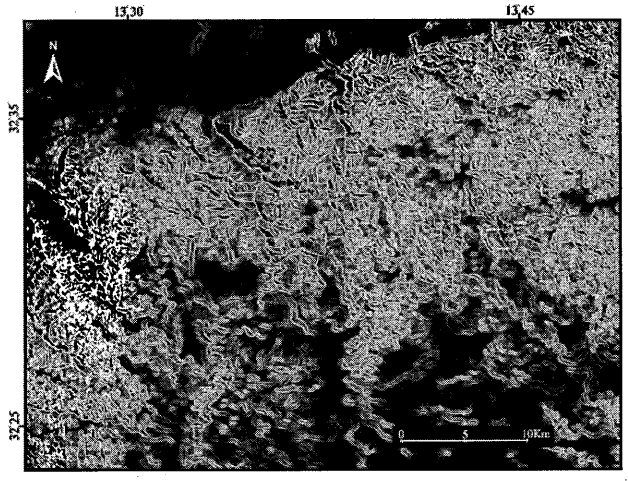

Fig. 4. Partial frame slope map

4. Results and Discussion

The general results indicate that ETM+, ERS-2, and DEM data are ab le to discriminate different rock units and ex tract geological lin eaments in the Ji fara Pla in. The foll owing eighteen rock and sediments units were identified and plotted on the new lithological map (Fig.5).

1- Al Az iziyah F ormation: T his u nit consists mainly of bedded li mestone charact erized by its dark grey colo r. This formation was recognized using FCC image RGB- MIR, NIR, and G
2- Abu Shaybah Formation: This unit consists of sandstone alternating wi th layers of cla ys and sc attered li mey bands. This f ormation w as re cognized using f used image RGB- TIR, VNIR, and ERS-2 C band.
3- Abu Ghaylan Fo rmation: This u nit con sists m ainly o f limestone. This fo rmation was reco gnized using FCC image RGB- NIR, TIR, and MIR.
4- Bir al Ghanam Formation: This unit consists mainly of white to g rey system. Thi s fo rmation wa s re cognized using f used image RG B- TIR, VNI R, a nd ERS-2 C band.
5- Takbal Fo rmation: Thi s unit consists of li mestone with clayey and m arly i ntercalations. This f ormation w as recognized using FC C image RG B- NIR , TIR , a nd MIR.
6- Sidi as Sid Fo rmation: Th is un it consists of limestone and m arl. Thi s fo rmation was recogni zed using FCC image RGB- NIR/G, MIR and TIR.
7- Nalut Formation: This u nit c onsists of lim estone and dolomitic limestone. Thi s fo rmation was recogni zed using FCC image RGB- NIR/G, MIR and TIR.
8- Qasr T igrinnah Formation: Th is uni t consists of a succession of s oft m arls and white to rosy lim estone. This formation was recognized using FCC image RGB- MIR, NIR, and G
9- Mizda Formation: This unit consists of marl, shale, and chalky limestone. This formation was recognized using FCC image RGB- NIR, TIR, and MIR.
10- Al Khums Formation: T his u nit co nsists of lim estone and algal li mestone. Thi s fo rmation was recogni zed using FCC image RGB- NIR/G, MIR and TIR.
11- Volcanic rock s: Thi s unit con sists of phono lite and trachyte intrusions, basalt cones, and basalt flo ws. This formation was recognized using fused image RGB- TIR, VNIR, and ERS-2 C band.
12- Quaternary: Fiv e types of Quatern ary sedi ments were discriminated a nd m apped: Q asr A l H aj F ormation, Jifara F ormation, S ebkha sediments, Fluv io-eolian sediments and Eo lian de posits. T hese sediments were recognized u sing FCC i mage RGB- NIR/G, M IR and TIR, RGB- MIR, NIR, a nd G, a nd fused image RGB- TIR, VNIR, and ERS-2 C band.

The RG B- TI R, VNIR, and ERS- 2 C ba nd and RGB- MIR, NI R, and G images p ermitted the s uccessful identification of lithological units in the study area.

Structurally, the DEM data id entified 641 geological

lineaments (Fig. 5). The low illumination angle was most suitable for detecting lineaments. Lineaments extracted from the DEM have different trends, but the main trend is NW-SE, parallel to the main tectonic line of the Jabal Uplift. The NE-SW lineaments represent a secondary trend. Lineaments extracted from the DEM were divided into six groups on the basis of the ages of the surrounding geological formations. Lineaments in the Upper Triassic rocks trend dominantly NW-SE. Lineaments in the Upper Triassic - Middle Jurassic rocks trend dominantly NW-SE. The prevailing trend of the Middle Jurassic rock lineaments is NE-SW. Lineaments in the Upper Cretaceous rocks are dominantly NW-SE. Lineaments in the Tertiary rocks are mostly NW-SE, with the NE-SW direction being subordinate. Lineaments in

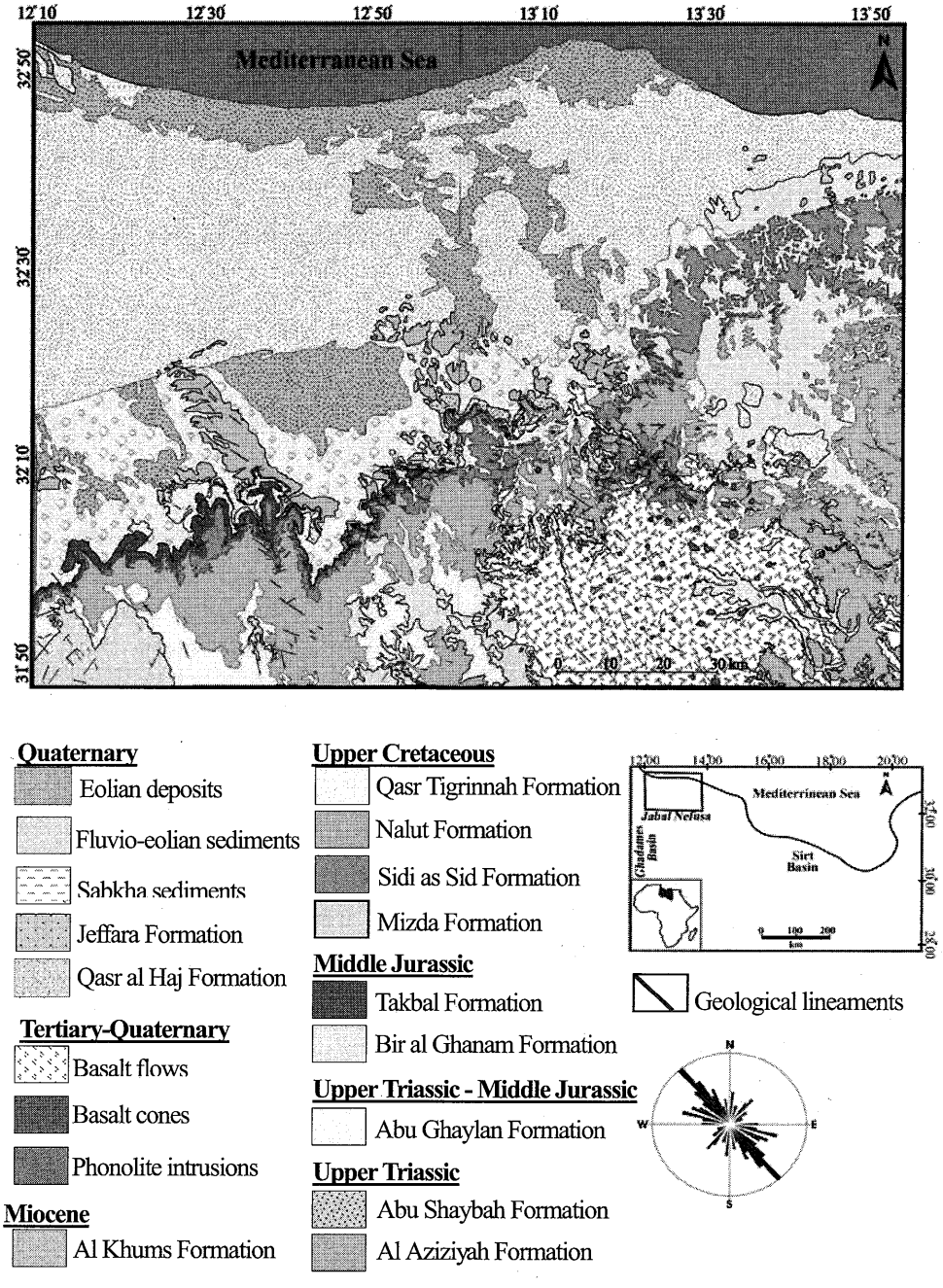

Fig. 5. Geologically interpreted map of the study area

Quaternary sedimentary units trend dominantly NW-SE. Analysis of extracted lineaments was based on the principle of cross-cutting relationships (Rowland and Du ebendorfer, 1994). Analysis and interpretation of the DEM results indicates that the different lengths of the NW-SE lineaments in the Upper Cretaceous rocks probably indicate reactivated faulting. Lithologically, the arrangement of phonolite hills and basalt cones in lines parallel to the dominant lineament trends (NW-SE) indicates that the volcanic activity is related to the tectonic activity of the Jabal Uplift.

Acknowledgements

This work was supported in part by the Japanese Society for the Promotion of Science (JSPS) and by the Global-Centre of Excellence in Novel Carbon Resource Sciences.

References

1) Abdelsalam, M.G., Stern, R.J., and Berhane, W.G., 2000. Mapping gossans in arid regions with Landsat TM and SIR-C images: the Beddaho alteration zone in northern Eritrea. Journal of African Earth Sciences, 30 (4), 903–916.
2) Antonovic, A., 1977. Geological map of Libya, explanatory booklet, sheet Mizdah NH 33-1," I.R.C., Tripoli.
3) Cengiz, O., Sener, E. and Yagmurlu, F., 2006. A satellite image approach to the study of lineaments, circular structures and regional geology in the Golcuk Crater district and its environs (Isparta, SW Turkey). Journal of Asian Earth Sciences, 27 (2), 155_163.
4) Chavez, P.S., Berlin, G.L., and Sowers, L.B., 1982. Statistical methods for selecting Landsat MSS ratios. Journal of Applied Photographic Engineering, 8, 23–30.
5) Chen, F.W., 2006. Satellite-based precipitation retrieval using neural networks, principal component analysis, and image sharpering. In: C.H. Chen, ed. Signal and image processing for remote sensing. Boca Raton, FL: CRC Press, 233–266.
6) Christie, A.M., 1966. Geology of Gharyan Area, Tripolitania, Libya. Ministry of Industry, Geological Section Bulletin, No. 5, Tripoli.
7) Conant, L.C. and Goudarzi, G.H., 1967. Stratigraphic and tectonic framework of Libya. AAPG Bull., vol. 51, no. 5, pp. 719–730.
8) Demirkesen, A.C., 2008. Digital terrain analysis using Landsat-7 ETM+ imagery and SRTM DEM: A case study of Nevsehir province (Cappadocia), Turkey. Int. J. Remote Sens., vol. 29, no. 14, pp. 4173–4188.
9) El Hinnawy, M. and Cheshitev, G., 1975. Geological map of Libya. Explanatory booklet, sheet Tarabulus NI 33_13. Industrial Research Centre, Tripoli.
10) Gibson, P.J. and Power, C.H., 2000. Introductory remote sensing. Digital image processing and applications. London: Routledge.
11) Gloaguen, R., Marpu, P.R. and Niemeyer, I., 2007. Automatic extraction of faults and fractal analysis from remote sensing data. Nonlinear Proc. Geoph., vol. 14, no. 2, 131–138.
12) Hoffman, R.R. and Markman, A.B., eds. 2001. Interpreting remote sensing imagery: human factors. Boca Raton, FL: Lewis Publishers.
13) Industrial Research Centre (I.R.C), 1975. Geological map of Libya, 1:250,000, sheet: Tarabulus, Tripoli-Libya.
14) Jensen, J.R., 1996. Introductory digital image processing. Prentice Hall Series in Geographic Information Science. 2nd Ed., New Jersey: Prentice Hall Publishers.
15) Jordi, H.A. and Lonfat, F., 1963. Stratigraphic subdivision and problems in Upper Cretaceous–Lower Tertiary deposits in Northwestern Libya. In Saharan Symposium Tripoli, Petrol. Expl. Soc. of Libya, pp. 114–122.
16) Leech, D.P., Treloar, P.J., Lucas, N.S. and Grocott, J., 2003. Landsat TM analysis of fracture patterns: a case study from the Coastal Cordillera of northern Chile. Int. J. Remote Sens., vol. 24, no. 19, pp. 3709–3726.
17) Lipparini, T., 1940. Tettonica e geomorfologia della Tripolitania. Bulletin of the Geological Society of Italy, Roma 59, 221-301.
18) Masoud, A. and Koike, K., 2006. Tectonic architecture through Landsat-7 ETM+/SRTM DEM derived lineaments and relationship to the hydrogeologic setting in Siwa region, NW Egypt. Journal of African Earth Sciences, 45 (4–5), 467–477.
19) Mather, P.M., 2004. Computer Processing of Remotely-Sensed Images. 3rd ed. Chichester, U.K, Wiley.
20) Miller, V.C., 1971. A Preliminary Investigation of the Geomorphology of the Jebel Nefusa. In Symp. Geol. of Libya, Univ. of Libya, Tripoli, pp. 365–385.
21) Pereira, A. J.S.C., Victória, S., Vicente, A.M.P. and Neves, L.J.P.F., 2008. Structural lineaments in a volcanic island evaluated through remote sensing techniques. The case of Santiago Island (Cape Verde). International Geoscience and Remote Sensing Symposium (IGARSS), art. No. 4423127, 1632_1635.
22) Rowland, S.M. and Duebendorfer, E.M., 1994. Structural analysis and synthesis: 2nd edition. Blackwell Scientific Publications, Palo Alto.
23) Saadi, N.M. and Watanabe, K., 2008. Lineaments extraction and analysis in Eljufra area, Libya. Journal of Applied Remote Sensing, 2, 023538.
24) Saadi, N.M., Aboud, E. and Watanabe K., 2009. Integration of DEM, ETM+, geologic, and magnetic data for geological investigations in the Jifara Plain,

Libya, IEEE Transactions on Geoscience and Remote Sensing, Vol. 47, No. 10, pp. 3389-3398.
25) Sabins, F., 1997. Remote sensing principles and interpretation. New York: W.H. Freeman Company.
26) Solberg, A.H.S., 2006. Data fusion for remote sensing applications. In: C. H. Chen, ed. Signal and image processing for remote sensing. Boca Raton, FL: CRC Press, 515–537.
27) S.P.L.A.J., 1979. Topographic map of Libya, 1:50,000. Polservice-Geokart, Poland.
28) Yang, J.M., Zhang, Y.J. and Yao, F.J., 2007. Lithology identification of the Weiya complex by means of ETM+ remote sensing. Acta Petrologica Sinica, 23 (10), 2397–2402.
29) Zivanovic, M., 1977. Geological map of Libya. Explanatory booklet, sheet Bani Walid NH 33-2. Industrial Research Centre, Tripoli.

Developing decision tree classification system based on discrimination of spectral and textural characteristics to identify land use using ALOS AVNIR-2

S. Darmawan, I. H. Ismullah, K. Wikantika, A. Budi Harto

[1]. Center for Remote Sensing
[2]. Remote Sensing and Geographical Information Science Research Division
Institute of Technology Bandung
Jl. Ganesha 10 Bandung 40132, Indonesia
Email : soni_darmawan@yahoo.com

Abstract

There are many classification strategies to identify and monitor land use in remote sensing. Further study to develop classification technique using hierarchy classification by decision tree model that parameters are based on spectral and textural characteristics. The use of both spectral and textural characteristics in remotely sensed image data has been proven promising for land use and land cover classification. The main objective of the research is to develop decision tree model based on spectral and textural characteristics of the ALOS AVNIR-2. The study includes image preprocessing, calculation of vegetation index, calculation of textural measures, evaluation separability analysis and develop tree model. Image preprocessing focuses on image registration while vegetation index generate NDVI, RNDVI, GNDVI, NDRGI, GRVI and MPRI, respectively. Finally, textural measures are calculated based on the gray level co-occurrence matrix (GLCM). The results indicated that decision tree model which is based on combination of band spectral, normalized difference vegetation index (NDVI), Modified Photochemical reflectance Index (MPRI) and —mean" texture measure were accurate for discrimination of different land uses over the study area.

Keywords : spectral, textural, ALOS AVNIR-2, discrimination, land use, decision tree

1. Introduction

In recent years, decision tree classifiers have been successfully used for land cover classification from remote sensing data. The advantages of using a multistage or tree approach to classification include that different data sources, different sets of features, and even different algorithms can be used at each decision stage. (Richard & Jia, 2006). Many researcher have investigated decision tree classification for vegetation cover mapping (Simrad et al., 2000), forest mapping (Huang & Yang, 2001) urban landscape dynamics (Pavuluri et al., 2002), national park vegetation mapping (Colstoun et al., 2003), habitat and agricultural mapping (Lucas, 2007), habitat classification and change detection (Sensie et al., 2008), updating land cover (Raclot et. al., 2005 and Wentz et. al., 2008).

However land use classification using decision tree based on single features of spectral characteristic have limitation (Pal & Mather, 2003), another limitation decision tree classification are instability of tree (Miller & Franklin, 2002) and requiring a large number of training samples for tree construction (Joy et al., 2003).

Basically, remote sensing technology can detect reflectance energy from land use and it also provides spectral response in image. Separability analysis indicated that spectral ALOS AVNIR-2 data provided adequate spectral discrimination of land use. Other features which can discriminate land use are using textural characteristics. Texture can improve classification result. Classification of Mediterranean land cover from Landsat TM imagery, texture information was found beneficial for certain land covers (Berberoglu et al., 2007) and combination of spectral and textural aspects significantly improved the classification accuracy compared with

classification with only pure spectral features (Wikantika et al., 2004).

The main objective of this research is to construct a decision tree (expert system) for land use classification by determining the optimal spectral and textural measures. The research focuses on investigation of spectral and textural characteristics of land uses in study area, investigation of separation value for discriminating different land uses, and construction of a decision tree.

2. Methodology

2.1 Study area and data

Location of study area is in Southern part of Bandung, West Java, Indonesia, roughly between latitude 6°59' – 7°04' S and longitudes 107°34' – 107°41' E. ALOS AVNIR-2 collected in Juni 2007 and total of training site distributed in study area is 65 samples.

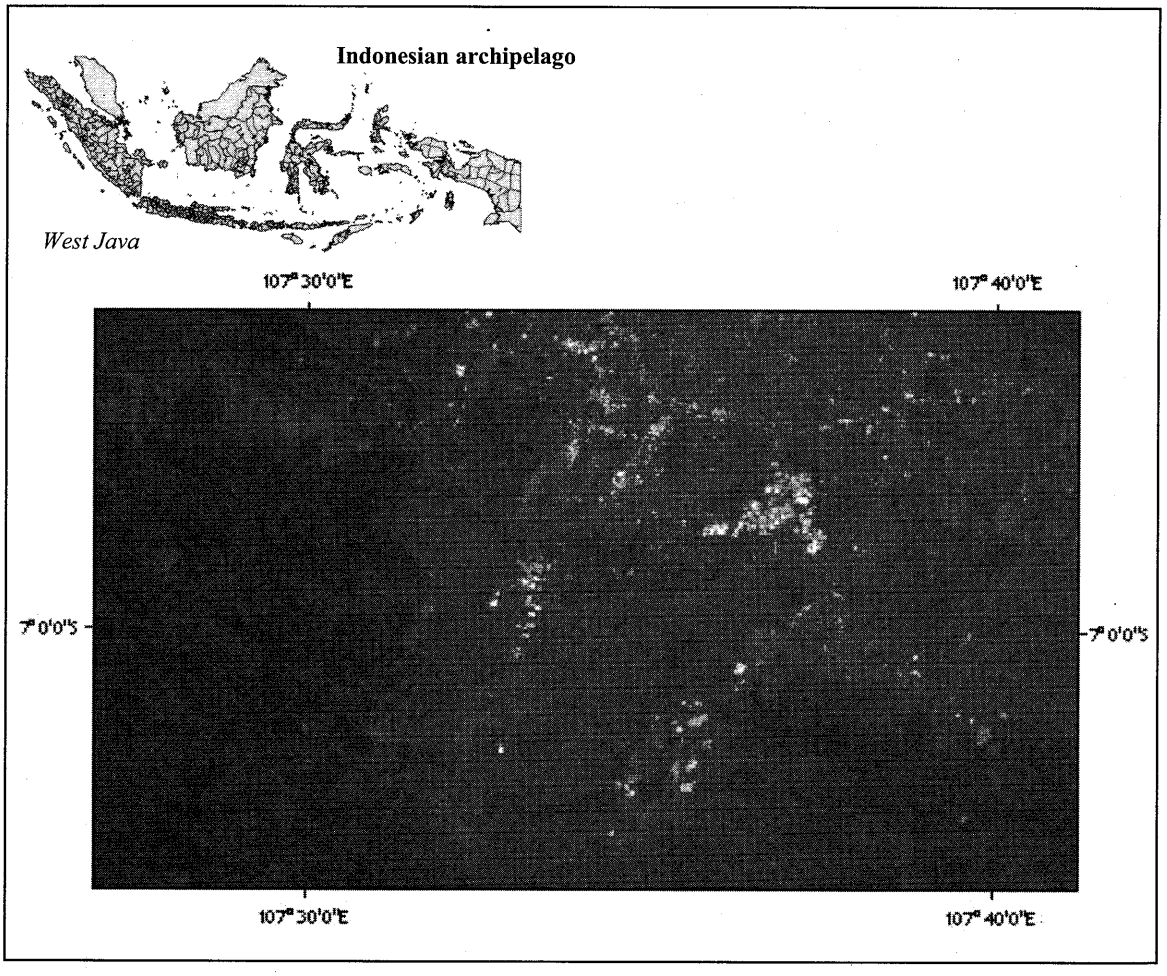

Figure 1. Study area

Basically land use classification systems level II used in this study based on Anderson (1976) and Indonesian's land use classification systems such as industrial area, water body, forest, mixed plantation, agricultural, grassland, wet paddy field, dry paddy field, minning area, fallow land, shrubland, field area, and urban area

2.2 Method

a. Preprocessing

ALOS AVNIR-2 has been systematically geometric corrected but must be registered to reference data. In this study reference data used was SPOT 5 with spatial resolution 2.5 m. Distribution of ground control point for image registration is nine control points distributed within study area. Selection of ground control point was based on geographic characteristics such as branch of rivers and roads. To wrap the satellite image, polynomial orde-1 was used and resampling method of nearest neighbor was applied.

b. Calculation of spectral, texture and separability analysis

The study used several vegetation index as following below :

Normalized Difference Vegetation Index (NDVI) (Rouse et al. 1974):

$$NDVI = \frac{NIR - \mathrm{Re}\,d}{NIR + \mathrm{Re}\,d} \quad \text{.....(1)}$$

Ratio Normalized Difference Vegetation Index (RNDVI) (Gong et al. 2003)

$$RNDVI = \left(\frac{NIR - red}{NIR + red}\right) * \left(\frac{NIR}{red}\right) \quad \text{.....(2)}$$

Green Normalized Difference Vegetation Index (GNDVI) (Gitelson et. al 1996)

$$GNDVI = \frac{NIR - green}{NIR + green} \quad \text{.....(3)}$$

Normalized Difference Red Green Index (NDRGI) (Yang et. al 2008)

$$NDRGI = \frac{red - green}{red + green} \quad \text{.....(4)}$$

Green Ratio Vegetation Index (GRVI)

$$GRVI = \frac{NIR}{green} \quad \text{.....(5)}$$

Modified Photochemical Reflectance Index (MPRI) Yang et. al (2008)

$$MPRI = \frac{green - red}{green - red} \quad \text{.....(6)}$$

For separation not only based on spectral characteristic but also used texture information. Five textural measurement such as mean, homogeneity, correlation and contrast are proposed by haralick et. al. (1973). All profiles are based on land use in the research area.

Mean texture: $\mu_{ij} = \frac{\sum_{i,j=0}^{N-1} P_{ij}}{N^2}$ .....(7)

Homogeneity: $\sum_{i,j=0}^{N-1} \frac{P_{i,j}}{1 + (1 - J)^2}$ .....(8)

Contrast: $\sum_{i,j=0}^{N-1} P_{i,j}(i - j)^2$ .....(9)

Correlation : $\sum_{i,j=0}^{N-1} \left[\frac{(i - \mu)(j - \mu)}{\sqrt{(\sigma_i^2)(\sigma_j^2)}} \right]$ .....(10)

To separate different land use needed threshold value. Threshold values were derived from training site. This study collected 65 training sites. Threshold values were determined based on median values both mean and standard deviation values for each class. Threshold (Th) value can be as follows:

$$Th = \frac{(\bar{x}_i \pm \sigma) + (\bar{x}_j \pm \sigma)}{2} \quad \text{.....(11)}$$

3. Results and Discussions

ALOS AVNIR-2 has 4 band they are blue (0.42 – 0.50 μm), green (0.52 – 0.60 μm), red (0.61 – 0.69 μm) and near infrared (0.76 – 0.89 μm). The result of calculation of NDVI, RNDVI, GNDVI, NDRGI, GRVI, and MPRI and textural measures such as mean, varian, homogeneity, contrast and correlation, can be shown by figure 2, respectively.

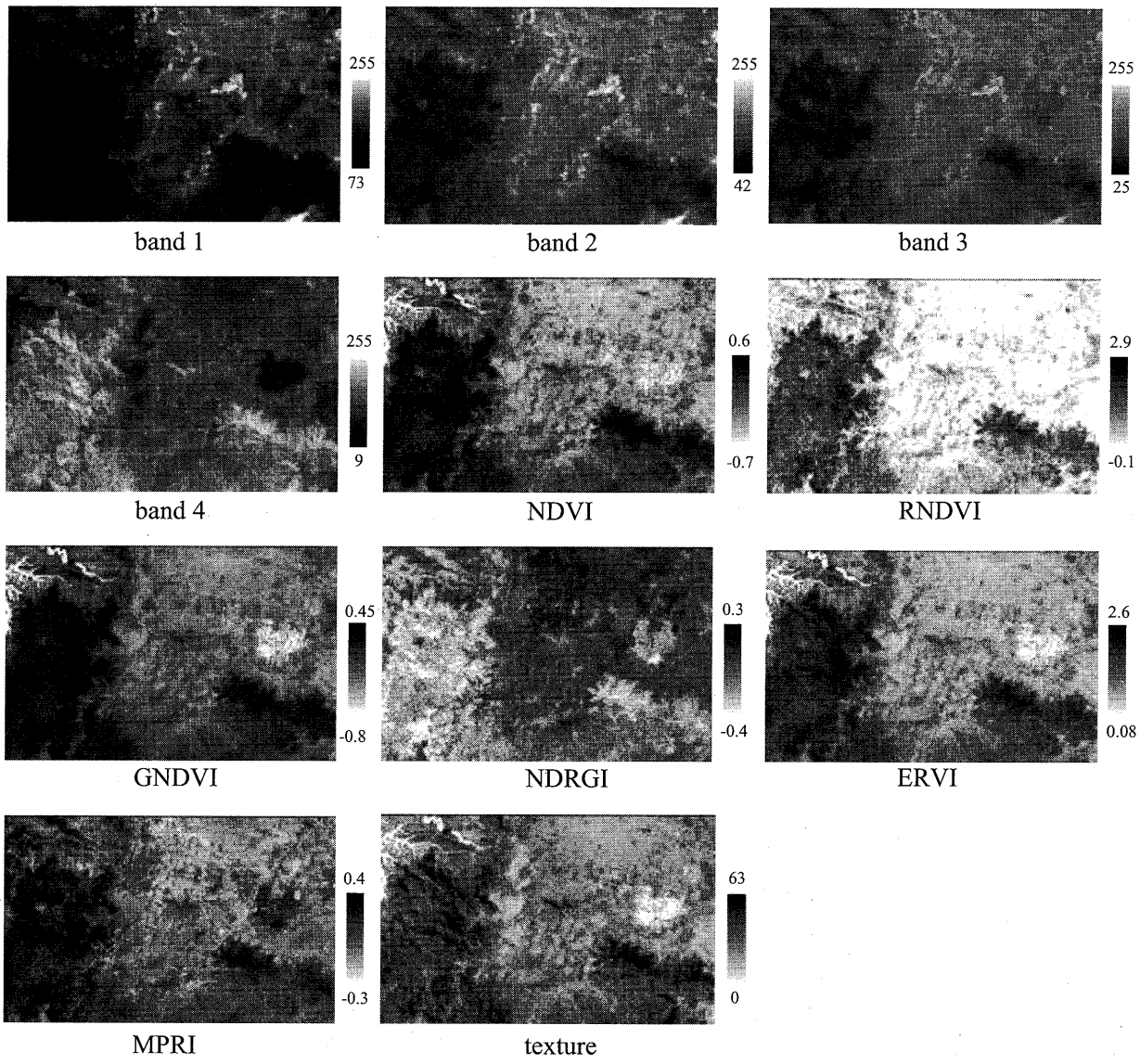

Figure 2. Spectral and textural characteristics

Figure 3 shows spectral characteristic for each land use class in study area. According to figure 3, industrial zone has higher spectral performance in band 1, band 2 and band 3, respectively. Vegetation land use such as agricultural land, mixed plantation land, forest, grassland, shrub land, and dry paddy, increase in band NIR but another land use decrease.

Vegetation index characteristic for each land use can be shown by figure 4. Based on figure 4, forest, shrub land, mixed plantation and grassland have higher NDVI values than others but in NDRVI forest, shrub land, mixed plantation and grassland have lower values. Non vegetated land use such as water, industrial zone, mining zone, rural and urban have similar values in RNDVI but vegetation

land use such as forest, shrub land, mixed plantation and grassland have different values. Water and wet paddy have lower values in GNDVI but higher values in NDRVI and MPRI, respectively.

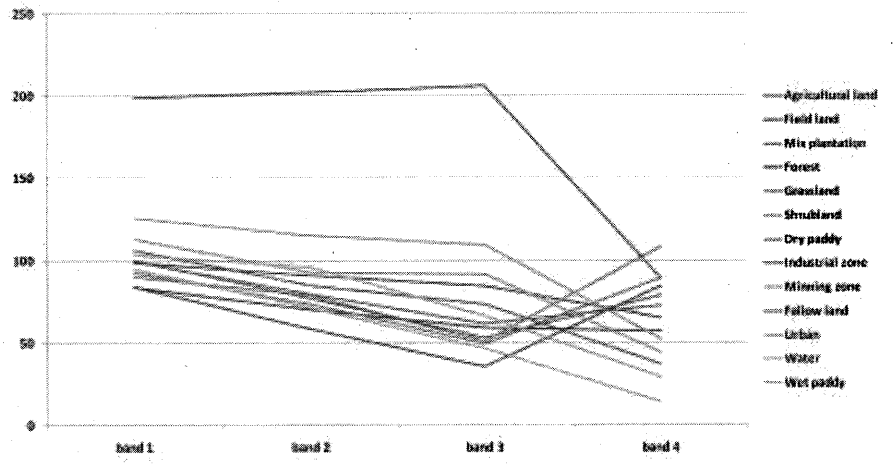

Figure 3. Spectral characteristic for each land use

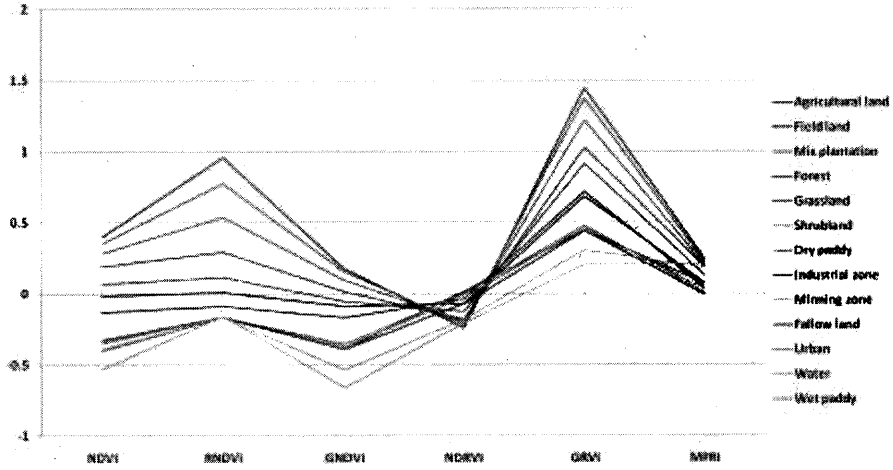

Figure 4. Vegetation index characteristic for each land use

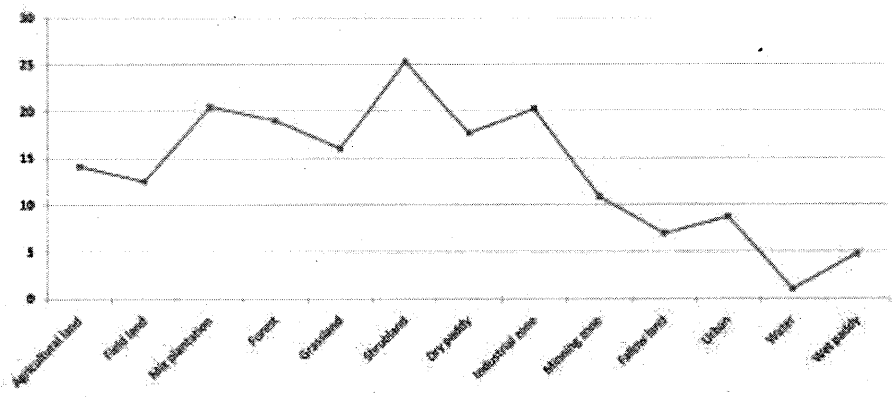

Figure 5, Textural characteristic for each land use

Textural characteristic for each land use can be shown by figure 5. Based on figure 5, water and wet paddy have lower values while shrub land has higher values than other land uses. Based on spectral and textural characteristics for each land use and separability analysis therefore it can be discriminated each land uses consisted of some steps as follows :

Step 1. Mean texture can discriminate water body, wet paddy and industrial zone, minning zone, fallow area, urban, agricultural, field, grassland, forest, mixed plantation, shrubland.
Step 2.1. band 2 can discriminate water body and wet paddy
Step 2.2 NDVI can discriminate industrial zone, minning zone, fallow land, rural, urban area and agricultural, field, grassland, forest, mixed plantation, shrubland
Step 3.1 band can discriminate industrial zone, minning zone and fallow land, rural, urban
Step 3.2 NDVI can discriminate agricultural, field, grassland and forest, mixed plantation, shrubland
Step 4.1 NIR can discriminate industrial zone and minning area
Step 4.2 band 3 can discriminate fallow land, and urban
Step 4.3 MPRI can discriminate agriculture, field and grassland, dry paddy
Step 4.4 band 1 can discriminate forest and mixed plantation, shrubland
Step 5.1 band 3 can discriminate grassland and dry paddy
Step 5.2 band 1 can discriminate agriculture and field
Step 5.3 NDVI can discriminate mixed plantation and shrubland

Decision tree analysis derived from discrimination of land uses based on spectral and textural characteristic as shown by figure 6. Land use classification using decision tree analysis can see in figure 7.

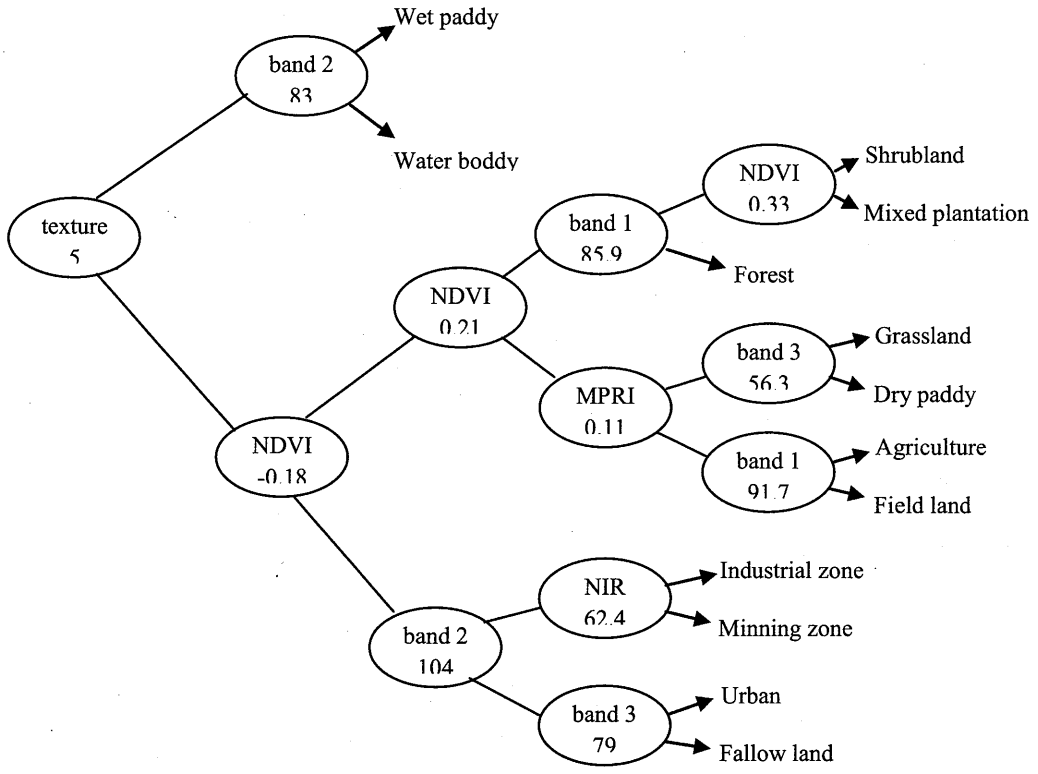

Figure 6. Separation of land uses using decision tree analysis

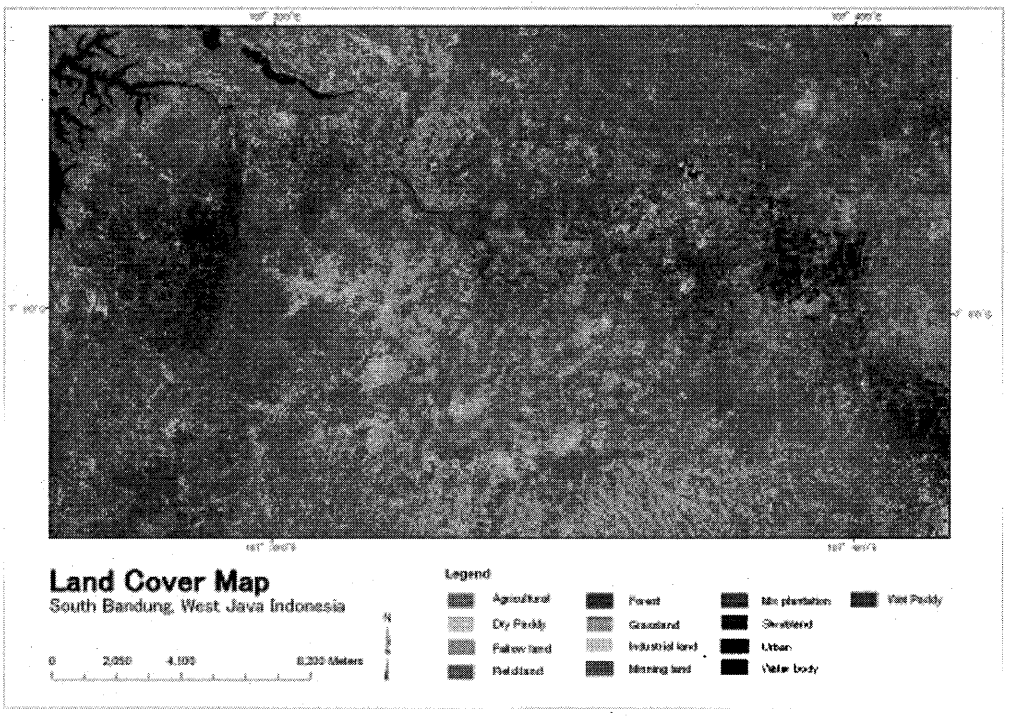

Figure 7. Land Use and Land Cover classification result by decision tree analysis

4. Conclusions

It has been shown that use of spectral and textural measures can identify and separate land use and land cover in level II classification systems. Separation of each land use with decision tree analysis can use band 1, band 2, band 3, band 4, NDVI, MPRI and textural information derived from ALOS AVNIR-2 image.

Acknowledgments

Firstly, I would like to thank Directorate Higher Education, Ministry of National Education, The Republic of Indonesia for the fellowship. I would also like to thank Prof. Ryutaro Tateishi of Center for Environmental Remote Sensing (CEReS), Chiba University for supporting laboratory.

References

1. Berberoglu S., Curran P.J, Lloyd C.D, Atkinson, P.M., 2007, Texture Classification of Mediterranean Land Cover, International Journal of Applied Earth Observation and Geoinformation 9, 322–334
2. Colstoun, E., C., B., Story, M., H., Thompson, C., Commisso, K., Smith, T., G., dan Iron, J., R., 2003 –National Park vegetation mapping using multitemporal Landsat 7 data and a decision tree classifier", Remote Sensing of Environment 85, 316–327
3. Gitelson, Anatoly A., 2004. Wide dynamic range vegetation index for remote quantification of biophysical characteristics of vegetation, *J. Plant Physiology*, No. 161, pp. 165–173.
4. Haralick R.M., et al., 1973, Tekstural Feature for Citra Classification, IEEE Transaction on systems,

Man and Cybernetics Vol. SMC-3 No. 6, 610-621.

5. Huang C., and Yang L., 2001, Synergistic Use of FIA Data and Landsat 7 ETM+ Images for Large Area Forest Mapping. The thirty-fifth annual Midwest forest Mensurationists and Th Third Annual FIA Symposium
6. Joy S.M., Reich R.M and Reynolds R.T., 2003 A Non-parametric Supervised Classifications of Vegetation Types on The Kaibab National Forest Using Decision Trees. International Journal of Remote Sensing, 24, 1835 – 1852.
7. Miller J., and Franklin J., 2002, Modeling the Distribution of Four Vegetation Alliances Using Generalized Linear Model and Classification Trees with Spatial Dependence. Ecological Modeling, 157, 227-247
8. Lucas R., et al., 2007, Rule-based Classification of Multi-temporal Satellite Imagery for Habitat and Agricultural Land Cover Mapping, International Society for Photogrammetry and Remote Sensing (ISPRS), Journal of Photogrammetry & Remote Sensing 62, 165–185.
9. Pavuluri M.K., Ramanathan S., and Daniel Z. 2001 A Rule-based Classifier Using Classification and Regression Tree (CART) Approach for Urban Landscape Dynamics. International Geosciences and Remote Sensing Symposium vol. 2 (pp.24-28)
10. Pal M., and Mather P.M., 2003, An Assessment of the Effectiveness of Decision Tree Method of Land Cover Classification. Remote Sensing of Environment 86, 554-565
11. Raclot D., F. Colin, C. Puech, 2005. Updating land cover classification using a rule-based decision system, International Journal of Remote Sensing, 26:7, 1309 - 1321
12. Richard A.R., and Jia. X., 2006. "Remote Sensing Digital Image Analysis" Springer.
13. Rouse, J., W., R. H. Haas, J. A. Schell and D.W. Deering, 1974, —Monitoring Vegetation Systems in Great Plains with ERTS", Proceedings, Third Earth Resources Technology satellite-1 Symposium, Greenbelt:NASA SP-351, 3010-317
14. Simrad M., Saatchi S.S., and Grandi G.D., 2000, The Use of Decision Tree and Multiscale Texture for Classification of JERS-1 SAR Data Over Tropical Forest, IEEE Transaction on Geosciences and Remote Sensing, 38(5), 2310-2321
15. Sesnie S. E., et al., 2008, Integrating Landsat TM and SRTM-DEM Derived Variable with Decision Tree for Habitat Classification and Change Detection in Complex Neotropical Environment, Remote Sensing of Environment 112, 2145–2159
16. Wentz, Elizabeth A., Nelson, David, Rahman, Atiqur, Stefanov, William L. and Roy, Shoursaseni Sen (2008) 'Expert system classification of urban land use/cover for Delhi, India', International Journal of Remote Sensing, 29:15, 4405 — 4427
17. Wikantika K., 2004, —Spectral and Textural Aspect of Multisensor and Multitemporal Satellite Data for Land Use/Land Cover Mapping in A Tropical Area", Thesis Doctoral, Chiba University, Japan
18. Yang, Z., Willis, P., Mueller, R., 2008, —Impact of band ratio enhanced awifs image to crop classification accuracy, Procceding, Denver Colorado

Spatial Pattern of the oasis landscape Ecotone in Ebinur Lake,Xinjiang,northwest of China

Chu Xinzheng[1,3],Ye Mao[2,3],Ma Qian[2]

1 School of Geographic Science and Tourism,Xinjiang Normal University,Urumqi 830054,China;

2 Institute of Desert Meteorology,China Meteorology Administration,Uruqi 830002,China;

3 Key Laboratory of Lake Envrionment and Resources in Arid Zone,Urumqi 830054,China;

Corresponding author:E-mail address: chuxinzh@yahoo.com.cn; mq1979@yahoo.cn;

Tel:+86-991-4332235; Fax:+86-991-4332229

Abstract: Based on methods of lanscape ecology and TM images of the Ebinur lake during the diffierent period, This paper studies the characteristics of landscape pattern, function and its variation. The ecological process, mechanism and intensity of variation influenced by the human activities and physical factors are analyzed in order to offer the countermeasure and references for restoring and reconstructing destroyed ecological function in the study areas. The results showed that: (1)Landscape ecotone of Ebinur Lake, with higher complex spatial heterogeneity in ecological system,was fragile and unstable to disturbance of the human activities and environment factors, which mainly include rainfall variation, frequency and intensity of wind as well as population,agriculture and livestock changes. (2)The grassland is a dominant type of land use. The proportion of grassland, woodland and the unutilized land is nearly 80% while the agricultural land and inhabitant location is less, less than 8%. Thus, the land use structure should be adijusted to sustain the stability of oasis in Ebinur Lake .Especially three farms near the lake should control the increase of agricutural lands and livestock. (3)The land that not to utilize and the patches of woodlands are 94.78%, but this two kinds of landscape's average area is small, landscape fragment is obvious. (4)The shapes of grassland patches are not regulations and complicated,the bend level of boundary is distinct.The index of the landscape diversity and homogeneity is high, dominant is small, the distribution of landscape patches is symmetrical. The results indicate the landscape the landscape is complete, and have not

phenomenon of obvious fragment. (5)Study on ecological restoration of the unutilized lands should be strenthen, which is important for optimizing the composition structure and spatial pattern of landscape ecotone of Ebinur Lake. The unutilized lands including salina land , wind-erode land and water corrisive land, were distributed in areas with large population. Therefore, it is essential that we should prevent desertification and protect present vegetation and improve vegetation coverage. (6)The landacape ecology system was charactered by complicated and landscape patches fragment and higher diversity and homogenecity, which is related climate change, human activities, groundwater level and lake volume change. Thus,we need ensure the water supply for lake, which provide references and information for bionomical resources, agrichuture and railroad security.

Keywords: Ebinur Lake, oasis landscape ecotone, landscape pattern

1introduction

Oasis are unique intrazonal landscapes in arid and semi-arid regions of the world. In China they mainly distributed in temperate and warm temperate desert area been the west of the Helan Mountain and north of Qinghai-Tibet Plateau. Oasis take up only 7-8% of the total area of XinJiang, over 90% of the population and over 95% of social wealth are concentrated within the oasis. Thus, oasis is very important for economic development and environmental protection in arid and semi-arid regions. To study the stability of oasis, what need to be discussed are the conditions for the stability of vegetation in the transitional zone between oasis and desert: oasis-desert ecotone. Oasis-desert ecotone, with the function of oasis and desert ecosystem, forms especial structure and shape. Under the condition of global climate warming, Landscape ecotone of oasis is better weak and significant to indicating and forecasting future. Based on methods of landscape ecology and TM images of the Ebinur Lake during the different period, this paper studies the characteristics of landscape pattern, function and its variation, which will provide some theoretical information for protecting the ecological environment and utilizing the natural resources.

2Study area

The study area is located in Northwest China between the range of 82°35′ ~83°10′ E, 44°54′ ~45°09′ N. The Ebinur lake covers area of 4327.04km^2 and is a centralof catchments basin.Tstrong-wind day (>20m/s)per year is more than 165 days in the Alsankou mountain, northern Ebinur lake . The desert vegetation in stduy areas wound adjust ecological fouction because of its especial location and degraded envirnment.

3Methodology

This paper studies the characteristics of landscape pattern, function and its variation,the ecological process, mechanism and intensity of variation influenced by the human activities and physical factors are analyzed in order to offer the countermeasure and references for restoring and reconstructing destroyed ecological function in the study areas.

Number of pitchs(NP):NP=N_i

Mean patch areas(MPA): MPA=a_i/n^i

Percentage of average pitches perimeter to area (PARA$_i$): PARA$_i$= $PARAi = \frac{\sum P_i / A_i}{N_i}$

Patch density(PD): $PD = N_i / A$

Fragment index(FRAC): $FRAC = \frac{2\ln 0.25P_i}{\ln A_i}$

Landscape shape index: $LSI = \frac{P_k}{2 \cdot \sqrt{\pi \cdot A_k}}$

Diversity index: $H = -\sum P_k \bullet \ln(P_k)$

Dominancy index: $D = H_{\max} + \sum P_k \bullet -\ln(P_k)$

Even index: $\varepsilon = \frac{H}{H_{\max}} = \frac{-\sum P_k \cdot \ln(P_k)}{\ln(m)}$

Cracked index: $C = n_i / MPA$

4Result and analysis

4.1Spatial structure of land cover/use

Form the land types of oasis ecotone in Ebinur lake (Table 1), the grassland,

forest land and unutilized land were the dominant land types, their areas were 40.38%, 22.38% and 16.83% of the total study areas, respectively. While the percentage of agrarian land and residential land was least, only7.18% and 0.1%.

Table 1 Landscape areas of different land type in Ebinur Lake

Land type	Land areas（m^2）	Percentage of total（%）
Agrarian land	310818030.7	7.18
Woodland	968450078.8	22.38
Grassland	1747473240	40.38
Waterland	567674738	13.12
Residential area	4329971459	0.10
Unutilized land	728289856.7	16.83
Total	4327035616	100

The patch numbers were 721 with regard to the landscape types in study areas (Table 2), in which number of unutilized land was most ,up to 48.68%,the second most was forest land ,up to 46.19%, but their areas were less and cracked intensity was stronger. The least the patch number was grassland and water area while the landscape shape index of grassland was largest, up to 125.89. The landscape shape index of water areas was least, up to 1.4414. Thus, landscape ecotone of Ebinur lake was higher complex spatial heterogeneity in ecological systen, with grassland as a based landscape, woodland as a zonal distribution in northeastern lake and roadway or channel as path of landscape.

Table 2 Landscape index of land use in oasis ecotone of Ebinur Lake

Type	NP	PD	MPA/m^2	$PARA_i$	FRAC	LSI
Agrarian land	27	6.24E-09	11511778.91	0.0039	1.2235	10.0391
Woodland	333	7.70E-08	2908258.49	0.0123	1.3209	31.1974
Grassland	1	2.31E-10	1747473239.75	0.0107	1.4431	125.8859
Waterland	1	2.31E-10	567674738.94	0.0002	1.0243	1.4414
Residential area	8	1.85E-09	541246.43	0.0082	1.1578	3.7681
Unutilized land	351	8.11E-08	2074899.88	0.0223	1.3899	61.1683

The diversity of landscape in study area was more abundant(Table3).The diversity index(H)was 1.4637.the dominancy index was less, up to 0.33, while the

even index was higher, up to 0.8169.The cracked index(C)was 1.67E-07,which means that the distribution of landscape type was xonparatively symmetrical and integrated.

Table3 the landscape index of oasis ecotone in Ebinur lake

H	D	E	C
1.4637	0.33	0.8169	1.67E-07

4.2Spatial chatacteristicdesertification landscape structure

From the cause types of desertification(table4):the salination land and wind erosion land was the main landscape type, was 41.23% and 30.13% of the total areas, respectively. This indicate that the salination and wind erosion were the main factors threatening ecological environment of oasis ecotone in Ebinur lake.

Table 4 The desertification landscape area of oasis ecotone in Ebinur Lake

Type		Area/m^2	Percentage of total area/%
Not-desertification		45142828	1.04
Desertification	Wind erosion	1.31E+09	30.13
	Water erosion	5.54E+08	12.77
	water	6.44E+08	14.83
	Salination	1.79E+09	41.23
	Total	4.34E+09	100.00

Form the landscape index(Table5),the patch numbers of salination and wind erosion lands were largest, up to 455 and 260, repectively. Both of them were 89.60% of total numbers and their areas were up to 71.37%,which were the main types of desertification landscape.The salination lands were located in southern plains of Ebinur lake and around the Alsankou mountain, which were strongly affected by the human activities. The wind erosion lands were distributed mainly in northern and western areas of Ebinur lake. Affected by the wind, the indices if $PARA_i$ and LSI in wind erosion areas were small .The phenomena showed that the shape of desertification landscape was simple and large-scale distributed.

Table 5 he desertification landscape index of oasis ecotone in Ebinur Lake

Type	NP	PD	MPA/m^2	$PARA_i$	FRAC	LSI

Not-desertification		60	1.38E-08	752380.47	7.67E-03	22.74	14.53
Desertification	Wind erosion	260	5.99E-08	5033547.74	3.06E-03	27.64	31.28
	Watererosion	22	5.07E-09	25203310.48	1.23E-03	24.10	8.19
	water	1	2.30E-10	643929119.74	1.73E-04	20.46	1.24
	Salination	455	1.05E-07	3936041.59	2.87E-03	28.13	34.27

The diversity of desertification landscape was 1.32, as shown in Table6, which show a higher abundance in desertification landscape.The index of D was less, less than 0.3 while the index of E was higher, up to 0.82.Furthermore, the index of D was 1.47E-04,indicating that the desertification landscape was comparatively even and integrated.

Table6 desertification landscape index of oasis ecotone in Ebinur Lake

H	D	E	C
1.32	0.29	0.82	1.47E-04

4.3Variation ofvegetation landscape structure

The vegetation type is mainly composed of Haloxylon Ammodendron desert and salt marsh. Their areas are 34.69% and 14.71% of the all vegetation areas (Table 7). Haloxylon Ammodendron desert is distributed continually in northwest, north, northeast and east areas of Ebinur Lake. Salt marsh appears in the paralimnion and bottom of dried lake. The areas of agrarian land, half-shrub desert and succulent saline desert are similar and distributed scatteredly, up to 9.36%, 9.31%,8.16% and 8.06%, respectively, while the areas of other vegetation types are small.

Table7 the vegetation landscape areas of oasis ecotone in Ebinur Lake

Type	Area（m^2）	Percentage of total areas(%)
Agrarian land	420619788.64	9.32
Succulent saline desert	368731427.00	8.16
Half-shrub desert	422768476.16	9.36
Tamarix ramosissima	364103140.05	8.06
Haloxylon Ammodendron	1567722293.26	34.69
Sbrub desert	11096792.36	0.25
Saliniuzed meadow	149069574.98	3.30
Salt marsh	664745199.29	14.71

Ture steppe	8978015.16	0.20
Reed-swamp	280576552.66	6.21
Desert steppe	31755912.58	0.70
Deciduous forest	94759924.51	2.10
Artemisia desert	133548854.04	2.96
Bare land	327450.29	0.01
Total areas	4518803400.97	100.00

Table 7 shows the vegetation landscape index of oasis ecotone in Ebinur Lake. The numbers of patch in all vegetation types are 733, in which the NP of Haloxylon Ammodendron desert is largest, up to 247, amounting 33.7% of all patches. The second largest NP is half-shrub desert and Reed-swamp. Both of them are 126, up to 17.19% of all patches. The NP of Tamarix ramosissima is 70. The NP of other vegetation is small. The PARAi of most vegetation types is smaller while their LSI is different significantly. For example, the LSI of Reed-swamp is 31.01. that results shows that there exist complex landscape shape in different vegetation types of oasis ecotone in Ebinur Lake.

Table8the vegetation landscape index of oasis ecotone in Ebinur Lake

Type	NP	PD	MPA/m^2	PARA$_i$	FRAC	LSI
Agrarian land	32	7.08E-09	1.31E+07	4.48E-03	26.13	25.95
Succulent saline desert	13	2.88E-09	2.84E+07	1.93E-03	24.17	10.43
Half-shrub desert	126	2.79E-08	3.36E+06	3.92E-03	25.87	22.73
Tamarix ramosissima	70	1.55E-08	5.20E+06	4.16E-03	25.69	22.37
Haloxylon Ammodendron	247	5.47E-08	6.35E+06	2.50E-03	27.59	27.96
Sbrub desert	2	4.43E-10	5.55E+06	2.13E-03	17.36	2.00
Saliniuzed meadow	4	8.85E-10	3.73E+07	3.44E-03	23.52	11.85
Salt marsh	3	6.64E-10	2.22E+08	5.19E-04	22.73	3.78
Ture steppe	1	2.21E-10	8.98E+06	2.29E-03	17.09	1.93
Reed-swamp	126	2.79E-08	2.23E+06	6.56E-03	26.08	31.01
Desert steppe	1	2.21E-10	3.18E+07	1.27E-03	18.43	2.02
Deciduous forest	37	8.19E-09	2.56E+06	5.39E-03	23.51	14.80
Artemisia desert	1	2.21E-10	1.34E+08	4.02E-04	19.01	1.31

The diversity of vegetation landscape and the index of D were higher, up to 2.03 and 0.53, respectively. The salina plants were dominant vegetation type.

However, the index of E was less, 0.79. The index of C was 9.76E-05, indicating there were higher even and sufficiently not cracked in vegetation landscape(Table 9).

Table9 The vegetation landscape index of oasis ecotone in Ebinur Lake

H	D	E	C
2.03	0.53	0.79	9.76E-05

4 Discussion

The landscape pattern, function and its variation in oasis ecotone of Ebinur Lake are mainly caused by human activities and climate change. The human activities are mainly represented by changing lake water areas and agrarian land. Based on data from meteorologic and hydrological satations in study areas, compared with 1950's, the temperature is higher $0.3^{\circ}C$ in 1990's, while the precipitation increased by 20% - 50%. Thus, the rainfall in Ebinur Lake basin would increase 5% - 20%, which result in increasing the runoff and enlarge the lake water areas. The lake water areas keeps 500 km^2 in recent years. However, with continually increasing population in study areas, the agrarian land areas expand greatly and the demand for water also increased dramatically. From 1980's to 1990's, the agrarian land areas enlarge 244.75 km^2, increasing by 16.96%. The irrational human activities results to decline water supply for Ebinur Lake basin and cause some ecological problems. Therefore, the human activities is an important factor to disturbing landscapes spatial structure of oasis ecotone in Ebinur Lake.

5 Conclusions

(1) Landscape ecotone of Ebinur Lake, with higher complex spatial heterogeneity in ecological system, was fragile and unstable to disturbance of the human activities and environmental factors, which mainly include rainfall variation, frequency and intensity of wind as well as population, agriculture and livestock changes.

(2) The grassland is a dominant type of land use, the proportion of grassland,

woodland and the unutilized land is nearly 80% while the agricultural land and inhabitant location is less, less than 8%.

(3) The unutilized lands including salinaland, wind-erode land and water corrosive land, were distributed in areas with large population. Therefore, it is essential that we should prevent desertification and protect present vegetation and improve vegetation coverage.

(4) The landscape ecology system was charactered by complicated and landscape patches fragment and higher diversity and homogeneity, which is related climate change, human activities, groundwater level and lake volume change.

Acknowledgement

This work is supported by National desert-metrological Research Foundation of China (Grant No.SKJ2007006).

References:

[1]Zhang Panpan,Hu Yuanman.Research progress on multifunctional landscape[J].Jarnaal of Anhui Agri.Sci.2006,36(28):12454-12457.

[2]Han Wenquan,Chang Yu,Hu Yuanman,etal.Progress on landscape structure optimization[J].Journal of bionomics,2005,24(12):1487-1492.

[3]Chun Xinzheng,Zhang Suhong.A Preliminary Research Oil Nature,Founction and Dynamic Changes of Landscape Ecotone-A case study on oasis ecotone[J].Journal of Xinjiang Normal University(Natural Science edition),2002,21(3):50-54.

[4]zhao Zhenyong,Wang Ranghui,Xue Ying.Natual Vegetation Conservation of Oasis Margin in Arid Zone – A case Study in Shanshan Oasis.xinjiang Wei Autonous Region[J].Bulletin of Soil and Water Conservation,2008,28(1):130-134.

[5]Wang Xiao,Zhang Zengxiang,Wang Changyou.Dynamic monitoring of oasis soil desertification,in lake Aibi,Xinjiang[J].Research of arid area,2007,24(6):741-746.

[6]Yuan Shun.Environment evaluation and coutermeasure in Ebinur lake area[J].Journal of arid resources and environment,1996,10(1):30-37.

[7]Qian Yibinm,Wu Zhaoning,Zhang Liyun.Ground Surface conditions of Sand Dust Event

Occurrence and Soil Conservation in Aibi lake Region of Xinjiang[J].Reaources Science,2006,28(5):185-189.

[8] Qian Yibinm,Jiang Jin,Wu Zhaoning.Soil heterogeneity and its impact on eological distribution of plant community in Aibi lake area[J].Arid land geography,2003,26(3):217-222.

[9]Li Hu,Chen Donghua,Ci Longjun,eral.Time and space distribution changes of land desertification in Aibinur Lake region of Xinjiang[J].Science of Soil and Water conservation,2008,6(4):28-40.

[10]Li hu,Gao Junfeng,Wang Xiaofeng,etal.The dynamic monitoring of desertification in Xinjiang Lake Aibi wetlands basing on RS and GIS[J].Journal of Lake Sciences,2005,17(2):127-132.

[11]Yang Qing,He Qing,Li Hongjun,etal.Study on the sand-dust climate change trend and jump in Ebinur lake area[J].Journal of desert reaearch,2003,23(5):503-508.

[12]Ji Lili,Abuduwaili.Effects of wind erosion on the saltemission, transport process of salts:a case study of the area of lake Ebinur,Xinjiang,China[J].Arid land geography,2009,32(2):211-216.

[13] Ji Lili,Abuduwaili,Mu Guijin.Analysis on the dust storms and their disasters in the lakebed region of Ebinur Lake,Xinjiang [J]. Arid land geography,2002,25(2):149-155.

[14]Chen Shujiang,Hou Ping,Li Wenhua,etal.Synthetical research on nature resources conservation of Ebinur lake wetlands[M].Xinjiang science and technology Press,Urumqi,2007:20-24.

Multiple Scattering Model for Measurement of Particle Size Distribution in Clouds

Hiroki Yoshida

Faculty of Engineering, Gifu University, 1-1 Yanagido, Gifu 501-1193, Japan

hiroki@gifu-u.ac.jp

Abstract

The size distributions of water particles at the bottom of clouds had been analyzed by a multiple-scattering simulation code for standard lidars. In order to expand it for inside the cloud, the code is modified and applied to the bistatic lidar geometry. It simulates the intensity and polarization of the extracted light image from clouds by using Stokes vectors under Monte Carlo method.

Keywords **:** lidar, bistatic lidar, multiple scattering, Monte Carlo method

1. Introduction

Lidars were developed as powerful tools for the remote sensing of clouds. A polarized laser beam of the lidar is scattered by the water particles in the cloud. The size distribution of water particles strongly affects extracted image intensity and polarization from the cloud. In order to extract its information from the image, accurate computation of contribution of the multiple scattering is required. The Monte Carlo Method code for polarized light has been developed and evaluated with experimental results by using standard size particles[1]. The analyzed results were limited around the bottom part of clouds by the lidar geometry. In order to expand the analysis region, the code is modified and applied to the bistatic lidar geometry.

2. Multiple-Scattering Model for a Bistatic Lidar

The geometric arrangement of the bistatic lidar model is shown in Fig.1. A polarized laser beam is vertically transmitted to the bottom of a cloud. The receiver composed of a telescope with an analyzer obtains scattered image intensity and polarization. The image is a result of multiple scattering between the size distributed water particles. To simulate it, we defined the size distribution and number density as the formula shown in Fig.1. The distribution of radii is divided into thirty-bin classes from 0.1 to 30 μm. Typically 10^5 photons are incident to the bottom part of the cloud. The n-th scattering particle is found by contribution of each class according to the density and overall angular Mie-scattering-pattern. The n-th scattered angle is defined and weighted by the Mie-scattering-pattern. To calculate the polarization, the Mueller matrix was calculated with the Stokes vector by each scattering. After calculations of all photons' paths, extracted image is obtained.

Figure 2 shows the simulated results for single layer cloud. One can see the intense point at the incident position and linearly decayed pattern toward to the top of cloud. The s-polarized image is relatively intense for spherical particles.

Figure 3 shows the two-layer cloud case. The upper layer form center of the image has five times higher number density than lower one. The second bright spot is shown at the binding surface of two layers in Fig. (a). In Fig. (b), the s-polarized image is relatively weak and insensitive the density change.

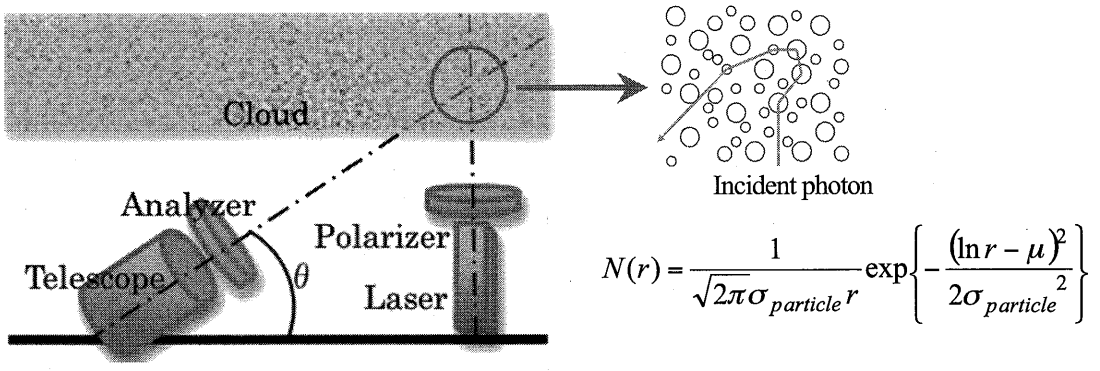

Fig. 1 Model of a bistatic lidar.

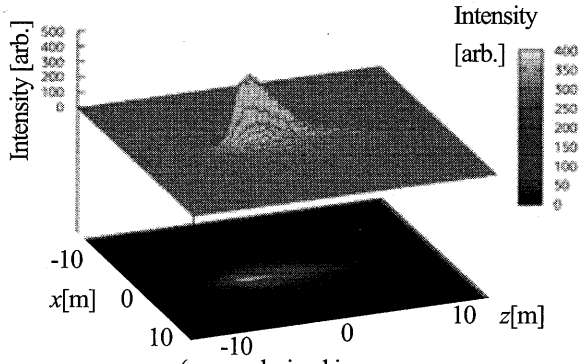

(a) p-polarized image

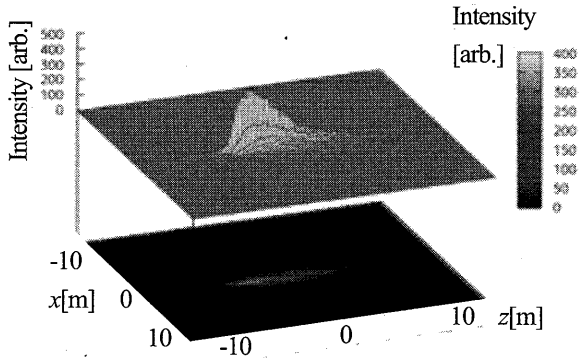

(b) s-polarized image

Fig. 2 Extracted light image of a Single layer Cloud for bistatic lidar geometry
($\rho = 10^{-2}$ cm^{-3}, $\sigma = 1.0$)

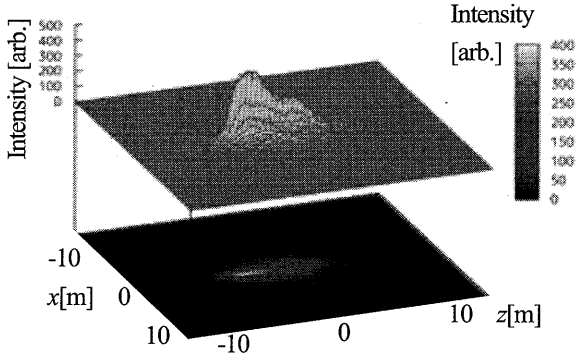

(a) p-polarized image

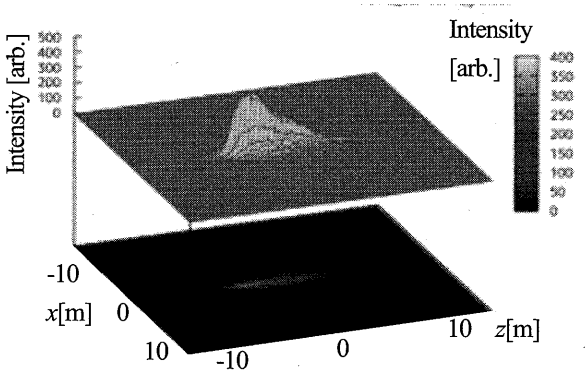

(b) s-polarized image

Fig. 3 Extracted light image of two-layer cloud
(upper: $\rho = 5 \times 10^{-2}$ cm^{-3}, lower: $\rho = 10^{-2}$ cm^{-3})

3. Observation by the Bistatic Lidar

The pulsed laser for the lidar was a frequency doubled Nd:YAG laser (Excel Technology, Surelight S-10) having energy of 180 mJ max. The linearly polarized laser beam is expanded and steered by the transmitter optics. The receiver is a 300mm diameter Dobsonian type telescope (Kokusaikoki, WHITEY DOB) with a digital camera (Nikon, D70s). The system is operated in the bistatic configuration with a separation distance around tem meters between the transmitter and the receiver. Figure 4 shows the observed image at the 50m-separation distance.

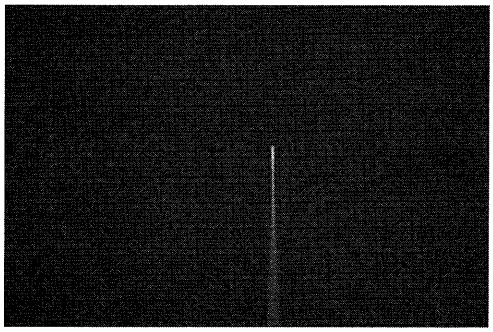

(a) p-polarized image

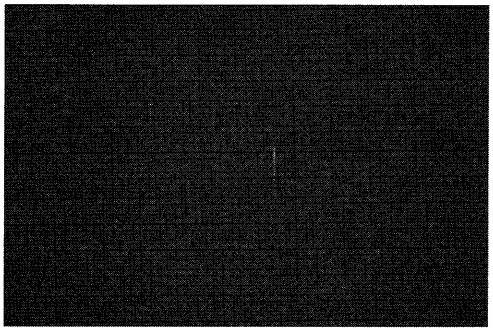

(b) s-polarized image

Fig. 4 Multiply-scattered light image obtained by the bistatic lidar.

2. Conclusion

The simulation code was expanded to the bistatic lidar geometry. Typical simulated observations and fundamental experimental results are presented. This analysis with bistaic lidar seems feasible to analyze the particle size distribution in clouds.

Acknowledgements

The author would like to thank Prof. Kuze of CREes Chiba University. And this study was partially supported NEDO and NIFS.

References

1) H. Yoshida, Proceedings of 14th CEReS Int'l Symposium and SKYNET Workshop , Nov. 13-14, 2008, p168.

Atmospheric turbidity estimated from visual range with microphysics and active remote sensing data at SKYNET sites

Yoko Inoue[1], Mayumi Hibino[1], Makoto Kuji[1], Tadahiro Hayasaka[2]

[1]*Faculty of Science, Nara Women's University, Kita-uoya Nishimachi, Nara 630-8506, Japan*

[2]*Center for Atmospheric and Oceanic Studies, Tohoku University, 6-3 Aoba, Aramaki, Aoba, Sendai 980-8578, Japan*

Corresponding: Makoto Kuji (makato@ics.nara-wu.ac.jp)

Abstract

Aerosol has a crucial role in earth radiation budget on a global scale as well as in a source of air pollution on a regional scale. We investigated atmospheric visual range with aerosol particle size and extinction coefficient using in-situ observation and ground-based remote sensing data to estimate the atmospheric turbidity. In this study, we analyzed the data observed at two SKYNET sites, Fukue-jima (32.6°N, 128.8°E) and Amami-oshima (28.2°N, 129.2°E) islands from 2003 to 2004. Both islands are considered as the best sites to observe the aerosol all through the year because they are located at downwind region where we can observe the Asian aerosol with little influence of local pollution. We have several kinds of in-situ observations and remote sensors at both islands, such as Optical Particle Counter (OPC), LIDAR, skyradiometer, and so on. We estimated the extinction coefficient from OPC and LIDAR measurement data to compare it with atmospheric visual range data obtained by eye observation. We made detailed match-up data analyses based on the report of the atmospheric visual range by Japan Meteorological Agency. We obtained the following results: 1) there is a consistent relationship between OPC and LIDAR measurements, related to the atmospheric visual range; 2) a coefficient in the theoretical relationship between extinction coefficient and atmospheric visual range are consistent to the previous studies; 3) the coefficient is more than double when the atmospheric visual range is less than 10 km. These results suggest that aerosol ground-based measurements with atmospheric visual range observation could provide an index of atmospheric turbidity statistically.

Keywords **:** Atmospheric turbidity, Visual range, OPC, LIDAR, SKYNET

1. Introduction

Aerosol has a crucial role in earth radiation budget on a global scale as well as in a source of air pollution on a regional scale. We investigated atmospheric visual range with aerosol particle size and extinction coefficient using in-situ observation and ground-based remote sensing data to estimate the atmospheric turbidity.

2. Observation data

In this study, meteorological observation data, LIDAR and Optical Particle Counter (OPC) data were used to evaluate the atmospheric turbidity at two SKYNET sites, Fukue-jima (32.4°N, 128.4°E) and Amami-oshima (28.2°N, 129.2°E) islands from 2003 to 2004. Both islands are considered as the best sites to observe the aerosol all through the year because they are located at downwind region where we can observe the Asian aerosol with little influence of local pollution.

Weather conditions and visual range (km) data are provided by Japan Meteorological Agency (JMA) for public use. These meteorological observation data are available from Jan. 2003 to Dec. 2004. In this study, non rainy day and daytime observation (6:00, 9:00, 12:00, 15:00, and 18:00 JST) were used to a make match-up dataset.

LIDAR aerosol extinction coefficient profiles are kindly provided by National Institute of Environmental Studies (NIES)[1)]. These profiles are available from surface to 5970m altitude every 30m from Jan. 2003 to Nov. 2004. We estimated average aerosol extinction coefficients for the lower atmosphere.

OPC data were kindly provided by Chiba University. Particle number per Litter was observed every ten minutes with particle diameter (d in μm) bins: $d \geq 0.3$, $d \geq 0.5$, $d \geq 1$, $d \geq 2$, and $d \geq 5$. These archived data is available from Feb. 2003 to Dec. 2004.

3. Methodology

Generally, meteorological visual range V in km is inversely proportional to atmospheric extinction coefficient σ in km^{-1} as

$$V = \frac{1}{\sigma} \ln \frac{1}{\varepsilon}, \quad (1)$$

where ε is a is threshold of human eye sensitivity for black object[2]. World Meteorological Organization (WMO) recommends 0.05 as ε, for example[3]. In this case, the recommend relationship by WMO is expressed as

$$V = \frac{3.00}{\sigma},$$

which is equivalently expressed as

$$\sigma_{inv} = 0.333V, \quad (2)$$

where σ_{inv} is an inverse of atmospheric extinction coefficient σ. There is other relationship based on the observation[4]

$$\sigma_{inv} = 0.526V. \quad (3)$$

It seems that different proportional coefficients in Eqs. (2) and (3) are relevant to atmospheric condition as well as human eye sensitivity.

In this study, we investigated the relationship between the inverse of the extinction coefficients σ_{inv} derived from LIDAR or OPC measurements and visual range V:

$$\sigma_{inv} = S \cdot V. \quad (4)$$

That is, linear regression curve with zero intercept is estimated with a least square analysis. We discuss the slope S of the regression line in terms of the data with visual range V less than 10 km as well as all match-up data.

Spectral atmospheric extinction coefficients σ_λ are estimated with following relationship

$$\sigma_\lambda = \sigma_{a,\lambda} + \sigma_{m,\lambda} + \sigma_{w,\lambda} + \sigma_{O_3,\lambda} + \sigma_{x,\lambda}, \quad (5)$$

where $\sigma_{a,\lambda}$, $\sigma_{m,\lambda}$, $\sigma_{w,\lambda}$, $\sigma_{O_3,\lambda}$ and $\sigma_{x,\lambda}$ are the spectral extinction coefficients of aerosol, molecular scattering, water vapor, ozone, and other gases, respectively.

The aerosol extinction coefficient $\sigma_{a,\lambda}$ is estimated from LIDAR or OPC observation assuming Mie particles as a constant value over the human eye sensitive spectral range, while other gaseous extinction coefficients are estimated with LOWTRAN 7 assuming US standard atmosphere 1976. We further take the human eye sensitivity every 10 nm into consideration to estimate extinction coefficient σ which is comparable to visual range observation..

4. Results and discussion

We estimated the extinction coefficient from OPC and LIDAR measurement data to compare it with atmospheric visual range data obtained by eye observation. We made detailed match-up data analyses based on the report of the atmospheric visual range by Japan Meteorological Agency.

Figure 1a shows the relationship between atmospheric extinction coefficients using LIDAR aerosol extinction coefficients and visual range at Fukue-jima and Amami-oshima islands from 2003 to 2004. The slope of the regression line is 0.381 for all data (1246 samples), which is consistent to the previous studies within 0.333 to 0.526 in Eqs. (2) and (3). The slope of the regression line is, on the other hand, 0.811 for the data with visual range less than 10 km (79 samples), which is by more than twice all the data.

We could estimate aerosol extinction coefficients using OPC volume spectrum to make Mie simulations assuming bi-modal volume log-normal size distribution:

$$\frac{dV}{d\ln r} = C_1 \exp\left[-\frac{1}{2}\left(\frac{\ln r - \ln r_{m1}}{\ln s_1}\right)^2\right] + C_2 \exp\left[-\frac{1}{2}\left(\frac{\ln r - \ln r_{m2}}{\ln s_2}\right)^2\right], \quad (6)$$

where r is aerosol particle size, C_1 and C_2 are the constants relevant to total volume. The parameters r_{m1} and r_{m2} are the mode radii, while the parameters s_1 and s_2 define size distribution width. The subscripts 1 and 2 for each parameter are for the accumulation and coarse mode, respectively. Using the OPC volume spectrum, we could determine the two parameters C_1 and C_2 out of six parameters in Eq. (6), since it seems that OPC data are most sensitive to the aerosol volume. For the other four parameters r_{m1}, r_{m2}, s_1 and s_2, we assigned the values 0.13μm, 2.00μm, 1.7 and 2.0, respectively, based on the previous study with skyradiometer data analyses. We further assume the accumulation and coarse modes are sea salt and dust, respectively, to provide the refractive index for the Mie calculations. The simulations are carried out at

10nm interval over the visible spectrum range and weighted with the human eye response.

As a result, we obtained the same relationship in Fig. 1b as in Fig. 1a. The slopes of the regression line are 0.342 and 0.807 for all data (626 samples) and the data with visual range less than 10 km (87 samples), respectively.

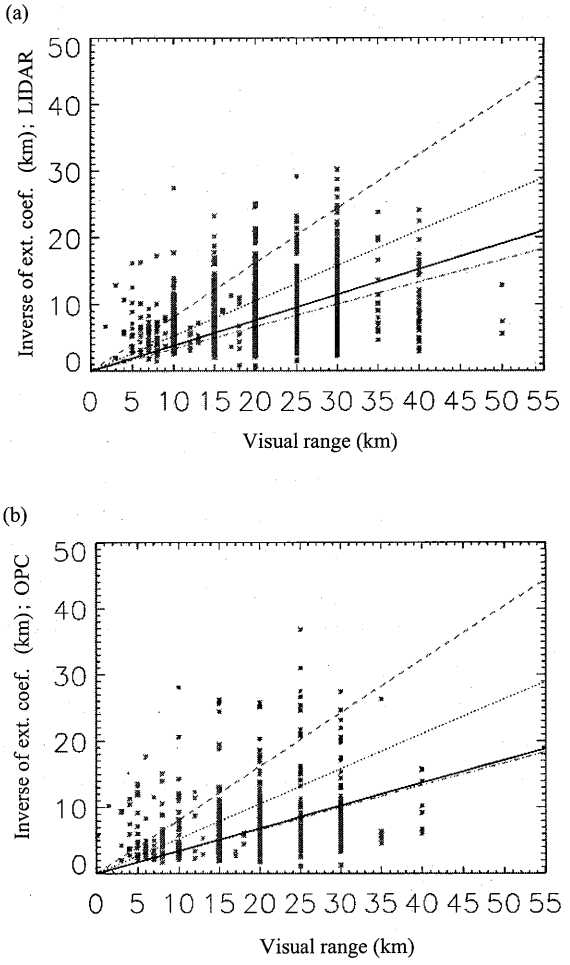

Fig. 1. (a) Relationship between the inverse of atmospheric extinction coefficients estimated with LIDAR observation and visual range at Fukue-jima and Amami-oshima islands in 2003 and 2004. Black and red lines show regression lines for all data and for the data with visual range less than 10 km, respectively. The orange and green lines correspond to Eqs. (2) and (3), respectively as references. (b) Same as Fig. 1a, but for the extinction coefficients estimated with OPC observation.

Table 1 summarizes the above results on the relationships LIDAR and OPC respect to Visual range, respectively (Fig. 1).

Table 1. Statistics of the Slope in Eq. (4).

	All data		Low Visibility*	
	Slope	Number	Slope	Number
LIDAR	0.38	1246	0.81	79
OPC	0.34	626	0.81	87

* Visual range is less than 10 km.

As a consequence, we obtained following points: 1) LIDAR and OPC measurements are consistent in terms of extinction coefficients compared to the visual range. 2) Fukue-jima and Amami-oshima islands are best sites for monitoring atmospheric environment since the slope of the regression lines are consistent to the WMO's. But 3) some deviation from the WMO line suggests the influence of cloud and surface reflection, for example, other than atmospheric attenuation, which encourages that aerosol ground-based measurements with atmospheric visual range observation could provide more detailed atmospheric turbidity statistically.

5. Concluding remarks

We investigated the relationship between the atmospheric extinction coefficient and visual range at Fukue-jima and Amami-oshima islands from 2003 to 2004. As a result, the relationship is consistent to the previous studies, while there exists some deviation in case of lower visibility in particular, which suggests that aerosol ground-based measurements with atmospheric visual range observation could provide more detailed atmospheric turbidity statistically on a basis of monitoring of the atmospheric environment.

Acknowledgements

This study is supported by SKYNET project (NIES / RIHN / CEReS / CCSR) with observation data and valuable comments.

References

1) Shimizu, A., N. Sugimoto, I. Matsui, K. Arao, I. Uno, T. Murayama, N. Kagawa, K. Aoki, A. Uchiyama, and A. Yamazaki (2004), Continuous observations of Asian dust and other aerosols by polarization lidars in China and Japan during ACE-Asia, J. Geophys. Res., 109, D19S17, doi:10.1029/2002JD003253.

2) Bohren, C. F. and E. E. Clothiaux, 2006, Fundamentals of Atmospheric Radiation, pp472, WILEY-VCH Verlag GmbH & Co. KGaA.

3) WMO, WMO GUIDE TO METEOROLOGICAL INSTRUMENTS AND METHODS OF

OBSERVATION □WMO-No.8, CHAPTER9, 2008.
4) Griffing G. W.: Relations between the prevailing visibility, nephelometer scattering coefficient and sunphotometer turbidity coefficient, *Atmos. Environ.*, 14, 577-584, 1980.

Development of West Java Spatial Based Disaster Public Domain

K. Wikantika[1,2], F. Hadi[1,2], A. Hadiyana[1], S. Darmawan[1,2], R. Oktapiana[2]

[1]Center for Remote Sensing, Institute of Technology Bandung
[2]Remote Sensing and GIS Research Division
Faculty of Earth Science and Technology, Institute of Technology Bandung
Gedung LabTek IX-C, Lt. 3, Jl. Ganesha 10, Bandung 40132, Indonesia
Email : ketut@gd.itb.ac.id

Abstract

Indonesia is one of the most disaster-prone countries in the world. On December 26, 2004, a magnitude 9.0 earthquake, whose epicenter was off the west coast of the Indonesian island of Sumatra, caused a tremendously powerful tsunami in the Indian Ocean that devastated 12 Asian countries. Indonesia was the heaviest hit, with more than 150,000 casualties. Many of the deaths occurred in the war-torn province of Nanggroe Aceh Darussalam (NAD). During the initial stage of the reconstruction phase, it is important to know the extent of infra-structural and environmental damage in NAD. This information is used to design a planning development of NAD's infrastructure. To fulfil this purpose, it is necessary to identify areas devastated by Tsunami is needed. This research aims to developing spatial based system which can provide information or data to the communities regarding hazard maps, base maps and other related information needed in evacuation and relocation after disaster events. The system developed is based on the internet which can be accessed, easily and quickly. For the first step, we use West Java as a case study. The system is developed using CartoWeb Open Source. CartoWeb is a web-based geographical information system (WebGIS) which is comprehensive and can be used easily to develop advanced application. Other important thing has been also developed in the system is that the users can design and print the interested areas as map. At a preliminary stage, the system is useful for volunteer, local government officer, and other people who support in evacuation and relocation phases in terms of disaster management.

Keywords : spatial data, disaster, public domain, CartoWeb, open source, webGIS

1. Introduction

A natural disaster is the effect of a natural hazard such as flood, tornado, volcano eruption, earthquake, tsunami or landslide that affects the environment, and leads to financial, environmental and or human losses (wikipedia.org). Indonesia is one of the most disaster-prone countries in the world. On December 26, 2004, a magnitude 9.0 earthquake, whose epicenter was off the west coast of the Indonesian island of Sumatra, caused a tremendously powerful tsunami in the Indian Ocean that devastated 12 Asian countries. At least 225,000 people died in the disaster, and millions were left homeless. Indonesia was the heaviest hit, with more than 150,000 casualties.

Many of the deaths occurred in the war-torn province of Nanggroe Aceh Darussalam (NAD). During the initial stage of the reconstruction phase, it is important to know the extent of infra-structural and environmental damage in NAD. This information is used to design a planning development of NAD's infrastructure. To fulfil this purpose, it is necessary to identify areas devastated by Tsunami is needed. Figure 1 shows the stages of implementing spatial-data management for NAD in carrying out its sustainable development (Wikantika et al. 2007, Wikantika et al. 2009). The stages generally consist of two steps: quick responses and mid-long term responses. The quick-response step yields unsystematic and moderate precision spatial data. While mid-long term focuses on how to produce systematic and accurate spatial data through spatial analysis in detail, modeling, spatial based development including development of spatial based decision support system.

The paper discusses how to develop a system which is based on spatial data to contribute in evacuation and relocation stages in terms of quick response. The system is also developed by using webgis open source. It can be accessed on the internet by communities who want to support

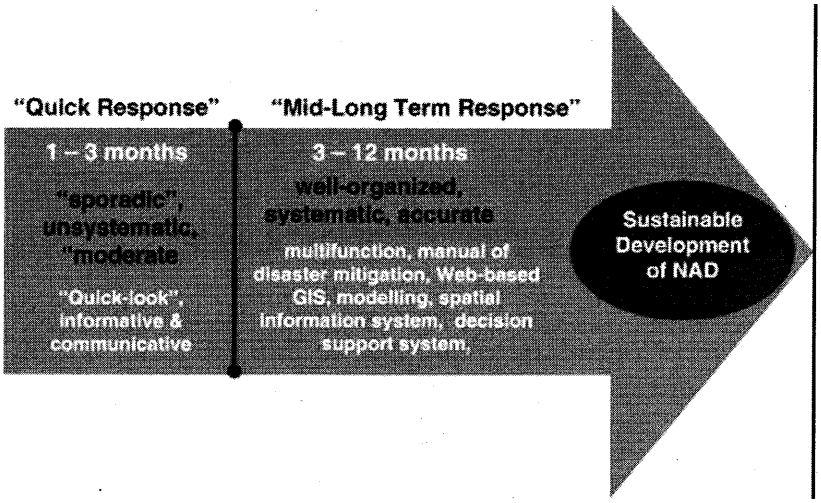

Figure 1. NAD's spatial disaster data management

quick response activities as easily and quickly. In other words, the system can be a spatial disaster public domain. As a case study, part of West Java was chosen for preliminary stage. Several spatial data are used such as topographic and thematic maps as well as remote sensing data.

2. Overview of CartoWeb

Geographical information system (GIS) is a computerized combination between a graphic representation and textual description of a geographic location. GIS also provides the decision maker with a logical and graphic representation of geographically referenced information (webgis.net). GIS is now being developed to run within the internet and worldwide web as well as within private intranets. This also includes how to develop GIS functionality within cline-server networks.

Many applications of GIS are now available based on the internet such as web-based GIS for forest management, urban monitoring, agricultural mapping, population growth analysis even web-based GIS for crime identification. One of the commonly used webgis is CartoWeb. It is based on open source which the source code is freely available. Instantly, we can use the software freely then improve it in appropriate with the applications are being made.

CartoWeb is an advanced GIS for the web. It is a comprehensive and ready to use webgis as well as a convenient framework for building advanced and customized applications (CartoWeb.org). CartoWeb is based on the UMN MapServer engine and is released under the GNU General Public License (GPL). MapServer is an open source platform for publishing spatial data and interactive mapping applications to the web (mapserver.org). The latest version of CartoWeb is 3.5.2 which can be downloaded through internet. CartoWeb adds many functionalities to the raw queries supported by Mapserver. In particular, the queries may be persistent and the hilighting can be defined on a layer by layer basis.

In this research we used Apache 2, Mapserver 5.4.2.1, *php5* (php5-pgsql, php5-mapscript, php5-cli, php-pear , php-mdb2, php-mdb2-driverpgsql), *library* (libpng, freeype, GD, zlib, libproj, libcurl, OGR, GDAL, AGG, libpq, pdflib(lite), PostgreSQL, Postgis, respectively to run CartoWeb. In addition the system is based on Unix platform.

3. Spatial based Disaster Public Domain

As explained above that the system is developed to support local government, volunteers, rescue team and also decision maker therefore it has been designed as simply. Several spatial data are used to build the system such as digital topographic map, land use and land cover map, disaster hazard map (flood, earthquake, landslide, forest fire, volcanic eruption), administration boundary map. West Java area is chosen as a case study because this region is one of the most disaster prone provinces in Indonesia.

The system has three main functions for the first stage of its development, they are

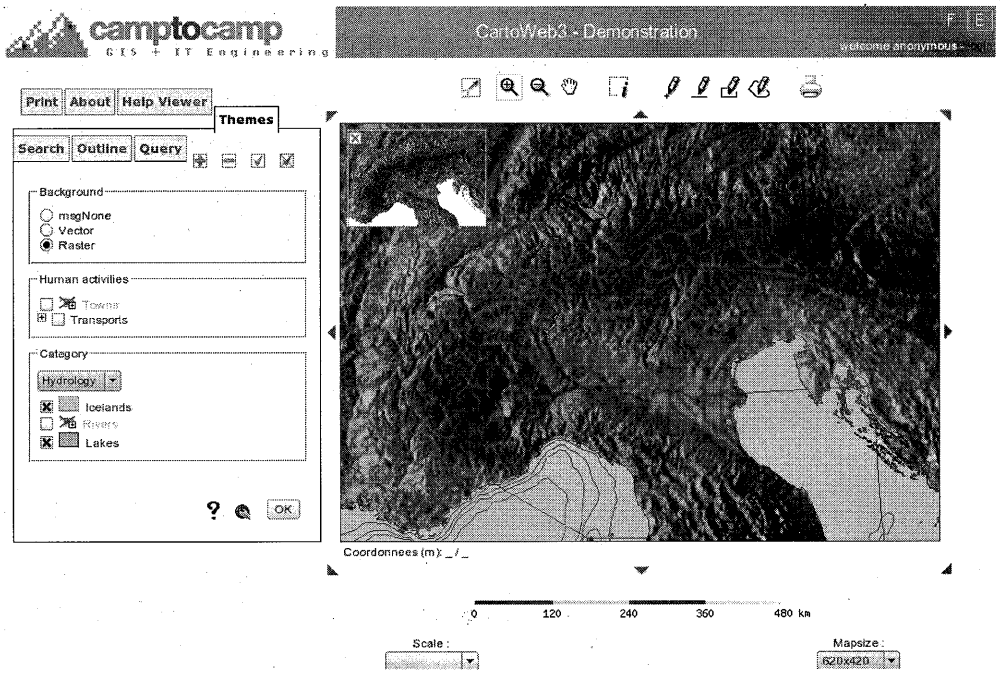

Figure 2. Example of CartoWeb visualization

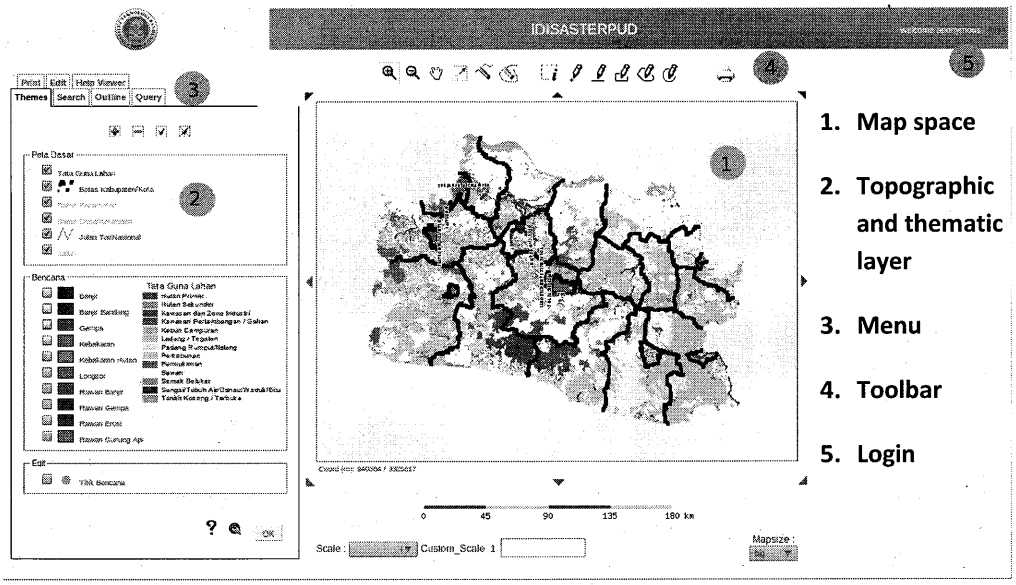

Figure 3. Visualization of disaster types and land use-land cover classes

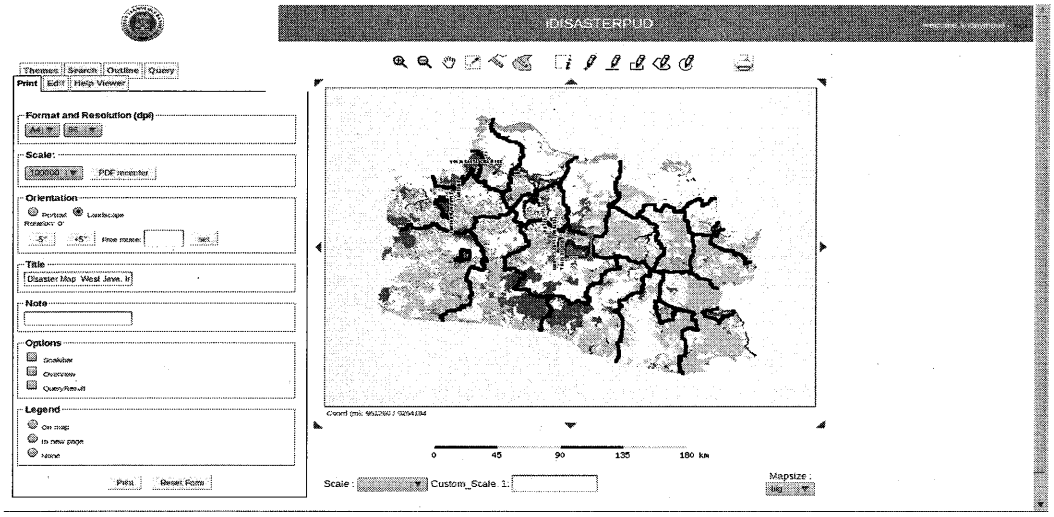

Figure 4. Designing and printing map in PDF

visualization of type of natural disaster derived from disaster hazard maps, searching villages, district, city based on administration boundaries, printing map in PDF format and updating the information regarding disaster events in a certain area within West Java province. The users can visualize thematic information regarding disaster events and also overlay each others with land use and land cover map within study area (Figure 2). To show location of villages, district or cities we can use searching menu. In case of evacuation and relocation steps, we need maps to bring in supporting the activities. Therefore the system can be designing map as simply and print it (Figure 3). To maintain the contents of the system, it is important to accommodate updating function. The users can add new information due to natural disaster events including its attribute.

4. Conclusions

In terms of disaster management, spatial data are very important to support mitigate impacts of the disaster. Local government, volunteers, rescue team, and other people or communities need to access spatial data as simply and quickly. Spatial based disaster public domain can be accommodating the users in evacuation and relocation steps. At a preliminary result, however the research can support the users in assessing impacts of disaster events. In the future, more spatial data are needed to improve the system including how to set qualified networks in distributing the data to the communities. In addition, more spatial data analysis efforts especially from remote sensing data are also important to be conducted. By using some extraction techniques and approaches, remote sensing data can provide thematic information which is useful to modify the system.

Acknowledgments

This research was supported by Directorate General Higher Education, Ministry of National Education, The Republic of Indonesia under contract Competitive Research Grant: National Priority 2009.

References

_____wikipedia.org

_____cartoweb.org

Wikantika, K., Sinaga, A., Hadi, F. and Darmawan, S. 2007 , 'Quick assessment on identification of damaged building and land-use changes in the post-tsunami disaster with a quick-look image of IKONOS and Quickbird (a case study in Meulaboh City, Aceh)', International Journal of Remote Sensing, 28:13, 3037 – 3044

Wikantika, K., Darmawan, S., Hadi, F., 2009, 'Application of Remote Sensing in Demography, Land Use & Land Cover and Disaster: An Indonesia Experience' Proceeding of The ICALRD – JIRCAS Workshop on Enhancement of Remote Sensing and GIS Technologies for Sustainable Utilization of Agricultural Resources in Indonesia,37-43

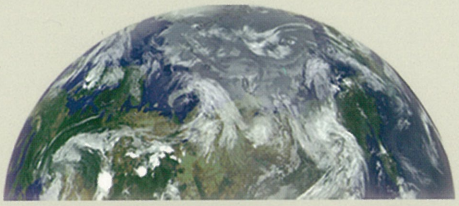

CEReS

Center for Environmental Remote Sensing,
Chiba University